



universität
wien

DISSERTATION / DOCTORAL THESIS

Titel der Dissertation / Title of the Doctoral Thesis

„Novel states of matter for topological polymers“

verfasst von / submitted by

Iurii Chubak, MSc

angestrebter akademischer Grad / in partial fulfilment of the requirements for the degree of

Doktor der Naturwissenschaften (Dr. rer. nat.)

Wien, 2020 / Vienna, 2020

Studienkennzahl lt. Studienblatt /
degree programme code as it appears on
the student record sheet:

UA 796 605 411

Dissertationsgebiet lt. Studienblatt /
field of study as it appears on
the student record sheet:

Physik

Betreut von / Supervisor:

Univ.-Prof. Dipl.-Ing. Dr. Christos N. Likos

Abstract

Functionalized polymeric structures have recently attracted considerable interest due to their responsiveness to externally imposed stimuli. Such systems can be used to design next-generation materials with controllable properties. This work focuses on two classes of polymeric systems with nontrivial architectural composition, stars and rings, that contain functionalized blocks. In each case, the coupling between a stimulus and functionalized blocks introduces distinctive microscopic dynamics that can yield unique macroscopic self-organization pathways. In the case of stars, where the stimulus leads to the solvent quality dependent attraction strength between the functionalized blocks, we find the formation of interconnected micellar aggregates in very dilute solutions and the development of a network-like system structure as the polymer concentration is increased. In the case of rings, where the stimulus is introduced in a non-equilibrium way through different activity levels between functionalized and non-functionalized blocks, we find the formation of a hitherto unobserved state of matter that is built on topological threading constrains and activity at high polymer concentrations — the so-called active topological glass. The properties of equilibrium ring polymer melts as well as of the active topological glass are further discussed in relation to biophysical phenomena in the cell nucleus.

Zusammenfassung

Funktionalisierte Polymerstrukturen haben in letzter Zeit aufgrund ihrer Reaktion auf extern auferlegte Stimuli großes Interesse geweckt. Mithilfe solcher Bausteine können Materialien der nächsten Generation mit kontrollierbaren Eigenschaften entwickelt werden. Diese Arbeit befasst sich mit zwei Klassen von Polymersystemen mit nichttrivialer Architektur, Sternen und Ringen, die funktionalisierte Blöcke enthalten. In beiden Fällen führt die Kopplung zwischen einem Stimulus und funktionalisierten Blöcken zu einer charakteristischen mikroskopischen Dynamik, die einzigartigen makroskopischen Selbstorganisationswege eröffnet. Im Fall von Sternen, bei denen der Stimulus zu einer von der Lösungsmittelqualität abhängigen Anziehungskraft zwischen den funktionalisierten Blöcken führt, finden wir die Formation miteinander verbundener Mizellenaggregate in sehr verdünnten Lösungen und die Entwicklung einer netzwerkartigen Systemstruktur, wenn die Polymerkonzentration erhöht wird. Im Fall von Ringen, bei denen der Stimulus auf eine Nichtgleichgewichtsweise durch unterschiedliche Aktivitätsniveaus zwischen funktionalisierten und nicht funktionalisierten Blöcken eingeführt wird, finden wir die Bildung eines bisher nicht bekannten Materiezustands, der auf topologischen Threading-Einschränkungen und Aktivität bei hohen Polymerkonzentrationen beruht — das sogenannte aktive topologische Glas. Die Eigenschaften von Gleichgewichtsringspolymer-schmelzen sowie diejenigen des aktiven topologischen Glases werden in Bezug auf biophysikalische Phänomene im Zellkern weiter diskutiert.

Acknowledgments

During the last three years I have been fortunate to interact with many outstanding people who helped me a lot along the way to this thesis. I would like to express my immense gratitude to all of you.

First and foremost, I would like to thank my supervisor, Christos Likos, for giving me the opportunity to pursue a PhD in his group and for providing me excellent guidance throughout the years. Christos, thank you for teaching me so much about physics, for showing me how to ask relevant questions, untangle complex problems and pay attention to details, for our countless meetings with enlightening discussions, and for the constant support and helpful advice you have been offering me. I am also extremely grateful for you giving me the freedom to pursue research directions that I found interesting and for encouraging me on the way there. I am hopeful that we will still have a chance to work on many exciting projects in the future!

Without the persistent support and guidance of Jan Smrek, this thesis would certainly be different. Jan, I was incredibly lucky to meet you two years ago, and I would like to thank you for teaching me many aspects of physics and biology, especially about rings and threading, for involving me in many fascinating projects, and for your encouragement, helpful advice, and insightful suggestions. I have certainly learned a lot from you and I will miss our daily discussions and working habits that we have developed over the years. We still have many problems to crack and, hopefully, not all of them were already solved in the sixties!

This thesis would not have been possible without the collaboration with many remarkable scientists, to whom I would like to express my sincere gratitude. I would like to thank the whole team of the SUSTUP project for the fruitful and long-lasting cooperation. I am deeply indebted to Esmael Moghimi and Dimitris Vlassopoulos for important insights into the experimental findings and our far-reaching and illuminating discussions about stars, rings, and beyond; to Nikos Hadjichristidis for helpful comments about polymer synthesis; and to Antonia Statt, Michael Howard, and Athanassios Panagiotopoulos for many valuable discussions about computational modeling and our joint work on sim-

ulations, from which I was able to learn a lot. I would like to especially thank Kurt Kremer and Stanard Pachong for the extremely interesting and productive collaboration on equilibrium and non-equilibrium ring polymer melts and for many valuable insights into polymer physics and computer simulations. Furthermore, I want to thank Zahra Ahmadian Dehaghani and Mohammad Reza Ejtehadi for our exciting work on polycatenanes, and Sergei Egorov for the pleasant ongoing collaboration on confined ring polymer solutions. Lastly, I would like to acknowledge helpful and interesting discussions with Roman Barth, Barbara Capone, Roberto Cerbino, Kostas Daoulas, Haitham Shaban, Panagiotis Theodorakis, Mukta Tripathi, and Manos Vereroudakis.

I also want to express my special thanks to friends and colleagues at the Soft Matter Theory and Simulation Group. Nataša Adžić, Emanuela Bianchi, Ronald Blaak, Thiago Colla, Ioana Gârlea, Adam Höfler, David Toneian, Diego Jaramillo Cano, Martin Jehser, Maximilian Liebetreu, Emanuele Locatelli, Ilian Pihlajamaa, Ivonne Ventura Rosales, Lisa Weiß, Eva Wildfellner thank you all for your warm welcome and for the very pleasant time that I have had in the group! Ioana, Nataša, Emanuele thank you for plenty of valuable advice and many interesting and helpful discussions, for all the teaching that we did together, and your readiness to help whenever I had a question. Emanuele, thank you for supporting me during my first project when I joined the group as a Master's student and for many useful tricks that I learned from you afterwards. Ioana, I am glad that we could share the office during the past years! Adam, it has been enjoyable to co-supervise you on the way to your thesis. David, Diego, Martin, Max, Ivonne, Lisa, thank you for many valuable discussions and good company that we had as PhDs in the group. I am also grateful to the whole Computational and Soft Matter Physics Group at the University of Vienna and the Vienna Doctoral School in Physics for providing a friendly and stimulating working environment.

Lastly and most importantly, I want to thank my wife Olesya Stankevych and my family for love, support, valuable advice, constant encouragement and inspiration on the way to completing this thesis.

This work was supported by KAUST under grant OSR-2016-CRG5-3073-03, the Austrian Science Fund (FWF) through the Lise-Meitner Fellowship No. M 2470-N28 and the SFB ViCoM (F41), Vienna Doctoral School in Physics, and the European Research Council under the European Union's Seventh Framework Programme (FP7/2007–2013)/ERC Grant Agreement No. 340906-MOLPROCAMP. I am grateful for generous computational resources at the Vienna Scientific Cluster and the Max Planck Computing and Data Facility.

Contents

Abstract	2
Zusammenfassung	3
Acknowledgments	4
Table of contents	6
1 Introduction	8
2 Self-organization and flow of low-functionality telechelic star polymers with varying attraction	17
2.1 Introduction	18
2.2 Methods	19
2.3 Results	21
2.4 Conclusions	27
2.5 Supplementary Information	28
3 The influence of arm composition on the self-assembly of low-functionality telechelic star polymers in dilute solutions	45
3.1 Introduction	46
3.2 Materials and methods	47
3.3 Experimental results	51
3.4 Simulation results	55
3.5 Conclusions	61
4 Active topological glass	63
4.1 Introduction	63
4.2 Results	65
4.3 Discussion	74

4.4	Conclusions	79
4.5	Supplementary Information	80
5	Emergence of active topological glass through directed chain dynamics and non-equilibrium phase segregation	96
5.1	Introduction	97
5.2	Model	101
5.3	Onset of glassy dynamics	103
5.4	Conformational properties	109
5.5	Phase separation	115
5.6	Conclusions	121
5.7	Supplementary Information	124
6	Melts of nonconcatenated rings in spherical confinement	126
6.1	Introduction	126
6.2	Model	129
6.3	Results	131
6.4	Discussion and conclusions	145
6.5	Supplementary Information	148
7	Active topological glass as a model for coherent motion of chromatin	155
7.1	Introduction	156
7.2	Model	158
7.3	Results	160
7.4	Conclusions	167
8	Conclusions and outlook	170
	Bibliography	173
	Curriculum vitae	199

Chapter 1

Introduction

Modern chemistry enabled the synthesis of a variety of polymeric and colloidal systems that, often mimicking recurrent biological phenomena, can respond in a controlled manner to the influence of external stimuli [1, 2, 3, 4, 5]. The latter can be either of physical (light, temperature, mechanical force, electromagnetic or flow fields), chemical (pH, solubility, ionic strength), or biological (enzymatic activity, protein bindings) origins [2, 6, 7, 8, 9, 10, 11, 12]. A prototypical example of such systems are polymer solutions, in which polymer chains contain functionalized blocks that are sensitive to one or more of the above-mentioned factors. Then, for example, the solubility of such blocks can be tuned through an external stimulus, like temperature or pH, which can lead to a distinct self-assembly pathway both at the single-molecule as well as on the many-chain level. As a result, potential inter-molecular associations between the blocks can give rise to supramolecular gel-like assemblies that have profoundly different macroscopic properties [2, 13]. Furthermore, of prime importance is the reversibility of such states of matter that is simply achieved through the removal of external stimuli, and results in the relaxation of the system to its original state. Therefore, the available variety of possible stimuli offers an unprecedented flexibility in designing materials at a range of length scales that can operate both at equilibrium and non-equilibrium conditions, surpassing traditional capabilities of atoms and molecules as fundamental material building blocks [1, 2, 13]. A formidable challenge in this vast landscape of constituting blocks is to be able to design and predict the system response in line with a specific technological or biomedical application [14]. This includes a proper understanding of self-assembly scenarios of the system as a function of the external stimulus as well as of its resulting macroscopic (e.g., rheological) response.

This thesis focuses on two classes of objects, in which architectural and topological constraints are of particular importance: polymer rings and polymer stars. In both

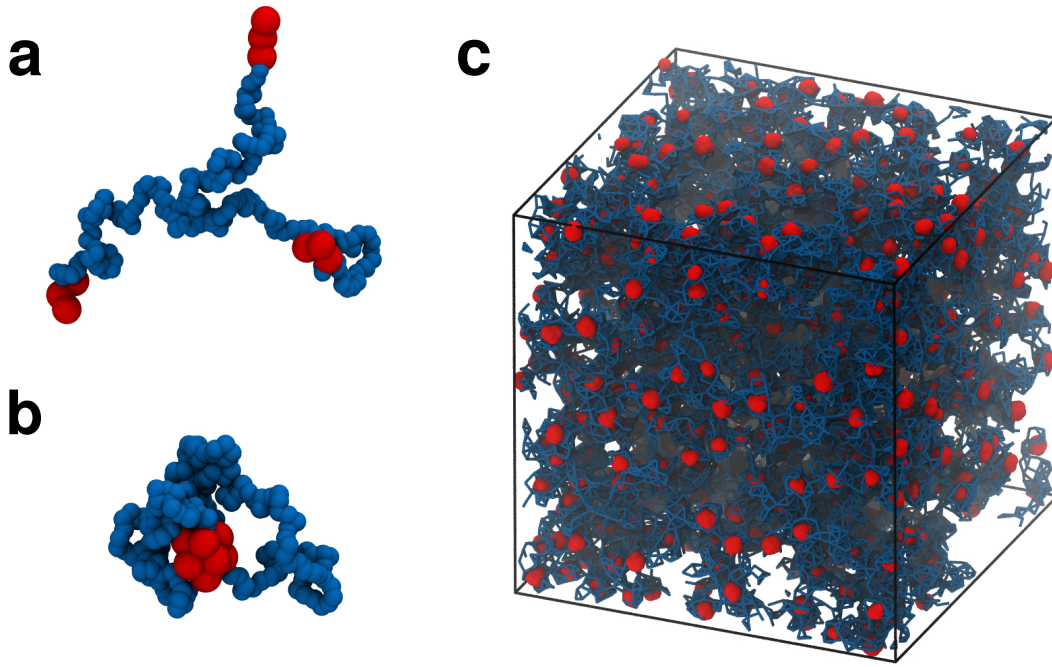


Figure 1.1: Self-assembly of low-functionality telechelic star polymers. **a**, A single telechelic star with three arms in good solvent conditions for both inner (blue) and outer (red) blocks. **b**, A well-defined patch is formed if the solvent quality becomes worse for the outer (functionalized) block but remains good for the inner one. **c**, At the latter condition, the system self-assembles into an interconnected network-like structure at dilute TSP concentrations. In this case, the TSP concentration is around $c \approx 0.6c^*$, where c^* is the overlap concentration.

cases, the polymers are assumed to contain functionalized blocks that can be controlled through an external stimulus. The presence of stimuli affects the *microscopic* dynamics of responsive blocks, which, due to nontrivial architectural and topological properties of considered polymeric structures, can lead to unique *macroscopic* self-assembly scenarios. In this work, we will explore the response of the systems to a stimulus and the resulting single-molecule and many-chain states, with a notable difference that the external control is achieved in an equilibrium fashion for stars, however, in a highly non-equilibrium way for rings. In what follows, we will introduce the investigated systems and we will provide a short overview of the main problems considered in this work in relation to recent developments in soft and active matter physics.

Star polymers are composed of a certain number of linear chains, often called arms, connected to a common center. In the first part of this thesis (Chapters 2 and 3), we will focus on a special type of stars that contain functionalized blocks attached to the tips of their arms, the so-called Telechelic Star Polymers (TSPs) [15]. Such structures have recently attracted interest due to a high degree of their tunability that offers flexibility

in designing smart, responsive, and self-healing materials [16, 17]. Indeed, the changes in the external control parameter (like temperature or pH, as described above) can induce a propensity for associations between the functionalized blocks. This, on the other hand, leads to a variety of self-assembly scenarios at multiple length scales that are particularly sensitive to *(i)* system density, *(ii)* association strength, and *(iii)* TSP architecture [16]. The TSP architecture, given by the number of star arms, their length, as well as the length of functionalized blocks, determines the self-assembly pathway at the single star level upon increasing the association strength [16, 18, 17]. This typically results in the formation of one or few well-defined attractive patches (see Figure 1.1), reminiscent of patchy colloids [19, 20], albeit with a soft core in this case. Upon increasing the TSP concentration, diverse self-organized structures have been shown to exist. The latter include spherical and wormlike micellar aggregates in very dilute solutions [16, 21, 22, 23, 24] as well as network-like structures at TSP concentrations comparable to their overlap one [25, 17, 26]. It is expected that more ordered structures emerge at higher concentrations, in line with the behavior of diblock co-polymers in selective solvents [27]. In any case, even in quite dilute TSP systems, inter-star associations induce a nontrivial network connectivity that might strongly influence the solution's flow behavior. Therefore, the combination of the above-described control parameters allows to fine-tune the macroscopic response of TSP systems. In Chapter 2, we will consider a specific realization of a three-arm TSP solution and we will apply a combination of experimental and computational approaches to shed light on its behavior in dilute conditions. Furthermore, a particular focus will be placed on the relationship between the end-block association strength and the ensuing TSP structure formation. The influence of the TSP architecture will be considered in more detail in Chapter 3.

The rest of this thesis deals with melts of ring polymers. The latter can be created by splicing together the ends of a linear chain. Despite the apparent simplicity, such an operation has profound consequences for properties of ring polymer systems. The differences stem from a unique topological state of a ring, which is set during the synthesis, that in the simplest and most studied case represents an unknotted chain that is not linked with any of its neighbors. Indeed, to change the initial ring's topology at least some bond crossings are necessary, which is comparable to overcoming an energy barrier of a typical covalent bond, $E_{\text{bond}} \approx 100k_{\text{B}}T$, which is practically impossible if only energy exchange with a heat bath at temperature T is present. Therefore, the ring's topological state imposes a significant entropic constraint in the phase space of attainable configurations [28]. Even at dilute and semi-dilute conditions this brings about a series of interesting

phenomena that demarcate rings from linear chains. In particular, such phenomena, among many others, include self-avoiding statistics for rings with no excluded volume interactions but properly taken into account uncrossability constraints [29], an effective topological repulsion between two rings at infinite dilution [30, 31, 32], a higher propensity of rings to structure at the confining walls [33, 34] and a lower θ -temperature of ring polymers in solution as compared to linear counterparts [35], as well as hydrodynamic swelling of rings in shear flow [36].

The role of topological constraints becomes even more important as concentrated solutions and melts of long unknotted and nonconcatenated rings are considered. While linear polymers at such conditions assume ideal random walk statistics and their dynamics is well understood in terms of tube and reptation models due to Edwards and de Gennes [37, 38], the situation is much more complex for rings [39], where the snake-like reptation is clearly impossible due to the absence of chain ends. Instead, rings feature an amoeba-like motion, in which they explore the neighboring environment by forming branched and folded segments that constantly protrude and retract in the mesh of obstacles imposed by other rings [39, 40]. A series of effective models have been constructed since the 1980s to rationalize the behavior of rings in the concentrated regime. In particular, such models rely on (i) considering rings as being on a lattice of fixed obstacles [41, 42, 43], (ii) assuming a double-folded annealed branched structure for rings, as in the annealed tree model [44, 45, 40], (iii) using certain fractal curves to reconstruct ring conformations [46, 47], (iv) approximating topological effects with an effective excluded volume [48], as well as others [49]. A major success of these advances, largely backed up by computer simulations [50, 51, 52, 49, 53, 54, 55, 56] and catching up experiments [57, 58, 59, 60, 61], was to establish that long unknotted and nonconcatenated rings in the melt assume crumpled globule conformations with their size R scaling with the polymerization degree N as $R \sim N^{1/3}$, unlike to $R \sim N^{1/2}$ for linear chains. On the other hand, despite the collapsed structure, the rings feature relatively penetrable conformations with the number of their “surface” monomers, that is the number of monomers in contact with other chains, scaling as $\sim N^\beta$ with β close to (but smaller than) 1 [50]. As for the dynamics, the rings feature a significantly prolonged subdiffusive regime before the diffusion onset in their mean-square displacements in the melt as well as a much weaker scaling of viscosity with N as compared to linear polymers [51]. As a consequence of such properties, the ring melts relax stress differently, featuring a power-law regime with absent entanglement plateau, which is characteristic for linear counterparts [57, 51]. While the predictions for the scaling of various static and dynamic quantities depend on the structure of the

underlying effective theory [44, 45, 47], it is difficult to single out the best model because the available estimates are generally close to each other and consistent with simulations to date [50, 51, 52, 53]. However, it has been shown that the conformations of a single ring from the melt are quantitatively consistent with the tree-like structure [52, 53, 62].

There exists, however, a paradox. In the melt state, rings are subject to a special type of constraints, where one ring pierces through the opening of another one, forming the so-called threading [63, 64, 65, 54]. While most of the available theories neglect the presence of threadings or treat them in a simplified fashion, it has recently been conjectured that they can actually dominate the behavior of sufficiently long rings [65, 66, 67]. The conjecture relies on the observation that the dynamics of a threading pair of rings is slowed down until the unthreading takes place [67]. Since threading events become more likely with increasing N , a hierarchical network of interpenetrations can develop, causing a significant slow-down of rings' diffusivity [68], the so-called state of topological glass that is built up solely on inter-molecular entanglements [69]. A similar conclusion has been inferred from pinning perturbations of ring melts [66, 70] as well as for ring polymers confined to a gel matrix [65, 71]. Nevertheless, in none of such cases the topologically jammed state has been observed explicitly, whereas the predicted critical ring lengths for the transition were beyond the reach of numerical simulations. On the other hand, the success of theoretical tree models [44, 45] in explaining static and dynamic properties of rings in the melt implies that threadings must be quantitatively insignificant (at least for the examined range of N). Note, however, that the picture of double-folded ring conformations with randomly branched tree-like structure is not entirely complete, as it underestimates threadings, as recently shown in Ref. [72]. What is then the precise role of threadings for the dynamics of rings in the melts? Do they eventually lead to a topologically jammed state in the asymptotic limit of increasing N or their effect becomes marginal as inferred from current theoretical models?

While in equilibrium melts inter-ring threading is mainly enhanced by increasing the ring length, currently making the progress in this direction unfeasible, the question has been raised, whether the topological glass can be obtained in other ways. In the second part of this thesis (Chapters 4 and 5), we will show how such topological jamming arises from the deformation of rings under the influence of local non-equilibrium activity mechanisms, giving rise to a novel state of matter — the so-called active topological glass. In particular, we will focus on a model where rings in the melt contain functionalized blocks that are subject to uncorrelated, thermal-like fluctuations, stronger than for the rest of the chain. We will show that the presence of active segments results in significantly stretched

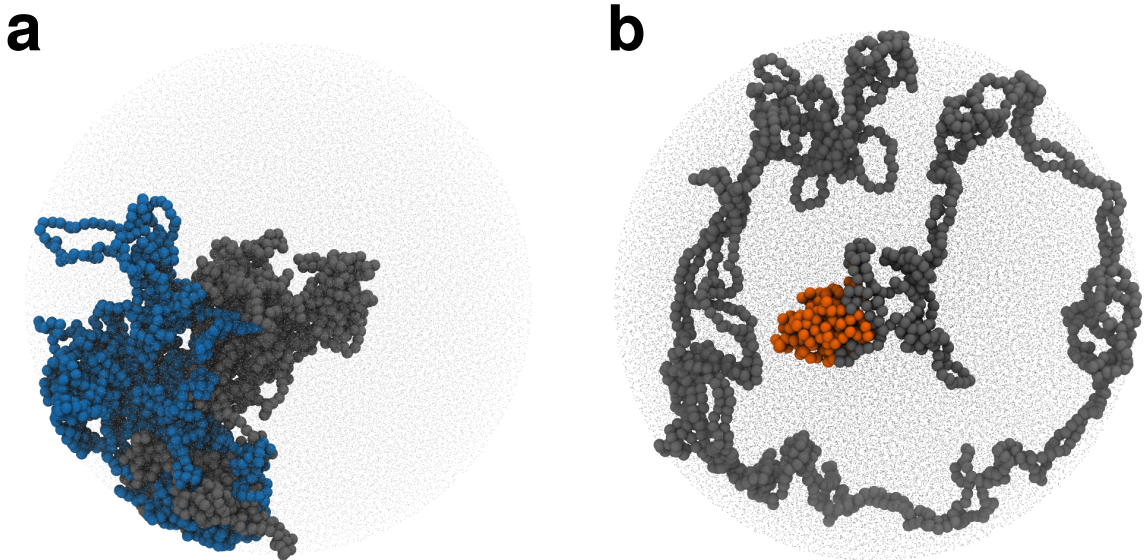


Figure 1.2: Comparison between conformations of equilibrium and non-equilibrium rings in a spherically confined system. **a**, A pair of two threading rings in the melt. **b**, A single partly active ring in the melt. The active monomers are highlighted in orange. In both cases, the system consists of $M = 46$ rings of length $N = 1600$ confined within a sphere of the same radius at density $\rho = 0.85\sigma^{-3}$ (σ is the diameter of one monomer).

and elongated ring configurations (see Figure 1.2 for a comparison between steady-state conformation of equilibrium and activity-driven rings in the melt state). Such rearrangements lead to increased inter-ring threading that pronouncedly inhibits relative motion of the rings. In general, the employed model mimics a heterogeneous mixture of particles that operate at different levels of activity and are effectively described by having two distinct temperatures [73, 74, 75, 76]. It was shown that a two-temperature mixture of colloidal particles with purely repulsive interactions can demix, provided that their temperature difference is quite high [73, 77]. On the other hand, the activity difference necessary for phase segregation is reduced in mixtures of active and passive polymers [78, 79]. The latter behavior reminisces that of equilibrium polymer mixtures, where the phase segregation between polymer chains occurs due to small differences in their inter-monomer interactions [80]. However, for the activity-driven demixing to happen it is apparently necessary to have $\chi \gtrsim 1/\sqrt{N}$ [78, 75], where χ is an appropriately defined Flory parameter in the non-equilibrium case [78] and N is the polymer length, being in sharp contrast to $\chi \gtrsim 1/N$ in equilibrium [80]. The role of the non-equilibrium phase segregation for the formation of the active topological glass is discussed in Chapter 5.

In the third part of the thesis (Chapters 6 and 7), we will focus on a relatively small system of rings enclosed in a sphere at melt conditions. We will consider both detailed

static and dynamic properties of equilibrium ring polymer melts as well as the formation of the active topological glass in such setting. Furthermore, we will discuss these systems in the context of the interphase chromatin organization problem within the eukaryotic cell nucleus. Note that here and in what follows we will refer to chromatin as to a combination of the double-stranded DNA fiber and histone proteins on which DNA is wrapped on [81, 82]. Very long chains of chromatin that carry genetic information form multiple independent chromosome molecules in the nucleus (e.g., 46 for the human genome). Individual chromosomes can be clearly observed during mitosis (the cell division stage) where they embrace very compact, condensed conformations [81]. On the other hand, during the interphase, when the transcription of relevant genes into RNA occurs, the chromosomes attain swollen conformations and occupy well-defined territories that do not intermix much [83]. Such territoriality markedly contrasts with the equilibrium arrangement of linear polymer chains in concentrated solutions or melts, where the former feature expanded conformations with ubiquitous inter-chain contacts. From the polymer physics perspective, the territoriality of chromosomes can be explained from topological uncrossability constraints that dominate chromatin dynamics at nuclear conditions [84, 85, 86]. Provided that chromosomes have free ends (which is strictly speaking not always the case due to their possible attachment to the nuclear lamina [85, 86]), the chains will relax *via* the slow reptation mechanism [37, 38]. However, as estimated in Ref. [84], the relaxation time for this process is much greater than typical physiological time scales in higher eukaryotes. Therefore, during the interphase, the chain ends can be neglected entirely, whereas the chromosome conformations should resemble that of unknotted and nonconcatenated rings in concentrated solutions [84]. This surprising analogy is further supported by the fact that both ensembles of configurations are consistent [87, 88, 51] with the so-called crumpled (fractal) globule model [89, 90]. The latter model assumes self-similar polymer conformations that feature $R \sim N^\nu$ with $\nu = 1/3$ together with the probability of finding two monomers separated by the contour distance s close to each other scaling as $P(s) \sim s^{-\gamma}$ with $\gamma \simeq 1$. While ring polymer melts have been studied extensively in the bulk, it is not clear what happens with the properties of a relatively small system of rings subject to spherical confinement. This is especially relevant in the biological context, as explained above. A detailed account on this problem is provided in Chapter 6 of this thesis.

The interest behind investigating the active topological glass in spherical confinement, following up on the results obtained in Chapter 6, is twofold. First of all, it is interesting to verify if the topological glass can generally form in such conditions. As explained above,

this state of matter arises from significantly elongated ring conformations that result in enhanced topological constraints. It is therefore questionable if a sufficient degree of inter-molecule threading for the topological glass formation can eventually develop within a cavity, as confinement naturally limits the potential expansion of the rings. On the other hand, as explained in Chapter 4, the numerical simulations of the active topological glass in periodic boundary conditions require rather large systems to ensure that spurious self-threadings of rings do not happen. This, therefore, restricts the studies to rather short ring lengths ($N \lesssim 400$). We will show in Chapter 7 of this thesis that the presence of active segments in a relatively small system of rings confined within a sphere similarly leads to glassy states. Furthermore, we find that active segments in such systems are generally colocalized and form a phase-segregated blob. Interestingly, we also observe that threading in this case can be enhanced through multiple reflections of the stretched rings from the confining wall, as for example seen in Figure 1.2. Second of all, it is interesting to explore if the active topological glass phenomenology can be relevant for other chromatin organization problems, in particular those related to active processes on the chromatin fiber (e.g., remodeling or loop extrusion [81, 82]). In this case, we generally focus on the phase segregation between more dilute, actively transcribed parts of the genome (euchromatin) and its more dense, inactive regions (heterochromatin) [91, 92, 87]. It has long been questioned if the latter phenomenon is mainly driven by differences in chemical interactions between eu- and heterochromatin [93] or by active, non-equilibrium processes that happen in chromatin fibers on smaller scales [94, 95, 96, 97, 98]. While it is obvious that the structure of the active topological glass breaks territoriality of rings and, thus, cannot be used to describe the large scale chromosome arrangement, in Chapter 7 we discuss its possible role for smaller-scale chromatin organization, where loop extruders induce a unique loopy structure [99]. More specifically, we will focus on the correlated chromatin dynamics [100, 101] that arises from topological constraints and active processes.

In summary, this thesis is structured as follows:

Chapter 2 examines the self-assembly and flow behavior of a solution of three-arm TSPs in the dilute regime for different association strengths between the end-blocks.

Chapter 3 considers the effect of star architecture on the self-assembly properties of three-arm TSPs in dilute solutions.

Chapter 4 discusses the formation of the active topological glass in the systems of rings with functionalized active blocks. Elaborates on the possible type of this glass

transition by considering systems with a different fraction of partly active chains.

Chapter 5 elucidates the role of the non-equilibrium phase segregation for the active topological glass formation and provides a detailed study on dynamic and static steady-state properties of partly active rings in such systems.

Chapter 6 contains a detailed study of static and dynamic properties of equilibrium ring melts composed of a fairly small number polymer chains confined within a sphere. A systematic comparison with the bulk results is provided.

Chapter 7 is devoted to the formation of the active topological glass in spherical confinement and its potential relation to phenomena observed within the eukaryotic cell nucleus.

Chapter 8 summarizes all results of this thesis and provides a broad outlook for the directions of future work.

Chapter 2

Self-organization and flow of low-functionality telechelic star polymers with varying attraction

Published: Esmael Moghimi, Iurii Chubak, Antonia Statt, Michael P. Howard, Dimitra Founta, George Polymeropoulos, Konstantinos Ntetsikas, Nikos Hadjichristidis, Athanasios Z. Panagiotopoulos, Christos N. Likos, and Dimitris Vlassopoulos, Self-organization and flow of low-functionality telechelic star polymers with varying attraction, *ACS Macro Letters* **8**, 766-772 (2019). DOI: 10.1021/acsmacrolett.9b00211¹

We combine state-of-the art synthesis, simulations and physical experiments to explore the tunable, responsive character of telechelic star polymers as models for soft patchy particles. We focus on the simplest possible system: a star comprising three asymmetric block copolymer arms with solvophilic inner and solvophobic outer blocks. Our dilute solution studies reveal the onset of a second slow mode in the intermediate scattering functions as the temperature decreases below the θ -point of the outer block, as well as the size reduction of single stars upon further decreasing temperature. Clusters comprising multiple stars are formed and their average dimensions, akin to the single star size, counterintuitively decrease upon cooling. A similar phenomenology is observed in simulations upon increasing attraction between the outer blocks and is rationalized as a result of the interplay between inter-star associations and steric repulsion between the star cores. Since our simulations are able to describe the experimental findings reliably, we can use them

¹Author contributions: G. P., K. N., and N. H. synthesized the polymers. E. M., D. F., and D. V. performed the experiments. I. C. and C. N. L. developed the blob model. I. C. numerically derived the coarse-grained potentials and performed the coarse-grained blob simulations. A. S., M. P. H., and A. Z. P. carried out the study of star behavior in shear flow. All authors interpreted the results and wrote the manuscript.

with confidence to make predictions at conditions and flow regimes that are inaccessible experimentally. Specifically, we employ simulations to investigate flow properties of the system at high shear rates, revealing shear thinning behavior caused by the break-up of inter-star associations under flow. On the other hand, the zero-shear viscosity obtained experimentally exhibits a rather weak activation energy, which increases upon rising star concentration. These findings demonstrate the unusual properties of telechelic star polymers even in the dilute regime. They also offer a powerful toolbox for designing soft patchy particles and exploring their unprecedented responsive properties further on.

2.1 Introduction

Recently, soft responsive materials have gained a steadily increasing relevance in engineering applications and research because of their functional properties that can be selectively tailored during preparation and/or via external fields [1, 102, 103]. Supramolecular polymeric assemblies are of particular interest in industrial applications because of their outstanding stimuli-responsiveness and their concomitant reversible properties such as self-healing and shape memory [103, 104, 105, 106]. In fact, these materials can dramatically change their shape and/or phase under the influence of external stimuli, e.g., temperature, irradiation, pH, electromagnetic fields or flow [107, 108, 109]. Moreover, the use of biologically relevant composites as building blocks of such assemblies opens up a road for designing novel materials for biomedical or environmental technologies. Single DNA strands serve as a notable example of such programmable units that have been exploited for versatile structure formation [110, 111, 112].

In this work, we present a strategy for developing and investigating well-defined star-shaped block-copolymer systems in solvents of varying quality that act as building blocks for supramolecular assemblies using a combination of synthesis, simulations and physical experiments. Given the broad scope and advances in the field of associating polymers [113, 114], we focus on telechelic star polymers (TSPs), which carry associating monomers at their ends [115, 116, 117]. A TSP comprises f AB-block copolymers (arms) grafted on a common center with their solvophilic A-blocks being at the interior of the star and their solvophobic B-blocks attached to the end of each arm. In what follows, N_A and N_B denote the number of A- and B-type monomers in a star arm, respectively, and $\alpha = N_B/(N_A + N_B)$ is the relative size ratio between the two block lengths.

The behavior of dilute and concentrated TSP solutions is predominantly governed by the functionality f of the stars, the block size ratio α , and the attraction strength between

the solvophobic B-blocks that becomes stronger upon worsening solvent quality. Likewise, structural and viscoelastic properties of melts, in which end-blocks of TSPs associate due to the enthalpic A-B interactions, have been shown to be controlled by the temperature-dependent interplay of intra- and inter-molecular associations [15, 118, 119, 120]. At infinite dilution, TSPs under such selective solvent conditions form well-defined patches, which allows us to regard them as an experimental realization of soft patchy particles [116, 121, 122, 17]. Their conformational state-diagram at θ -like conditions for the B-blocks has been set forward in Refs. [17, 26] based on simulations of an effective blob model. It has been shown that the patchiness of high functionality TSPs is maintained at finite concentrations and can facilitate the formation of ordered lattices having coordination compatible with the number of patches of a single TSP, suggesting the use of TSPs as tunable building blocks for the formation of multiscale hierarchical supramolecular structures [104, 17, 26, 18]. In contrast, as shown by means of extensive on-lattice simulations, solvophobic blocks of low functionality TSPs tend to form micellar aggregates [24, 23, 22, 123] that can subsequently self-organize at higher concentrations into long wormlike micelles bridged by arms of individual stars [24, 21]. Finally, compared to triblock copolymers (i.e., $f = 2$), which tend to self-organize into flower-like micelles that interconnect at higher concentrations [124, 125], star-shaped copolymers have a higher propensity to form intermicellar bridges, as they can split their three arms into three distinct micelles. Therefore, they are expected to have distinct rheological properties.

These predictions have not yet been fully tested, let alone materialized experimentally, in a systematic way that exploits the versatility of TSP structures and properties. In particular, of prime importance are the exact role of tunable attractions between the outer blocks of TSPs, the corresponding structure formation in concentrated systems, and the associated change of macroscopic properties (such as viscosity) due to microstructural reorganization in flow. In this article, we address these questions to demonstrate the exciting possibilities for designing and fabricating novel materials with tailored rheology.

2.2 Methods

Well-defined 3-arm star diblock copolymers (PS-*b*-PB_{1,4})₃ were synthesized by anionic polymerization and chlorosilane chemistry using high-vacuum techniques in custom made glass apparatuses. The weight-average total molar mass was $M_{w, \text{LS-SEC}} = 26700$ g/mol, the associated polydispersity was $\text{D} = 1.03$, and the weight fraction of terminal polystyrene blocks was $f_{\text{PS}} = 23$ %w/w. The stars were dissolved in 1-phenyl dodecane, which is a

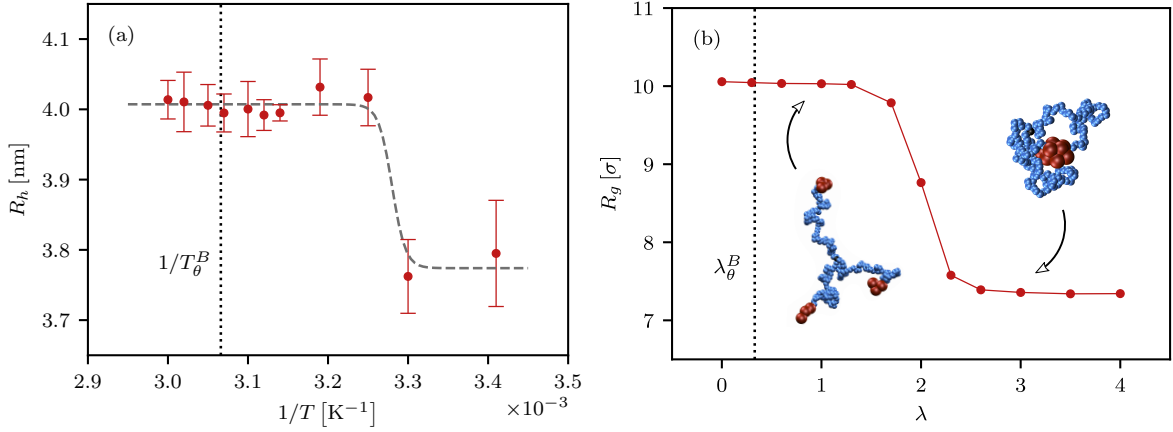


Figure 2.1: Comparison between single star properties for a star with $f = 3$ arms of $N_A = 65$ and $N_B = 3$, in experiments and simulations. **a**, Hydrodynamic radius, R_h , extracted from the fast process in the experimentally determined ISFs at $c = 0.11c^*$. The dashed line is a guide to the eye. **b**, Simulated radius of gyration of the same TSP in units of the A-monomer diameter σ as a function of the attraction parameter, λ . Insets illustrate typical conformations of the TSP at corresponding values of λ . Dotted vertical lines in **a** and **b** correspond to the θ -point of the outer block.

θ -solvent for the outer PS block [126] with a cloud-point at 53.5 °C and a θ -solvent for the inner PB block at 22 °C. In addition, this solvent has a boiling point of 330 °C at atmospheric pressure and is therefore amenable to rheological experiments. The dynamics of the system were measured by Dynamic Light Scattering (DLS) and the shear viscosity by rheology. Details about the synthesis and solution preparation, as well as DLS and rheological measurements, can be found in the Supporting Information 2.5.

We developed a complementary coarse-grained simulation model for the TSPs based on the Kremer–Grest model [127] for linear polymer chains in a good solvent. Interactions between the A-A and A-B pairs were purely repulsive, mimicking good solvent conditions, while the B-B pairs had a Lennard-Jones-type attraction with a controllable strength λ , which denotes the depth of the potential well [128] and is proportional to an inverse temperature. $\lambda = 0$ is a good solvent, $\lambda = 0.33$ is a θ -solvent for a linear homopolymer, and increasing it decreases the solvent quality. To directly compare with experiments, we simulated 3-arm stars with $N_A = 65$ and $N_B = 3$, which correspond to the number of Kuhn segments in the studied TSP sample (see Supplementary Section 2.5.7 for model details). Finally, we note that the employed model aims at capturing essential physical mechanisms at work in associating polymer solutions but not at quantitatively reproducing the specific interactions and dynamics in the experiments.

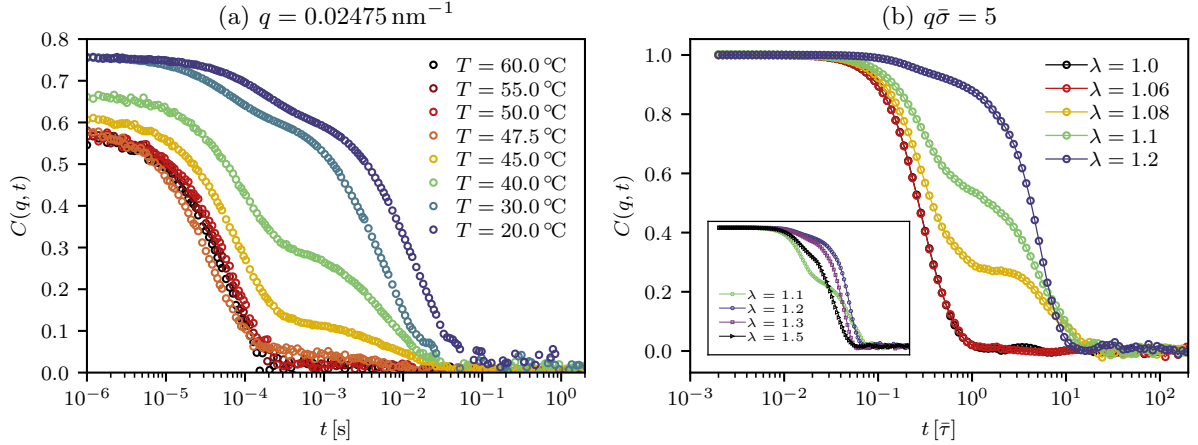


Figure 2.2: ISFs at different temperatures from (a) experiments and (b) simulations of the coarse-grained blob model at $c = 0.11c^*$. The evolution of a second slow mode is apparent for $T < 47.5 \text{ }^\circ\text{C}$ in experiments and for $\lambda > 1.06$ in simulations. Inset in **b** illustrates the decrease of the plateau height corresponding to the second step of the ISF observed in simulations for $\lambda > 1.2$. $\bar{\sigma}, \bar{\tau}$ are the units of the blob model simulations (Supplementary Table 2.3). The values of experimental $C(q, t)$ smaller than 1 at the lowest t reflect measurement statistics (number fluctuations due to non-constant number of scatterers in the scattering volume) in these dilute solutions.

2.3 Results

We first investigated the change of the structure at the single TSP level upon cooling. Figure 2.1a shows the hydrodynamic radius R_h associated with the fast process in the experimentally measured intermediate scattering functions (ISFs) in the dilute regime and calculated using the Stokes-Einstein-Sutherland relation, which effectively represents the size of a single molecule. As a direct comparison, Figure 2.1b contains the radius of gyration R_g of the star in units of the A-monomer diameter σ obtained from bead-spring model simulations at different values of λ . Note that the radius of gyration was too small to be probed by DLS, hence the comparison will be made between experimental R_h and simulated R_g . The former, R_h , is an apparent size of the TSP and it is often assumed that $R_h(T)/R_g(T)$ is a constant ratio; this is not strictly true because of the different origin of these quantities [80]. Nevertheless, the existence of a transition temperature for the single TSP caused by interarm association is an apparent feature of both quantities.

In both cases, we observe reduction of the molecular size upon cooling. Representative snapshots of the TSP given in Figure 2.1b help to shed light on the self-assembly process that takes place as λ increases for this particular (f, α) combination. When the B-monomers, colored in red, are in a good solvent (i.e., for small values of λ), the star is open and the attraction between star arms is negligible. In this regime, TSPs resemble

usual athermal star polymers. Upon worsening the solvent quality, solvophobic monomers first start to form transient patches ($1 < \lambda < 2.5$) that can be easily destroyed by thermal fluctuations. On further increasing λ , this ultimately leads to the collapse of all three arms of the TSP into one large patch ($\lambda > 2.5$) accompanied by a significant decrease in R_g [121]. Similarly, R_h of a single TSP reduces upon cooling below $T = 30$ °C. Furthermore, in both cases the decrease in TSP size occurs within a narrow region of inverse temperature and λ that is notably shifted away from the θ -point of the outer block. Therefore, we argue that cooling (increasing attraction) triggers a similar self-assembly process in both the experiments and simulations. On the other hand, in the experiments we observe only 5% reduction in size, being at the limits of measurement resolution, whereas this reduction amounts to 25% in the simulations. Such a discrepancy is highly plausible to originate from the simulation model, which includes neither details of the atomistic intermolecular interaction that are relevant for the precise values nor details or possible modifications of the A-A and A-B interactions upon cooling. Nevertheless, it captures the basic physics of self-organization, i.e., the end-monomer association. Finally, the different nature of R_h and R_g renders the main value of this comparison qualitative, but even a 5% size reduction can significantly influence properties that depend on the volume fraction in dense systems.

Next, we examine the dynamics of TSPs. To be able to study self-assembly in larger systems and to reach longer time-scales, we developed an even coarser simulation model from the bead-spring model by grouping certain segments of a star arm into blobs and subsequently deriving effective potentials between the blobs by means of a rigorous approach that incorporates the many-body correlations that become important at finite densities [129] (see Supplementary Section 2.5.8 for details). Figure 2.2 shows the ISFs from both experiments and blob model simulations at a fixed wavevector and various temperatures (attraction strengths) for $c = 0.11c^*$, where c^* is the TSP overlap concentration (see Supplementary Section 2.5.9). The ISF shows two distinct patterns, as seen in Figure 2.2a. At temperatures above T_θ of the outer block, the ISF exhibits a single exponential decay, demonstrating the existence of freely moving stars in solution. However, upon cooling the system well below the T_θ of the outer block ($T < 47.5$ °C in experiments and $\lambda > 1.06$ in simulations) a two-step decay in the ISF is observed. The slow process becomes more pronounced as T is decreased. Identical trends emerge in the ISFs extracted from blob model simulations, as shown in Figure 2.2b, although the difference between the fast and slow mode relaxation times is an order of magnitude smaller than the one observed experimentally. We attribute this discrepancy to the minimal character of the blob model, which

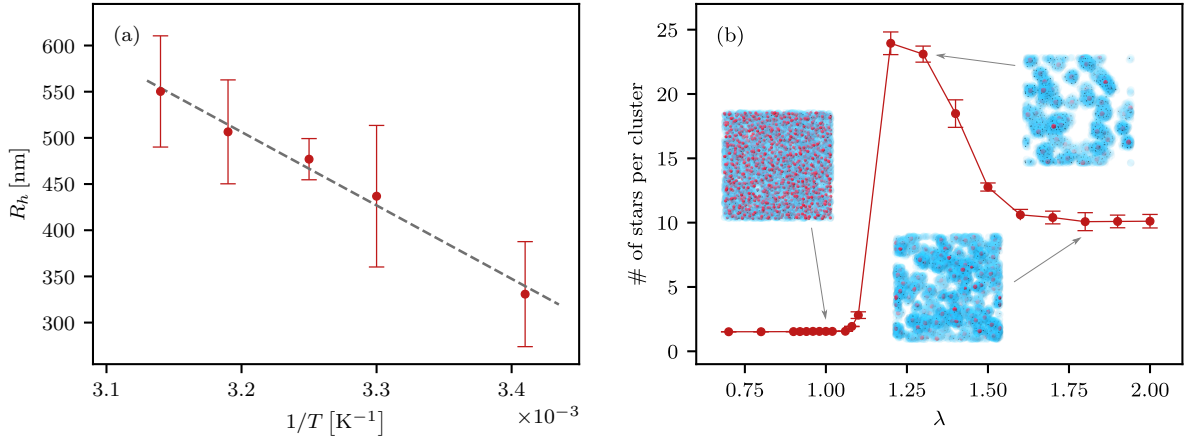


Figure 2.3: **a**, Hydrodynamic radius, R_h , extracted from the slow process in the experimental ISFs. **b**, Average aggregate size as a function of λ extracted from simulations of the coarse-grained blob model. Insets: representative configurations of TSPs for indicated λ with the grey arrows (attractive blobs – red, repulsive blobs – light blue, star centers – black). Both results correspond to $c = 0.11c^*$.

features soft inter-blob steric potentials and does not take into account hydrodynamic interactions mediated by the solvent, and to the finite box size that limits the growth of the clusters that constitute the slow component of the solution. Furthermore, similar information is recovered when ISFs at various wavevectors are examined: at high $T = 60$ °C or low $\lambda = 1.0$, the ISF shows a single exponential decay at all q -values, whereas at low $T = 40$ °C or high $\lambda = 1.2$, the ISF exhibits a clear two-step decay both in experiments and simulations (Supplementary Figure 2.7 and 2.8). Finally, a few characteristic data points available in both the experiments and simulations allow us to establish a relation between λ and $1/T$ (Supplementary Figure 2.9 and the associated discussion).

The two-step relaxation of the dynamics indicates the coexistence of clusters (slow process) and single TSPs (fast process). The relaxation spectrum deduced from the inverse Laplace transformation of the ISF using the constraint regularized method [130] reveals two well-separated peaks which represent the relaxation times of single stars and clusters (Supplementary Figure 2.3). The corresponding relaxation times are used to calculate the diffusion coefficient and, subsequently, the hydrodynamic radius of a TSP and clusters using the Stokes-Einstein–Sutherland relation. Figure 2.3a shows R_h corresponding to the slow process. The obtained values exceed the full stretch length of the $(\text{PS-PB})_3$ copolymer, which clearly indicates the formation of the inter-chain aggregates that decrease in dimensions on cooling.

Simulations provide insights into such change and reveal how the morphology of the TSP network and its rearrangements depend on λ . Figure 2.3b shows the average cluster

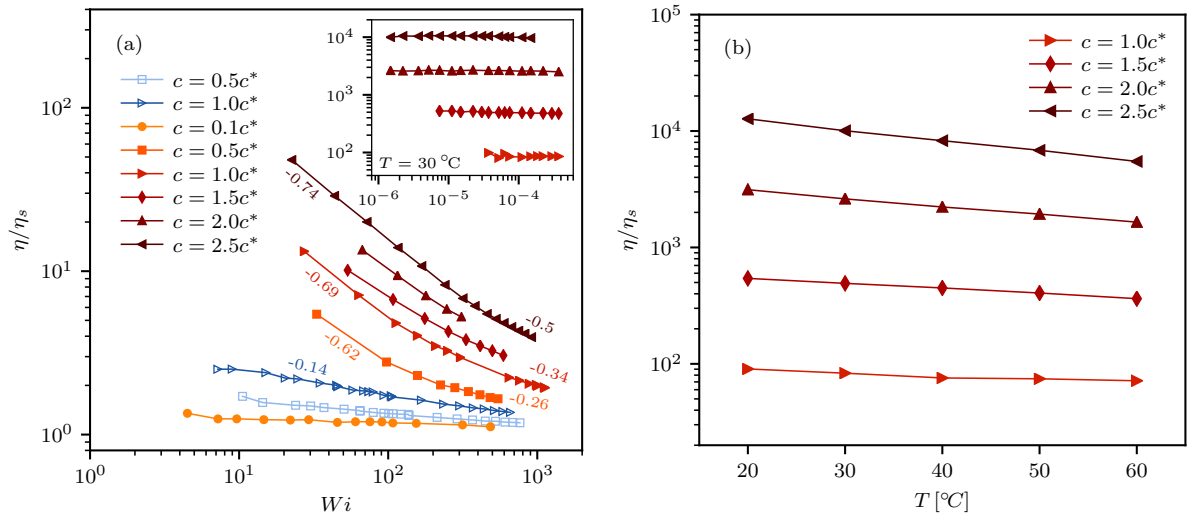


Figure 2.4: **a**, Shear viscosity as a function of Weissenberg number Wi from monomer-resolved simulations obtained at $\lambda = 1$ (open symbols) and $\lambda = 3$ (closed symbols) for various TSPs concentrations. The numbers next to the viscosity curves indicate the slopes of the latter in the corresponding range of Wi . Inset: viscosity data from experiments at $T = 30$ °C and low Wi numbers. **b**, Temperature dependence of the zero-shear viscosity from experiments at different concentrations indicating a small activation energy ranging from 20 to 35 kJ/mol for $c/c^* = 1$ –2.5.

size as a function of λ for $c = 0.11c^*$ together with the corresponding simulation snapshots of the TSP structures. At high temperatures ($\lambda < 1.06$), the dynamics of the TSPs are predominantly diffusive: stars occasionally form intra- and inter-molecular patches encompassing few arms, which quickly dissociate due to thermal noise. Further cooling ($1.06 < \lambda < 1.2$) dramatically increases aggregation capabilities of a patch: we observe the formation of micelles composed out of attractive B-blocks externally shielded by the inner self-avoiding A-blocks, see Figure 3b. The micelles feature a rather broad size distribution and can be interconnected, i.e., there are TSPs whose arms belong to distinct patches, giving rise to clusters (see Supplementary Figure 2.6 for characteristic distributions of patch and cluster sizes). Another structural rearrangement of the system occurs by further reducing the temperature ($\lambda > 1.2$): stronger attraction between outer blocks causes tightening of the respective micellar cores, which simultaneously leads to enhanced steric constraints between self-avoiding inner blocks distributed on the exterior of these micelles. Eventually, due to core crowding some arms or even TSPs leave a micelle, which results in smaller aggregation sizes of patches and clusters and decreased intermicellar separation, as seen in the insets of Figure 2.3b. This reorganization, however, increases micellar interconnectivity, as more stars attach their arms to two or even three distinct patches (see Supplementary Figure 2.5 for patch sizes and TSP interconnectivity). This scenario

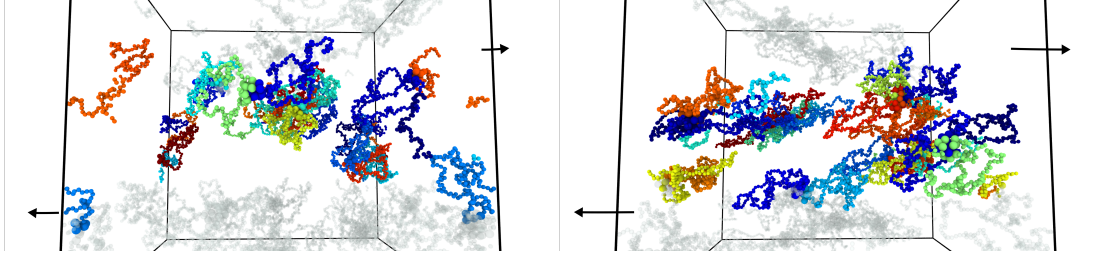


Figure 2.5: Representative configurations from the bead-spring model simulations of TSPs at $Wi = 14.6$ (left) and $Wi = 107.4$ (right) at $c = 0.1c^*$ and $\lambda = 3$.

calls for a strong interplay between intra- and inter-star association, which is an important design consideration for tailoring the properties of soft patchy particles. We argue that the combined structural and dynamical information from Figures 2.2 and 2.3 provides strong evidence about the tunability of TSPs.

Next, we examine the steady state response of TSPs to simple shear flow. We carried out a study combining experiments that probed the system at low shear rates, thereby capturing only the Newtonian regime, and simulations at very high shear rates, where clear shear-thinning behavior was detected. In simulations of the bead-spring model, shear flow was generated by the reverse nonequilibrium simulation method [131] with an explicit solvent modelled by multiparticle collision dynamics [132] in the HOOMD-blue simulation package (modified version 2.3.0) [133, 134, 135, 136]. The effect of shear flow on TSPs was investigated at $\lambda = 1$ and $\lambda = 3$, where the stars are open and collapsed at the single molecule level, respectively, under different concentration regimes.

Figure 2.4 shows the viscosity measurements from simulations and experiments for TSPs at various shear rates, concentrations, and temperatures. In both cases, the TSP viscosity was normalized by the solvent viscosity, η_s , and the shear rate, $\dot{\gamma}$, was multiplied by the Brownian time of a single TSP, τ_0 , to define the Weissenberg number, $Wi = \dot{\gamma}\tau_0$. The results from both experiments and simulations indicate an increase in the relative solution viscosity upon decreasing T (increasing λ). For TSPs with moderate attraction ($\lambda = 1$) at $c \leq c^*$, as well as for $\lambda = 3$ at $c = 0.1c^*$, we observe a Newtonian regime at small Wi combined with a weak shear-thinning of viscosity at higher Wi with the slope of viscosity, $\eta/\eta_s \sim Wi^{-\delta}$, $\delta \approx 0.1$ (see Figure 2.5 for representative TSP conformations). Upon increasing c for the system with higher attraction ($\lambda = 3$), we first detect a transition from a Newtonian to a weakly-thinning response, and then to a strongly-thinning response. In this case, the slope of viscosity at high Wi is reduced, suggesting a tendency towards an infinite-rate limiting viscosity, which implies saturation of deformation of the inner blocks in shear flow (at $\lambda = 3$ and $c = 2.5c^*$, for example, δ decreases from 0.74 to 0.5 upon rising

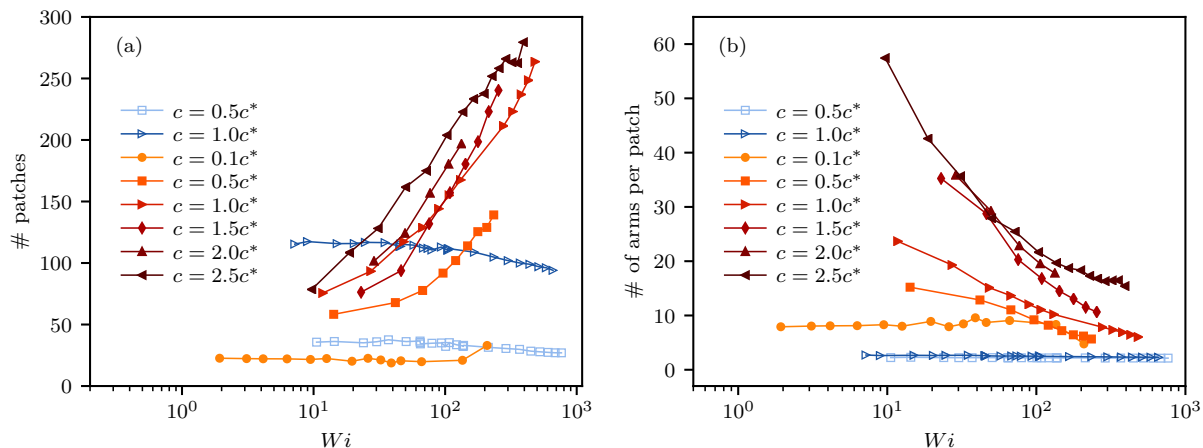


Figure 2.6: (a) Number of patches and (b) their size as a function of Wi obtained from bead-spring model simulations at $\lambda = 1$ (open symbols) and $\lambda = 3$ (closed symbols) and various concentrations.

Wi). This is further confirmed by the fact that TSPs stretch and tend to align their arms along the flow direction (Supplementary Figure 2.10). In addition, experimental data for very dilute solutions of linear polymers ($c < 0.2c^*$) indicates very low slopes, similar to that of c^* solution at $\lambda = 1$ in our case, both in good and θ -like solvent conditions. The slope grows with increasing concentration and reaches 0.5 in the semidilute unentangled regime [137, 138], while simulations provide even higher values, up to 0.75 [139, 140]. Slopes ranging from 0.3 to 0.4 for increasing c have been reported for dilute solutions of star polymers with up to 50 arms in good solvent [141]. The wide range of slopes reflects the complexity of these multi-scale TSP systems, which are very different from simple polymers, yet their thinning is associated with deformation of segments and break-up of patches.

As determined by simulations, the microscopic origin of shear-thinning in solutions of TSPs can be qualitatively linked to the fission of patches between outer blocks in shear flow. The dependence of the number and size of patches on Wi are shown in Figure 2.6a and 2.6b, respectively. For $\lambda = 1$, the shear rate had only a small effect on the patches. On average the patches contained 2-3 arms and the number of patches decreased slightly with increasing flow rate because the patches were broken up by the rearrangement of the polymers under shear, leaving behind free arms. Such behavior is consistent with the weak shear-thinning of viscosity observed in Figure 2.4a. On the other hand, for $\lambda = 3$, the patches were broken up into smaller ones under strong shear rates, resulting in a steep increase of their number, and hence implying a strongly-thinning response.

2.4 Conclusions

In conclusion, we have shown how a simple 3-arm telechelic star polymer, a soft patchy particle, is a paradigm for a designer material with tunable structure and rheology. Tunability is easily achieved by varying the strength of attraction between the associating terminal monomers of the TSP, i.e., by selecting a proper solvent that is at the same time good for the inner blocks but poor for the outer ones and then controlling the temperature. We demonstrated this promising possibility in dilute solutions, where such tuning leads to an interplay between intra- and inter-star associations that result first in the formation of clusters comprising multiple stars in the system and then to reduction of their size upon cooling. The clusters are gel precursors that can be characterized by a weak flow activation energy, but have substantial deformability in strong shear fields due to the disintegration of inter-star patches. The combination of system simplicity and unprecedented richness of material behavior make this approach particularly promising. The satisfactory agreement between experiment and simulations suggests a powerful strategy to design soft responsive patchy particles with tunable macroscopic properties.

2.5 Supplementary Information

2.5.1 Materials

Styrene (Sigma-Aldrich, 99%) was purified *via* consecutive distillations over CaH₂ (Sigma-Aldrich, 95%) and dibutyl-magnesium (1 M in heptane, Sigma-Aldrich) and stored in pre-calibrated ampoules. 1,3-Butadiene (Bd) (Sigma-Aldrich, 99%) was purified *via* consecutive distillations over *n*-BuLi, at -10 °C using ice/salt bath, prior addition to the polymerization reactor. Benzene (Sigma-Aldrich, 99.8%) methyltrichlorosilane (Sigma-Aldrich, 99%) and methanol (terminating agent, Sigma-Aldrich, 99%) were purified according to the standards required for anionic polymerization, using well-established high-vacuum procedures. *sec*-Butyllithium (*s*-BuLi, 1.4 M in cyclohexane, Sigma-Aldrich) was used without purification and was diluted with dry *n*-hexane. The diluted reagents were stored at -20 °C in ampoules equipped with break-seals before use. The polymerization and linking reaction were performed under high vacuum conditions in sealed glass reactors equipped with break-seals. The reactor was purged with *n*-BuLi solution after its removal from the vacuum line by flame sealing-off.

2.5.2 Instrumentation

Size exclusion chromatography measurements were carried out at 35 °C through a Viscotek GPCmax VE-2001 with THF as the eluent at a flow rate of 1.0 mL/min, equipped with an isocratic pump, Styragel HR2 and HR4 columns in series (300 mm × 8 mm) and a differential refractive index detector (DRI). The system was calibrated with polystyrene (PS) standards (M_p : 370 to 4,220,000 g/mol). Triple-detection measurements were performed in the same instrument, which was also equipped with a two-angle light scattering detector (15° and 90°, $\lambda_0 = 658$ nm) and a viscometer. These measurements were used for the calculation of the weight-average molecular weight (M_w) and polydispersity index (\mathcal{D}) of the linear and final star block copolymers. Proton nuclear magnetic resonance spectroscopy (¹H-NMR) spectrum was recorded at Bruker AVANCE III spectrometer operating at 500 MHz. Chloroform-*d* (CDCl₃) was the solvent at room temperature.

2.5.3 Synthesis of the 3-arm star diblock copolymer

A typical procedure for the synthesis of the (PS-*b*-PBd_{1,4})₃ 3-arm star copolymers is as follows. Styrene (1g) was polymerized at room temperature, using *sec*-butyllithium (1.1 mmol) as initiator and benzene as solvent. The mixture was left to react for 18 hours

Sample	$(\bar{M}_w^{\text{star}})_{\text{LS-SEC}}$ (g/mol)	$(\bar{M}_w^{\text{linear}})_{\text{LS-SEC}}$ (g/mol)	\bar{D}^{SEC}	f_{PS}^* ($^1\text{H-NMR}$) %(w/w)	f_{PB}^* ($^1\text{H-NMR}$) %(w/w)
$(\text{PS-b-PB})_3$	26700	8800	1.03	0.23	0.77

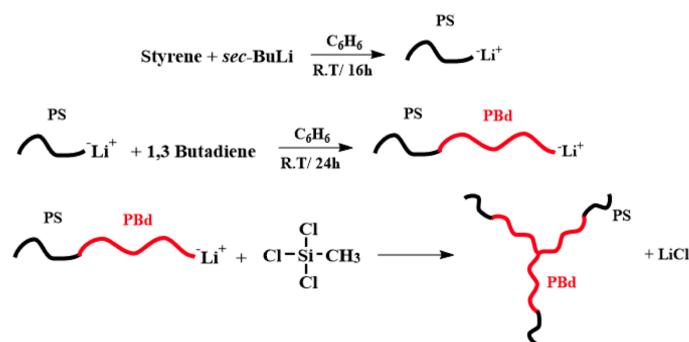
* Mass fraction was calculated via $^1\text{H-NMR}$ spectroscopy in CDCl_3 at 25 °C.

Table 2.1: Molecular characteristics of the linear PS-b-PB and the final star diblock copolymer $(\text{PS-b-PB})_3$.

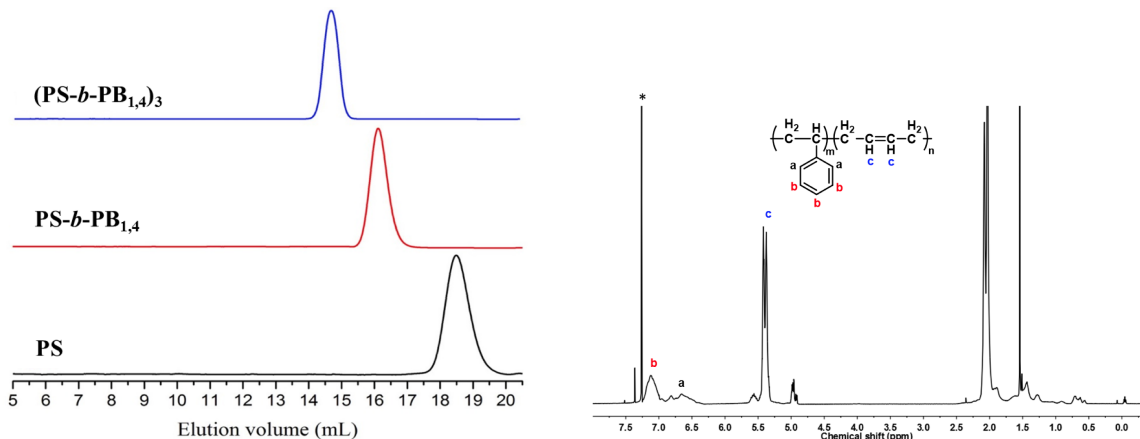
and then an aliquot was taken by heat-sealing the corresponding constriction tube for molecular characterization. Afterwards, the appropriate amount of 1,3-butadiene (9g) was added to the reaction mixture and the polymerization left until completion. After 24 hours an aliquot was taken for molecular characterization. The rest of the “living” polymer solution was reacted with methyltrichlorosilane (0.28 mmol) to form the 3-arm star diblock copolymer. The linking reaction was monitored by SEC and lasted for 2-3 weeks. After the completion of the reaction, the excess of the living chains were terminated by addition of degassed methanol and the solution precipitated in a large amount of methanol. The 3-arm star diblock copolymer $(\text{PS-b-PBd}_{1,4})_3$ was purified from the unreacted linear chains by repeated solvent/non-solvent (toluene/methanol) fractionations. The synthetic strategy is presented in Supplementary Figure 2.1. All intermediates and final products were analyzed by SEC and $^1\text{H-NMR}$ (Supplementary Figure 2.2).

2.5.4 Sample preparation

Solutions were prepared by mixing an appropriate amount of telechelic star polymers (TSPs) and solvent (1-phenyldodecane) to reach a desired concentration. The sample degradation was inhibited by adding 0.1 wt% of TSP of the antioxidant BHT (2,6-Di-*tert*-butyl-4-methylphenol). In order to fully dissolve TSPs, methylene chloride was used as



Supplementary Figure 2.1: Synthesis of 3-arm star diblock copolymers $(\text{PS-b-PBd})_3$.



Supplementary Figure 2.2: Left: SEC traces of the synthesized linear PS precursor, linear $PS-b-PB_{1,4}$, and the corresponding 3-arm star $(PS-b-PB_{1,4})_3$. Right: 1H -NMR spectrum of $(PS-b-PB_{1,4})_3$ star block copolymer.

the cosolvent. Then, the cosolvent was removed under ambient conditions until constant weight was achieved.

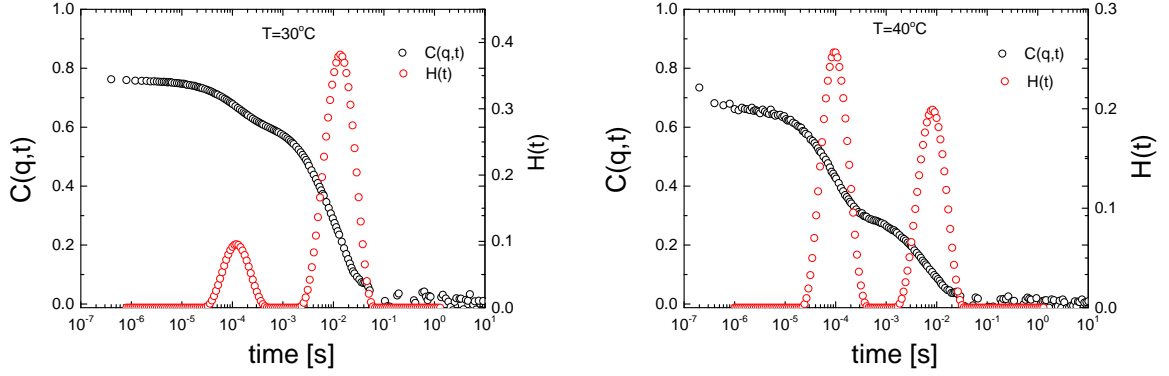
2.5.5 Dynamic light scattering

In Dynamic Light Scattering (DLS), the experimental normalized autocorrelation function $G(q, t) = \langle I(q, 0)I(q, t) \rangle / \langle I(q, 0) \rangle^2$ of the instantaneous light scattered intensity $I(q, t)$ at the scattering wavevector $q = (4\pi n / \lambda_0) \sin(\theta/2)$ (n is the refractive index, θ denotes the scattering angle, and λ_0 is the wavelength of the incident laser beam) is related to the normalized time correlation function $g(q, t) = \langle E^*(q, 0)E(q, t) \rangle / \langle |E(q, 0)|^2 \rangle$ of the scattered electric field $E(q, t)$ by the Siegert relation:

$$G(q, t) = 1 + f^* |\alpha g(q, t)|^2 = 1 + f^* |C(q, t)|^2, \quad (2.1)$$

where f^* is the coherence instrumental factor, α is the fraction of the total scattered intensity $I(q)$ associated with fluctuations relaxing with times longer than 0.1 μs [142, 143, 144], and $C(q, t)$ is the intermediate scattering function (ISF).

DLS experiments were performed on an ALV-5000 goniometer/correlator setup (ALV-GmbH, Germany). The light source was a Nd:YAG dye-pumped, air-cooled laser (100 mW) with the wavelength $\lambda_0 = 532$ nm. The refractive index of 1-phenyldodecane is $n = 1.482$. Before each experiment, the sample was equilibrated at $T = 60$ °C (above the θ -temperature of the outer PS-block) for 10 min to erase thermal history. Then, the sample was quenched to the desired temperature and equilibrated. The equilibration



Supplementary Figure 2.3: ISF (black circles, left axis) and its corresponding relaxation times spectrum deduced from the constrained regularization method (red circles, right axis) at $q = 0.02475 \text{ nm}^{-1}$ for $T = 30 \text{ }^\circ\text{C}$ (left) and $T = 40 \text{ }^\circ\text{C}$ (right).

process was probed by measuring the ISF until it reached steady values over time. The duration of equilibration depended on the temperature and ranged from 10 min for $T = 60 \text{ }^\circ\text{C}$ to 10 hr for $T = 20 \text{ }^\circ\text{C}$.

To analyze the computed relaxation functions $C(q, t)$, the inverse Laplace transformation using the constrained regularization method was applied. This method assumes that $C(q, t)$ can be written by a superposition of exponentials:

$$C(q, t) = \int_{-\infty}^{+\infty} H(\ln \tau) \exp(-t/\tau) d(\ln \tau), \quad (2.2)$$

where $H(\ln \tau)$ is the relaxation spectrum. The characteristic relaxation times correspond to the maximum values of $H(\ln \tau)$, whereas the area under the peak defines the value α in Eq. 2.1 and hence the intensity $\alpha I(q)$ associated with the particular dynamic process. The transformation was performed by means of the program CONTIN [130], and yielded the relaxation time and intensity of the partitioning modes. Typical results of such analysis are shown in Figure 2.3.

2.5.6 Rheology

Rheological experiments were conducted on an ARES-HR strain controlled rheometer (TA Instruments, USA) with stainless steel cone-plate geometry (8 mm diameter, 0.166 rad angle and a truncation of 0.21 mm). Temperature was controlled using a standard Peltier plate. A solvent trap was used to ensure the elimination of evaporation, although 1-phenyldodecane did not evaporate due to a high boiling point ($T_B = 330 \text{ }^\circ\text{C}$). To erase history effects, before each experiment the sample was heated up at $T = 60 \text{ }^\circ\text{C}$ for about

10 min, which was enough for the system to reach equilibrium. The latter was checked by probing linear elastic and viscous moduli until both reached the steady state values. The system was then quenched to the desired temperature and equilibrated. Finally, shear viscosity measurements were performed by applying a constant shear rate and measuring the steady state value of viscosity.

2.5.7 Simulation model

As stated in the experimental part, arms of TSPs are diblock copolymers chemically composed out of an inner, solvophilic PB- and an outer, solvophobic PS-block. In what follows, ‘A’ refers to repulsive PB-monomers, ‘B’ to sticky, terminal PS-monomers, and ‘C’ to star centers. In order to accurately handle disparities in physical properties of the blocks, we developed a specific bead-spring (BS) model for the experimental TSPs. The number of A- and B- monomers in an arm was chosen as $N_A = f_{\text{PB}} \bar{M}_w^{\text{linear}} / M_{\text{PB}}^0 \approx 65$, and $N_B = f_{\text{PS}} \bar{M}_w^{\text{linear}} / M_{\text{PS}}^0 \approx 3$, respectively, where $M_{\text{PB}}^0 = 105$ g/mol, $M_{\text{PS}}^0 = 720$ g/mol are the molar masses of a single Kuhn monomer [80, p.53], and $f_{\text{PB}}, f_{\text{PS}}, \bar{M}_w^{\text{linear}}$ are listed in Table 2.1. In other words, each repeating unit in the model polymer chain corresponds to one Kuhn segment of either PB (A) or PS (B). As a consequence, the fraction of terminal, PS, Kuhn monomers is now modified and takes for the bead-spring model the value $\alpha = 0.044$.

The solvent-dependent attractions between B-monomers are incorporated into our simulations by means of a generalized Lennard-Jones potential [145, 128]:

$$\beta V_{ij}^{\text{LJ}}(r) = \begin{cases} 4 \left[\left(\frac{\sigma_{ij}}{r} \right)^{12} - \left(\frac{\sigma_{ij}}{r} \right)^6 \right] + 1 - \lambda_{ij}, & r \leq 2^{1/6} \sigma_{ij}, \\ 4 \lambda_{ij} \left[\left(\frac{\sigma_{ij}}{r} \right)^{12} - \left(\frac{\sigma_{ij}}{r} \right)^6 \right], & r > 2^{1/6} \sigma_{ij}, \end{cases} \quad (2.3)$$

where $i, j = \text{A, B, C}$ (star centers), and $\beta = (k_{\text{B}}T)^{-1}$. By taking into account that the outer part is much stiffer, the Kuhn length of a PS-monomer $b_{\text{PS}} = 1.8$ nm is almost twice as large as that of a PB-monomer $b_{\text{PB}} = 0.96$ nm [80, 146], we set $\sigma_{\text{BB}} = 2\sigma_{\text{AA}}$. All other σ_{ij} are listed in Table 2.2. The above-defined dimensionless coupling parameters λ_{ij} denote the depth of the potential well between ij -pairs and effectively control solvent quality. More specifically, higher values of λ worsen the solvent, and therefore it is proportional to inverse temperature in experiments. Moreover, the value $\lambda = 0$ reduces Eq. (2.3) to the Weeks-Chandler-Andersen (WCA) potential [147] between monomers and hence mimics good solvent conditions, whereas $\lambda = 1$ corresponds to the standard Lennard-

ij	σ_{ij}	λ_{ij}	$r_{\text{cut}}^{\text{LJ}}/\sigma_{ij}$	R_{ij}^0/σ_{ij}
AA	1	0	$2^{1/6}$	1.5
AB	1.5	0	$2^{1/6}$	1.5
AC	1	0	$2^{1/6}$	4.5
BB	2	λ (varies)	3	1.5
BC	1.5	0	$2^{1/6}$	—
CC	1	0	$2^{1/6}$	—

Table 2.2: Parameters of pair interactions in the bead-spring model.

Jones potential.

As usual, neighboring monomers along the backbone are bonded *via* a finitely extensible nonlinear elastic (FENE) potential:

$$\beta V_{ij}^{\text{FENE}}(r) = \begin{cases} -\frac{\kappa}{2} \left(\frac{R_{ij}^0}{\sigma_{ij}} \right)^2 \ln \left[1 - \left(\frac{r}{R_{ij}^0} \right)^2 \right], & r \leq R_{ij}^0, \\ +\infty, & r > R_{ij}^0, \end{cases} \quad (2.4)$$

with $\kappa = 30$, $R_{ij}^0 = 1.5\sigma_{ij}$ for $i, j = A, B$, and $R_{AC}^0 = 4.5\sigma_{AC}$ for monomers directly bonded to star centers. Accordingly, we set $m_B = 40m$ and $m_A = m_C = 5m$, where $m = 1$ is the mass of a solvent particle (the inclusion of explicit solvent and shear flow generation are discussed in the following Section 2.5.12), originating from the fact that $m_{\text{PS}} \approx 8m_{\text{PB}}$ [80, 146]. For efficiency reasons, the Lennard-Jones potentials (2.3) are truncated and shifted. The parameters of all pair interaction in the model, as well as the cutoff radii, are listed in Table 2.2. All simulations were performed at $k_B T = 1$. In what follows, σ denotes the smallest length scale in the system, σ_{AA} .

In experiments, the overlap concentration was estimated using $c^* = 3M_W/(4\pi\mathcal{N}_A R_{g,0}^3)$, where M_W is the molecular weight of the studied polymer, \mathcal{N}_A is the Avogadro number, and $R_{g,0}$ denotes the radius of gyration at high T . Note that c (and c^*) is measured in the units of mass density when referring to experiments, and in the units of number density in simulations. Furthermore, to match the experimental and simulated concentrations, we converted $R_{h,0}$ to $R_{g,0}$ assuming that $R_{g,0} = 1.2R_{h,0}$ [80, p. 347], where $R_{h,0}$ stands for the hydrodynamic radius at high T . In simulations, c^* was then calculated as $3/(4\pi R_{g,0}^3)$.

2.5.8 Coarse-graining

To be able to study structure and relaxations of larger systems of TSPs in equilibrium, reaching thereby long time scales, we have developed, on the basis of the bead-spring model introduced above, an even coarser multi-blob (MB) model, in which segments of a star arm are grouped into blobs, whose centers of mass (CM) interact *via* suitably derived effective potentials. Such a MB approach has been proven to deliver accurate results for versatile systems in different concentration regimes [148, 149, 150, 17, 151, 26, 18].

In particular, we used $N_A^{\text{blob}} = 32$ for composing an A-blob, and $N_B^{\text{blob}} = 3$ for a B-blob. With such parameters, an arm of a TSP from the experimental sample consists only out of two repulsive A-blobs, and a single attractive B-blob. Moreover, such choice of blob sizes ensures that the ranges of all effective interactions are similar. This approach not only enables us to reduce to initial number of degrees of freedom in more than one order of magnitude, but also allows to flexibly construct TSPs with higher functionalities as well as various arm composition.

The derivation of the effective pair potentials $V_{\alpha\beta}^{\text{eff}}(r)$ between blobs ($\alpha, \beta = A, B$) is based on the exact relation between the inter- and intra-molecular (connected by a bond) pair distribution functions (denoted by $g_{\alpha\beta}(r)$ and $s_{\alpha\beta}(r)$, respectively) between the CMs of the blobs, and the effective potentials at low densities [129]. More specifically, these correlation functions can be obtained from simulations of two α - β diblocks [152, 148, 153] (in what follows, $f_{\alpha\beta}(r) = e^{-\beta V_{\alpha\beta}^{\text{eff}}(r)} - 1$ denotes the Mayer f -function):

1. Simulations of two A–A diblocks yielding $g_{AA}(r)$ and $s_{AA}(r)$ pair correlation functions. The effective interaction $V_{AA}^{\text{eff}}(r)$ can be then obtained as a solution of the following integral equation:

$$\begin{aligned}
 g_{AA}(\mathbf{r}) = & \left[1 + f_{AA}(\mathbf{r}) \right] \left\{ 1 + \int d^3x \left[f_{AA}(\mathbf{x}) s_{AA}(\mathbf{x} - \mathbf{r}) + s_{AA}(\mathbf{x}) f_{AA}(\mathbf{x} - \mathbf{r}) \right] \right. \\
 & + \int d^3x \int d^3y s_{AA}(\mathbf{x}) s_{AA}(\mathbf{y} - \mathbf{r}) \left[f_{AA}(\mathbf{x} - \mathbf{y}) + f_{AA}(\mathbf{y}) f_{AA}(\mathbf{x} - \mathbf{y}) \right. \\
 & \left. \left. + f_{AA}(\mathbf{x} - \mathbf{r}) f_{AA}(\mathbf{x} - \mathbf{y}) + f_{AA}(\mathbf{y}) f_{AA}(\mathbf{x} - \mathbf{r}) + f_{AA}(\mathbf{y}) f_{AA}(\mathbf{x} - \mathbf{r}) f_{AA}(\mathbf{x} - \mathbf{y}) \right] \right\}
 \end{aligned}
 \tag{2.5}$$

2. Simulations of two B–B diblocks providing $g_{BB}(r)$ and $s_{BB}(r)$ pair correlation functions, from which $V_{BB}^{\text{eff}}(r)$ can be computed using Eq. (2.5) by replacing ‘A’ with ‘B’.

3. Simulations of an A–A and a B–B diblocks providing $g_{AB}(r)$ pair correlation functions. The effective interaction $V_{AB}^{\text{eff}}(r)$ can be obtained by inverting

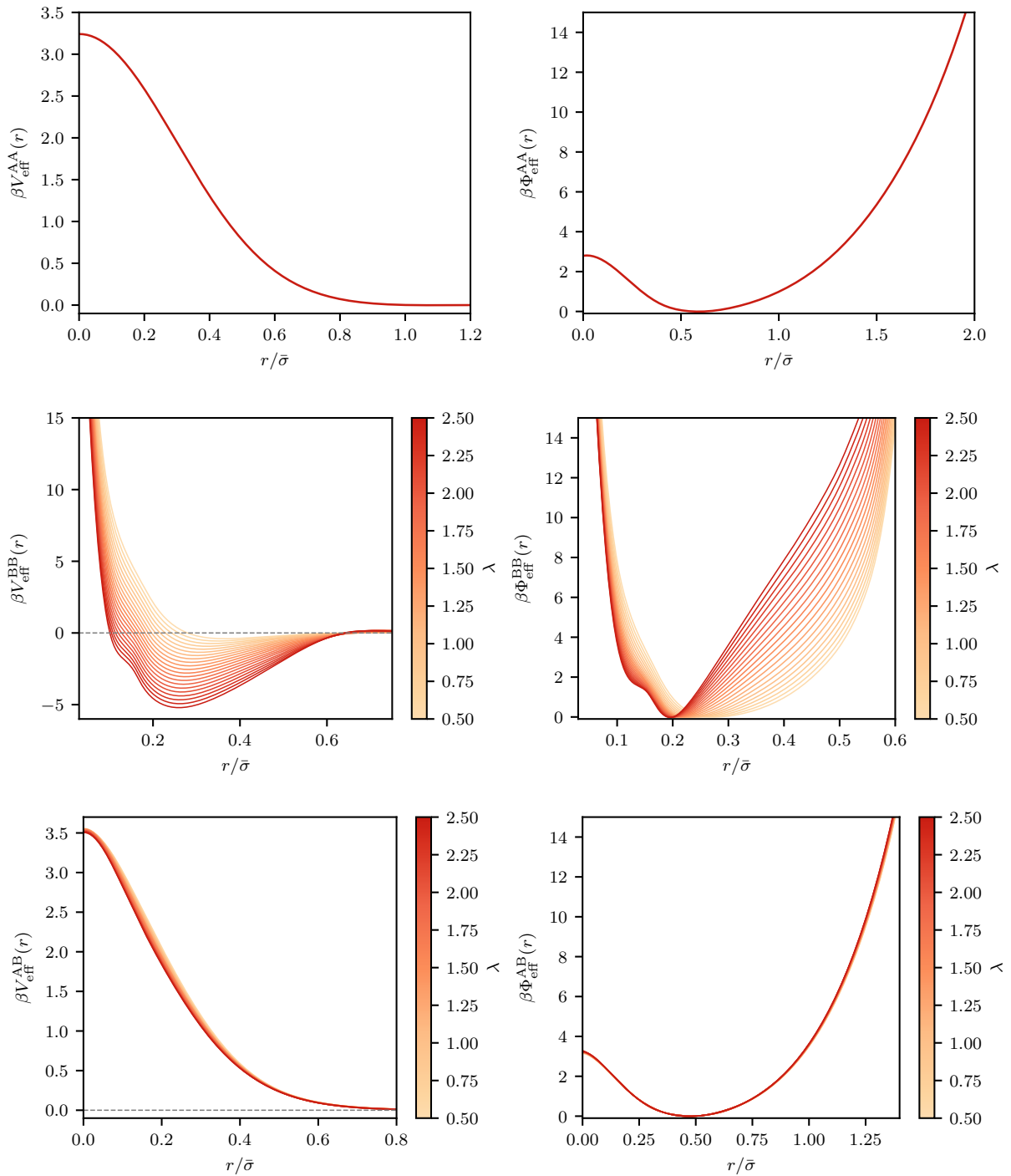
$$\begin{aligned}
g_{AB}(\mathbf{r}) = & \left[1 + f_{AB}(\mathbf{r}) \right] \left\{ 1 + \int d^3x \left[f_{AB}(\mathbf{x}) s_{BB}(\mathbf{x} - \mathbf{r}) + s_{AA}(\mathbf{x}) f_{AB}(\mathbf{x} - \mathbf{r}) \right] \right. \\
& + \int d^3x \int d^3y s_{AA}(\mathbf{x}) s_{BB}(\mathbf{y} - \mathbf{r}) \left[f_{AB}(\mathbf{x} - \mathbf{y}) + f_{AB}(\mathbf{y}) f_{AB}(\mathbf{x} - \mathbf{y}) \right. \\
& \left. \left. + f_{AB}(\mathbf{x} - \mathbf{r}) f_{AB}(\mathbf{x} - \mathbf{y}) + f_{AB}(\mathbf{y}) f_{AB}(\mathbf{x} - \mathbf{r}) + f_{AB}(\mathbf{y}) f_{AB}(\mathbf{x} - \mathbf{r}) f_{AB}(\mathbf{x} - \mathbf{y}) \right] \right\}
\end{aligned} \tag{2.6}$$

4. Simulations of a single A–A or B–B diblocks provide only the $s_{AA}(r)$ or $s_{BB}(r)$ pair correlation function, which can be used to compute effective intra-molecular potentials $\Phi_{\alpha\beta}^{\text{eff}}(r)$:

$$\beta\Phi_{\alpha\beta}^{\text{eff}}(r) = -\log [s_{\alpha\beta}(r)] \tag{2.7}$$

Note that all integrals, except the last double one, in Eqs. (2.5) and (2.6) are convolution integrals and therefore can be evaluated efficiently in Fourier space. The integral involving five factors is known a ‘bridge’ integral, which cannot be decomposed into a product of convolutions. We employed the method of Attard for evaluating them[154, 155]. All the above-defined pair distribution functions were obtained in Monte Carlo simulations with umbrella sampling to ensure good statistics over a wide region of interaction energies, which especially applies to short CM separations.

Eqs. (2.5) and (2.6) are nothing else as the RISM equations for diatomic molecules obtained by Ladanyi and Chandler [129]. For polymeric molecules in general, and for star-shaped in particular, the application of RISM equations hinges on a few approximations: 1) it is assumed that a polymer is composed out of multiple segments, i.e. blobs, that are treated as a single interaction site (in our case segments of a star arm are described only by the coordinates of its center of mass); 2) pair distribution functions between each segment’s center of mass that are subsequently used in the RISM inversion are computed from simulations of diblocks, not from simulations of whole polymeric molecules. We stress, however, that such approximations are necessary to 1) substantially reduce the number of internal degrees of freedom, which is the central goal of any first principles coarse-graining approach and to 2) perform necessary simulations in a reasonable amount of computational time. On the other hand, this approach explicitly includes finite density correlations between blobs, which is a great advantage in comparison to more simplistic



Supplementary Figure 2.4: Effective potentials between the CMs of two A (top row), an A and a B (middle row), and two B (bottom row) non-bonded (left column) and bonded (right column) blobs.

Model	Length	Energy	Mass	Time
BS	σ	ϵ	m	τ
MB	$\bar{\sigma} = 10\sigma$	$\bar{\epsilon} = \epsilon$	$\bar{m} = 120m$	$\bar{\tau} \approx 110\tau$

Table 2.3: Comparison between units in the bead-spring and multi-blob models.

methods that ignore them completely. For example, effective potentials computed as $\beta V_{\text{eff}}(r) = -\log P(r)$, where $P(r)$ is the probability density of observing the centers of mass of two polymers at a distance r , would provide much less accurate predictions because they do not take into account finite-density effects.

The resulting set of effective potentials covering the range $\lambda \in [0.5, 2.5]$ are shown in Figure 2.4. As expected, $V_{\text{AA}}^{\text{eff}}(r)$ and $V_{\text{AB}}^{\text{eff}}(r; \lambda)$ feature a Gaussian shape [156], where the latter one has a slight λ -dependence. $V_{\text{BB}}^{\text{eff}}(r; \lambda)$ potentials develop a deep negative minimum with increasing λ , and diverge for $r \rightarrow 0$, as there are only 3 monomers in a B-blob.

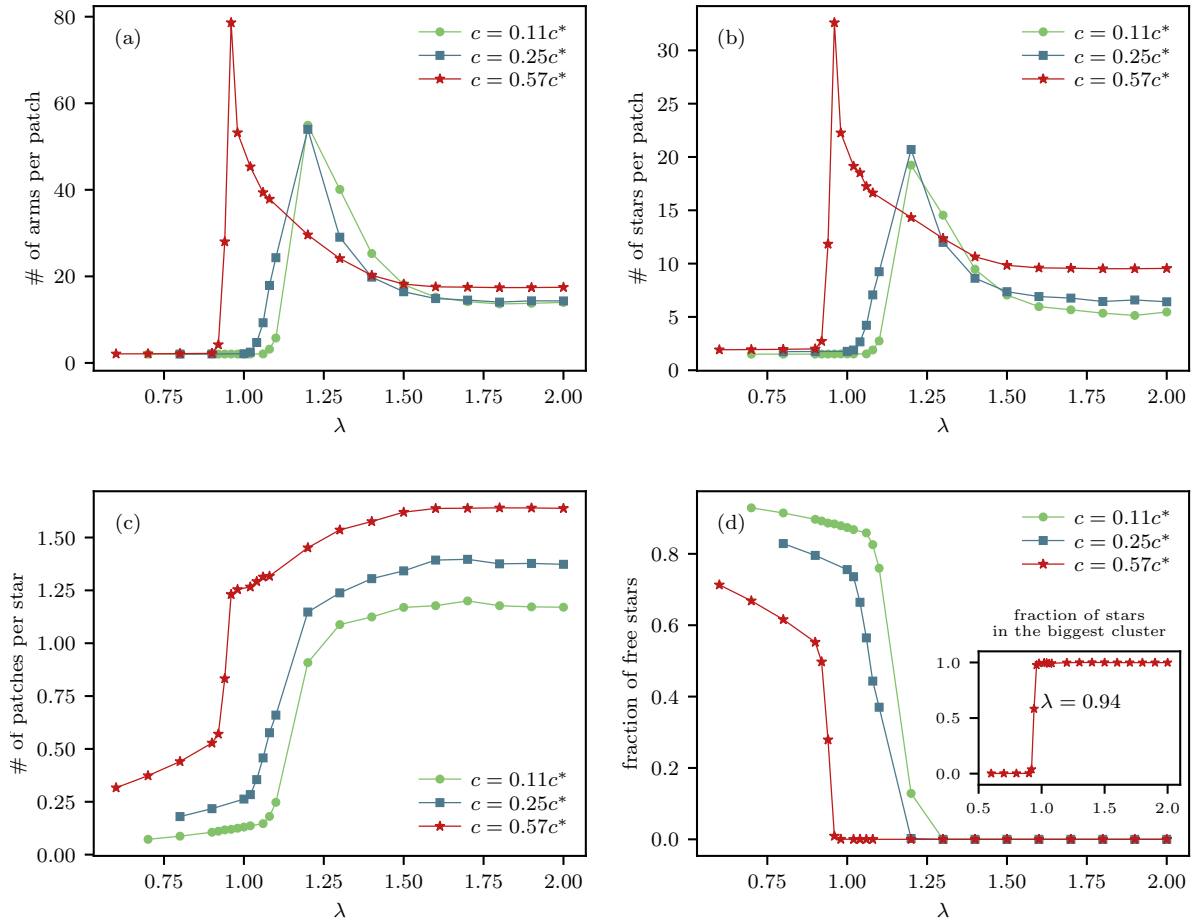
2.5.9 Structure in equilibrium

According to the chemical composition outlined in Table 2.1, a TSP in a MB simulation consists out of $f = 3$ arms, every of which contains $n_{\text{A}} = 2$ A-blobs, and $n_{\text{B}} = 1$ B-blobs, tethered to a central, point-like particle, i.e. 10 particles in total. The masses of single blobs were calculated as follows: $m_{\text{A}}^{\text{blob}} = N_{\text{A}}^{\text{blob}} m_{\text{A}} = 32 \times 5m = 160m$ for an A-blob, and $m_{\text{B}}^{\text{blob}} = N_{\text{B}}^{\text{blob}} m_{\text{B}} = 3 \times 40m = 120m$ for a B-blob. The latter mass, $m_{\text{B}}^{\text{blob}}$, was chosen as the unit of mass in MB simulations. In addition, as the unit of length we set $\bar{\sigma} = 10\sigma$, which approximately corresponds to the R_{g} of a single free star at high temperature. Further comparison between BS and MB units is given in Table 2.3.

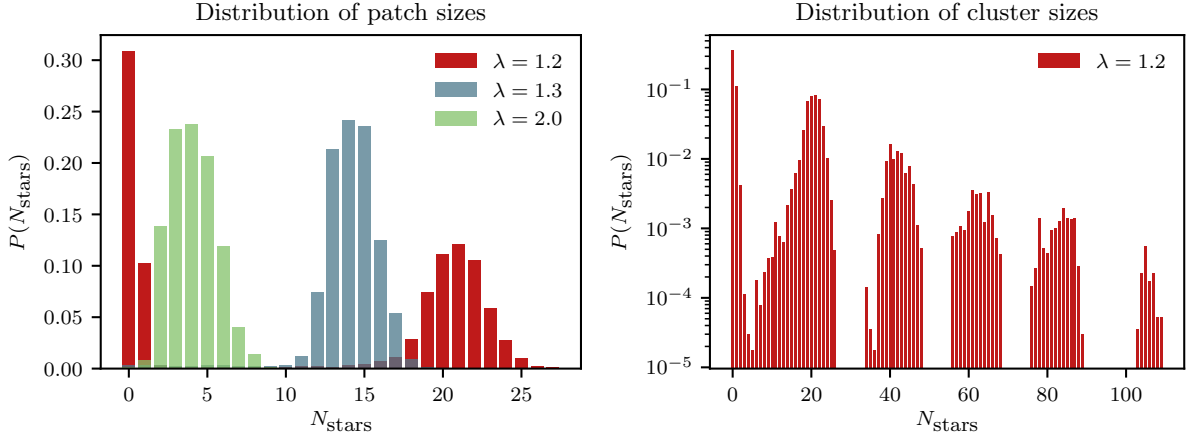
We performed Langevin dynamics ($T = 1.0 \epsilon/k_{\text{B}}$, $\gamma = 1.0 \bar{m}/\bar{\tau}$, $\Delta t = 0.005\bar{\tau}$) simulations of TSPs modeled by effective potentials shown in Supplementary Figure 2.4 in the dilute regime ($c/c^* = 0.11, 0.25, 0.57$) at various values of the interaction parameter λ using the simulation package HOOMD-blue [134, 135]. The overlap concentration, c^* , was estimated as

$$c^* = \frac{3}{4\pi R_{g,0}^3}, \quad (2.8)$$

where $R_{g,0}$ is the radius of gyration of a TSP at low $\lambda = 0.5$. We used a cubic box of size $L = 30\bar{\sigma}$, containing 898, 2040, 4651 stars in the system for $c/c^* = 0.11, 0.25, 0.57$, respectively. In addition, at the lowest concentration, $c/c^* = 0.11$, we also performed simulations in a bigger box with $L = 50\bar{\sigma}$ (4155 stars) to obtain better statistics of the cluster size distribution.



Supplementary Figure 2.5: Average number of (a) arms and (b) TSPs per patch as a function of λ for $c/c^* = 0.11, 0.25, 0.57$. The aggregation numbers significantly increase within a narrow region of λ indicating the formation of micelles, first featuring a peak and then saturating at a constant value upon increasing λ further on. The average number of distinct patches, in which a star participate, (c) follows a similar trend, and indicates higher interconnectivity of the TSP network upon increasing concentration. The fraction of free stars (d) steadily decays to zero, which is located approximately at the micellization point. Inset in d illustrates the fact that at $c = 0.57c^*$ all TSPs in the simulation box belong to a single cluster for $\lambda > 0.94$.



Supplementary Figure 2.6: Probability density of finding N_{stars} TSPs in a patch (left) and a cluster (right) at $c = 0.11c^*$. The shape of the cluster size distribution indicates the presence of multiple connected micelles with TSPs serving as bridges between them.

The resulting TSP structure formation upon cooling is given in Supplementary Figure 2.5. As explained in the main text, we observe the following chain of structural rearrangements:

1. At low λ (high temperatures), TSPs form only short-lasting bonds, with a typical patch including only two arms that belong either to the same star or two distinct stars. In this phase, most of TSPs are free, as shown in Supplementary Figure 2.5d.
2. Further increasing of λ leads to the formation of polydisperse micellar aggregates, with B-blobs located in their cores, and A-blobs distributed on the exterior. Two micelles form a cluster, if two arms of a TSP that participates in both contribute to two distinct cores. For example, at $c = 0.11c^*$ the biggest average aggregation numbers can be observed at $\lambda = 1.2$: a patch on average contains more than 50 arms belonging to more than 17 different stars, and an average cluster encompasses almost 25 TSPs, Figure 2.5a and Figure 2.5b. The distribution of patch and cluster sizes at $c = 0.11c^*$ is shown in Supplementary Figure 2.6. It is worth noting that in this case the maximal cluster size can exceed the average more than in 5 times. In simulations of the system with $L = 50\bar{\sigma}$ we observed identical distribution of patch sizes, although increased sizes of the biggest cluster, originating from the fact that there are more micelles that can potentially interconnect *via* bridging.
3. At high λ (low temperatures), strong attractions between B-block cause tightening of the micellar cores, which results in reduced aggregation numbers, Supplementary Figure 2.5b, but enhanced micellar interconnectivity, Supplementary Figure 2.5c.

The simulations at all concentrations considered here feature similar self-assembly trend. However, at higher c we observe bigger patch sizes and increased number of distinct patches per TSP. Finally, at high enough concentrations, the micellization goes along with a percolation transition, in which all TSPs form a single cluster spanning the whole simulation box. This is illustrated for $c = 0.57c^*$ in the inset of Figure 2.5d.

2.5.10 Intermediate scattering functions

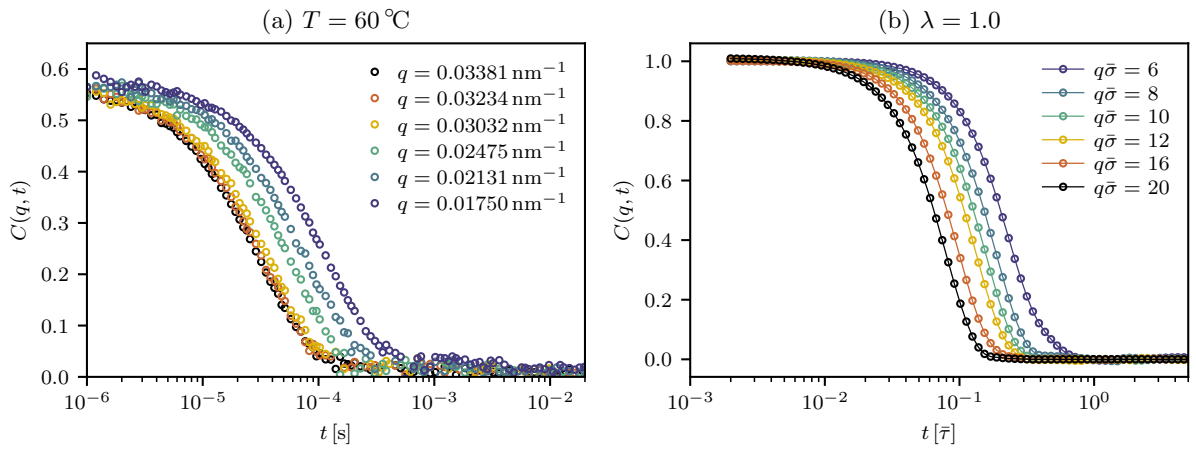
In MB simulations, ISFs at a fixed wavevector q were computed from NVE trajectories ($\Delta t = 0.002\bar{\tau}$) using [157, 158, 159]

$$C(q, t) = \frac{1}{N} \sum_{i=1}^N \sum_{j=1}^N \left[\frac{\sin(qr_{ij}(t))}{qr_{ij}(t)} \right] \Delta_{ij}(t, R) - \frac{4\pi\rho}{q^2} \left(q^{-1} \sin(qR) - R \cos(qR) \right), \quad (2.9)$$

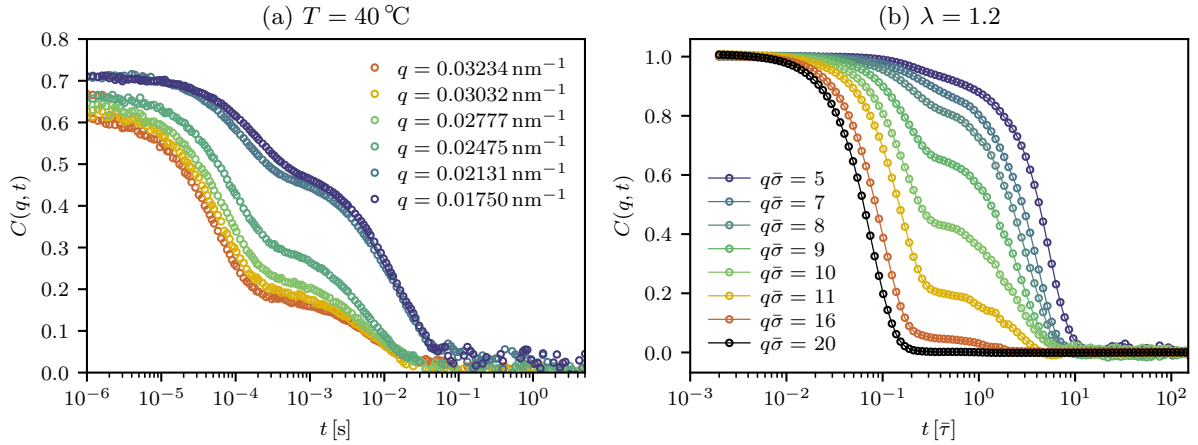
normalized with its equal-time value, $C(q, 0)$, and averaged over multiple independent simulation runs. In Eq. (2.9), ρ denotes the number density of the system, $r_{ij}(t)$ is the distance between particle i at time $t = 0$ and particle j at later time t , i.e., $r_{ij}(t) = |\mathbf{r}_i(t) - \mathbf{r}_j(0)|$, R is the cutoff distance chosen to be half of the box size, and

$$\Delta_{ij}(t, R) = \begin{cases} 1, & \text{if } r_{ij}(t) \leq R \\ 0, & \text{if } r_{ij}(t) > R. \end{cases} \quad (2.10)$$

The resulting high (one-step relaxation) and low (two-step relaxation) temperature ISFs at various wavevectors, and their comparison to the experimental ones obtained from DLS are shown in Supplementary Figures 2.7 and 2.8. We attribute the second



Supplementary Figure 2.7: ISFs at different scattering wavevectors q for experiments at (a) $T = 60\text{ }^\circ\text{C}$ and simulations at (b) $\lambda = 0.9$.



Supplementary Figure 2.8: ISFs at different scattering wavevectors q for experiments at (a) $T = 40$ °C and simulations at (b) $\lambda = 1.2$.

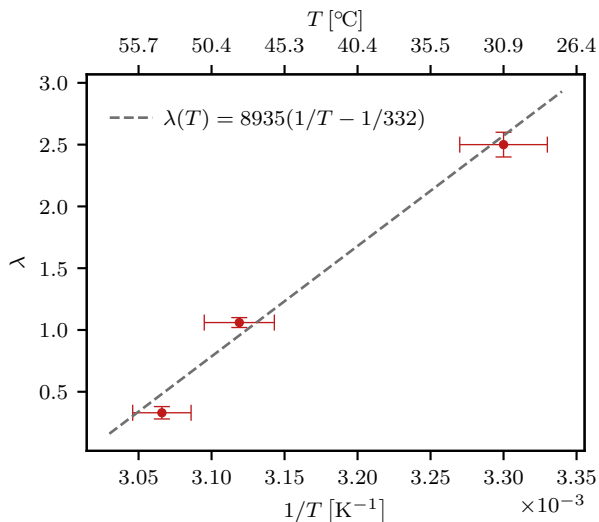
step in the ISF to the relaxation of big aggregates that diffuse slower in comparison to single stars. As differently sized clusters should remain in a dynamic equilibrium state due to permanent inter-cluster arm exchanges, such dynamics might leave a footprint on the relaxation of the system. However, we note that once the clusters formed during equilibration phases of our simulations, their reorganization was an extremely rare event over the course of a typical total simulation time. Therefore, we think that such dynamic rearrangements had a only minor effect on the observed ISF of the system.

2.5.11 Relation between λ and T

Since λ has been introduced as a parameter of the model and a quantitative connection to the temperature is still lacking, we can now fulfill this task. Indeed, the comparison between three characteristic data points, namely (i) the θ -point of the outer block, (ii) the temperature, where a second relaxation mode in the ISFs appears, and (iii) the temperature, at which a single TSP collapses, offers us a possibility to establish a correspondence between λ and $1/T$, valid within the range of experimentally accessible temperatures (Supplementary Figure 2.9):

$$\lambda(T) = \kappa \left(\frac{1}{T} - \frac{1}{T_0} \right), \quad T \leq T_0,$$

where $\lambda(T) = 0$ for $T > T_0$ with $T_0 = 332$ K, and $\kappa = 8935$ K.

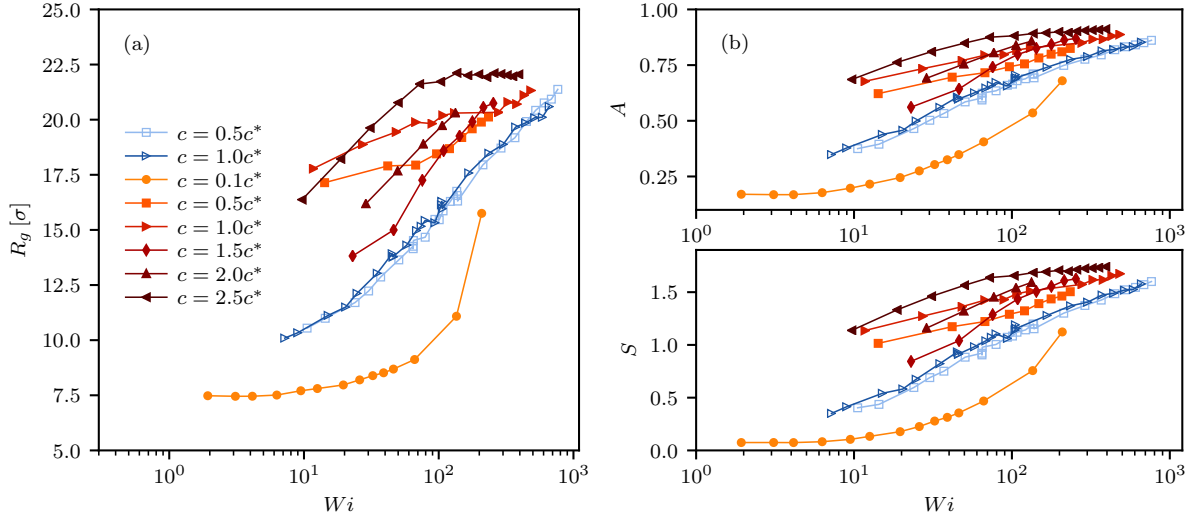


Supplementary Figure 2.9: Relation between λ and $1/T$ based on (i) the θ -point of the B-block, (ii) the temperature, where a second step in the ISFs appears, and (iii) the temperature, at which a single TSP collapses.

2.5.12 Solvent and shear

We chose multiparticle collision dynamics (MPCD) as a solvent because this particle-based mesoscale model faithfully resolves hydrodynamic interactions with a modest computational cost [160]. The properties of the MPCD fluid are controlled by the particle number density, the rotation angle, the temperature, and the time between collisions [132, 161, 162]. We chose the density as $\rho = 5\sigma^{-3}$ and the rotation angle as 130° , and performed a collision every 20 MD timesteps with $\Delta t = 0.005\tau$ (every 0.1τ). Each solvent bead mass was set to have a mass of $m = 1$. We additionally applied a Maxwell–Boltzmann rescaling thermostat [163, 164] to each cell to maintain a constant temperature $T = 1.0\varepsilon/k_{\text{B}}$ throughout the fluid, where k_{B} is the Boltzmann’s constant. The viscosity ν can be estimated for the MPCD fluid using kinetic theory [165], giving $\nu = 3.96\varepsilon\tau/\sigma^3$ for our parameters.

We determined the relaxation time τ_0 of this TSP model system for three different values of $\lambda = 1, 2$ and 3 . The diffusion coefficient D was computed from the mean-squared displacement using six independent single star simulations. Then, the relaxation time was defined as the time a polymer needed to diffuse its own size, $\tau_0 = R_{\text{g}}^2/D$. The results are $\tau_0 = 71411\tau$ for $\lambda = 1$, $\tau_0 = 44028\tau$ for $\lambda = 2$, and $\tau_0 = 30655\tau$ for $\lambda = 3$. The estimate obtained from the Zimm relaxation time for a single arm would be much lower, because the dependence of the relaxation time on star functionality and attraction strength along the arms would be neglected. With τ_0 known, the more relevant Weissenberg number



Supplementary Figure 2.10: **a**, Radius of gyration as a function of Weissenberg number for $\lambda = 1$ (open symbols) and $\lambda = 3$ (closed symbols). **b**, Anisotropy and sphericity values for the same systems. The colors and symbols of the latter match the ones in the legend of **a**.

$Wi = \dot{\gamma}\tau_0$ instead of the shear rate was used to facilitate comparison between simulations and experiments.

For implementing shear flow, we used the reverse nonequilibrium simulation (RNES) method [166]. It imposes a momentum flux on the system in an unphysical way by swapping momentum of MPCD-particles in certain regions of the box. Consistent with the standard implementation, we picked the regions to be at $0.25L_z$ and $0.75L_z$ with a thickness of 1σ each. The momentum flows back through the fluid by friction in a physically correct way, causing a velocity gradient in the system. This results in a gradient in the z -direction, with x being the flow direction. By measuring the imposed perturbation P_x on the system and the resulting flow field, the viscosity as function of shear rate can be calculated very accurately as $\eta = \tau/\dot{\gamma}$, where the stress can be calculated from the imposed perturbation $\tau = P_x/2tA$. The main advantage of RNES is, that by performing simulations of non-equilibrium TSP solutions, structure and shear viscosity can be obtained at the same time with no substantial additional computational effort. Because unexpected nonlinear flow profiles have been observed when using RNES in non-cubic boxes [167], we performed all simulations in cubic boxes of size $100\sigma^3$. We then exchanged the momentum of different number of pairs to create a steady state flow. By using a modified version, where pairs with momenta close to a target value instead of the maximum were exchanged, we were able to tune flow rate more precisely [168, 169].

The influence of shear rate on the size of the star polymers is shown in Supplementary

Figure 2.10. The radius of gyration for all λ and c considered increases with shear rate because the star polymers extend in the flow direction. The shape changes from approximately spherical on average to rod-like, as illustrated by the anisotropy A and sphericity S values in Supplementary Figure 2.10b. A perfect sphere would have $A = S = 0$ and a perfect rod would have $A = 1, S = 2$.

Chapter 3

The influence of arm composition on the self-assembly of low-functionality telechelic star polymers in dilute solutions

To appear in Colloid and Polymer Science: Esmaeel Moghimi, Iurii Chubak, Dimitra Founta, George Polymeropoulos, Konstantinos Ntetsikas, Nikos Hadjichristidis, Christos N. Likos, and Dimitris Vlassopoulos, The influence of arm composition on the self-assembly of low-functionality telechelic star polymers in dilute solutions, in press (2020).¹

We combine synthesis, physical experiments, and computer simulations to investigate self-assembly patterns of low-functionality telechelic star polymers (TSPs) in dilute solutions. In particular, in this work we focus on the effect of the arm composition and length on the static and dynamic properties of TSPs, whose terminal blocks are subject to worsening solvent quality upon reducing the temperature. We find two populations, single stars and clusters, that emerge upon worsening the solvent quality of the outer block. For both types of populations, their spatial extent decreases with temperature, with the specific details (such as temperature at which the minimal size is reached) depending on the coupling between inter- and intra-molecular associations as well as their strength. The experimental results are in very good qualitative agreement with coarse-grained simula-

¹Author contributions: E. M. and I. C. contributed equally. G. P., K. N., and N. H. synthesized the polymers. E. M., D. F., and D. V. performed the experiments. I. C. and C. N. L. performed the simulations. All authors interpreted the results. I. C. and E. M. wrote the paper with contributions from D. V. and C. N. L.

tions, which offer insights into the mechanism of thermoresponsive behavior of this class of materials.

3.1 Introduction

Self-organization of building blocks due to external stimuli is ubiquitous in most materials and all living organisms in nature. Inspired by this, a remarkable body of work has been performed to understand and emulate their response to temperature [170, 171, 172], pH [173, 174, 175] and light [176, 177], enabling the controlled design of their structure assembly. Recent advances in polymer chemistry have led to the synthesis of various building blocks with complex architectures and functionalized properties. Such responsive building blocks that can self-organize into higher-order structures may form soft patchy particles, which have directional interactions and varying softness. Furthermore, topological effects that arise in systems with complex architecture can alone lead to a range of interesting phenomena in and out of thermodynamic equilibrium for both low [178, 33, 179, 36, 180, 181, 29] and high system densities [182, 34, 183, 184, 185, 186]. Functionalized biomolecules such as DNA-grafted colloidal particles represent a typical example where patchiness reflects the competition between inter- and intra-particle associations [187, 188, 189, 190]. However, despite its significance, DNA-based research is very specialized and yields limited amounts of samples. An alternative design of patchy particles is based on the so-called Telechelic Star Polymers (TSPs), that is star polymers with functionalized end groups [116, 191, 120, 15]. A TSP consists of f amphiphilic AB-block copolymer arms grafted on a common center. The solvophilic A-block is attached at the center of the star, whereas the solvophobic B-block is exposed to the exterior of the star. On changing the solvent quality through temperature variation, the outer blocks become attractive and form patches on the surface of the particle [121, 18, 192]. With such a TSP system, it is thus possible to cover the entire range of inter-particle interactions, from purely repulsive to attractive soft colloids simply by changing the solvent quality. The self-assembly of TSPs at the single molecule level and in concentrated solutions depends mainly on three parameters: (*i*) the functionality f of the stars, (*ii*) the outer block size ratio $\alpha = N_B/(N_A + N_B)$ (N_A and N_B denote the length of the respective block), and (*iii*) the attraction strength between the outer solvophobic blocks which is enhanced upon worsening solvent quality.

TSPs with low functionality ($f \leq 5$) collapse into a watermelon structure with one single patch on the surface of the particle [121]. However, more complex structures with a

richer distribution of patches are formed in TSPs with higher functionality [18]. Such soft patchy particles can preserve their properties such as the size, number and arrangement of patches upon increasing the TSP concentration [17]. The inherent flexibility of such soft-particles leads to formation of ordered structures in the case of high functionality [17]. On the other hand, low-functionally TSPs tend to form micellar aggregates [22, 24, 23, 123], which at relatively high concentrations self-assemble into long wormlike micelles [24, 21]. In previous work, we have examined the effects of temperature (or attraction strength) on the self-assembly of these low- f TSPs in dilute solution [192]. In the present work, we extend these investigations by addressing the effects of the block size ratio and arm length on the self-organization of TSPs with $f = 3$ in dilute solutions. The new results provide insight into the responsive behavior of TSPs, paving the way for the design of functional materials with tunable properties.

3.2 Materials and methods

3.2.1 Experimental details

Telechelic star polymers (TSPs) with three arms made of 1,4-polybutadiene (PB) as the inner A-block and polystyrene (PS) as the outer B-block were synthesized by anionic polymerization and chlorosilane chemistry using high-vacuum techniques. Detailed information on the synthesis procedure can be found in Ref. [192]. Three different TSP samples have been used in the present study. Two of them have a similar total molar mass of about 40000 g/mol, albeit a different PS weight fraction of $f_{\text{PS}} = 0.14$ and 0.33. The third sample, which was used in our previous work [192], has a lower molar mass of $M_{\text{W}} = 26700$ g/mol and $f_{\text{PS}} = 0.23$. The molar mass distribution in all three TSP

Sample	$M_{\text{w}}^{\text{star}}$ (g/mol)	$M_{\text{w}}^{\text{linear}}$ (g/mol)	f_{PS} %(w/w)	f_{PB} %(w/w)	c/c^*	n (mol/m ³)
1	40500	13000	0.14	0.86	0.03	0.14
2	40000	13000	0.33	0.67	0.04	0.11
3	26700	8800	0.23	0.77	0.05	0.31

Table 3.1: Molecular characteristics of investigated star diblock copolymers (PS-b-PB)₃. $M_{\text{w}}^{\text{star}}$ is the total molar mass of the TSP, $M_{\text{w}}^{\text{linear}}$ is the arm molar mass, f_{PS} , and f_{PB} , are the weight fractions of PS and PB blocks, respectively. c is the TSP concentration in terms of the overlap concentration $c^* = 3M_{\text{w}}^{\text{star}}/(4\pi R_{\text{h}}^3 \mathcal{N}_{\text{A}})$ (R_{h} is the star’s hydrodynamic radius at high temperatures and \mathcal{N}_{A} is the Avogadro number), and n is the number density of TSPs in solution.

samples is rather narrow with the corresponding polydispersity being around $\mathbb{D} = 1.03$. The detailed molecular characteristics of the samples are listed in Table 3.1.

We have used 1-phenyldodecane as the solvent. It has a cloud-point at 53 °C for PS [126] and 22 °C for PB (the corresponding θ -temperatures are expected to be slightly higher). Solutions were prepared by mixing an appropriate amount of the TSP with the solvent to reach the desired concentration. The sample degradation was inhibited by adding 0.1 wt% of the TSP of the antioxidant BHT (2,6-Di-tert-butyl-4-methylphenol). In order to fully dissolve TSPs, methylene chloride was used as the cosolvent. Then, the cosolvent was evaporated under ambient conditions until a constant weight was achieved.

Dynamic Light Scattering (DLS) was used to investigate the dynamics and self-assembly of TSPs in dilute solutions. In DLS, the normalized autocorrelation function $G(q, t) = \langle I(q, 0)I(q, t) \rangle / \langle I(q, 0) \rangle^2$ of the total scattered light intensity $I(q)$ at the wave vector $q = (4\pi n_0/\lambda) \sin(\theta/2)$ (n_0 is the refractive index, θ denotes the scattering angle, and λ is the wavelength of the incident laser beam) is related to the normalized time correlation function of the scattered electric field $E(q, t)$ by the Siegert relation:

$$G(q, t) = 1 + f^* |\tilde{\alpha}g(q, t)|^2 = 1 + f^* |C(q, t)|^2, \quad (3.1)$$

where f^* stands for the coherence instrumental factor, $\tilde{\alpha}$ is the fraction of $I(q)$ associated with fluctuations relaxing with times longer than 0.1 μs [142, 143, 144], and $C(q, t)$ denotes the intermediate scattering function (ISF). The inverse Laplace transformation using the constrained regularization method was applied to compute the relaxation spectrum $H(\ln \tau)$. This method assumes that $C(q, t)$ can be expressed as the superposition of exponentials:

$$C(q, t) = \int_{-\infty}^{+\infty} H(\ln \tau) \exp(-t/\tau) d(\ln \tau) \quad (3.2)$$

The characteristic relaxation times correspond to the peak positions of $H(\ln \tau)$, whereas the area under the peak defines the value of $\tilde{\alpha}$ in equation 3.1 and hence the intensity $\tilde{\alpha}I(q)$ associated with the particular dynamic process. The transformation was performed with the program CONTIN [130] that yielded the relaxation time and intensity of the partitioning modes.

DLS experiments were performed on an ALV-5000 goniometer/correlator setup (ALV-GmbH, Germany). The light source was a Nd:YAG dye-pumped, air-cooled laser (100 mW) with the wavelength $\lambda = 532$ nm. The refractive index of 1-phenyldodecane is $n_0 = 1.482$. Before each DLS experiment, the samples were equilibrated at $T = 60$ °C, which is above the cloud point of the outer PS-block, for 10 min to erase thermal

Sample	v_{PS} [L/mol]	v_{PB} [L/mol]	v_{total} [L/mol]	α_{PS}	α_{PB}	N
1	1.73	12.53	14.26	0.12	0.88	144
2	4.09	9.76	13.85	0.30	0.70	140
3	1.93	7.60	9.53	0.20	0.80	96

Table 3.2: Composition of investigated star diblock copolymers (PS–b–PB)₃. v_{PS} and v_{PB} are molar volumes of PS and PB, respectively, whereas v_{total} is the total molar volume of the TSP. N is the TSP’s polymerization degree computed on the basis of PS reference segment volume, and α_{PS} and α_{PB} denote the resulting number fractions of the two components.

history. Then, the sample was quenched to the desired temperature and equilibrated. The equilibration process was probed by measuring the ISF until it reached steady values over time. The duration of equilibration depended on the temperature and ranged from 10 minutes for $T = 60$ °C to 10 hours for $T = 20$ °C.

3.2.2 Simulation details

To model TSP dynamics under worsening solvent conditions for its outer block, we have employed a coarse-grained dissipative particle dynamics (DPD) model with explicit solvent. In what follows, the inner blocks of a TSP are labeled ‘A’, the outer ones – ‘B’, whereas solvent particles – ‘S’. In DPD, the total force \mathbf{F}_i acting on the i -th particle, is composed of the conservative \mathbf{F}^{C} , dissipative \mathbf{F}^{D} , and random \mathbf{F}^{R} contributions [193]:

$$\mathbf{F}_i = \sum_{j \neq i} (\mathbf{F}_{ij}^{\text{C}} + \mathbf{F}_{ij}^{\text{D}} + \mathbf{F}_{ij}^{\text{R}}). \quad (3.3)$$

In equation (3.3) above, $\mathbf{F}_{ij}^{\text{C}}$ is the conservative force acting between the i -th and j -th particle separated by a distance r_{ij} (here and in what follows, $\mathbf{r}_{ij} = \mathbf{r}_i - \mathbf{r}_j$, $r_{ij} = |\mathbf{r}_{ij}|$, $\hat{\mathbf{r}}_{ij} = \mathbf{r}_{ij}/r_{ij}$, and $\mathbf{v}_{ij} = \mathbf{v}_i - \mathbf{v}_j$):

$$\mathbf{F}_{ij}^{\text{C}} = A_{ij} w(r_{ij}), \quad (3.4)$$

where A_{ij} is the maximal repulsion between the particles and $w(r_{ij})$ is given by

$$w(r_{ij}) = (1 - r_{ij}/r_{\text{cut}})\theta(r_{\text{cut}} - r), \quad (3.5)$$

with $\theta(x)$ denoting the Heaviside step function and the cutoff distance r_{cut} being chosen as the unit of length ($r_{\text{cut}} = 1$). Furthermore, $\mathbf{F}_{ij}^{\text{D}}$ is the pairwise dissipative force

$$\mathbf{F}_{ij}^{\text{D}} = -\gamma w(r_{ij})^2 (\hat{\mathbf{r}}_{ij} \cdot \mathbf{v}_{ij}), \quad (3.6)$$

and $\mathbf{F}_{ij}^{\text{R}}$ is the pairwise random force

$$\mathbf{F}_{ij}^{\text{R}} = -\sqrt{2\gamma k_{\text{B}}T/\Delta t} \cdot \eta_{ij} w(r_{ij}), \quad (3.7)$$

where η_{ij} is a Gaussian random number with zero mean and unit variance. The unit of mass is set by the (same) mass of every particle m , whereas the unit of energy was chosen to be $k_{\text{B}}T$ ($k_{\text{B}}T = 1$). The simulation were performed using the HOOMD-blue simulation package [135, 134, 133, 194] using friction coefficient $\gamma = 4.5m\tau^{-1}$ and the equations of motion were integrated using the Velocity-Verlet algorithm [195] with time step $\Delta t = 0.04\tau$, where $\tau = r_{\text{cut}}\sqrt{m/k_{\text{B}}T}$ is the DPD unit of time.

To obtain the total polymerization degree N of the star arms in the experimental samples considered, we first estimated the molar volumes of PB and PS, given by $v_{\text{PS/PB}} = M_{\text{W}}/\rho_{\text{PS/PB}}$, where $\rho_{\text{PS/PB}}$ is the corresponding molar density ($\rho^{\text{PS}} = 1.05$ g/mL and $\rho^{\text{PB}} = 0.892$ g/mL). N and $\alpha_{\text{PS/PB}}$ were then computed on the basis of the PS reference segment volume 99.2 mL/mol and are listed in Table 3.2. In general, we are interested in the behavior of experimental systems in a rather narrow temperature range 20 °C $< T < 60$ °C, where the Flory-Huggins incompatibility parameter $\chi_{\text{PS-PB}} = 18.78/T - 9.6 \cdot 10^{-4}$ [196] does not change substantially (experimental values of $\chi_{\text{PS-PB}}N$ for the three samples in such temperature range are $\chi_{\text{PS-PB}}N \lesssim 10$), implying that the self-assembly is mainly controlled by the solvent selectivity towards the outer block.

Given the computational cost of simulations with explicit solvent particles, we focused on a star polymer model with $f = 3$ arms containing $N = 64$ monomers, and systematically varied the outer block ratio α by changing N_{A} and N_{B} . All our simulations were performed at total particle density $\rho r_{\text{cut}}^3 = 3$. Bonded interactions were given by $V_{\text{bond}}(r) = \frac{K}{2}(r - r_{\text{cut}})^2$ with $K = 50k_{\text{B}}T$. The central particle, to which all arms were connected to, was treated as a monomer of type A. In DPD, repulsion amplitudes A_{ij} can be directly related to the Flory-Huggins χ_{ij} parameters [197]:

$$A_{ij} \approx A_{ii} + \kappa(\rho)\chi_{ij}, \quad (3.8)$$

where $\kappa(\rho)$ depends on the DPD density such that $\kappa(3) = 3.49$. In all simulations,

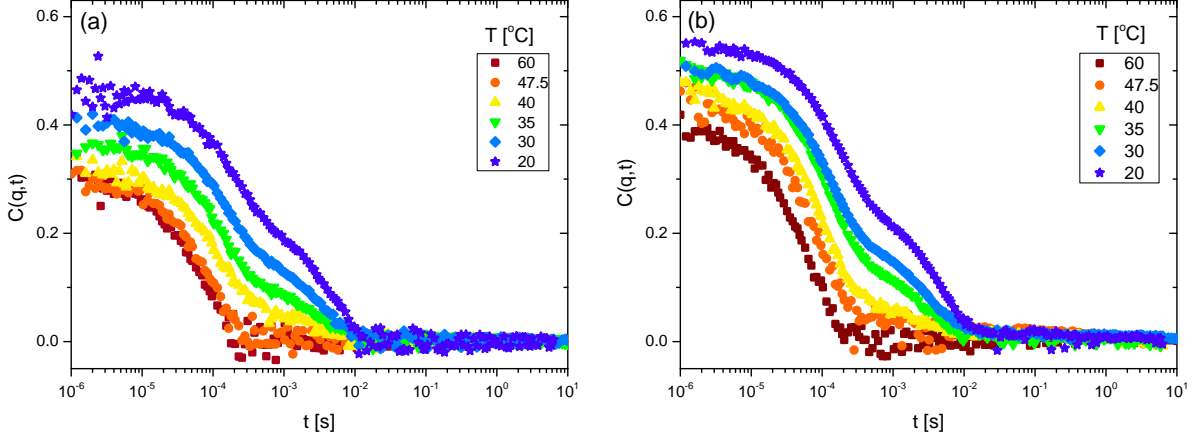


Figure 3.1: Experimental ISFs at constant wave vector $q = 0.02475 \text{ nm}^{-1}$ and different temperatures for TSPs with outer PS-block fractions of $f_{PS} = 0.14$ (a) and $f_{PS} = 0.33$ (b). Note that the plateau values of the ISF at short times is well below one. This is due to the fact that a part of the scattered intensity originates from density fluctuations of solvent molecules.

we fixed the inter-block incompatibility parameter $\chi_{AB} = 0.23$, which corresponds to $A_{AB} = 25.8$ at $pr_{\text{cut}}^3 = 3$. Such value of χ_{AB} was obtained from a conservative experimental value $(\chi_{AB}N)_{\text{exp}} = 10$ by taking into account finite polymer chain length corrections: $\chi_{AB} = (\chi_{AB}N)_{\text{exp}} \cdot (1 + 3.9N^{2/3-2\nu})/N$ with $N = 64$ and $\nu = 0.588$ [197]. The incompatibility parameter χ_{AS} for the inner block and effective solvent particles was always set to $\chi_{AS} = 0$, which corresponds to $A_{AS} = 25$. Moreover, χ_{BS} was systematically varied between 0 and 7 with step ≈ 0.72 , corresponding to A_{BS} in the range between 25 and 50. Finally, note that the main goal of our simulations using such a coarse-grained model is not to quantitatively reproduce the change of star properties with increasing χ_{BS} , for which atomistic simulations with realistic solvent interactions would be necessary, but to qualitatively assess the effect of self-associations on the change of TSPs static and dynamic behavior.

3.3 Experimental results

We first focus on the effect of the outer PS-block fraction on the dynamic relaxation of the TSP system at low densities. In Figure 3.1, we show the experimental ISFs at a fixed wave vector and various temperatures for the two samples with comparable total molecular weights but with distinct PS weight fractions. The ISFs show two distinct trends upon changing temperature. At high temperatures, the ISFs show a single exponential decay that demonstrates the existence of individual stars in solution. However,

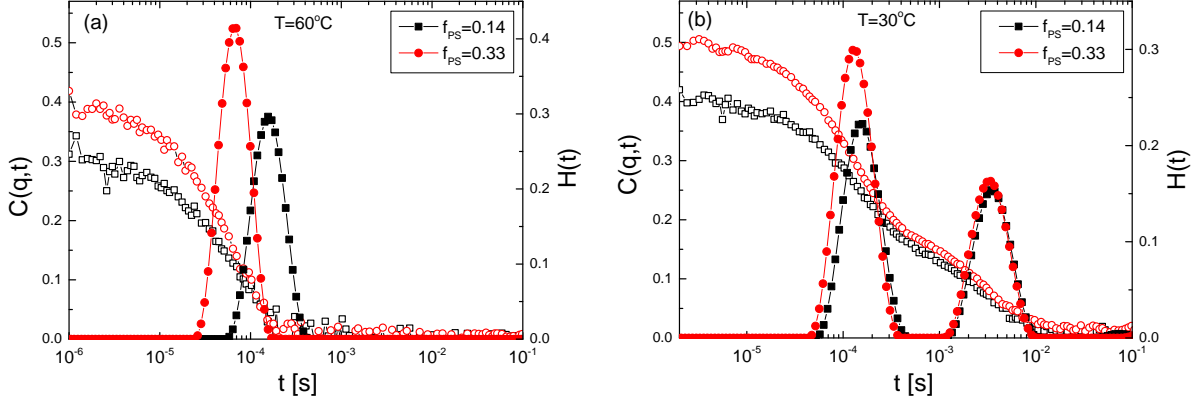


Figure 3.2: ISF (open symbols, left axis) and its corresponding relaxation times spectrum (closed symbols, right axis) deduced from the constrained regularization method for the TSPs with PS fractions of $f_{\text{PS}} = 0.14$ (black squares) and 0.33 (red circles) at $q = 0.02475 \text{ nm}^{-1}$ for $T = 60 \text{ }^\circ\text{C}$ (a) and $T = 30 \text{ }^\circ\text{C}$ (b).

when temperature is reduced below the cloud temperature of the outer-block, the ISF features a two-step decay which indicates the coexistence of two distinct populations in the system. The first decay (fast process) in the ISF is similar to the one observed at high temperatures and hence represents the individual stars in solution. On the other hand, the second decay (slow process) taking place at longer times suggests the presence of larger aggregates (clusters of TSPs). The slow process becomes more pronounced as the temperature is decreased. Interestingly, the two-step decay in the ISF appears at a slightly higher temperature for the TSP with a larger PS-fraction.

To extract hydrodynamic sizes associated with the two processes in the solution, that is individual TSPs and clusters, the relaxation spectrum is calculated from the inverse Laplace transformation of the ISF using the constraint regularized method [130] discussed in Section 3.2.1. Typical results of such analysis for the TSPs with two different PS fractions at $T = 60 \text{ }^\circ\text{C}$ and $30 \text{ }^\circ\text{C}$ are shown in Figure 3.2. The relaxation spectrum at $60 \text{ }^\circ\text{C}$ shows a single peak, which is rather sharp, reflecting single exponential decay of the ISF mode. The position of the peak shifts to a slightly longer time for the TSP with a smaller PS fraction, indicating a larger hydrodynamic radius. At the lower temperature of $30 \text{ }^\circ\text{C}$, the relaxation spectrum exhibits two well-separated peaks, as seen in Figure 3.2b. Similarly to high temperatures, the position of the first peak shifts to a slightly longer time for the TSP with a smaller PS fraction, whereas the position of the second peak in both TSP samples is located at a similar time. These two peaks represent the relaxation times associated with individual TSPs and clusters, respectively. Subsequently, the two relaxation times are used to calculate the diffusion coefficients associated with each component. The diffusion coefficient for the fast mode (where $qR < 1$) is q -independent,

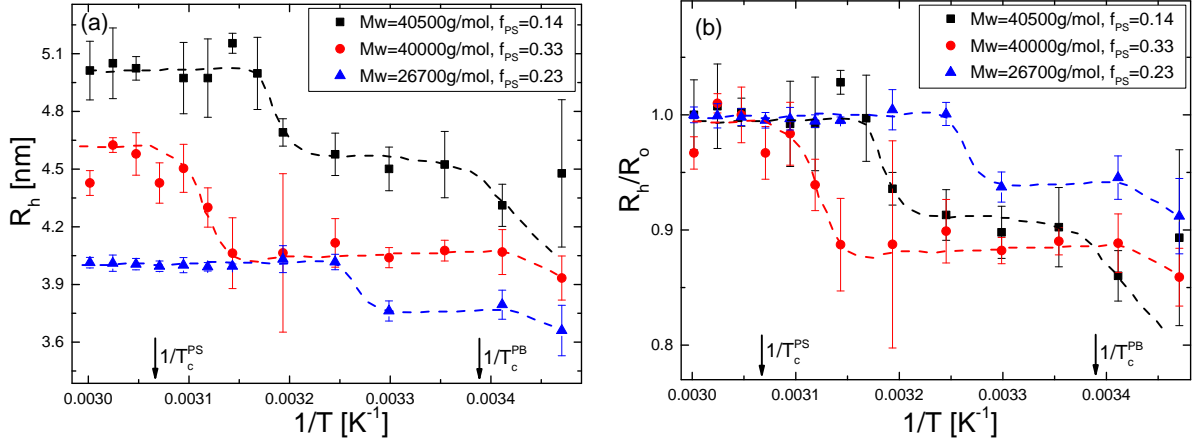


Figure 3.3: **a**, The hydrodynamic radius, R_h , of individual TSPs in the dilute solution calculated from the fast process in the experimentally determined ISFs. **b**, R_h normalized by its plateau value at high temperatures. The dashed lines serve as a guide to the eye. The black arrows indicate the cloud-points of inner PB and outer PS blocks.

whereas D for the slow mode (where $qR \geq 1$) shows some q -dependence. In the latter case, D extrapolated to $q = 0$ is used to calculate R_h . Then, the hydrodynamic sizes of TSPs and clusters are obtained using the Stokes-Einstein-Sutherland relation.

We first examine the effect of the block size ratio α on the single TSP size upon cooling. In experiments, the radius of gyration was too small to be probed by DLS. Instead, we focused on the hydrodynamic radius R_h of individual TSPs in dilute solution, as calculated from the fast process in the ISF using the Stokes-Einstein-Sutherland relation. The temperature dependence of R_h for the three studied TSP samples is shown in Figure 3.3. The single star size exhibits a two-step shrinkage upon reducing temperature or equivalently worsening the solvent quality. The first decay in size takes place at temperatures well below the cloud-point of outer PS-blocks, whereas the second drop is seen when temperature is reduced further below the cloud-point of the inner PB-block. Hence, the first decrease in size is associated with the collapse of outer blocks, whereas the second decay corresponds to the case when inner blocks start to collapse. At high temperatures, for the TSP with $f_{PS} = 0.14$, we find $R_h \approx 5$ nm and for $f_{PS} = 0.33$, $R_h \approx 4.6$ nm (see Figure 3.3a). Although both TSPs have almost the same molar mass of about 40000 g/mol, the difference in their size originates from the difference in the fraction of PS. The radius of gyration of a star homopolymer in good solvent conditions is given by $R_g \approx \kappa(f)bN^\nu$, where $\nu = 0.588$, N is the number of Kuhn segments in a star arm, b is the size of a Kuhn segment, and $\kappa(f)$, which depends on the number of star arms f , is a numeric constant that takes into account the star functionality [198, 199, 200]. Using the latter relation it can be found that the size of a star made of purely PB is about 65% larger compared to

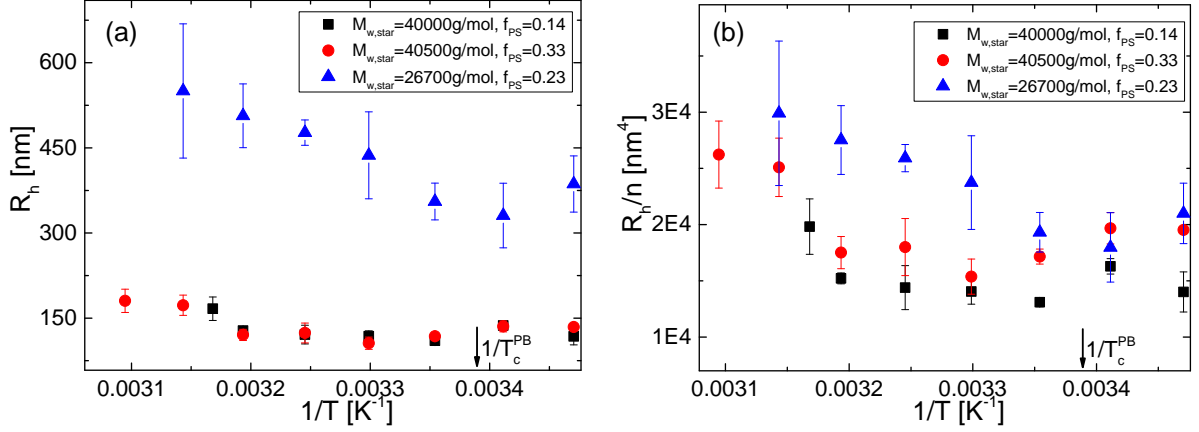


Figure 3.4: **a**, The hydrodynamic radius, R_h , of clusters extracted from the slow process in the experimental ISFs. **b**, The ratio of R_h to the number density n (see Table 3.1) of TSPs in the solution. The black arrow indicates the cloud-point of inner PB blocks.

that made of purely PS, $R_g^{\text{PB}} \approx 1.65R_g^{\text{PS}}$, given that their molar mass is the same [80]. Hence, it is expected that the increase in PS fraction reduces the size of a TSP. In order to compare the collapse process for stars of different size, we have normalized the TSP size by the plateau value of R_h at high temperatures.

The TSP with a larger fraction of outer PS-blocks ($f_{\text{PS}} = 0.33$) shows the first-step reduction in size at higher temperatures and the second-step drop at slightly lower temperatures compared to the TSP with a smaller PS fraction ($f_{\text{PS}} = 0.14$). In both stars, the decrease in size is about 15%, as seen in Figure 3.3b. In addition, in Figure 3.3 we show the results for a TSP with a smaller molar mass (26700 g/mol) with the outer PS-block fraction $f_{\text{PS}} = 0.23$, which is between the other two higher molar mass TSPs with $f_{\text{PS}} = 0.14$ and 0.33. The main difference is that the TSP with the smaller molar mass exhibits the decay in size at a much lower temperature compared to the other two, which originates from a smaller value of the incompatibility parameter $\sim \chi_{\text{PS-S}}N$. Moreover, the decrease in size is also rather weaker (about 10%), which can be attributed to a shorter length of its arms.

In Figure 3.4, we present the temperature dependence of clusters' R_h for the systems of TSPs with the same molar mass but two different PS fractions ($M_W = 40000$ g/mol, $f_{\text{PS}} = 0.14$ and 0.33). In both TSPs, the cluster size shrinks on cooling. However, a slight but consistent increase in the cluster size is observed when temperature is further reduced below the cloud-point of the inner PB-block. Moreover, the hydrodynamic cluster size does not show change with the fraction of outer PS block. In Figure 3.4a, we additionally show the results for the TSP with smaller molar mass ($M_W = 26700$ g/mol) and $f_{\text{PS}} = 0.23$. In this case, the temperature dependence of the cluster size is the same as for the

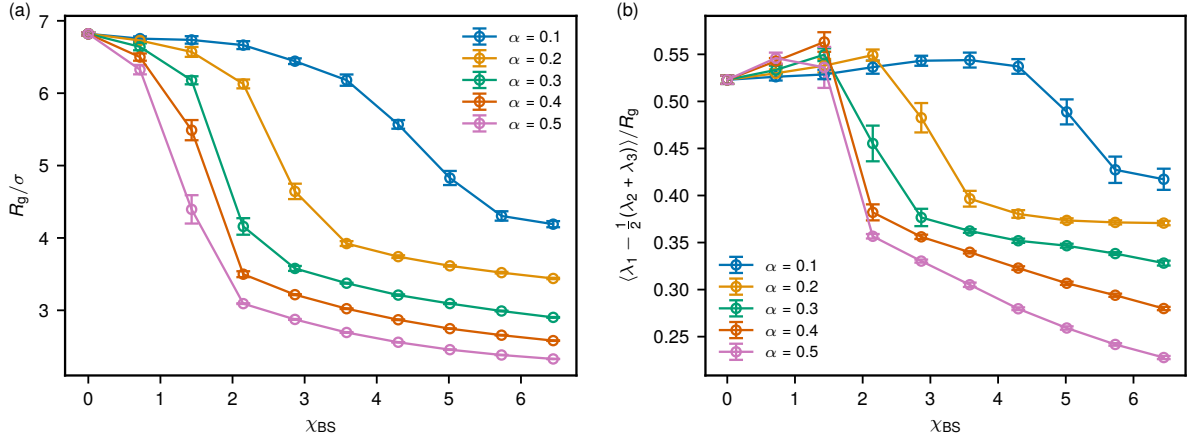


Figure 3.5: **a**, Mean radius of gyration of a TSP R_g as a function of χ_{BS} for different fractions of the outer block $\alpha = N_B/N$. **b**, Mean asphericity of a TSP, computed as $\langle \lambda_1 - \frac{1}{2}(\lambda_2 + \lambda_3) \rangle$, scaled with its mean radius of gyration R_g as a function of χ_{BS} for different α .

other two TSPs ($f_{PS} = 0.14, 0.33$). However, the smaller molar mass TSP shows a cluster size that is nearly three times larger. This could be due to a higher concentration of these TSPs. To rule out the effect of concentration, we have normalized the cluster size by the number density of TSPs in solution (see Figure 4b). The number density takes into account for the number of stickers available in the solution. With such normalization, the differences in cluster size between different TSPs are reduced to a great extent. The minor differences could originate from the complex nature of self-organization of TSPs due to small differences in their molecular characteristics.

3.4 Simulation results

We now focus on static and dynamic properties of single TSPs under worsening solvent conditions for the outer B block, that is under increasing χ_{BS} . To do so, we simulated single stars with $f = 3$ arms of length $N = 64$ using a coarse-grained DPD model with explicit solvent particles, as described in detail in Section 3.2.2. The outer block ratio was systematically varied from 0.1 to 0.5 with step 0.1. The exact number of A- and B-type monomers in an arm was $N_A = 58, 52, 45, 39, 32$ and $N_B = 6, 12, 19, 25, 32$, respectively (the corresponding $\alpha = 0.1, 0.2, 0.3, 0.4, 0.5$). For each state point (α, χ_{BS}) , we performed 10-12 independent simulation runs of length $10^5\tau$, followed after a shorter equilibration period of $10^4\tau$. Single TSPs were simulated in a box of size $L = 30r_{cut}$ at the total particle density $\rho r_{cut}^3 = 3$. To check if such box size is sufficient to accommodate a TSP, we initially simulated the same star in good solvent conditions ($\chi_{BS} = 0$) in a larger

box with $L = 35r_{\text{cut}}$, and we did not observe any substantial changes in its properties. In selective solvents, the TSP size is even smaller due to the formation of patches, which justifies the use of the same box size $L = 30r_{\text{cut}}$ in this case.

To assess single star shape properties, we computed the eigenvalues λ_i ($i = 1, 2, 3$, $\lambda_1 \geq \lambda_2 \geq \lambda_3$) of the star's gyration tensor

$$G_{ij} = \frac{1}{fN + 1} \sum_{k=1}^{fN+1} \Delta r_i^{(k)} \Delta r_j^{(k)}, \quad (3.9)$$

where $\Delta r_i^{(k)}$ is the i -th component of the k -th monomer's position in the star's center of mass frame. In Figure 3.5, we report the TSP's mean radius of gyration $R_g = \langle R_g^2 \rangle^{1/2}$ ($R_g^2 = \lambda_1 + \lambda_2 + \lambda_3$) as well as the mean asphericity parameter $\langle \lambda_1 - \frac{1}{2}(\lambda_2 + \lambda_3) \rangle$, which is positive and can vanish only for a completely symmetric configuration, as a function of χ_{BS} for different block length ratios α . The angles $\langle \dots \rangle$ denote an ensemble and time average. We find that the behavior of a single TSP size is generally very similar to the experimental one (see Figure 3.3): upon increasing χ_{BS} , we first observe a rather small decrease in R_g , followed by a major drop at higher χ_{BS} . Such behavior of R_g is associated with the formation of a single patch, where all three arms of a TSP clump together (see Figure 3.6). We find that the transition point shifts towards a higher χ_{BS} , that is a lower temperature because $\chi \sim 1/T$, with decreasing α , which is in full accordance with the experimental behavior of the two samples with $f_{\text{PS}} = 0.14$ and 0.33 that have a very similar total molar mass (see Figure 3.3b). Afterwards, only a small reduction of R_g is observed upon increasing χ_{BS} , as seen in Figure 3.3a. We also note that simulations do not capture

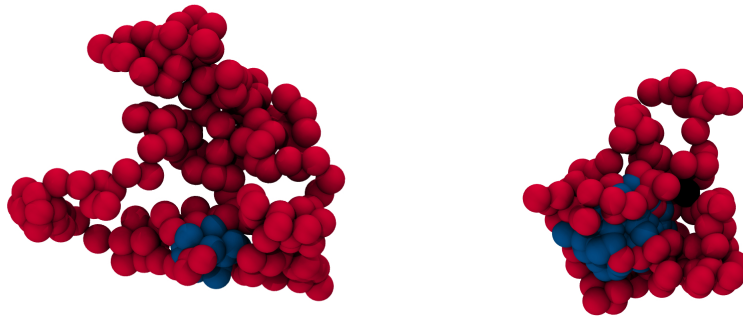


Figure 3.6: Characteristic TSP conformations with $\alpha = 0.1$ (left) and $\alpha = 0.3$ (right) at a high $\chi_{\text{BS}} \approx 7$. B-monomers are blue, A-monomers – red, star centers are black. Solvent particles are not shown for clarity.

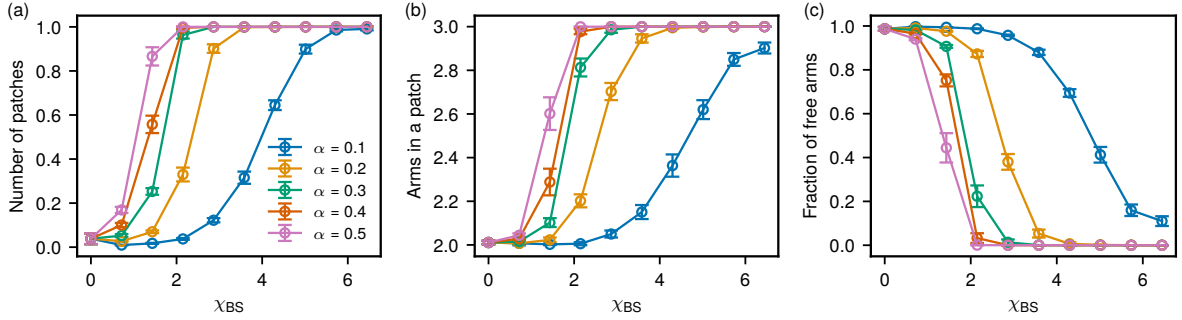


Figure 3.7: **a**, The total number of formed patches as a function of χ_{BS} for different α . Two arms are defined as being in a common patch if there is at least one pair of monomers from the two distinct arms lying at a distance $r \leq r_{cut}$. The average number of arms in a patch **(b)** and the average fraction of free arms **(c)** as a function of χ_{BS} for different α . **a**, **b**, and **c** share the same legend shown in **a**.

the second drop in size which is observed in experiments for temperatures below the cloud-point of inner-block. The reason for this discrepancy is that in simulations, for simplicity reasons, the inner-block is assumed to be always in a good solvency condition. Hence, it only captures single step shrinkage process due to collapse of outer-block monomers.

We furthermore find that the final TSP size decreases with increasing α , also in accordance with the experimental findings for the samples with $f_{PS} = 0.14$ and 0.33 (see Figure 3.3b). This behavior is associated with generally more open configuration of collapsed TSPs with small α that permit solvent flow through the TSP's interior. On the other hand, in the case of larger α , the solvophobic B-blocks form a single large patch that expels the solvent from its interior, resulting in more compact and symmetric configurations (see Figure 3.6 and Figure 3.5b). Interestingly, as can be seen in Figure 3.5b,

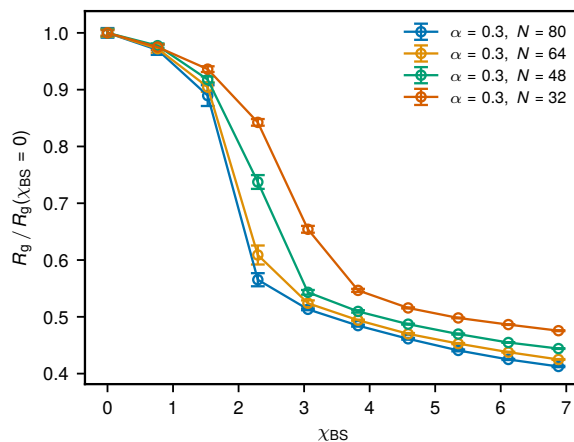


Figure 3.8: The mean radius of gyration R_g of a TSP as a function of χ_{BS} for the same fraction of the outer block $\alpha = 0.3$ but different arm lengths N .

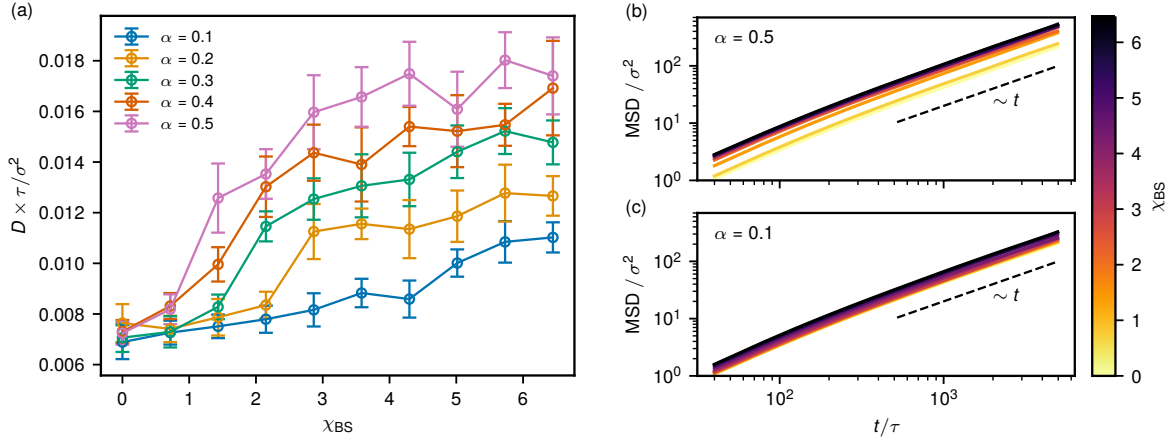


Figure 3.9: **a**, The diffusion coefficient D of the TSP’s center of mass as a function of χ_{BS} for different α . D was extracted from the long-time behavior of the MSD of the star’s center of mass, $\text{MSD} = 6Dt$. Typical MSD as a function of χ_{BS} are shown for $\alpha = 0.5$ (**b**) and $\alpha = 0.1$ (**c**).

upon slightly increasing χ_{BS} from 0, the stars first become more aspherical, which can be attributed to the formation of transient patches between two out of three star arms. This is confirmed in Figure 3.7 that reports the average number of patches formed by the star, the average number of arms in a patch, as well as the fraction of free arms as a function of χ_{BS} for different arm compositions. In agreement with earlier results [121], we find that such TSP with $f = 3$ forms only one patch for all α with all three arms contributing to it at high enough χ_{BS} . In addition, as seen from Figure 3.7a and 3.7b, the point when all arms start to form a single patch corresponds to the point when R_g drops significantly (see Figure 3.5a). Finally, to assess the influence of arm length N on the transition point for the watermelon-like structure formation, for $\alpha = 0.3$ we additionally simulated stars with arm length $N = 32, 48, 80$ for different values of χ_{BS} . The comparison between the behavior of the radius of gyration of the TSPs with different N for $\alpha = 0.3$ is shown in Figure 3.8. We find that the TSP with shorter arms features the star collapse at higher values of χ_{BS} , which therefore corresponds to lower temperatures in the experiments, being in line with the trend observed for the experimental sample with $f_{\text{PS}} = 0.23$ that has a lower molar mass, see Figure 3.

The presence of faithful hydrodynamic interactions in DPD allows us to assess the influence of patch formation on the dynamics of single stars in solution. We did this by considering the mean-square displacement of TSP’s center of mass, computed as

$$\text{MSD}(t) = \frac{1}{T-t} \int_0^{T-t} \langle [\mathbf{R}(t'+t) - \mathbf{R}(t')]^2 \rangle dt', \quad (3.10)$$

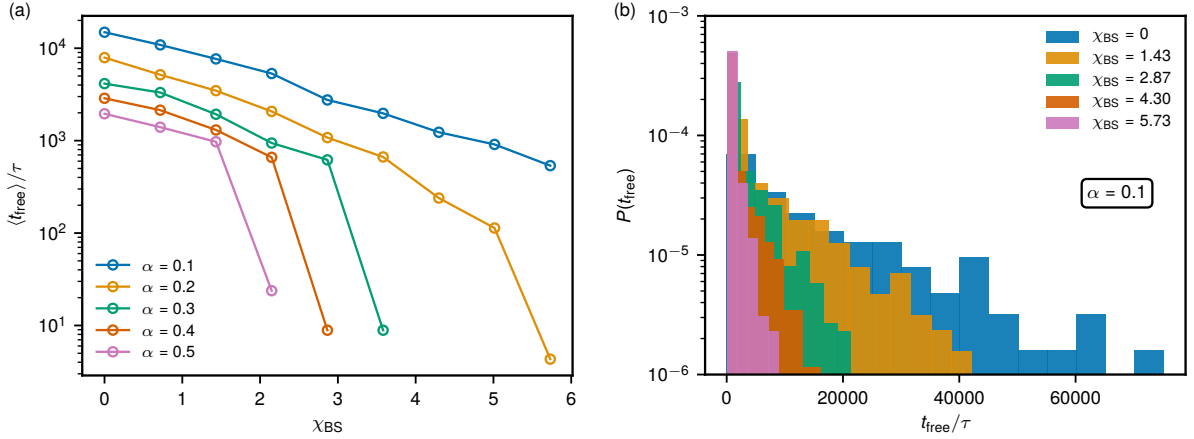


Figure 3.10: (a), The mean time of an arm not belonging to a patch $\langle t_{\text{free}} \rangle$ as a function of χ_{BS} for different α . (b), The normalized distribution of t_{free} for $\alpha = 0.1$ and various χ_{BS} .

where $\mathbf{R}(t)$ is the position of the star’s center of mass at time t , T is the total simulation time, and $\langle \dots \rangle$ stands for the average over independent simulation runs. Typical behavior of the MSD for different α as well as the extracted diffusion coefficients D are shown in Figure 3.9. We find that the tendency to form patches, causing more compact watermelon-like structures, increases the diffusivity of the TSP. In the experiments, this behavior corresponds to a reduction in the hydrodynamic radius R_h , which is in good agreement with results shown in Figure 3.3. Furthermore, this effect is especially significant for the case of high α , where D at high χ_{BS} can become about two times bigger compared to athermal conditions with $\chi_{\text{BS}} = 0$, as seen in Figure 3.9a, again in agreement with the experiments, where a larger reduction in R_h is seen for the TSP with a higher PS fraction. Finally, more open conformations of collapsed TSPs with low α makes the increase in diffusivity less pronounced (for example, about 30% increase for $\alpha = 0.10$).

In addition, we have considered the dynamics of internal patch reorganizations at the single-star level. In Figure 3.10, we show the times t_{free} for an arm spent in the free state, that is not forming an association with other arms, as a function of χ_{BS} for different α . We find that for all α , the mean value of t_{free} initially decreases exponentially fast with increasing χ_{BS} [Figure 3.10(a)], up to a point where a single patch forms. At this point, $\langle t_{\text{free}} \rangle$ drops to 0, indicating that the single patch is stable over the course of the whole simulation. The value of χ_{BS} where it happens compares with the point where a significant reduction of R_g occurs [Figure 3.5(a)]. Furthermore, in Figure 3.10(b) we show the distribution for t_{free} for $\alpha = 0.1$ at various χ_{BS} , featuring tails that decay exponentially fast with increasing t_{free} in all cases.

Finally, we consider the formation of inter-star aggregates in the dilute solution. To

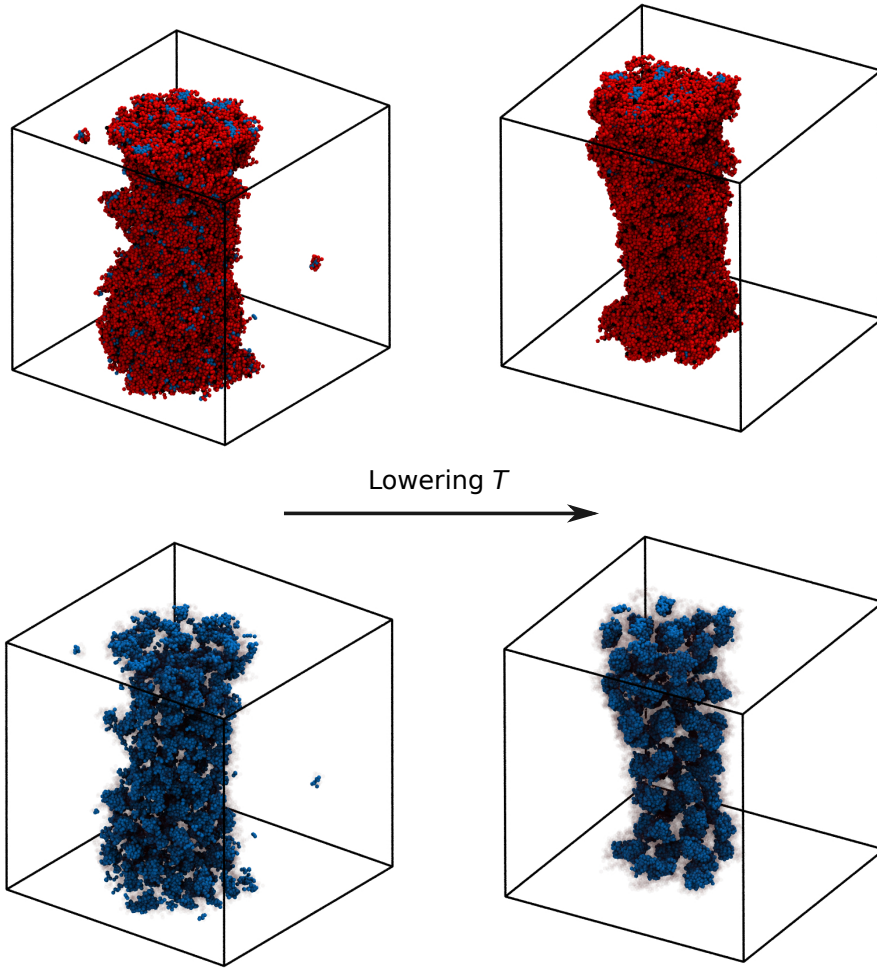


Figure 3.11: Left column: self-assembly of three-arm TSPs with $N = 10$ and $\alpha = 0.3$ into a giant cylindrical aggregate at $c \approx 0.4c^*$. The bottom row shows only the solvophobic B-blocks. Right column: the aggregate shrinks in the transverse directions upon increasing the solvophobicity of the B-monomers that become more ordered (bottom image).

asses such behavior, it is necessary to simulate a sufficiently large number of stars, which becomes computationally restrictive if using the model with $N = 64$ that was employed for single star behavior discussed previously. We therefore resort to an even coarser model with, similarly, $f = 3$ but with $N = 10$, and in what follows we focus on the case with $\alpha = 0.3$. We simulated 2000 such stars in a box with $L = 70r_{\text{cut}}$ at particle density $\rho r_{\text{cut}}^3 = 3$. In this model, the corresponding star concentration is $c \approx 0.4c^*$, which is higher than the one used in the experiments (to reach an equivalent experimental concentration of $c \approx 0.04c^*$, it would be necessary to simulate about a ten times bigger system containing $\sim 10^7$ particles). Nevertheless, even in this regime we remain at concentrations considerably below c^* . Initially, TSPs were initialized uniformly in the box and subse-

quently equilibrated in athermal solvent conditions for both blocks with $\chi_{AS} = \chi_{BS} = 0$ (χ_{AB} was set to $\chi_{AB} = 28.6$ to match the experimental value $(\chi_{AB}N)_{\text{eff}} = 10$, as explained in Section 3.2.2). Afterward, the incompatibility parameter for the outer block was increased to 4.3 ($A_{BS} = 40$) over $2 \cdot 10^6$ integration time steps and then further equilibrated for another $2 \cdot 10^6$ steps. During the latter stages, the TSPs initially began to form small micelles that subsequently merged into worm-like structures, which then again merged into a single giant cylindrical aggregate, shown in the left column of Figure 3.11. Note that such cylindrical architecture is rather a consequence of periodic boundary conditions. It is likely that symmetric spherical aggregates would form in a more dilute system with a larger simulation box size, as, for instance, recently shown in Ref. [201]. Nonetheless, this illustrates the tendency of the TSPs to form large aggregates even at dilute conditions, as previously shown in the experimental cluster sizes in Figure 3.4. We also considered the effect of lowering temperature on the structure of such aggregate by quenching χ_{BS} to 10 ($A_{BS} = 60$) and equilibrating the system for another 10^6 integration time steps. As shown in the right column of Figure 3.11, as a result of the χ_{BS} increase, the aggregate shrinks in the two transverse directions. This occurs because the solvophobic TSP blocks that lie in the aggregate’s interior become more ordered and thus push away the remaining solvent (see the bottom row of Figure 3.11). This further agrees with the experimental trend of decreasing cluster size with decreasing temperature (Figure 3.4).

3.5 Conclusions

In summary, we have investigated the self-assembly of TSPs with a variable size of the outer block as well as the arm length, which is subject to worsening solvent conditions, in dilute solutions. We find that two distinct modes in the experimental ISF appear upon lowering the temperature below a critical value: the fast-relaxing mode that corresponds to free stars in solutions as well as a slow-relaxing mode that indicates the presence of large aggregates. We find that the size of both populations decreases upon cooling. For single TSPs, the decay is associated with the formation of a single patch, where all three arms come together. From both experiments and simulations, we find that the temperature that corresponds to such transition increases with growing fraction of solvophobic monomers. However, we find that the transition temperature increases with the polymerization degree of TSP arms, when keeping the fraction of solvophobic monomers constant. The formed aggregates in solution are much bigger than single stars (~ 100 nm versus ~ 5 nm). In simulations, albeit at a higher concentration of TSPs, we have found the formation of

micellar aggregates with complex internal structure. Upon worsening the solvent quality for the outer block, the solvent is becoming more strongly expelled from the aggregate's interior, which causes the reduction of its size, similarly to the experimental behavior. We therefore speculate that similar objects also form at concentrations similar to the experimental ones, in line with assembled structures that have been recently observed in large-scale DPD simulations of linear diblock co-polymers in dilute conditions [201].

Chapter 4

Active topological glass

Published: Jan Smrek, Iurii Chubak, Christos N. Likos, and Kurt Kremer. Active topological glass. *Nature Communications* **11**, 26 (2020). DOI: 10.1038/s41467-019-13696-z.¹

The glass transition in soft matter systems is generally triggered by an increase in packing fraction or a decrease in temperature. It has been conjectured that the internal topology of the constituent particles, such as polymers, can cause glassiness too. However, the conjecture relies on immobilizing a fraction of the particles and is therefore difficult to fulfill experimentally. Here we show that in dense solutions of circular polymers containing (active) segments of increased mobility, the interplay of the activity and the topology of the polymers generates an unprecedented glassy state of matter. The active isotropic driving enhances mutual ring threading to the extent that the rings can relax only in a cooperative way, which dramatically increases relaxation times. Moreover, the observed phenomena feature similarities with the conformation and dynamics of the DNA fibre in living nuclei of higher eukaryotes.

4.1 Introduction

Tremendous interest has been devoted to understanding of the glass transition driven by an increase in packing fraction or a decrease in temperature in soft and deformable systems [202, 203]. Ultra-soft particles can be realized experimentally using polymers, such as long polymeric stars or rings, which are highly deformable but possess a fixed topology imposed during the synthesis. While it is known that the polymer topology

¹Author contributions: J. S. and I. C. contributed equally. C. N. L. and K. K. jointly supervised this work. J. S. and K. K. designed the research with the contributions from I. C. and C. N. L. J. S. and I. C. performed the simulations and data analysis. J. S., I. C. and C. N. L. interpreted the results. J. S. wrote the paper with the contributions of I. C., C. N. L. and K. K.

has strong impact on the stress relaxation mechanism [57], it has been questioned if the topology can independently induce a glass transition [66].

Such a topological glass has been conjectured for the system of long, unknotted, and nonconcatenated polymer rings in dense equilibrium solutions [66, 70]. The rings cannot cross each other, but are known to thread — one ring piercing through an eye of another ring, which temporarily topologically constraints the motion of the two rings. Mutual threadings of many rings can yield a conformation that is relaxed only if a cascade of threadings is sequentially undone, which could give rise to very long relaxation times, e.g. exponential in the ring length [204]. The glassy behavior in an equilibrium melt of rings has been observed in computer experiments, but only under a pinning perturbation, which immobilizes a fraction f of all rings. Then, for sufficiently long rings and high density a glassy behavior can be extrapolated to $f \rightarrow 0$ [66, 70]. Unfortunately, the conjectured critical length, ninety entanglement lengths, of unpinned rings is currently beyond the reach of experiments and, although the pinning deepens our theoretical understanding of the glass transition [205, 206, 207], creating it experimentally to drive the topological glass transition would be challenging.

Whereas many questions remain open in the traditional glass transition of passive Brownian particles, recently a whole new research direction has been opened by considering system composed of active particles that are driven by non-thermal fluctuations [208]. While, intuitively, activity opposes glassiness by enhancing mobility of the particles, some active models can exhibit a more complex behavior as a function of the active control parameters. For example, increasing the persistence time of the active Ornstein-Uhlenbeck particles can either glassify or fluidize the active system, depending on the particular state point, as a result of nontrivial velocity correlations in the system [209, 210, 211, 212]. Indeed, some system properties, such as the time-dependent effective temperature are pertinent to active fluids and render also the corresponding glass transition distinct from the passive one. In particular, the location and the existence of the glass transition of active fluids are dependent on the microscopic details of the activity mechanism. Nevertheless, close to the transition region, universal features of the passive glassy dynamics have been found recently for active spin-glasses [208] and self-propelled particles in the non-equilibrium mode-coupling theory (MCT) [212]. For instance, the scaling of the relaxation time with activity control parameters is governed by the same exponent as in the passive MCT.

The impact of topology on the active glassy states has been studied almost solely in the context of active particles confined to a topologically nontrivial space, in particular

a sphere [213, 214, 215, 216, 217]. There, a range of dynamic phenomena arises as a consequence of the competition between directed flows, characteristic for active matter in euclidean space, and the ‘hedgehog theorem’ [218] that asserts the existence of topological defects in a smooth vectorial field on a sphere. In contrast to these studies, where the topology is a global property of space, here we focus on a system where the active particles themselves are not point-like but feature intrinsic circular topology, the embedding space being Euclidean with periodic boundary conditions.

Glassy dynamics also appears in various biological contexts ranging from the bacterial cytoplasm [219] to collective cell migration in tissues [220]. While on the subcellular level, glass-like properties have been attributed to the high crowding, as well as size and interaction heterogeneity of the constituents [219, 221], the confluent tissues modeled using vertex models exhibit a new type of rigidity transition at constant density without [222] and with active motion [223], attributed to an interplay of cells’ shape and persistence of motion. Although there is no topology involved in these models and, therefore, they are inherently different from our present work, the transition occurs due to shape changes at constant density similarly to the case studied here.

For dense solutions of ring polymers, we show that making the rings locally more mobile by introducing a moderate segmental activity, the system reaches a glassy state with dramatically slowed-down relaxation. This novel state of matter, the ‘active topological glass’, is a consequence of the interplay between internal polymer topology, activity, and the crowded polymer environment. In contrast to the conjectured equilibrium topological glass, here no imposed pinning is necessary and only relatively short rings are sufficient to observe the transition. Moreover, contrary to well-studied polymer glasses [224], where the monomers are arrested due to their nearest neighbors, here the centers of mass of the whole chains are inhibited due to multi-body, long-range effects of topological constraints. After detailed account of the physics of the active topological glass, we discuss its relevance for the organization and dynamics of chromosomes in living eukaryotic cells.

4.2 Results

4.2.1 Dynamics after the onset of activity

We start with a large, well-equilibrated, concentrated solution of $M = 1600$ passive, uncrossable, unknotted, and nonconcatenated rings of length $N = 400$ using the well-established polymer model as in Halverson *et al.* [50, 51]. A consecutive segment of length $N_h = 50$ monomers is made active on each chain by subjecting it to thermal-like

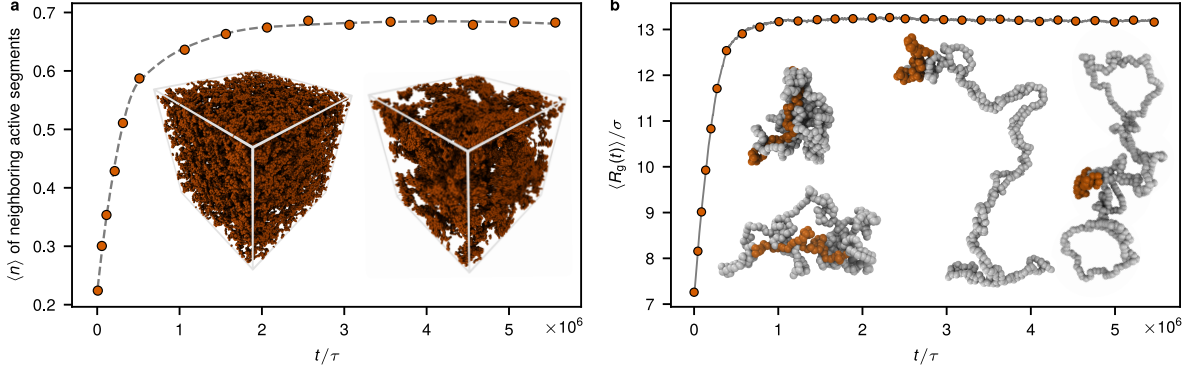


Figure 4.1: Structural properties of the system as a function of time after the onset of activity. **a**, Mean number of neighboring hot segment as a function of time. Two hot segments are neighboring if their centers of mass are within the distance of their radius of gyration (3.25σ). A complete uniform distribution corresponds to a value 0.3. The dashed gray line is a guide to the eye. Insets: snapshots of the system showing only the hot segments at an early (left) and a late (right) time. **b**, The mean radius of gyration $\langle R_g \rangle$ obtained as an average over all rings at a given time t after the onset of activity (Equation 4.4 in Supplementary Section 4.5.2). Insets: snapshots of two rings in equilibrium (left) and two at late times (right). The hot segment on the active rings is shown in orange (on the equilibrium rings the orange segment is highlighted for comparison only and has the same temperature as the rest of the system).

fluctuations of temperature three times higher than the rest of the chains (see Supplementary Section 4.5.1 for model details).

After switching on the activity, the initial equilibrium uniform spatial distribution of the active (hot) and the passive (cold) segments alters (Figure 4.1a). They progressively segregate to compensate for the local pressure imbalance and to decrease entropy production [73, 78, 77]. Simultaneously, we observe a gradual but dramatic conformational change of the rings as revealed by the mean radius of gyration $\langle R_g \rangle$ and other shape parameters (see Supplementary Section 4.5.4) that comes to a standstill after several equilibrium diffusion times $\tau_{\text{diff}} \simeq 4 \cdot 10^5 \tau$ (see Supplementary Section 4.5.2 for the definition). In an equilibrium system of linear block copolymers, the colocalization of like-blocks can drive local density inhomogeneities that affect chain conformations. We show in Supplementary Section 4.5.7 that analogous effect is not responsible for the conformational changes in the present non-equilibrium system. Foremost, we do this by simulating a system with a low fraction of active chains where the colocalization of hot segments is not present but the conformational changes persist (Supplementary Figure 4.7). Additionally, we show on a simplified effective equilibrium model that in a fully phase separated system the ring conformations do not differ substantially from the homogeneous equilibrium case (Supplementary Figure 4.4).

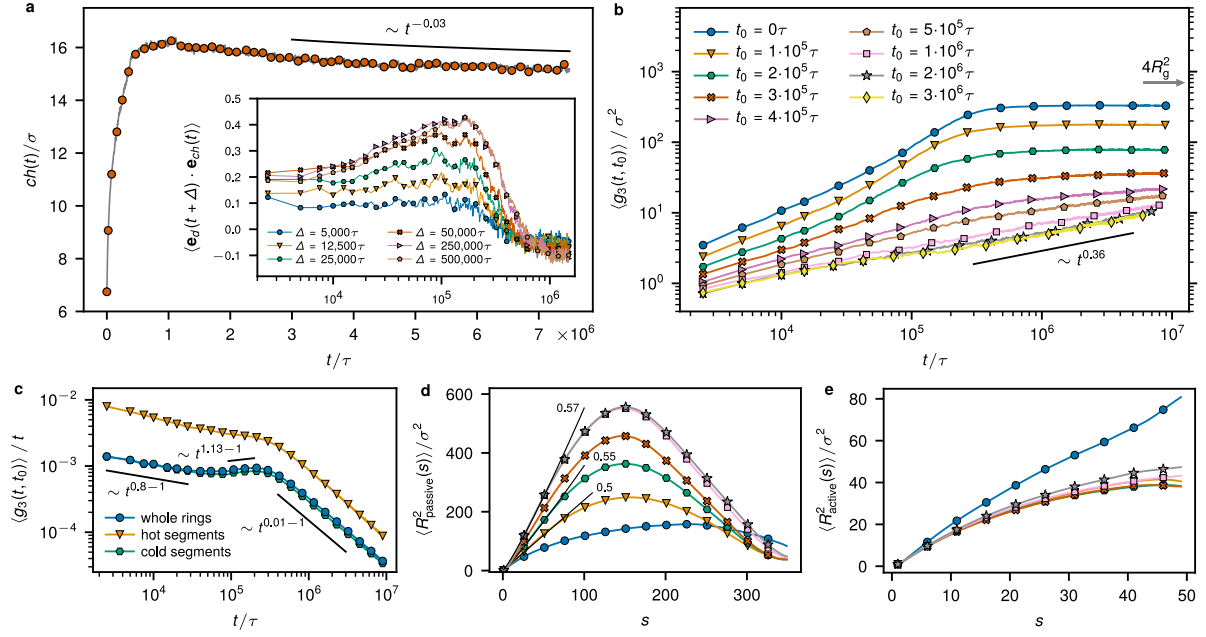


Figure 4.2: Evolution of the dynamics. **a**, Mean magnitude of the cold-hot vector \mathbf{ch} as a function of time. Inset: correlation of the \mathbf{ch} direction with the direction of the center of mass displacements of the rings in different lag times Δ as a function of time t after the activity onset ($\mathbf{e}_d(t + \Delta)$ and $\mathbf{e}_{ch}(t)$ are unit vectors in the direction of $\mathbf{d}(t) = \mathbf{R}(t + \Delta) - \mathbf{R}(t)$ and $\mathbf{ch}(t)$, respectively). **b**, Mean-square displacement of the centers of mass of the rings, $\langle g_3(t, t_0) \rangle$, as a function of time t measured from different times t_0 after the activity onset. **c**, $\langle g_3(t, t_0) \rangle / t$ as a function of time for $t_0 = 0$. **d**, **e**, Time-resolved mean-square internal distance for the passive (**d**) and the active (**e**) segment $\langle R^2(s)_{\text{passive/active}} \rangle$, computed for each segment length s as the squared distance of the endpoints of the segment averaged over the segments position within the passive/active block of a ring and averaged over rings. The black straight lines in **d** emphasize the scaling behavior $\langle R^2(s) \rangle \sim s^{2\nu_{\text{trail}}}$ for low s with the numbers indicating ν_{trail} for a few characteristic times after the activity onset. **b**, **d**, **e** share the same legend shown in **b**.

We observe that the hot segment is usually localized at one of the ends of a tree-like, doubly-folded conformation (Figure 4.1b). This suggests that the conformational change is caused by the differences between the dynamics of the active and passive segments. As the active segment undergoes stronger thermal fluctuations, its diffusivity is enhanced in comparison to the passive one. In fact, it essentially drags the cold tail through the mesh of other chains (Supplementary Movie² 1). We illustrate such emergent directionality of the ring's motion by computing the ‘cold-hot’ vector \mathbf{ch} connecting the centers of mass of the cold and hot segments of each ring. After the onset of the activity, the mean magnitude of \mathbf{ch} initially grows (Figure 4.2a). During this time, the direction of the

²The movie can be downloaded using the following link: https://static-content.springer.com/esm/art%3A10.1038%2Fs41467-019-13696-z/MediaObjects/41467_2019_13696_MOESM4_ESM.mpg

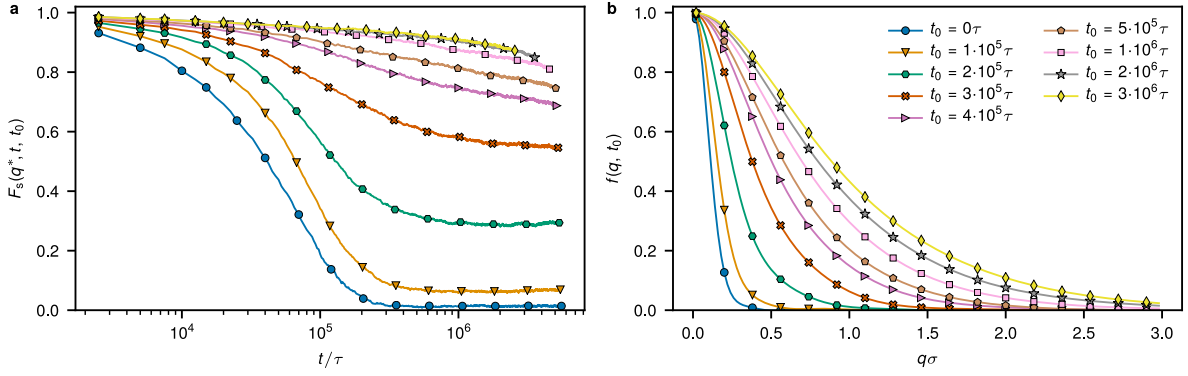


Figure 4.3: Evolution of the relaxation. **a**, Self-intermediate scattering function $F_s(q^*, t, t_0)$ as a function of t for different t_0 at $q^*\sigma = 0.35$. **b**, Non-ergodicity parameter $f(q, t_0)$ defined as $f(q, t_0) = F_s(q^*, t_{\max}, t_0)$, where t_{\max} is total time of our simulation, as a function of q for different times t_0 after the activity onset. **a**, **b** share the same legend shown in **b**.

motion is correlated with the direction of \mathbf{ch} (Inset of Figure 4.2a). At later times, $|\mathbf{ch}|$ decreases very slowly, generating a weak anticorrelation with the displacement vector, which is connected to the strengthening of topological constraints as detailed later. As we show in Supplementary Section 4.5.6, systems without topological constraints lose their directionality on a microscopic timescale, but the dense polymer environment generates a more intriguing global dynamics.

To describe the dynamics, we track in time the mean-square displacements of the rings centers of mass $\langle g_3(t, t_0) \rangle$ (see Equation 4.5 in Supplementary Section 4.5.2 and note that the mean is taken over the rings only because the dynamics are not stationary in general). Figure 4.2b shows $\langle g_3(t, t_0) \rangle$ as a function of time t measured from various times t_0 after the activity onset. $\langle g_3(t, 0) \rangle$ increases initially and after $10^6\tau$ displays a dramatic slow-down. The crossover time is the same as for the structural changes which underlines the fact that the two effects are dependent. More insight is provided by Figure 4.2c, where $\langle g_3(t, t_0) \rangle/t$ is plotted as a function of time separately for the active and the inactive segment. The initial decrease corresponds to subdiffusive $\langle g_3(t, t_0) \rangle \sim t^{0.8}$ regime consistent with the equilibrium rings dynamics below the diffusion time [51]. The following regime shows again the directional dynamics of the rings and explains its origin. While the passive segment, and hence the whole center of mass, move superdiffusively (exponent 1.13 ± 0.01), the active one temporarily displays standard diffusion (exponent 1). The both stages last for less than a decade in time before both segments cross over to an arrested state with exponent very close to zero.

The superdiffusive regime is a consequence of the specific non-equilibrium dynamics

through a mesh of topological constraints. As the detailed balance is violated due to the coupling to different thermostats, the pulling of the active segment forwards is stronger than the pulling of the cold tail backwards. The hot segment robustly explores new sites that are spontaneously freed due to density fluctuations and progressively drags behind itself the cold tail (see Supplementary Movie³ 1). Furthermore, such motion of the active segment away from its cold tail through the environment of neighboring rings introduces new topological constraints that the cold tail must obey. These constraints restrict the transversal motion of the chain. Finally, when the chain is getting more stretched some time after the activity onset, the motion of the hot segment backwards to the cold tail is compromised by the chain flexibility and, therefore, the motion away from the tail prevails. As a result, the cold tail follows the hot head slowly, but ballistically along a trail imposed by the topologically constrained neighboring rings. At these length scales, the trail is characterized by the size R of the static conformation of the tail and it scales with the contour distance s as $R(s) \sim s^{\nu_{\text{trail}}}$ where the exponent $\nu_{\text{trail}} = 0.57 \pm 0.01$ (Figure 4.2d). Therefore, the directed dynamics ($s \sim t$) along such contour is superdiffusive with $\langle g_3(t, t_0) \rangle \sim R^2(s(t)) \sim t^{2\nu_{\text{trail}}}$, which is in agreement with our observation (Figure 4.2c). Moreover, the onset time of the superdiffusion $t \approx 10^5\tau$ is consistent with the onset time of a configuration that is more open than a random walk, that is $\nu_{\text{trail}} > 0.5$ as seen in Figure 4.2d, and the dragging mechanism is consistent with the fact that the end points of the active segment are closer to each other than in the equilibrium case (Figure 4.2e).

4.2.2 Glassy behaviour

Subsequently, the system is slowing down, as revealed by $\langle g_3(t, t_0) \rangle$ (Figure 4.2b). To characterize the slowing-down of the relaxation of the rings in more detail, we measured the self-part of the intermediate scattering function (ISF) $F_s(q, t, t_0)$ (Equation 4.6 in Supplementary Section 4.5.2). As shown in Figure 4.3a, $F_s(q^*, t)$ depends on t_0 , similarly to the aging in classical glasses [225]. After about $2 \cdot 10^5\tau \simeq \tau_{\text{diff}}$ the system fails to relax and $F_s(q^*, t)$ plateaus at a nonvanishing value, defined as the non-ergodicity parameter f_q (Figure 4.3b). A striking characteristic of the ensuing arrested state is that it features a single, β -relaxation process and the subsequent α -relaxation is absent, in contrast to the common, two-step relaxation scenario [226] encountered for polymer glasses [227] or for repulsive colloids [228]. Indeed, we have not been able to observe the α -relaxation, despite the fact that we have extended our simulations to very long times, over $22\tau_{\text{diff}}$.

³See footnote 2.

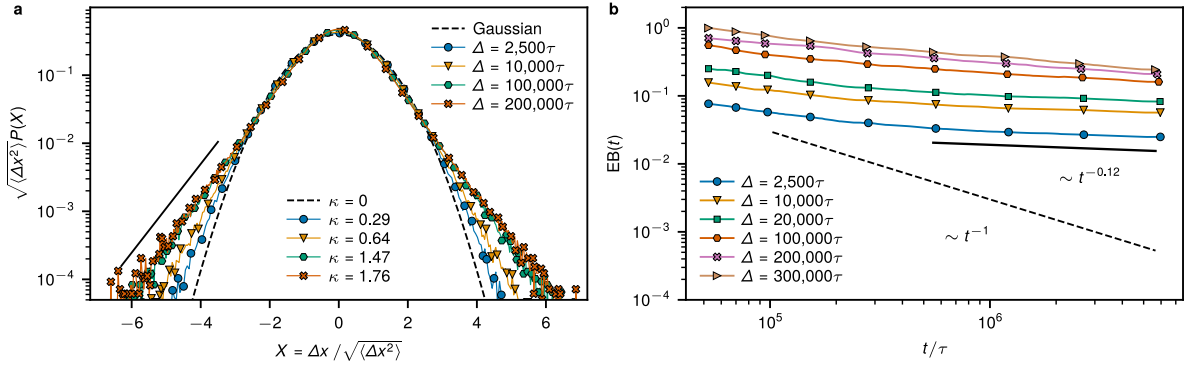


Figure 4.4: Properties of the steady state. **a**, Normalized distributions of the center of mass displacements in the x -direction for different lag times Δ measured after $2 \cdot 10^6 \tau$. Identical distributions are found for other directions (not shown). The bottom legend contains the computed values of the kurtosis $\kappa = (m_4/m_2^2) - 3$, where m_i is the i -th moment of the distribution, indicating strong non-Gaussian character of the distributions upon increasing Δ . **b**, Time evolution of the ergodicity breaking parameter (4.7) for various lag times Δ .

The absence of a two-step process is a feature associated with continuous, type-A glass-transitions, as opposed to the discontinuous, type-B transitions [229, 230, 231], and it implies the presence of higher-order singularities, the so-called A_3 - and A_4 - critical points, in the framework of MCT [232, 233, 234, 235]. There are strong indications that the system at hand features such higher-order singularities, a point to which we will return in the Discussion section. At later measurement start times, the non-ergodicity parameter is higher, that is, more wave vectors fail to relax, and we cannot even observe the β -relaxation (more details in Supplementary Section 4.5.8). In fact, as the system evolves towards a steady state ($10^6 \tau < t < 2 \cdot 10^6 \tau$), progressive strengthening of the topological constraints in the system takes place, which restricts the rings' motion and leads to the rise of the plateau height. This characteristic is similar to the strengthening of glassy behavior for colloidal systems as the packing fraction grows [236].

After about $2 \cdot 10^6 \tau$, $\langle g_3(t, t_0) \rangle$ becomes independent of t_0 and only small changes in $\langle g_3(t) \rangle$ and $F_s(q^*, t)$ are noticeable. These are due to the local system explorations of the hot segments (Supplementary Figure 4.2), reminiscent of a confined diffusion with occasional constraint release. $\langle g_3(t) \rangle$ is strongly subdiffusive ($\sim t^{0.36}$) and very slow, typical for polymeric glasses [224]. The corresponding relaxation time, extrapolated as $\langle g_3(\tau_{\text{relax}}) \rangle = 4R_g^2$, is $\tau_{\text{relax}} \approx 10^{12} \tau$, being more than six orders of magnitude higher than the equilibrium one. Such a strong dependence of the relaxation time on the control parameter is a hallmark of glassy systems. Linear polymers in an equilibrium melt relax slower than rings due to a reptation relaxation mechanism, but for the lengths considered

here, their relaxation time is only about twice as large as that of the equilibrium rings [51]. Therefore, the glassy behavior of partly-active rings, although they are somewhat doubly-folded and hence remind of linear polymers of length $N/2$, cannot be attributed to the reptation-like relaxation.

To further support the evidence of glassy dynamics, we measure the probability distribution of $1d$ displacements for various lag times Δ in the glassy regime, that is for $t > 2 \cdot 10^6 \tau$ (Fig 4.4a). For short $\Delta = 2500\tau$, the distribution is close to Gaussian, characterizing the standard diffusion (also in the non-equilibrium two-temperature case [237]), whereas for longer lag times ($\Delta > 10^5 \tau$) it becomes markedly non-Gaussian (see also Supplementary Figure 4.5a). Tiny displacements and their non-Gaussian distribution characterize a local constraint (cage) exploration which is another hallmark of glassy systems [238]. Interestingly, for long lag times the tails of the distribution are just simply exponential as in the equilibrium topological glass induced by pinning perturbations [70]. We attribute these ‘fat’ tails to a constraint release and a short relocation of the hot segments of an individual chain (Supplementary Movie⁴ 1). Additionally, we measured the ergodicity breaking parameter EB [70], defined by Equation (4.7) in Supplementary Section 4.5.2. The EB characterizes how quickly (averaged over rings), the time average of a single ring g_3 converges to the ensemble average $\langle g_3(\Delta) \rangle$. While in equilibrium EB typically decays as t^{-1} , the constraints with diverging lifetimes make glassy systems non-ergodic with $EB \sim t^0$. We plot EB in the steady state regime (Figure 4.4b), where we see a dramatic slowing down with exponent around -0.1 even for short lag times (see also Supplementary Figure 4.5b for $g_3(t, t_0, \Delta)$ of individual rings as a function of the integration time).

4.2.3 Threading analysis

We now show that the mutual ring threadings are responsible for the glassiness. We analyzed the ring threadings using computationally spanned minimal surfaces on the ring contours (Figure 4.5a). An intersection of one ring’s contour through another ring’s minimal surface defines a threading of the second ring. This method was used to clarify the extent and the role of threadings in equilibrium ring melts [63, 72] (details in Supplementary Section 4.5.3).

We characterize the threading depth in terms of the so-called separation length L_{sep} , defined by Equation (4.9) in Supplementary Section 4.5.3. It approximates how much of the threading rings material is on one side of the threaded ring. Then, the ratio

⁴See footnote 2.

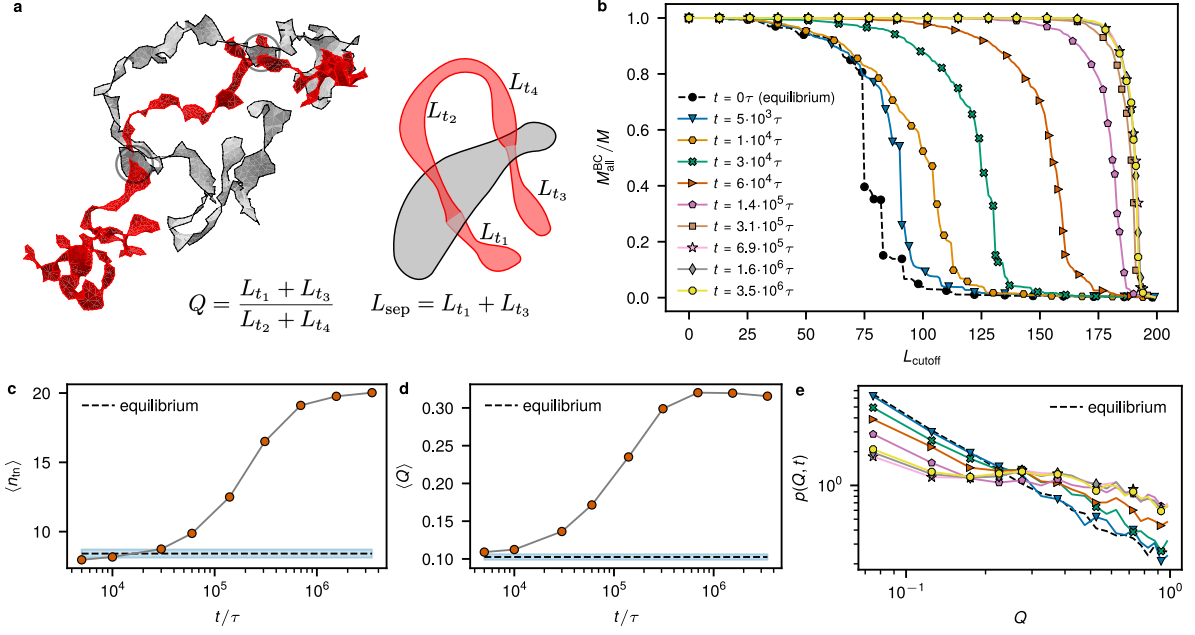


Figure 4.5: Threading analysis. **a**, The edge image is an example of two rings in a steady state and their minimal surfaces (the circles mark the locations of threadings). The schematic smooth image shows the definition of L_{sep} (measured in the number of monomers) and Q (see text). **b**, Relative size of the biggest threading cluster (the number of rings belonging to the biggest cluster, $M_{\text{all}}^{\text{BC}}$, divided by the total number of rings, M) as a function of the cutoff length L_{cutoff} . **c**, Mean number of threaded neighbors $\langle n_{\text{tn}} \rangle$ by a ring as a function of time from the activity onset. The n_{tn} is computed as the total number of threadings in the system n_{th} divided by M . **d**, Mean threading length ratio Q as a function of time. **e**, Distribution of Q for different times after the activity onset (the legend is the same as in **b**).

$Q = L_{\text{sep}}/(N - L_{\text{sep}})$ defines the relative portion of the material on one side compared to the other side of the threaded ring's surface. This ratio provides a model-independent view on threadings because its distribution in equilibrium is insensitive to the polymer model above the entanglement length scale N_e [72]. We found that more ring pairs are involved in threadings and that they are progressively deeper compared to equilibrium (Figure 4.5c and d, respectively). Moreover, we found a positive correlation of the location of threadings with the local mechanical stress (Supplementary Figure 4.3).

The glassy behavior should be connected to the emergence of a system-spanning cluster of rings that fails to relax due to mutual threadings. We define two rings belonging to the same cluster if at least one of them threads the other one with depth $L_{\text{sep}} \geq L_{\text{cutoff}}$. Therefore, we discriminate the cluster structure by the depth of threadings. Figure 4.5b shows the relative size of the biggest cluster as a function of L_{cutoff} for different times after the activity onset. For low L_{cutoff} , the whole system is one cluster as each ring has shallow

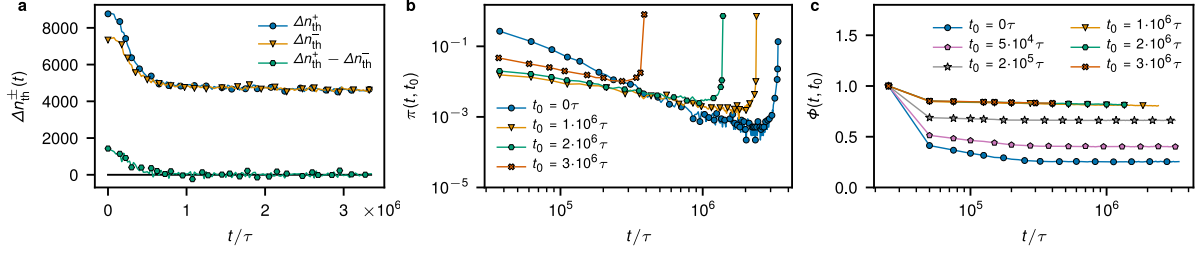


Figure 4.6: Threading dynamics. **a**, Threading gain Δn_{th}^+ and loss Δn_{th}^- (see Supplementary Section 4.5.3 for all definitions), as well as the net gain $\Delta n_{\text{th}}^+ - \Delta n_{\text{th}}^-$ as a function of time after the onset of activity. **b**, Threading survival time distribution $\pi(t, t_0)$ measured from different t_0 . The peak at late times represent the fraction of ring pairs threaded until the end of the analyzed data ($3.4 \cdot 10^6 \tau$). **c**, Threading correlation $\Phi(t, t_0)$ as a function of t measured from different t_0 .

threadings with many of its neighbors. However, in equilibrium ($t_0 = 0$) the threadings are rarely deeper than $3N_e$ and therefore for $L_{\text{cutoff}} > 100 \simeq 3N_e$ the system can be viewed as a set of many small disconnected clusters. This sharply contrasts with the structure in the glassy regime ($t_0 > 10^6 \tau$), where all rings form a single cluster practically independent of the choice of L_{cutoff} as a significant number of threadings of any depth occurs (Figure 4.5b).

While the cluster profile remains stable in the glassy regime, we still observe threading and un-threading events between ring pairs. Numbers of these events, however, balance each other, resulting in a steady state (Figure 4.6a). Interestingly, the threading life-time distribution shows a power-law with a peak at late times, meaning that the majority of threadings are persistent and survive for the total duration of our simulations with a minority having a short lifetime. The bimodal character is likely a consequence of the fat power-law tail as revealed by the shape of the distribution measured at different times after the activity onset (Figure 4.6b and Supplementary Movie⁵ 2). Additionally, the threading two-point correlation function $\Phi(t, t_0)$ (defined in Equation (4.10)) exhibits incomplete relaxation at all times, showing a dynamic threading steady state with persistent threadings (Figure 4.6c).

Although in equilibrium the threading depth is correlated with the diffusion slowdown of individual rings [63], in the case of partly-active rings, some specific shallow threadings (for example, see Figure 4.7a) can significantly increase the relaxation time. The directionality of the rings tightens these threadings and they can be relaxed only if the active segment backtracks the passive tail. However, the directionality and the

⁵The movie can be downloaded using the following link: https://static-content.springer.com/esm/art%3A10.1038%2Fs41467-019-13696-z/MediaObjects/41467_2019_13696_MOESM5_ESM.mov.

presence of other rings oppose the back-tracking. These threadings are likely members of the persistent class of threadings, but we could not determine the latter class yet. We suspect, that such threadings could also be relevant in the dramatic increase of the viscosity in stretched untangled melt of rings [239] (after this paper has been already accepted, the hypothesis has been confirmed in Ref. [240]). To prove at least that ring topology and threadings are essential for the glass transition, we took a configuration of the system in the glassy state and cut the bond connecting two cold monomers in the middle of the cold segment on each ring. We further simulated the system which now consisted of M linear triblocks of length N with two cold segments at the ends and a hot segment in the center. The chain conformations change only moderately, but it is clear from $\langle g_3(t, t_0) \rangle / t$ (Figure 4.7b) that the chains start to superdiffuse, releasing the accumulated mechanical stress (Supplementary Movie⁶ 3). Later on, the dynamics eventually crosses over to standard diffusion in analogy to orientational relaxation of self-propelled active particles [241]. As the non-topological properties of the system remained unchanged, we conclude that the phase segregation is not a crucial element stabilizing the glass⁷. The glassiness is driven by the enhanced threading due to the ring topology and the violated detailed balance [73].

4.3 Discussion

We now return to the question of the order (continuous or type-A vs. discontinuous or type-B) of the glass transition for the system at hand. The usual control parameters driving vitrification in molecular or colloidal systems are the temperature and the density, and the typical glass transition scenario there is discontinuous: the intermediate scattering function in the ergodic state develops a plateau, which grows in height and extends longer in time approaching the glass transition as the control parameters are changed [226, 224, 242]. In the continuous case, the non-ergodicity factor grows smoothly from zero to finite values. This second scenario is less common and its realization requires the presence of additional control parameters, such as porosity and randomness [229, 230, 231], tunable attraction widths in the interactions [243, 244] or confining periodic potentials [245] for which the amplitude and the wavelength can be independently varied. In such cases, lines of continuous glass transitions have been found in parameter space, and they are associated with higher-order singularities of the A_3 - or of the A_4 -type. The latter appear

⁶The movie can be downloaded using the following link: https://static-content.springer.com/esm/art%3A10.1038%2Fs41467-019-13696-z/MediaObjects/41467_2019_13696_MOESM6_ESM.mpg.

⁷The role of non-equilibrium phase segregation is explored in more details in Chapter 5.

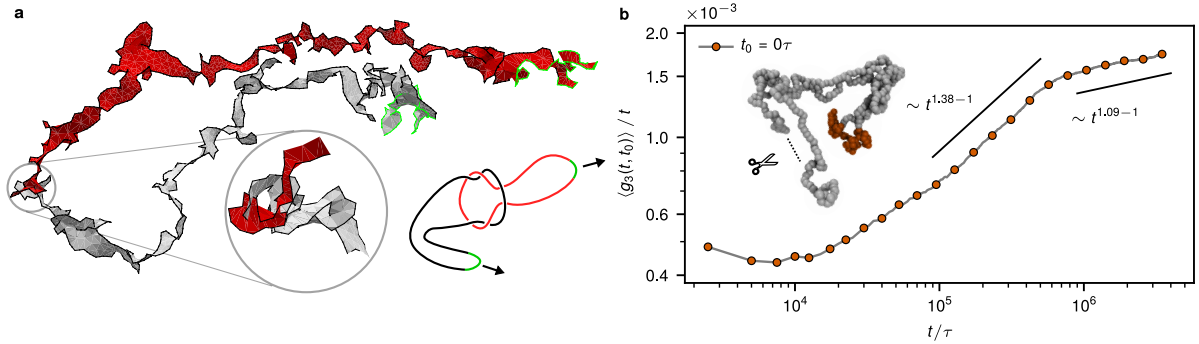


Figure 4.7: Tight threading and relaxation of cut rings. **a**, Two partly-active rings with their minimal surfaces revealing a tight threading (detail in the inset). Active segments are marked green. Their sketched conformation shows how the directionality tightens the threading and introduces long relaxation. These as well as other threadings pose no long-time constraint if the rings were cut. **b**, Mean-square displacement of the cut rings divided by time (t is measured from the cutting event). The initial decrease at short times is the residual effect of the glassy state, until the former topological constraints get released and the centers of mass of the rings switch to superdiffusion at intermediate times. Later on, the chains cross over to the usual diffusion. Inset: snapshot of a cut ring at late times.

as endpoints of type-A transition lines that merge with type-B lines, as endpoints of type-B lines separating two glasses or as endpoints of A_3 -lines in the latter case.

For the system at hand, several control parameters can be tuned: the fraction M_a/M of partly-active rings; the ratio T_h/T_c of the temperatures of the hot and cold segments; the fraction N_h/N of hot segments on a ring; and the number of monomers N of the rings. The richness of the system makes the possibility of existence of higher-order singularities in principle possible. A detailed investigation in the vast space spanned by these is beyond the scope of this work; we focused mainly on the first two cases above. In Figures 4.8a and 4.8b, we show the effect of gradually increasing the fraction of partly-active chains, which induces a glassy state, as witnessed by the saturation of the mean-square displacement, Figure 4.8a, and the growth of a non-ergodic plateau, Figure 4.8b, as the ratio M_a/M exceeds a number as small as 1/160. There is no evidence of the development of an intermediate plateau in the ergodic state preceding the glass, in full analogy with type-A transitions seen in the aforementioned systems [229, 230, 231, 245, 243, 244]. The presence of a subdiffusive regime in the mean-square displacements, Figure 4.8a, and of a logarithmic crossover intermediate scattering function, Figure 4.8b, offer additional corroboration that the transition for this choice of the remaining system parameters is continuous, and thus higher-order singularities are present. We have found similar be-

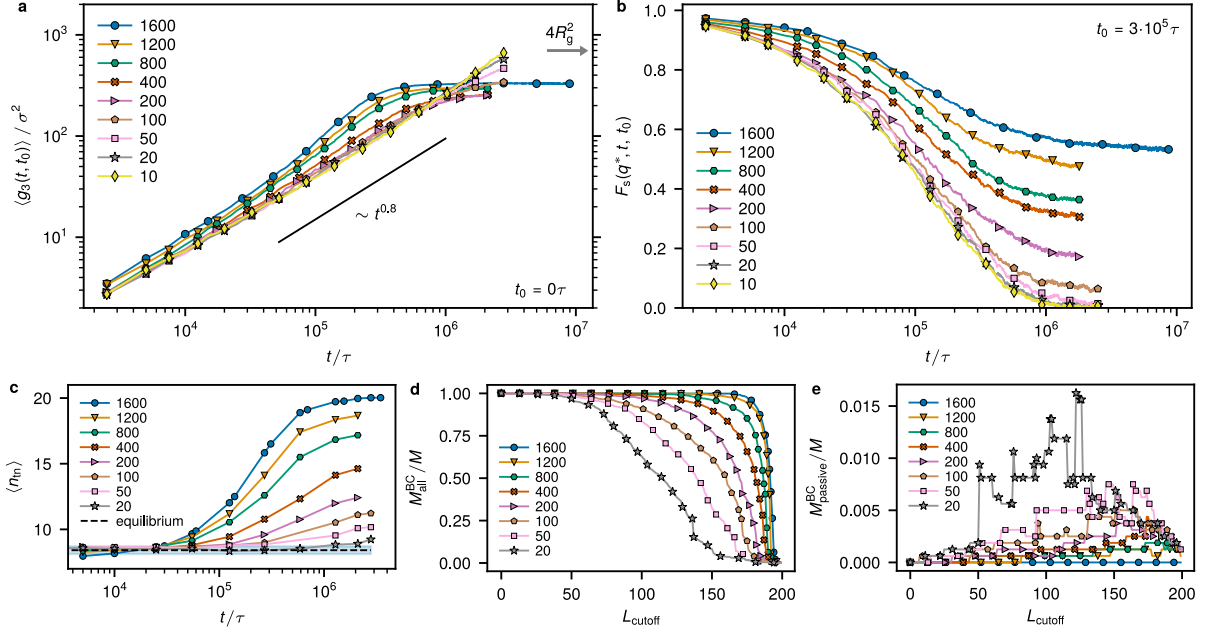


Figure 4.8: Varying the number of active rings. **a**, Mean-square displacement of the rings' centers of mass from the onset of the activity ($t_0 = 0$) as a function of time for different numbers M_a of partly-active rings indicated in the legend. **b**, Self-intermediate scattering function $F_s(q^*, t, t_0)$ as a function of t evaluated at $q^*\sigma = 0.35$ and $t_0 = 3 \cdot 10^5 \tau$ for different M_a . **c**, Mean number of threaded neighbors $\langle n_{tn} \rangle$ by a ring as a function of time from the activity onset for different M_a . **d** and **e**, Threading cluster analysis for systems at with different number of partly-active rings at $t = 2.1 \cdot 10^6 \tau$. **d**, Relative size of the biggest cluster of those clusters that contain any kind (active and passive) of rings. **e**, Relative size of the biggest cluster of those clusters that contain only passive rings (see Supplementary Section 4.5.3 for details). Note the difference in the scale of the ordinate for the passive ring clusters.

haviour (not shown) varying the ratio T_h/T_c . Naturally, this does not rule out that in other parts of the phase diagram the transition is governed by A_2 -singularities and it is thus of B-type. This would give rise to a number of additional scenarios for the behaviour of the relaxation functions, including the possibility of multiple relaxations observed in related models [245, 246]. The presence of deep and tight threadings in our system bears an intuitive analogy with colloidal attractions [244], random pinning [229, 230, 231, 242] or polymer-mediated bond formation [247, 246] in systems featuring similar glass-transition phenomenologies. A detailed investigation of this issue, however, is a problem for the future.

The present active topological glass is remarkable by its distinct role of activity in comparison to the known active glasses composed of self-propelled particles [212, 210]. There, the activity opposes the glassiness as indicated by the increase of the effective temperature defined through a long time limit of a generalized fluctuation-dissipation re-

lation. At the same time however, increasing the persistence time can lead to a decrease of the effective temperature and therefore promote the glass formation, and, conversely, decrease in persistence time favours fluidization. In contrast, the microscopic model of the active topological glass has zero persistence time, but nevertheless drives the vitrification. This can be the consequence of the polymeric nature of the particles and the topological constraints that together create some persistence as illustrated by the superdiffusive regime. Moreover, the activity clearly causes increase of the number and the severity of topological constraints. This ‘topological crowding’ then can be viewed as a specific, effective attraction or pinning that further promotes the glass as mentioned above.

As regards the system with only a fraction of active rings present, the threading cluster analysis (more details in Methods and Supplementary Note 6) has revealed that it is always the active rings that are involved in the formation and maintenance of the largest cluster (Figure 4.8c, 4.8d, and 4.8e). The onset time of the glassy regime increases with decreasing M_a (Figure 4.8a). This delay is related to the slower building up of the largest cluster as fewer active chains participate (Supplementary Figure 4.8). The ring length N governs the number of topological interactions⁸. Similarly to linear polymer melts in equilibrium, due to extended chain configurations, each partly-active ring overlaps with a number (extensive in N) of other rings. As a cooperative un-threading of rings is necessary for the relaxation to occur, we expect the relaxation time to grow at least exponentially with N [204]. Such a strong dependence is also known from the melts of polymeric stars, where it is due to the slow process of arm retraction that however, can take place even without cooperative motion of the other chains [248].

While our model system is interesting from the fundamental physics point of view, it is also inspired from biology and may well bear important ramifications for the organization of the DNA fibre (chromatin) of higher eukaryotic cells. The large-scale static properties of the equilibrium melt of unknotted rings, such as the territorial organization, the scaling of $\langle R_g \rangle$ with N or the so-called contact probability (Supplementary Figure 4.1d) are consistent with the population-average conformation of the interphase chromatin [85]. This can be due to the common governing role of the topological constraints in both systems [85]. The rationale behind the ring model is the time scale separation — the chromosomes are linear chains and as such equilibrate and tangle by reptation, however for the length and density of chromatin, such relaxation would take significantly longer than the cell’s life time [84]. Therefore, the constraints arising from the uncrossability of the chains can be modeled as permanent on biological time scales. This is done effectively by the closure

⁸The effect of varying ring length is considered in detail in Chapter 5.

of the chain's ends which inhibits the reptation. Furthermore, the chromatin association with the nuclear lamina [249] hinders reptation relaxation and the chromatin can be viewed as loops between lamina contact points. In contrast, the topoisomerase II enzyme can resolve the topological constraints, by cutting the fibre, passing segment through sealing up the cut back [250], although the extent to which it affects global topology on biological time scales in interphase is unclear. Alternatively, the rings can also represent small scale chromatin loops extruded or maintained by Structural Maintenance of Chromosomes protein complexes [99, 251], and/or Topologically Associating Domains [252] that do not link. Current experimental evidence for the topological state (knottedness) of the chromatin fibre also varies. While conformations inferred from contact probability measurements exhibit knots [253], the knot analysis [254] of the direct observations of fluorescently labeled chromatin segments finds mostly unknotted segments. Unable to refine the scales of the topological constraints completely at this point, we assumed their existence for the typical observation times and examined the consequences. Therefore, we mention phenomena on chromatin at various scales, for which the interplay of the topology and the activity could be relevant.

The segmental activity with thermal-like fluctuation spectra has been measured to be stronger in the normal living cell nuclei [100] as opposed to energy-deprived cells, and has its origins in the energy dependent processes, such as chromatin repair or remodeling, DNA transcription, or loop extrusion. We conjecture that the phenomena observed in our partly-active system could also be relevant in biological context, on the basis of the following similarities with our model: genes exhibit size increase upon transcription decoupled from the chromatin decondensation [255]; a highly transcribed gene shows directed motion [256]; overall chromatin loci exhibit heterogenous subdiffusive dynamics [100] reminiscent of glassy behavior [257, 221]; the active and inactive chromatin are spatially segregated [91]; and the chromatin exhibits a doubly-folded structure at small scales [258]. Naturally, these effects have also alternative explanations. The phase separation and glassy dynamics could be observed for a copolymer models where different chromatin segments have different interaction potentials based on their epigenetic state [93, 257, 221, 259] or by interaction with binding proteins [259, 260]. The double folded structure is likely to be attributed to supercoiling due to the torsional stress induced on the fibre in the process of transcription or loop extrusion [261, 99, 262]. Nevertheless, we show that the activity in combination with topological constraints at the fibre level can complement the observed phenomena and should be considered in a more complete picture of the chromatin organisation [263, 98]. As the models above typically do not consider topological constraints

and activity, our findings represent a completely new mechanism for the observed phenomena. Certainly, more work is required to determine the relative contributions of the different mechanisms in the various cases. Potentially, the different nature of the observed glassy states, namely the monomer glass due to caging in copolymer models [257, 221] and topological glass here, could be used to discern which one could be present or dominant in the chromatin context.

4.4 Conclusions

Activity complemented with topological constraints at the microscopic level can lead to rich system dynamics. We have demonstrated this on a model system of dense, unknotted and nonconcatenated ring polymers with active segments. Firstly, the directionality of polymers in a dense environment arises from the topological constraints and the isotropic noises of unequal strength. Similarly to Ref. [203], the superdiffusive motion is connected to a major particle deformation at high density. In contrast however, in our work, the superdiffusivity is triggered by the active noise. Secondly, a novel state of matter — the activity-driven topological glass — arises from the activity-enhanced ring threading. In contrast to the conjectured equilibrium topological glass [70], our present model allows the creation of a topological glass for rings of accessible lengths ($7N_e$) using activity. Moreover, only a low number of partly-active rings is necessary, making the present model suitable for experimental testing with extracted bacterial DNA [264] or synthetic ring polymers [57], driven by molecular motors fueled by ATP hydrolysis. The effective temperature ratio T_h/T_c of a factor of three⁹ that we used here is within reach, since ATP hydrolysis releases more than $10k_B T$ [265]. However, as our preliminary results suggest, even smaller temperature ratios can be sufficient. Other means of selective heating could be attempted by fluctuating external fields or infrared irradiation selectively coupling to individual groups in the polymer. The latter mechanism can yield a fluid material with reversible vitrification upon light exposure. What is the proper topological order parameter of the glass transition, or what are the fragility properties of the active topological glass, are just a few intriguing questions to be addressed in the future. The present work paves the way for a development and investigation of these novel, molecular, topology-based, responsive materials.

⁹As shown in Chapter 5, due to the heat flow in the system, the observed, effective cold and hot temperatures, T_c^{eff} and T_h^{eff} , differ from T_c and T_h that are imposed by the thermostats, which makes the ratio $T_h^{\text{eff}}/T_c^{\text{eff}} \approx 1.7$ almost two times smaller than $T_h/T_c = 3$.

4.5 Supplementary Information

4.5.1 Model

All particles interact via a purely repulsive Lennard-Jones potential

$$U_{\text{LJ}}(r) = \left(4\varepsilon \left[\left(\frac{\sigma}{r} \right)^{12} - \left(\frac{\sigma}{r} \right)^6 \right] + \varepsilon \right) \theta(2^{1/6}\sigma - r), \quad (4.1)$$

where $\theta(x)$ is the Heaviside step function. The connectivity of polymers is maintained by the finitely extensible nonlinear elastic potential

$$U_{\text{FENE}}(r) = -\frac{1}{2}r_{\text{max}}^2 K \log \left[1 - \left(\frac{r}{r_{\text{max}}} \right)^2 \right], \quad (4.2)$$

where $K = 30\varepsilon/\sigma^2$ and $r_{\text{max}} = 1.5\sigma$. These parameters make the chains essentially uncrossable. The angular potential is

$$U_{\text{angle}} = k_{\theta}(1 - \cos(\theta - \pi)) \quad (4.3)$$

with $k_{\theta} = 1.5\varepsilon$.

The studied systems are monodisperse at fixed volume with the total monomer density $\rho = 0.85\sigma^{-3}$. We used very large systems of $M = 1600$ chains to avoid unphysical self-threadings of extended rings due to periodic boundary conditions. As shown in Supplementary Figure 4.1c, our systems are large enough to assure that the rings are smaller than the simulation box at all times. All the simulations were performed at constant volume with two Langevin thermostats using the large-scale atomic/molecular massively parallel simulator (LAMMPS) engine [266]. The equations of motion were integrated with the time step $\Delta t = 0.005\tau$, where $\tau = \sigma(m/\varepsilon)^{1/2}$.

To model heterogeneous activity of the rings, on each polymer a consecutive segment of length $N_{\text{h}} = N/8$ monomers is considered active by subjecting it to stronger thermal-like fluctuations (isotropic, uncorrelated, white noise) in comparison to the rest ($N - N_{\text{h}}$) monomers of the ring that remain passive. In particular, the active monomers are connected to a Langevin thermostat of temperature $T_{\text{h}} = 3$ (units of ε and the Boltzmann constant set to unity are being used throughout), while passive ones are coupled to a second Langevin thermostat with temperature $T_{\text{c}} = 1$. The coupling constants of both thermostats are $\gamma = (2/3)\tau^{-1}$. From our earlier study [79] we know that such values of γ and T_{h} lie in the range of the onset of a non-equilibrium microphase separation in

the active-passive mixtures of polymers of 40 monomers, but colloidal systems would not demix [77, 73]. Our preliminary studies show that even a weaker temperature contrast is sufficient for the glassy state to occur. We leave a more detailed characterization of the phase diagram for the future study.

4.5.2 Methods

The employed model was frequently used not only for the melt of linear chains but also for the melt of rings [50, 51] at $T = 1$. Therefore, we already know a range of useful properties of the equilibrium system, such as the entanglement length $N_e = 28 \pm 1$ and the typical diffusion times of the rings. In equilibrium, the diffusion time $\tau_{\text{diff}}(N)$ of a ring is defined as the mean time required for its center of mass to diffuse over $2R_g$, where

$$R_g \equiv \langle R_g^2 \rangle^{1/2} = \left\langle \frac{1}{N} \sum_{i=1}^N (\mathbf{r}_i - \mathbf{R})^2 \right\rangle^{1/2} \quad (4.4)$$

is the mean radius of gyration. Above, \mathbf{r}_i denotes the position of the i -th monomer and \mathbf{R} is the position of the center of mass of the ring. The angles $\langle \dots \rangle$ stand for the average over different chains. As reported in [50, 51], $\tau_{\text{diff}}(N = 400) \simeq 4 \cdot 10^5 \tau$.

To quantify dynamical evolution of the system, we consider squared displacements of the centers of mass of the rings, $g_3(t, t_0)$, at a given time t provided that the measurement started at t_0 ($t_0 = 0$ is the activity onset, or, in the case of cut rings, the moment of the cutting):

$$g_3(t, t_0) = [\mathbf{R}(t_0 + t) - \mathbf{R}(t_0)]^2, \quad (4.5)$$

where $\mathbf{R}(t)$ is the position of the center of mass of a ring at time t with respect to the center of mass of the whole system at that time. Typically, we report the mean-square displacement $\langle g_3(t, t_0) \rangle$ averaged over the rings only, i.e. without additional averaging over multiple time origins as the dynamics of the system are not stationary in general.

The relaxation dynamics of the system is also characterized by the self-part of the intermediate scattering function defined as

$$F_s(q, t, t_0) = \frac{1}{M} \sum_{m=1}^M \exp(i\mathbf{q} \cdot (\mathbf{R}_m(t_0 + t) - \mathbf{R}_m(t_0))), \quad (4.6)$$

where \mathbf{R}_m is the position of the center of mass of the m -th ring. We evaluated it at $q^* \sigma = 0.35$ corresponding to the maximum of the static structure factor (see Supplementary Figure 4.6 for other q -values).

We define ergodicity breaking parameter as

$$\text{EB}(t) = \frac{\langle g_3(t, t_0, \Delta)^2 \rangle - \langle g_3(t, t_0, \Delta) \rangle^2}{\langle g_3(t, t_0, \Delta) \rangle^2}. \quad (4.7)$$

Here, $g_3(t, t_0, \Delta)$, being mainly a function of the lag time Δ , represents the time average:

$$g_3(t, t_0, \Delta) = \frac{1}{t - \Delta} \int_{t_0}^{t_0+t-\Delta} [\mathbf{R}(t' + \Delta) - \mathbf{R}(t')]^2 dt' \quad (4.8)$$

where \mathbf{R} is the position of the ring's center of mass with respect to the global center of mass.

4.5.3 Threading analysis

The minimal surfaces are spanned on the fixed contours of the rings from the molecular dynamics simulations and then minimized using the overdamped surface tension evolution under the constraint of fixed disc topology. We used the Surface Evolver software [267] and followed the protocol in [72] ensuring that for these ring lengths the area of the final surface is close to the minimum.

The separation length is defined as

$$L_{\text{sep}} = \min \left(\sum_{i=\text{even}} L_{t_i}, \sum_{i=\text{odd}} L_{t_i} \right), \quad (4.9)$$

where L_{t_i} is the (threading) length between the i -th and the $(i+1)$ -th penetrations of the surface (see Figure 4.5a). L_{sep} approximates how much of the threading rings material is on one side of the threaded ring. The approximation lies in the assumption that two following surface piercings are in the opposite direction with respect to the surface normal vector. In many cases, there are only two surface penetrations between two rings (see Supplementary Figure 4.3) and in such case the approximation is exact because of the non-concatenation constraint of the rings conformations.

The threading cluster analysis is performed in the following way. At first, each ring is analyzed for threadings with other rings. Two rings are assigned to the same cluster if at least one of them threads the other one with $L_{\text{sep}} > L_{\text{cutoff}}$. Then, the size (in terms of the number of members) of each cluster is determined and the biggest cluster is found. For mixtures of active and passive rings the size of the biggest cluster containing any kind of rings is considered (for example, Figure 4.8b) and separately the biggest cluster of those clusters that contain only passive rings is calculated, such as in Figure 4.8c.

To characterize the dynamics of threadings we compute the threading gain $\Delta n_{\text{th}}^+(t)$ and loss $\Delta n_{\text{th}}^-(t)$ as function of time. To do so, we compare the set $T(t)$ of pairs of rings that are threaded at time t with the set $T(t + \Delta t)$ of threaded pairs at time $t + \Delta t$. Then $\Delta n_{\text{th}}^+(t) = |T(t + \Delta t) - T(t)|$ and $\Delta n_{\text{th}}^-(t) = |T(t) - T(t + \Delta t)|$, where $|x|$ is the number of members of set x . Note that $\Delta n_{\text{th}}^\pm(t)$ is different from the derivative of the number of threaded neighbors, because there exist a state with the derivative zero, but high threading exchange, which is exactly the case in the steady state. For all calculations of the threading dynamics, we used $\Delta t = 2.5 \cdot 10^4 \tau$ and maximum simulation time $3.4 \cdot 10^6 \tau$.

A related quantity characterizing the threading correlation is

$$\Phi(t, t_0) = \frac{1}{n_{\text{tn}}(t_0)} \sum_{i,j=1}^{n_{\text{tn}}(t_0)} T_{ij}(t_0) T_{ij}(t_0 + t), \quad (4.10)$$

where $T_{ij}(t)$ is one, if threading between rings i and j exists at time t and zero otherwise, and $n_{\text{tn}}(t)$ is the number of threaded neighbors at time t . The $\Phi(t, t_0)$ gives the time correlation function for the existence of threadings.

Additionally, we compute the threading survival time distribution $\pi(t, t_0)$ measured from different t_0 . To construct $\pi(t, t_0)$, we look at all threaded ring pairs at time t_0 and track how long they remain threaded before they un-thread for the first time.

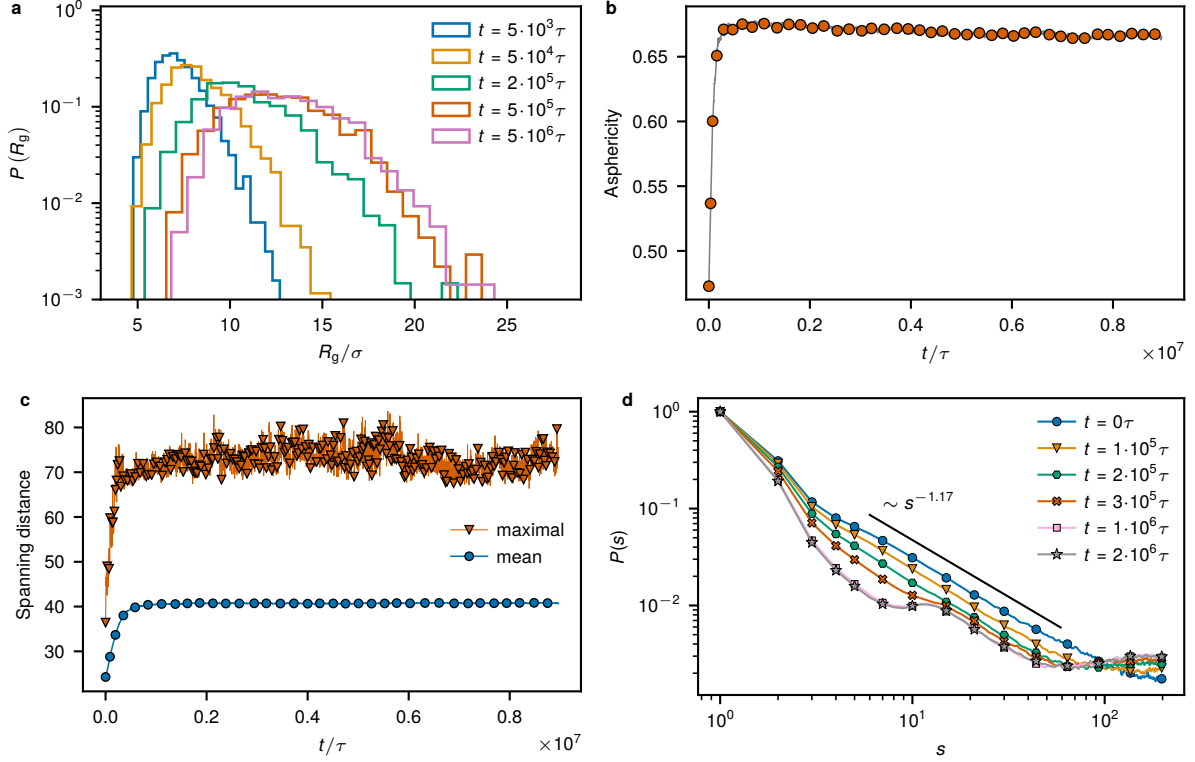
4.5.4 Details on static and dynamic properties of the rings

In Supplementary Figure 4.1, we present additional shape parameters of the rings, such as the asphericity a and the contact probability $P(s)$, as a function of time measured from the onset of activity.

After switching on the activity, the overall size of the rings grows, as indicated in Supplementary Figure 4.1a and Figure 4.1b, being a consequence of the directional dynamics of the rings in the presence of other chains. Simultaneously, the rings become more aspherical, as can be seen in Supplementary Figure 4.1b showing the dimensionless asphericity parameter a , defined as

$$a = \frac{\langle \lambda_1 - \frac{1}{2}(\lambda_2 + \lambda_3) \rangle}{\langle \lambda_1 + \lambda_2 + \lambda_3 \rangle} \quad (4.11)$$

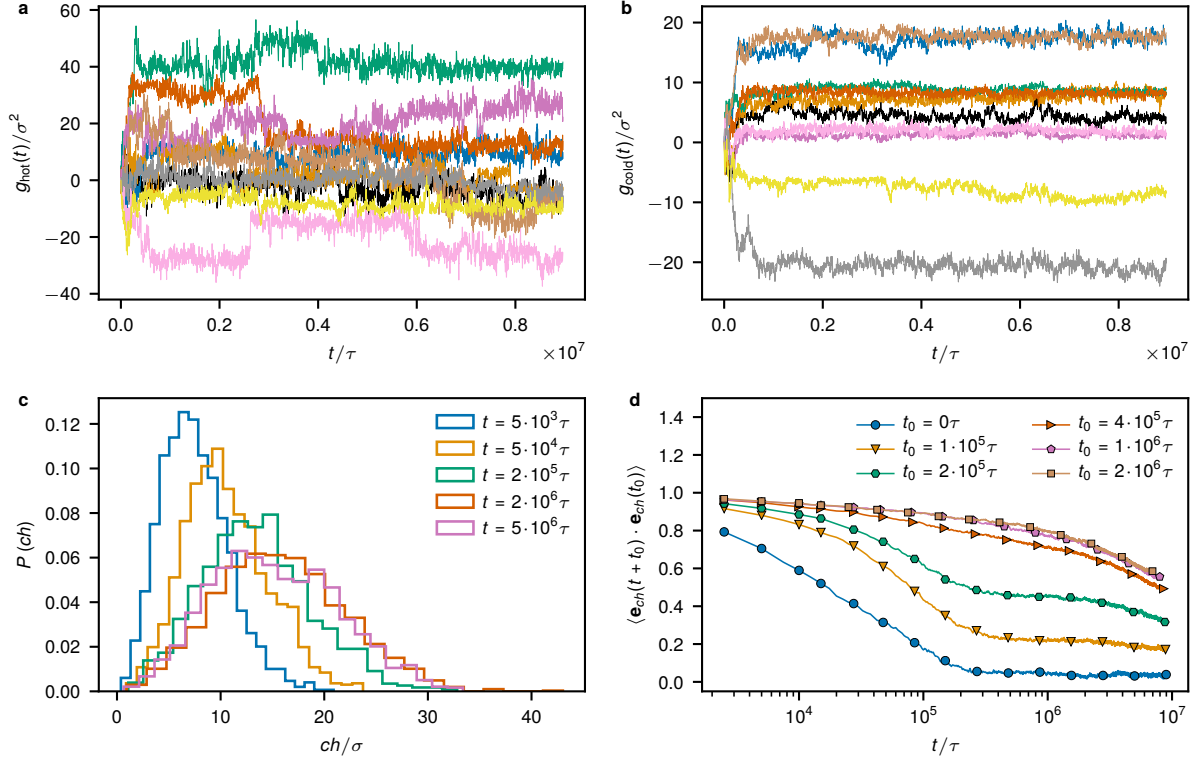
where λ_i 's are the eigenvalues of the ring's gyration tensor $G_{ij} = \frac{1}{N} \sum_{n=1}^N (r_i^{(n)} - R_i)(r_j^{(n)} - R_j)$ ($r_i^{(n)}$ is the i -th component of the position vector $\mathbf{r}^{(n)}$ of the n -th particle and \mathbf{R} is the center of mass position of the ring), ordered as $\lambda_1 \geq \lambda_2 \geq \lambda_3$. Furthermore, we checked that all rings are smaller than the linear box size at all times (see Supplementary



Supplementary Figure 4.1: Additional shape parameters of the rings as a function of time after the onset of activity. **a**, Time-resolved distribution of the radius of gyration. **b**, Time-resolved asphericity parameter (see Supplementary Equation (4.11)). **c**, Maximum and mean biggest spanning distance (in units of σ) of all rings as a function of time. At all times, all rings are smaller than the the linear box size ($L = 90.97\sigma$ for $N = 400$ and $M = 1600$). **d**, Contact probability $P(s)$ at different times t after the activity onset. Two monomers are considered as in a 3D contact if the distance between them is smaller than the cutoff distance 1.5σ . The $P(s)$ dependence is robust against changes in the cutoff distances as checked for values 1.12σ and 1.3σ (not shown).

Figure 4.1c). This is to make sure that the rings do not wrap around the periodic boundary conditions, which would cause unphysical dynamics due to self-threadings.

$P(s)$ represents the probability that two monomers separated by a contour distance s are in contact in 3D space. It is computed for each segment length s as the fraction of times the segments endpoints are within distance 1.5σ averaged over the segments position within the rings and averaged over rings. It becomes non-monotonic at short distances, as seen in Supplementary Figure 4.1d. Interestingly, at intermediate contour lengths ($[15, 50]\sigma$) it scales as a power-law with the same exponent (-1.17) as for rings in equilibrium. Note that the final steady-state conformations of the partly active rings are very extended and distinct from the crumpled globules found in equilibrium, as seen in Figure 4.2d and 4.2e.



Supplementary Figure 4.2: Additional details on the time evolution of the hot and cold segments. Time evolution of the squared displacements of hot (a) and cold (b) segments of ten randomly-chosen partly active rings in the system with $N = 400$ and $M = 1600$. For clarity, we subtracted from the square displacements the initial position of each ring: $g_{\text{hot/cold}} = (\mathbf{R}_{\text{hot/cold}}(t) - \mathbf{C}(t))^2 - (\mathbf{R}_{\text{hot/cold}}(0) - \mathbf{C}(0))^2$, where $\mathbf{C}(t)$ is the position of the center of mass of the system and $\mathbf{R}_{\text{hot/cold}}(t)$ is the position of the center of mass of the cold/hot segment. c, Distribution of the ch -magnitude after different times t after the onset of activity. d, Autocorrelation function of the unit cold-hot vector $\mathbf{ch}/|\mathbf{ch}|$ connecting centers of mass of the cold and the hot segment of a ring for different times after the onset of activity.

Additional information on the time evolution of the hot and cold segments is provided in Supplementary Figure 4.2. To get more insight into the strongly subdiffusive regime of the mean-square displacements, we track the squared displacements of the centers of mass of the hot and the cold segments separately, as shown in Supplementary Figure 4.2a and 4.2b, respectively. The squared displacements of the hot segments naturally display larger fluctuations, but, more interestingly, also occasional jumps around the plateau value. The system was simulated for $9 \times 10^6 \tau \simeq 22.5 \tau_{\text{diff}}$ and during that time only small sudden fast relocations of the segments could be observed, after which the rings practically did not move. However, the conformations of the rings remained extended, as already seen from the mean-square internal distance profiles (Figure 4.2d and 4.2e), and also from

the stable shape of the distribution of the \mathbf{ch} -magnitude (Supplementary Figure 4.2c). As noted in the main text, the late-stage dynamics feature a slight decrease of the mean magnitude of \mathbf{ch} in time (Figure 4.2a). We attribute such behavior to the resolution of weaker topological constraints and evolution of the system towards a locally ‘deeper’ steady state. In Supplementary Figure 4.2d, we show the auto-correlation function of the unit cold-hot vector $\mathbf{ch}/|\mathbf{ch}|$ for different times t_0 after the activity onset indicating a very slow decorrelation of its direction over time.

Typically, hydrodynamics plays an important role in the dynamics of active matter [268]. We neglected it here as our systems are at the melt density, for which the hydrodynamic interactions, if there is any solvent at all, are screened. Nevertheless, in fully active systems, directed flows can emerge and persist as a result of hydrodynamics with the orientational order of particles [269, 270].

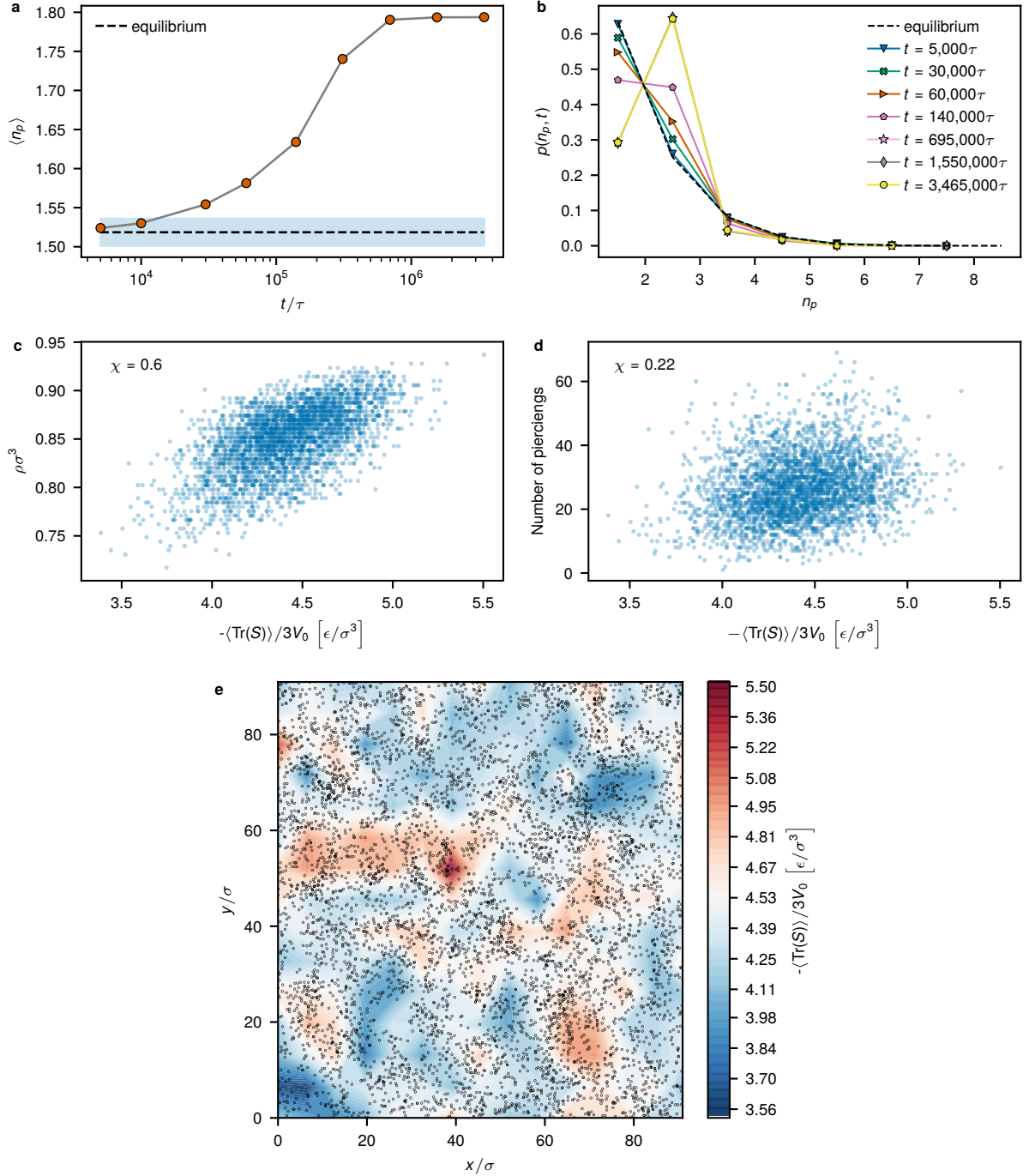
4.5.5 Details on threading statistics

A ring can penetrate the surface of another ring multiple times, as indicated by the number n_p . We take into account only those threadings that are longer than the entanglement length because very short ones are not model independent [72]. Note that in such case the number of the counted penetrations of a surface is not necessarily even as required by the nonconcatenation condition. We see that the mean number of penetrations per ring increases with time and reaches a plateau in the glassy phase, as shown in Supplementary Figure 4.3a and 4.3b.

We investigated whether threadings in the glassy state are responsible for the local enhancement of mechanical stress. Although momentum is injected into the present non-equilibrium system, we disregarded the kinetic contribution to the stress and concentrated only on the mechanical consequences of the system’s geometrical state. To do so, we computed the Cauchy stress tensor for each particle i :

$$S_i = - \sum_{j \neq i} \mathbf{r}_{ij} \otimes \mathbf{F}_{ij} \quad (4.12)$$

where \mathbf{r}_{ij} is the relative position of a neighboring particle j with respect to i , \mathbf{F}_{ij} is the force acting between i and j and \otimes denotes a dyadic product. We computed S_i for 200 consecutive time steps of the simulation in the glassy regime. Then, we divided the simulation box into sub-boxes of size 6σ and computed $-\langle Tr(S) \rangle / 3V_0$ ($V_0 = (6\sigma)^3$ is the volume of a sub-box), where $\langle Tr(S) \rangle$ is the trace of the stress tensor averaged over the short sampling time and over all monomers within a given sub-box. We plotted the result



Supplementary Figure 4.3: Surface penetrations statistics and correlation of threadings with mechanical stress. **a**, Mean number of surface penetrations longer than N_e per ring as function of time from the onset of activity. **b**, Probability distribution of the number of penetrations longer than N_e per ring for different times. **c**, Correlation between the local density ρ in a given sub-box and the local diagonal stress value. **d**, Correlation between the number of threadings in a given sub-box and the local diagonal stress value. **e**, An example slab section through the simulation box. The heat map: local averaged diagonal stresses (see Supplementary Section 4.5.5 for details). Black points: locations of threadings in space.

as a heat map, overlaid with the locations of threadings and computed the correlation between the number of threadings and such mechanical pressure (see Supplementary Figure 4.3d and 4.3e). The resulting Pearson correlation coefficient $\chi = 0.22$ suggests a weak correlation, as, clearly, not all threadings can contribute to the pressure. A much stronger correlation ($\chi = 0.6$) is found when local density is correlated with the pressure (Supplementary Figure 4.3c).

4.5.6 Emergent directionality of partly active polymers

Here, we use a toy model to discuss the possibility of a directed diffusion originating from different diffusivities of the hot and cold segments of a partly active polymer. We consider stochastic dynamics of two bonded particles that are coupled to two distinct thermostats (for simplicity, in 1d):

$$m\ddot{x}_1 = -\xi\dot{x}_1 - \partial_1 U + \sigma_1\eta_1 \quad (4.13)$$

$$m\ddot{x}_2 = -\xi\dot{x}_2 - \partial_2 U + \sigma_2\eta_2, \quad (4.14)$$

where $\sigma_{1/2} = \sqrt{2\xi T_{1/2}}$ with $T_1 > T_2$ ($k_B = 1$), and $\eta_{1/2}$ are white noises satisfying

$$\langle \eta_i(t)\eta_j(t') \rangle = \delta_{ij}\delta(t-t'). \quad (4.15)$$

We introduce the following set of coordinates:

$$r = x_1 - x_2, \quad R = \frac{x_1 + x_2}{2}, \quad (4.16)$$

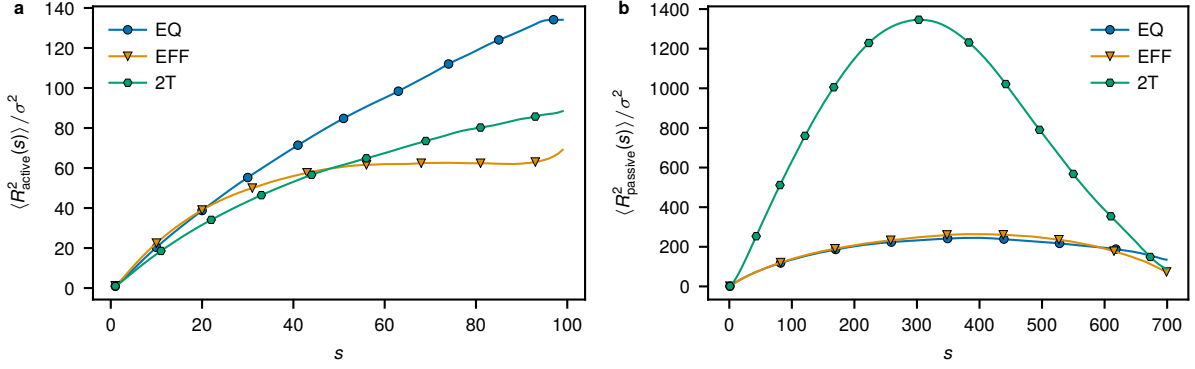
and assume that $U(x_1, x_2) = U(x_1 - x_2) \equiv U(r)$. Note that in this case r coincides with the cold-hot vector **ch**. The equations of motion (4.13) and (4.14) can be now rewritten in terms of the new coordinates:

$$M\ddot{R} = -\xi_R\dot{R} + \sigma_R\eta_R \quad (4.17)$$

$$\mu\ddot{r} = -\xi_r\dot{r} + F(r) + \sigma_r\eta_r, \quad (4.18)$$

where $M = 2m$, $\mu = m/2$, $\xi_R = 2\xi$, $\xi_r = \xi/2$, and $F(r) = -\partial_r U(r)$ is the force acting on the hot particle. More importantly,

$$\sigma_R^2 = 2\xi_R\bar{T}, \quad \sigma_r^2 = 2\xi_r\bar{T}, \quad \bar{T} = \frac{T_1 + T_2}{2}, \quad (4.19)$$



Supplementary Figure 4.4: Comparison between non-equilibrium and effective equilibrium models. The mean-square internal distance profiles of partly active rings of length $N = 800$ in a steady state in the two-temperature non-equilibrium model (2T), the segregated effective equilibrium diblock copolymer model (EFF), and the crumpled configuration of homopolymer rings in equilibrium (EQ). **a**, $\langle R^2(s) \rangle$ of the hot segment of partly active rings, or the effective model of the hot segment (see Supplementary Section 4.5.7 for details), or simply a segment of length N_h of the rings in equilibrium. **b**, $\langle R^2(s) \rangle$ for the corresponding cold segments in every model.

and the noises η_R and η_r satisfy

$$\langle \eta_R(t) \eta_R(t') \rangle = \langle \eta_r(t) \eta_r(t') \rangle = \delta(t - t'), \quad (4.20)$$

$$\langle \eta_R(t) \eta_r(t') \rangle = \left(\frac{T_1 - T_2}{T_1 + T_2} \right) \delta(t - t'). \quad (4.21)$$

Provided that $T_1 \neq T_2$, the motions of R and r are coupled through correlated noises, whereas being completely independent otherwise. The equation for the center of mass is an ordinary Langevin equation and, therefore, its motion is diffusive and isotropic in the long time limit. However, at short time scales ($\simeq m/\xi$) its velocity \dot{R} can be correlated to the relative (cold-hot) vector r . In particular, as follows from (4.21), $\langle \Delta \dot{R}(t) \Delta r(t') \rangle \sim (T_1 - T_2)$, where $\Delta \dot{R} = \dot{R}(t) - \langle \dot{R}(t) \rangle$ and $\Delta r = r(t) - \langle r(t) \rangle$. Additionally, as shown in [271] explicitly for a slightly more general toy model, a drift of the center of mass can arise only when the friction that the beads are subject to is dependent on their relative distance r , which is not part of our model. Thus, as stated in the main text, we conclude that the superdiffusion observed at intermediate times (Figure 4.2c) is explained by the effect of topological constraints, rather than by the directed diffusion.

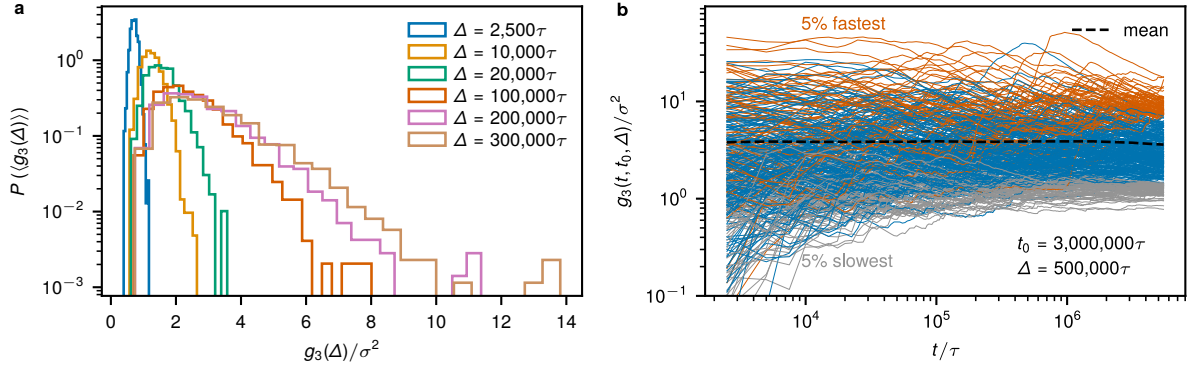
4.5.7 Effective equilibrium model and single ring conformations

In equilibrium linear block copolymers, a colocalization of like-blocks can drive local density changes, which force conformational changes of the chains. Such changes then

result in various global morphologies, e.g. vesicles or lamellae.

To show that the colocalization or phase separation of hot segments is not the main mechanism for conformational changes of the rings, we simulate a single partly active ring in the environment of passive rings, all of the same length $N = 800$. Initially, the radius of gyration of the chain grows in time and eventually plateaus. During this stage, the chain adopts a tree-like conformation that is substantially stretched ($R_g^2/\sigma^2 = 680 \pm 70$ obtained as an average over 100 conformations separated by $10^4\tau$), even when compared to a linear chain of length $N/2$ in a melt with similar parameters ($R_g^2 = 180\sigma^2$ [50]). This is true also for the system with $N = 400$ for low number fractions of active chains (see below).

To support these results, we construct a passive, effective equilibrium model consisting of ring diblock copolymer rings that, as we observe, exhibit a global segregation of the two block types. As is clear from Supplementary Figure 4.4, despite the spatial segregation, the rings in the effective diblock model do not exhibit a substantial conformational change when compared to the homogeneous homopolymer equilibrium state. In the effective equilibrium model, we mimic the effect of the hot monomers by representing them as beads with larger exclusion volume. To do so, we keep the FENE (4.2) interactions the same, while in the LJ (4.1) interaction we use different values of the σ parameter for the hot-hot (σ_{hh}), hot-cold (σ_{hc}) non-bonded interactions, and additionally σ_{hh}^b that governs the LJ interaction of the bonded hot monomers. Guided by the fact that the two-temperature density inhomogeneity is driven by the local pressure differences, we selected the values of different σ 's, based on the following criteria: fitting the pressure and mean bond length of a pure hot system ($T = 3.0$, in units of ε , for all chains) sets $\sigma_{hh} = 1.086\sigma$ and $\sigma_{hh}^b = 1.024\sigma$; fitting the pressure of a fifty-fifty mixture of hot and cold chains sets the value of $\sigma_{ch} = 1.067\sigma$. We do not use the angular interactions as their contribution to the pressure is of the same order as the pressure fluctuations. All these fits were performed on systems of $M = 1000$ linear chains of length $N = 40$ (in the case of two-temperature systems, Langevin thermostats with friction $\gamma = (3/2)\tau^{-1}$ were used). The bonded cold monomers have the original value of the parameter σ . In the case of partly active rings, the two hot-cold pairs of monomers that are bonded have $\sigma_{ch}^b = \sigma_{ch}$. To check if the effective model shares with the original two-thermostat model other properties, besides pressure and bond length, we performed the above-outlined procedure for temperatures also below 3.0 and ran the obtained effective models of equal mixtures of hot and cold linear chains. Similarly to [78], we observe phase separation of the active-like and the passive-like chains above certain threshold of the chains (temperature) asymmetry. This threshold would



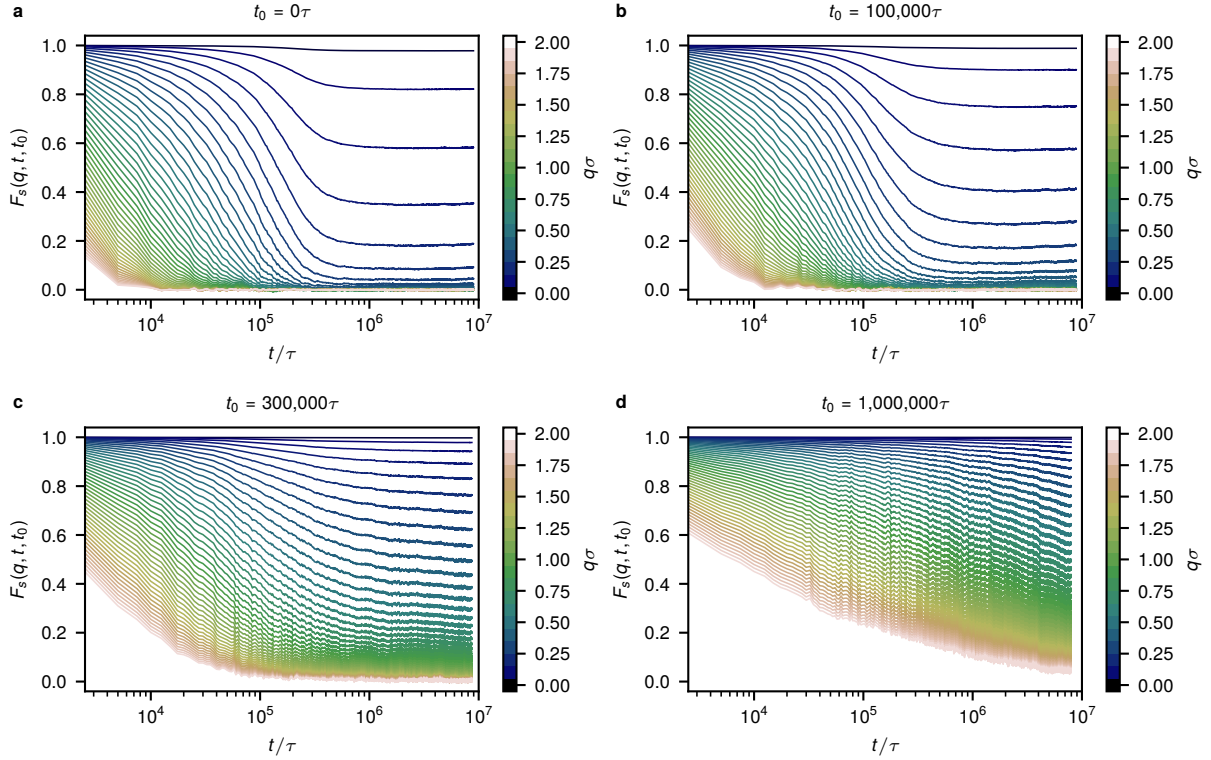
Supplementary Figure 4.5: Ergodicity breaking. **a**, Distribution of g_3 displacements for various lag times Δ . **b**, Time evolution of time averaged g_3 displacements (see Equation (4.8)) of individual rings as a function of the integration time t for $\Delta = 5 \cdot 10^5$ in the late simulation stage. The orange curves indicate the fastest 5% of the rings, whereas the gray ones — the slowest 5%. The dashed black line stands for the ensemble mean g_3 at a given t .

correspond to the temperature of the hot chains in the two-temperature system to be below 1.75, probably close to 1.5. The true two-temperature system of linear chains of length $N = 40$ phase separates around $T_h^{\text{crit}} \simeq 2.25$, for $\gamma = (3/2)\tau^{-1}$ and is only at the onset of phase separation at $T_h = 3.0$ for $\gamma = 2/3\tau^{-1}$ [79]. Therefore, the effective equilibrium model is somewhat stronger than its non-equilibrium counterpart, but it does not feature strong conformational changes of the chains despite its stronger asymmetry between the hot-like and cold-like particles. Hence, we expect that an equilibrium model with weaker asymmetry that reproduces more closely the non-equilibrium phase separation, does not exhibit such changes either.

Let us stress that the purpose of the effective model, as described above, is not to accurately reproduce the microscopic properties of the non-equilibrium model, as it is not clear if this was possible at all [73, 78], but simply to test whether a density inhomogeneity in a system of ring block copolymers could drive substantial conformational changes. We have shown this is not the case, as seen in Supplementary Figure 4.4.

4.5.8 Additional properties of the steady state

The distribution of g_3 displacements for different lag times is shown in Supplementary Figure 4.5a. As mentioned in the main text, it depends only weakly on the lag time for $\Delta > 10^5\tau$. Supplementary Figure 4.5b further illustrates the behavior of the time-averaged $g_3(t, t_0, \Delta)$ for individual rings as a function of the integration time and the failure of the time average to converge to the ensemble average at longer timescales. If



Supplementary Figure 4.6: Self-part of the intermediate scattering function as a function of wave vector. t_0 denotes the measurement start time after the activity onset. The wave vector q grow from top (blue) to bottom (orange) by step $\Delta q = 0.04\sigma^{-1}$ from the value $0.02\sigma^{-1}$.

the system was ergodic at these time scales, the spread around the ensemble average would decrease with time.

In Supplementary Figure 4.6, we show the self-part of the intermediate scattering function for q -values in range $0.02 \leq q\sigma \leq 2$ for different measurement start times t_0 after the activity onset. During the early and intermediate phase, i.e. for $t_0 < 2 \cdot 10^5\tau$, we observe that the system relaxes at high wave vectors, but intermediate and small wave vectors exhibit only the first β -relaxation stage ending up at a non-vanishing value, which we define as the non-ergodicity parameter f_q (Figure 4.3b). Although our simulations are very long, for very small q 's we do not observe even the β -relaxation stage. This is likely because the present system is deeply in the glassy state. For later phases with $t_0 > 10^6\tau$, we do not even reach the first relaxation for most of the wave vectors.

It is possible that one can get closer to the glass transition point if a lower number fraction of partly active chains is used. As shown below, we varied this number and observed the onset of glassy behavior, but we leave the detailed relaxation analysis for future work.

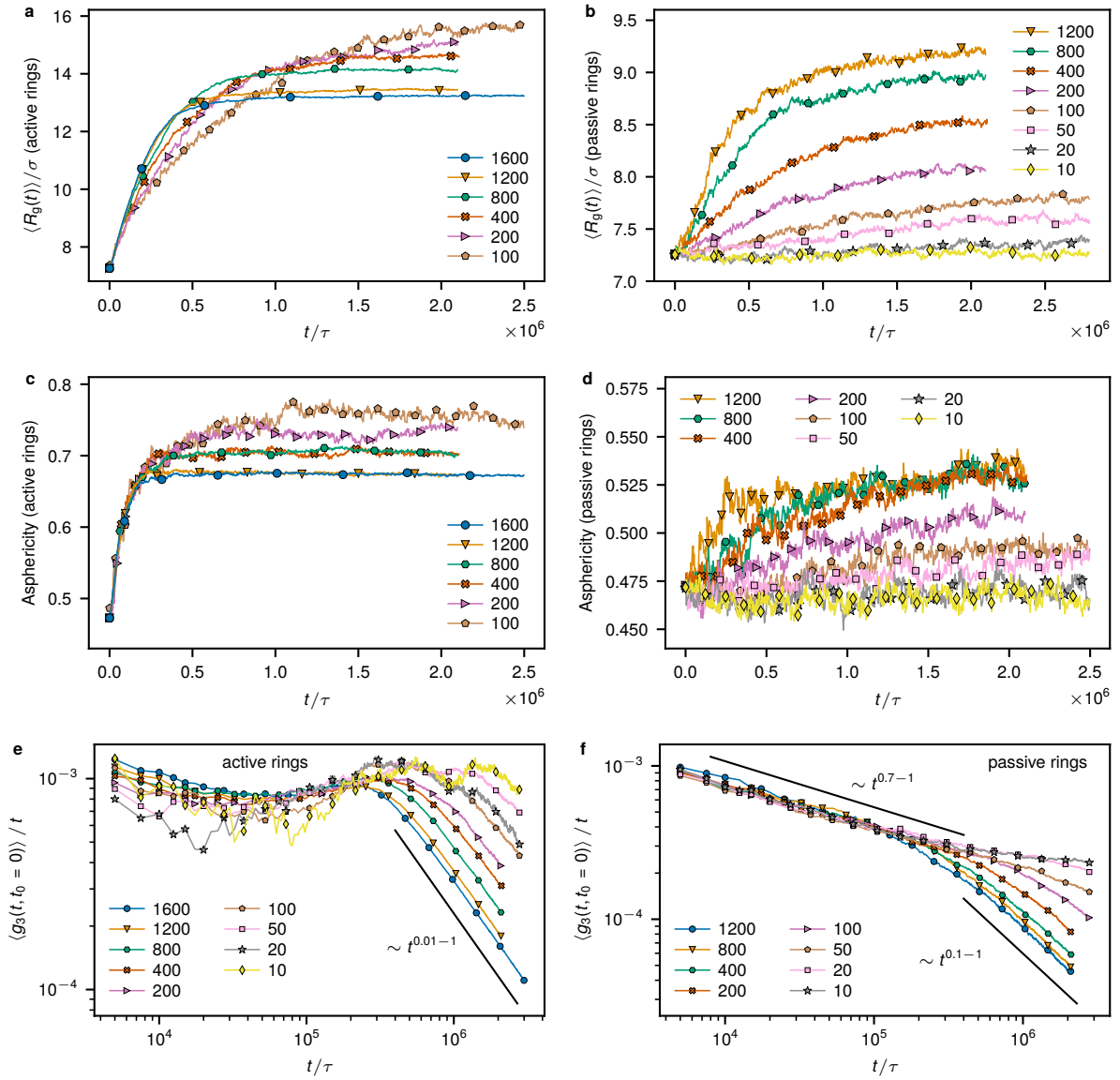
4.5.9 Varying number of partly active chains

We simulated systems with $M = 1600$ rings out of which only M_a were partly active while the rest were completely passive.

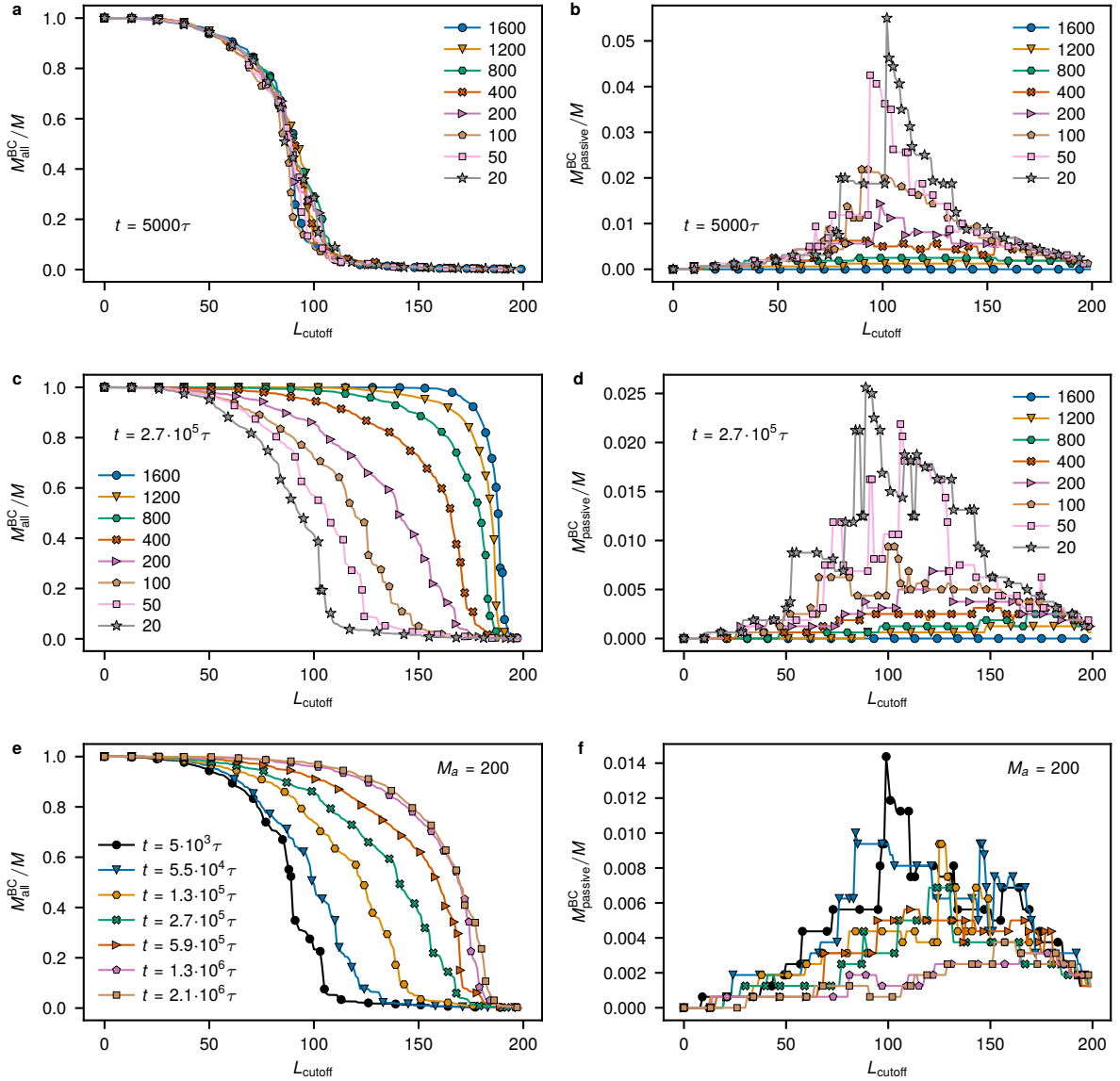
In Supplementary Figure 4.7, we plot the behavior of the radius of gyration and the asphericity for systems with different M_a separately for the active and for the passive rings. The active rings are even more stretched for lower M_a , which we attribute to the lower total number of the topological constraints as compared to system with only active rings. Based on the threading analysis, we conjecture that the active rings form more topological constraints than the passive ones due to their overall stretched configuration. If a certain number of constraints is necessary to stall the rings motion, the lower the M_a is the further each ring stretches before it reaches the number of constraints that stalls its motion. The passive rings are also slightly stretched, as compared to equilibrium, in the systems that evolve towards a glassy state.

We observe the onset of the active topological glass for M_a as low as 100, which corresponds to the number fraction $\Phi_a = 0.0625$ (Supplementary Figure 4.7e and 4.7f). As is evident from these figures, both the active and the passive rings are arrested in this case. Furthermore, as shown in Supplementary Figure 4.7, for lower M_a the glass onset happens later in time. This is because the glassy state is formed by the mutual threadings of the active rings, which become less frequent for lower M_a . Longer simulation of systems with even smaller Φ_a might also reveal a glassy state.

The above picture is consistent with the threading cluster analysis (see Supplementary Figure 4.8). This reveals that the biggest cluster is supported by the active rings interconnected with the passive ones. The passive rings themselves do not form a system-spanning cluster for any value of L_{cutoff} . Finally, relaxation properties of the systems with varying number of partly active rings are shown in Figure 4.8.



Supplementary Figure 4.7: Structural and dynamical properties of rings as a function of time for systems with different number of partly active rings. In every case, the system contains $M = 1600$ rings, out of which only M_a are active, whereas $M - M_a$ remain passive. The rows show (from top to bottom) the mean radius of gyration, asphericity, and $\langle g_3(t, t_0 = 0) \rangle / t$ separately for active (left column) and passive (right column) subspecies in the systems with different M_a , whose value is indicated in the legend of every plot.



Supplementary Figure 4.8: Time-resolved threading cluster analysis for systems with different number of partly active rings. Number of rings in the biggest cluster divided by the total number of rings as a function of the cutoff length L_{cutoff} for different numbers of active rings indicated in the legend. The first row represents the state of the system at an early $t = 5000\tau$, the second one at an intermediate $t = 2.7 \cdot 10^5\tau$. The late stage is shown in Figure 4.8. Bottom row: time-resolved cluster sizes for the system with 200 (out of 1600) active chains. Left column: clusters that contain active (and passive) rings were used. Right column: clusters that contain only passive rings were used (see Supplementary Section 4.5.3). Note the difference in the scale of the ordinate for the passive ring clusters.

Chapter 5

Emergence of active topological glass through directed chain dynamics and non-equilibrium phase segregation

Submitted for publication: Iurii Chubak, Christos N. Likos, Kurt Kremer, and Jan Smrek. Emergence of active topological glass through directed chain dynamics and non-equilibrium phase segregation.¹

Active matter states defy many notions that have been established for systems in thermodynamic equilibrium. Nevertheless, the lack of detailed balance might be utilized to design non-equilibrium materials with unique properties. Recently we have shown, employing a model of ring polymers with segments coupled to stronger than thermal fluctuations, that making polymers with intrinsic topology active can result in states that relax extremely slow, the so-called active topological glass. In this work, we focus on the role of non-equilibrium phase separation in the vitrification process. In particular, we detail the polymer dynamics and show that such activity-driven glassy states arise from heterogeneity of segmental dynamics that emerges on all scales. Provided that the activity quench is strong enough, the rings feature an oriented reptation-like motion, with the active segment serving as an effective chain's end, resulting into a dramatic increase of inter-ring treading that vitrifies the system. The scaling properties of the ensuing steady-state ring conformations, which are significantly elongated and usually possess a doubly-folded structure, are discussed and compared to equilibrium counterparts. We further examine the connection between the glass formation and the non-equilibrium phase

¹Author contributions: I. C. and J. S. performed the simulations and data analysis. All authors interpreted the results. I. C. wrote the paper with the contributions of J. S., K. K. and C. N. L.

separation and we find that both appear to be initiated by the contrasting dynamics of ring segments. Finally, we consider the effect of non-equilibrium phase separation in other active co-polymer architectures.

5.1 Introduction

Properties of ring polymer systems, albeit having been the subject of longstanding theoretical and experimental research, have not yet been understood in their entirety. The topology of each ring is fixed at the synthesis and the non-crossability of the chains gives rise to unique scaling and material properties that range from individual chains [29] to solutions and melts [57, 50, 51, 58, 272, 59, 273]. Furthermore, in contrast to other polymer architectures, the mathematical difficulties to capture topological constraints, even in the simplest problem of two interacting unknotted loops [274], make it a suitable problem for exploration and effective description with the aid of computer simulations [32, 275, 150, 35]. The semidilute and melt conditions that are relevant in biological applications [85, 185] present even a greater modelling challenge because many topological constraints of overlapping chains are not pairwise additive [276] and have to be satisfied simultaneously. Due to involved mathematical complexity despite the simple intuitive rule of fixed topology, extensive studies focused on the prototypical example of the melt of unknotted and non-concatenated rings. Yet, many fundamental questions remain open.

One of such questions pertaining from the beginnings of the field is the existence of topological glass [69]. The rings cannot cross but can thread each other by piercing through one another's opening. The threading restricts relative rings motion and prolongs their relaxation [67, 63, 277]. In melt conditions where many rings overlap, a hierarchical network of threadings would generate a glassy state when relaxation of a ring is conditioned on the sequence of relaxation of other rings. This conjectured novel type of glass arises without the change in volume fraction or temperature, the control parameter being the ring length, which impacts the propensity of mutual ring threading. The concept of topological glass has been recently put in test by so-called pinning perturbations of the melt [66, 70]. When a fraction of all rings is artificially immobilized, the whole system exhibits glassy characteristics. The longer the rings, the smaller the fraction of pinned rings is sufficient to observe the topological glass. The extrapolated ring length for zero pinned rings fraction is beyond the current reach of both experiment and simulation. In these works, the unpinned rings are in equilibrium and as such exhibit threading of their neighbors that is limited by (i) the entropically accessible conformations and (ii)

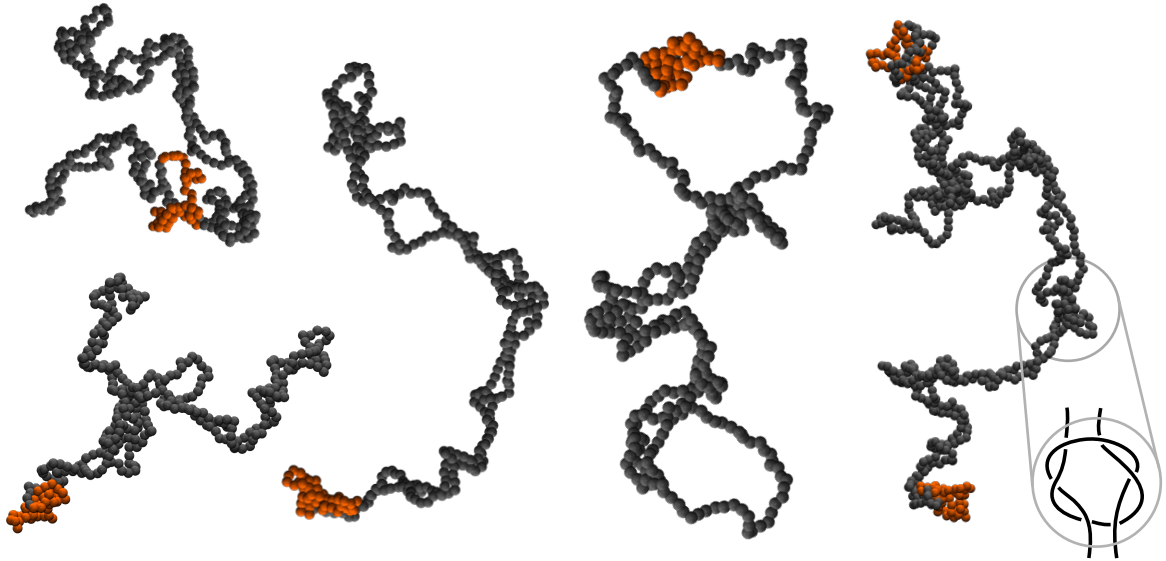


Figure 5.1: Typical conformations of partially active rings in the glassy state. The shown configurations were randomly chosen from the ensemble of rings in the system with $N = 400$. The orange monomers are active and the gray ones passive. Loopy openings on a ring highly likely correspond to other rings that thread it at a given place. In many cases, the conformations feature a doubly-folded structure with the hot segment located at one of its ends. The rightmost configuration depicts two rings entangled by a tight threading similar to the square knot structure schematically depicted in the inset.

the number of the neighbors, which saturates in the long ring limit due to the compact conformation of the rings [50]. Therefore, other ideas to enhance the threading of shorter rings and create a topological glass have been looked for.

Recently, we have shown [184] that a state of topological glass can be attained by rings of moderate length, provided that their segments are subject to heterogeneous activity. The activity in the latter case was induced by coupling a consecutive number of monomers on a ring to stronger thermal fluctuations than the rest, that is by making them effectively hotter. The non-equilibrium dynamics of such partially active rings, stemming from a strongly broken detailed balance, accesses conformations unfavourable in equilibrium, dramatically increases inter-ring threading and ensues substantial structural rearrangements of the system, ultimately resulting in a complete stall of the relative motion of the rings (typical ring conformations in the glassy state are shown in Figure 5.1). The relevance of such a complex non-equilibrium system arises from its connection to the chromosomes in living cells that feature both a structure consistent with topologically constrained dense polymer matter [85] and a thermal-like active processes acting on the DNA segments [100, 278]. While the biological aspect is certainly intriguing, here we are

interested in the physical properties and mechanisms behind the formation of this novel state of matter.

Many properties of such non-equilibrium, activity-driven glassy states in ring polymer melts remain elusive, such as the relation between the glass transition and the active-passive phase separation. While pressure, temperature, and chemical potential are necessarily uniform across the system with different particle species in thermodynamic equilibrium, this is not longer the case for steady states of non-equilibrium active matter systems [279, 280, 78, 79]. The active-passive phase separation is observed for various models of activity [281, 77], but coexistence conditions can depend on activity details [280].

In a two-temperature mixture, the degree of phase separation between two species strongly depends on the temperature difference between the hot and cold thermostats, the friction coefficient γ , which serves as a coupling constant between particles and thermostats, as well as on the polymerization degree of particles, provided they are polymers [78, 79, 77, 73, 75, 74]. In colloidal particle mixtures containing equal number fractions of both species, the phase segregation arises if the critical temperature ratio is quite high, $T_h/T_c \approx 30$ [77, 73, 75]. Such activity ratio roughly compares with the ratio of Péclet numbers necessary to observe phase separation of self-propelling active particles [281]. Nevertheless, as has been shown for the two-temperature case [78, 79, 75], the critical activity ratio decreases with the particles' polymerization degree N with the incompatibility parameter scaling as $\sim N^{-1/2}$ [78, 75], in contrast to $\sim N^{-1}$ dependence for equilibrium phase separation [80]. While the theoretical result [75] is built on a virial-like approximation and hence applicable to moderate densities, the scaling $\sim N^{-1/2}$ had been conjectured based on simulation of concentrated active-passive solutions [78].

In the active topological glass the sufficiently long active blocks would tend to segregate, but their diffusivity that plays a role in the enhancement of threading decreases with N . The natural questions arise: how is the vitrification related to the observed active-passive phase separation for polymer mixtures? What is the role of the ring length for a fixed activity ratio? How are the conformations, dynamics, and phase-separated morphologies of such non-equilibrium, activity-driven rings related to those of equilibrium and what are their scaling properties? We tackle these questions by considering melts of ring polymers of varying length subject to comparable activity quench.

In this work, we detail on how such a non-equilibrium system of rings arrives at a dynamically arrested state. The onset of activity implies a discrepancy between the dynamics of hot and cold segments that, as we show, if being strong enough, generates a slithering-snake-like motion of the active segment pulling the rest of the chain that has a

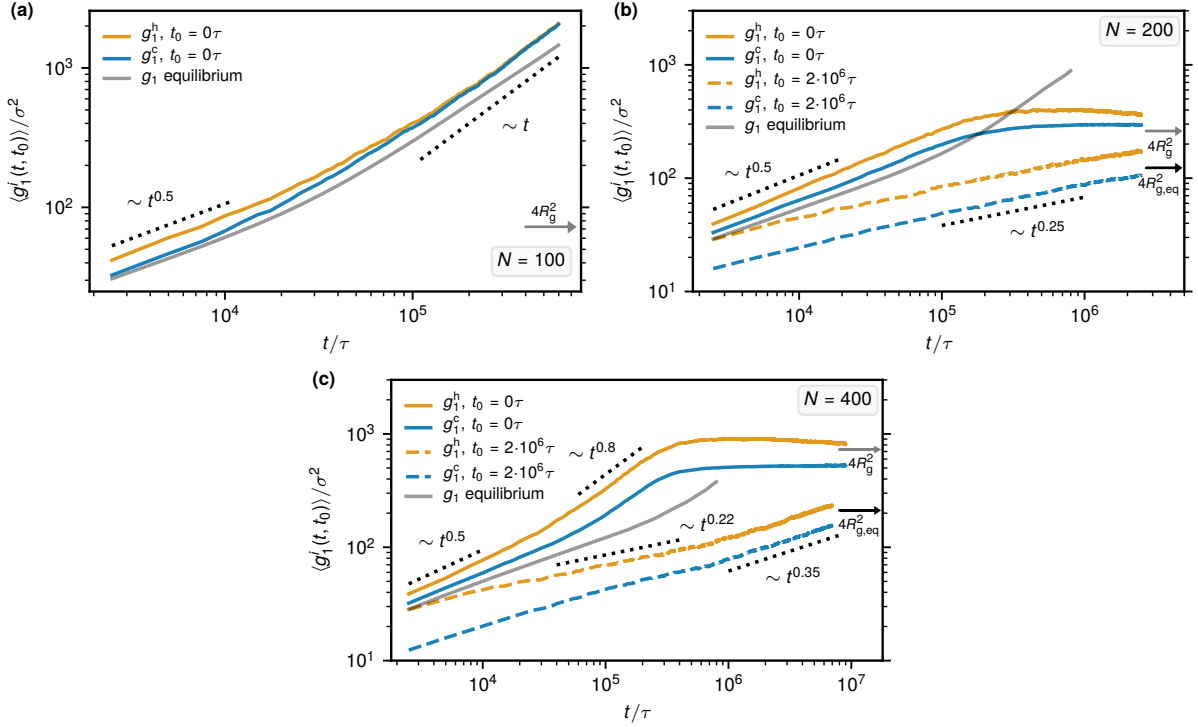


Figure 5.2: Dynamics of monomers. Mean-square displacements of active, $g_1^h(t, t_0)$, and passive, $g_1^c(t, t_0)$, monomers in the early ($t_0 = 0\tau$, solid lines) and late ($t_0 = 2 \cdot 10^6\tau$, dashed lines) stages for systems with $N = 100$ (a), $N = 200$ (b), and $N = 400$ (c). The partially active rings with $N = 100$ feature equilibrium-like dynamics that does not depend on t_0 , thus only the data for $t_0 = 0\tau$ is shown in a. The dashed lines indicate intermediate scaling regimes. The transparent gray lines correspond to g_1 in equilibrium for the respective case. The arrows indicate the squared equilibrium (black arrows) and non-equilibrium (gray arrows) diameter of gyration.

propensity to form tight threadings – topological constraints that are difficult to resolve. Some of these have the local form of square knots (see inset of Figure 5.1) and are found also to be responsible for a strong increase in viscosity for ring melts under extensional flow [239, 240]. Once a sufficiently high number of such constraints is formed, the cold part of a ring is essentially fixed in space, whereas the hot one intermittently continues diffusing through the system, causing a significant and rapid expansion of the rings. As a result, it leads to even stronger inter-ring tangling. In the final, deeply threaded state, the hot segments tend to phase segregate more, which reduces energy dissipation and increases their effective temperature, leading to further tightening of the constraints. At this steady state, the constraints cause the dynamics of each ring to lose the drift element. As we show, the aforementioned process of segregation between hot and cold segments comes to a halt due to the vitrification caused by the circular topology of the ring polymers. To investigate the possible morphologies of activity-induced phase separation, we also

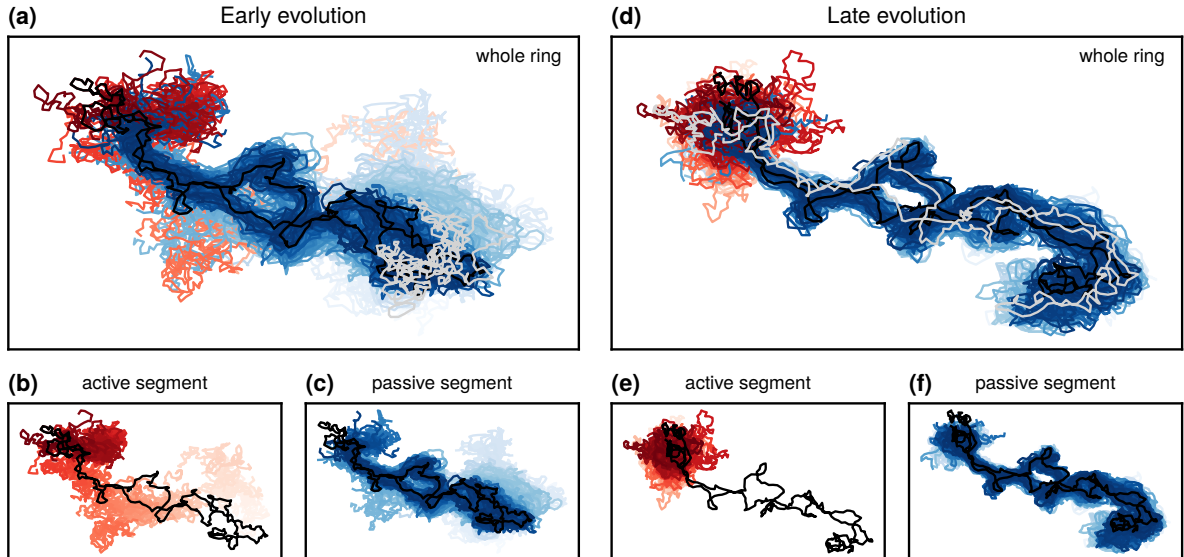


Figure 5.3: Evolution of a single ring with $N = 400$. Left panel: early rearrangements of the conformation of the whole ring (a), its hot (b) and cold (c) segment over $t = 5 \cdot 10^5 \tau$ starting from the activity onset at $t_0 = 0\tau$. Right panel: late rearrangements of the conformation of the whole ring (d), its hot (e) and cold (f) segment over the subsequent $t = 5 \cdot 10^6 \tau$. In all plots, the black curve indicates the final ring configuration, whereas in a and d, the light gray curve in the foreground indicates its starting configuration. In all cases, the xy -projection of the ring's coordinates is shown and the opacity increases linearly with time, that is, earlier configurations are lighter. The time trace of the hot and cold segments are shown in red and blue respectively. Finally, note that the length of the shown trajectory in d, e, f is ten times longer than in a, b, c.

examine steady states of other polymer architectures that can arise from cutting the rings, by which we remove the long-lasting topological constraints. In particular, linear mixtures of unequal lengths and linear triblock co-polymer systems, exhibit microphase separation, however in the extent and morphology different from both, their equilibrium phase-separated counterparts and the active topological glass.

5.2 Model

Our systems consist of $M = 1600$ monodisperse, semi-flexible ring polymers of length N ($N = 100, 200, 400$). We employ a standard model for polymer melts [127], in which excluded-volume interactions between monomers are given by the purely repulsive Lennard-Jones potential

$$U_{\text{LJ}}(r) = \left(4\varepsilon \left[\left(\frac{\sigma}{r} \right)^{12} - \left(\frac{\sigma}{r} \right)^6 \right] + \varepsilon \right) \theta(2^{1/6}\sigma - r), \quad (5.1)$$

where $\theta(x)$ denotes the Heaviside step function, σ is the diameter of each monomer having mass m , and ϵ sets the energy scale. The bonding potential between two neighboring monomers along the chain's contour is set by the finitely extensible nonlinear elastic potential

$$U_{\text{FENE}}(r) = -\frac{1}{2}r_{\text{max}}^2 K \log \left[1 - \left(\frac{r}{r_{\text{max}}} \right)^2 \right] \quad (5.2)$$

with $K = 30\epsilon/\sigma^2$ and $r_{\text{max}} = 1.5\sigma$. Finally, the bending potential is

$$U_{\text{angle}} = k_{\theta}(1 - \cos(\theta - \pi)) \quad (5.3)$$

with $k_{\theta} = 1.5\epsilon$. This choice of parameters prevents inter-chain crossings that would violate the initial non-concatenation constraint. Moreover, it achieves small entanglement length $N_e = 28$, below which the chains are still approximately Gaussian.

In each system, successive $N_h = N/8$ monomers on every ring are made active ($N_h = 13, 25, 50$ for $N = 100, 200, 400$, respectively). This is achieved by subjecting them to stronger thermal-like fluctuations, as compared to the remaining $N_c = N - N_h$ particles. Here and in what follows, active monomers are interchangeably called hot, whereas passive ones are named cold. In practice, we couple both species to two distinct Langevin thermostats with $T_h = 3\epsilon$ ($k_B = 1$) for active monomers, and $T_c = 1\epsilon$ for passive ones, such that the equations of motions read as

$$m\dot{\mathbf{v}}_i = -m\gamma\mathbf{v}_i + \mathbf{F}_i + (2m\gamma T_i)^{1/2}\boldsymbol{\eta}_i, \quad (5.4)$$

where γ is the coupling constant with the heat bath, \mathbf{F}_i is the total conservative force on the monomer, the components of $\boldsymbol{\eta}_i$ satisfy $\langle \eta_{i,\alpha}(t)\eta_{j,\beta}(t') \rangle = \delta_{ij}\delta_{\alpha\beta}\delta(t-t')$, and T_i is either T_h or T_c . The same $\gamma = (2/3)\tau^{-1}$, where $\tau = \sigma(m/\epsilon)^{1/2}$, is used for both thermostats. These choices of γ and T_h are sufficient to drive non-equilibrium phase separation in active-passive mixtures of short ($N \gtrsim 20$) polymers [78, 79], but by far not strong enough to observe demixing of colloids [77, 73]. All the Langevin dynamics simulations were performed at constant volume and density $\rho = 0.85\sigma^{-3}$ using the large-scale atomic/molecular massively parallel simulator (LAMMPS) engine [266]. The integration time step was set to $\Delta t = 0.005\tau$. Finally, as noted in the original work [184], relatively large system sizes with $M = 1600$ polymers were needed to ensure that unphysical self-threadings of extremely elongated rings due to periodic boundary conditions do not occur.

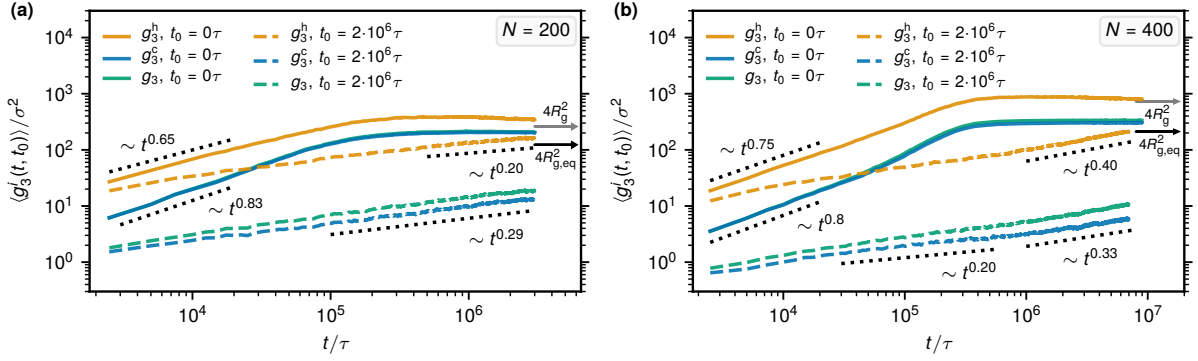


Figure 5.4: Dynamics of segments. Comparison between the center-of-mass mean-square displacements of active, $g_3^h(t, t_0)$, and passive, $g_3^c(t, t_0)$, segments, and the whole rings, $g_3(t, t_0)$, for $N = 200$ (a) and 400 (b) in the early ($t_0 = 0\tau$, solid lines) and late ($t_0 = 2 \cdot 10^6\tau$, dashed lines) stages. The dotted lines indicate different intermediate scaling regimes. The arrows indicate the squared equilibrium (black arrows) and non-equilibrium (gray arrows) diameter of gyration.

5.3 Onset of glassy dynamics

At time $t_0 = 0\tau$, the activity on all rings in a properly equilibrated sample of M chains is switched on. As shown below, the ensued dynamics differs across the three cases considered: whereas for the larger rings with $N = 200$ and 400 it progressively slows down and eventually results in a halt of the relative motion of the rings, the dynamics of the system with $N = 100$ is equilibrium-like.

To characterize in detail the rings' motion on all scales, we consider the mean-square displacements of active and passive monomers, $g_1^\alpha(t, t_0)$ ($\alpha = \text{hot/cold}$), their mean-square displacements with respect to the ring's center of mass, $g_2^\alpha(t, t_0)$, and the mean-square displacements of the center of mass of the whole ring, $g_3(t, t_0)$:

$$g_1^\alpha(t, t_0) = [\mathbf{r}^\alpha(t_0 + t) - \mathbf{r}^\alpha(t_0)]^2, \quad (5.5)$$

$$g_2^\alpha(t, t_0) = [\Delta\mathbf{r}^\alpha(t_0 + t) - \Delta\mathbf{r}^\alpha(t_0)]^2, \quad (5.6)$$

$$g_3(t, t_0) = [\mathbf{R}(t_0 + t) - \mathbf{R}(t_0)]^2, \quad (5.7)$$

where $\mathbf{r}^\alpha(t)$ is the position of an active or passive monomer at time t , \mathbf{R} is the center of mass position of the ring, and $\Delta\mathbf{r}^\alpha(t) = \mathbf{r}^\alpha(t) - \mathbf{R}(t)$ is the position of a monomer with respect to its ring's center of mass. In all cases the positions are relative to the total center of mass of the system at the given time to subtract the induced global drift. Additionally, we consider the mean-square displacements of the center of mass of active

and passive segments, $g_3^\alpha(t, t_0)$:

$$g_3^\alpha(t, t_0) = [\mathbf{R}^\alpha(t_0 + t) - \mathbf{R}^\alpha(t_0)]^2, \quad (5.8)$$

where $\mathbf{R}^\alpha(t) = N_\alpha^{-1} \sum_{i=1}^{N_\alpha} \mathbf{r}_i^\alpha(t)$ is the center of mass position of the active or passive segment on a ring. In general, we consider only the mean-square displacements averaged over rings, $\langle g_i^\alpha(t, t_0) \rangle$, without additional averaging over multiple time origins because of the explicit dependence of the dynamics on t_0 at early times. The steady-state properties for the systems with $N = 200$ and 400 correspond to the time when most conformational properties come to a standstill and to when the dynamic correlation functions do not feature a significant dependence on t_0 . For the former two systems, this time corresponds to about $t_0 \simeq 2 \cdot 10^6 \tau$. Thus, in what follows we will focus on the two cases: early rearrangements immediately after the activity onset ($t_0 = 0\tau$) as well as the steady state dynamics ($t_0 = 2 \cdot 10^6 \tau$). Finally, to give a perspective on the dynamics, we also simulated fully equilibrium systems with $T_h = T_c = 1$ and all other parameters the same as in the active cases.

As mentioned in the introduction, the friction coefficient γ is an important parameter that governs redistribution of heat between the cold and hot subsystems. In Langevin dynamics simulations, lower values of γ enhance the heat transfer between distinct particle species, and therefore result in apparent effective temperatures T_h^{eff} and T_c^{eff} of hot and cold particles that differ from the ones set by the thermostats [78, 79, 74]:

$$T_c < T_c^{\text{eff}} < T_h^{\text{eff}} < T_h. \quad (5.9)$$

Conversely, the increase of γ keeps the particles' temperatures closer to the thermostat ones, thereby amplifying the effective temperature difference and thus promoting phase segregation of hot and cold particles. Finally, due to the heat flow to the cold subsystem, even the diffusivity of passive monomers is increased because their effective temperature is higher than the one imposed by the thermostat, $T_c^{\text{eff}} > T_c$. In any case, we use thermostat coupling constant much lower than the effective bead-bead friction ($\simeq 20\tau^{-1}$) [282].

As shown in Figure 5.2, the early dynamics ($t_0 = 0\tau$) of both active and passive monomers is consistent with that of equilibrium melts [50, 51, 283], and is characterized by $g_1^{\text{h/c}}$ scaling as $g_1^{\text{h/c}} \sim t^{1/2}$ indicating standard Rouse behavior. For all N , in full accordance with (5.9), at early times $g_1^{\text{h}} > g_1^{\text{c}} > g_1$, where g_1 corresponds to a completely passive, equilibrium system with $T_h = T_c = 1$. In sharp contrast to $N = 200$ and $N = 400$, the $g_1^{\text{h/c}}$ for the system with $N = 100$ crosses over to free diffusion $g_1^{\text{h/c}} \sim t$ with no

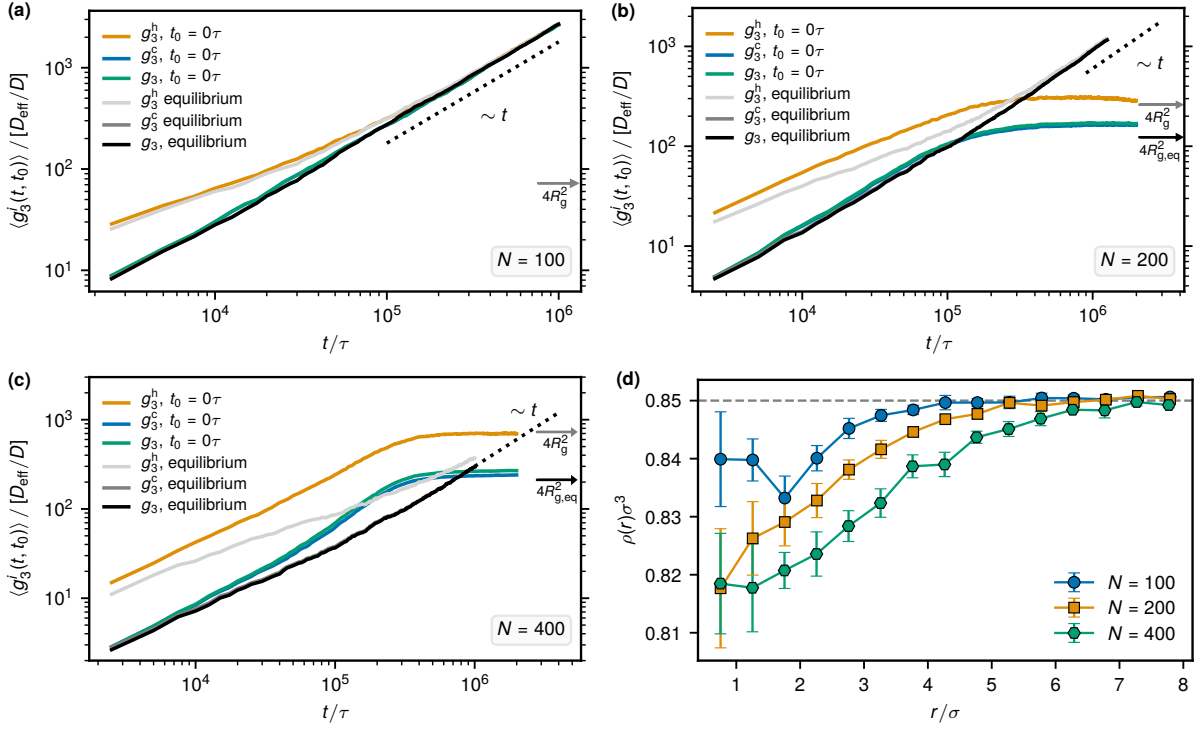


Figure 5.5: Dynamics of segments rescaled with effective diffusion coefficient. Comparison between the center-of-mass mean-square displacements of active, $g_3^h(t, t_0)$, and passive, $g_3^c(t, t_0)$, segments, and the whole rings, $g_3(t, t_0)$, for $N = 100$ (a), $N = 200$ (b), and 400 (c) in the early ($t_0 = 0\tau$) stage ($D_{\text{eff}}/D = 1.25$) and the equivalent dependencies in equilibrium ($D_{\text{eff}}/D = 1$). The mean-squared gyration radius in equilibrium $R_{g, \text{eq}}^2$ [50] and in the steady-state R_g^2 are marked by arrows for comparison to the mean-squared displacements. d, Average monomer density around the center of mass of the hot segment early after the activity onset ($t < 10^4\tau$). For all N , the dip in the density has width of about one diameter of gyration of the hot segment at that time. The gray dashed line corresponds to the mean monomer density $\rho\sigma^3 = 0.85$.

indications of glassy behavior (Figure 5.2a). Moreover, the dynamics of the system with $N = 100$ is equilibrium-like and it does not depend on t_0 . In contrast, the Rouse regime of $g_1^{h/c}$ for the two larger systems with $N = 200$ and 400 is followed by a gradual slow-down, see Figure 5.3 for time traces at early and late stages of the evolution. The steady-state dynamics of $g_1^{h/c}$ for active and passive monomers in these systems ($t_0 = 2 \cdot 10^6\tau$) is indicated by dashed lines in Figure 5.2: for short lag times, $g_1^{h/c}$ are generally slower than in the equivalent equilibrium case (especially, for passive monomers), g_1^h is typically 1.5-2 times higher than g_1^c , and both feature a more than two-decade long regime with $g_1^{h/c}$ exhibiting scaling close to $\sim t^{1/4}$. The exponent reminisces of linear polymer reptation along its chain contour [51]. In the present case, in the steady state the centers of mass of the rings are practically fixed due to numerous threadings, and their displacements are

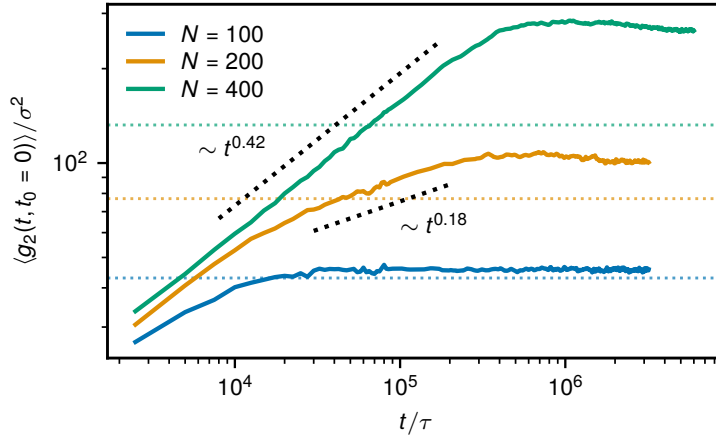


Figure 5.6: Dynamics of monomers with respect to the center of mass. $g_2(t, t_0)$ is shown immediately after the onset of activity, that is for $t_0 = 0\tau$, for systems with different N and is averaged over both hot and cold monomers in the system. There is practically no difference in $g_2^{c/h}$ computed separately for cold and hot monomers. The black dotted lines indicate intermediate scaling regimes. The colored dotted lines indicate the value $2.5\langle R_g^2 \rangle$, where $\langle R_g^2 \rangle$ is the squared equilibrium radius of gyration taken from [50] (different colors corresponds to different N as in the legend). After around $2.5\langle R_g^2 \rangle$, g_3 of an equilibrium-like system would cross over to diffusion, whereas g_2 would saturate (see more discussion in the main text).

only generated by occasional pulls of the active segments, as we detail below in Figure 5.4. This essentially corresponds to a directed reptation-like motion where the active segment serves as an effective ‘chain end’ that directs ring’s displacements.

For the two larger systems ($N = 200, 400$) that slow down, in Figure 5.4 we further compare the mean-square displacements of the center of mass of active and passive segments, $g_3^{h/c}$, as well as of the whole ring, g_3 , in the early ($t_0 = 0\tau$) and late ($t_0 = 2 \cdot 10^6\tau$) stages. Similarly to $g_1^{h/c}$, the early dynamics of $g_3^{h/c}$ and g_3 is consistent with the short-time dynamics of an equilibrium ring melt with $g_3 \sim t^{3/4}$ [51]. Naturally, due to a significant difference in length, the hot segment at early times diffuses faster than the cold one, as evidenced by about an order of magnitude difference between g_3^h and g_3^c . However, in the present cases, the hot segment still diffuses faster than it would be in a corresponding equilibrium-like model. As shown in appendix 5.7.1, the center of mass of a free polymer chain, parts of which are connected to two distinct thermostats, follows equilibrium-like dynamics with an effective temperature, T_{eff} , which is a weighted average of the two thermostat temperatures $T_{\text{eff}} = (T_c N_c + T_h N_h)/N$, directly translating into its enhanced diffusion coefficient $D_{\text{eff}} \sim T_{\text{eff}}$. Although the above relations are given in terms of the thermostat temperatures $T_{h/c}$, the same T_{eff} is obtained if $T_{h/c}$ are replaced with $T_{h/c}^{\text{eff}}$, which is due to the balance of heat fluxes that is discussed later on in Section 5.5. For all

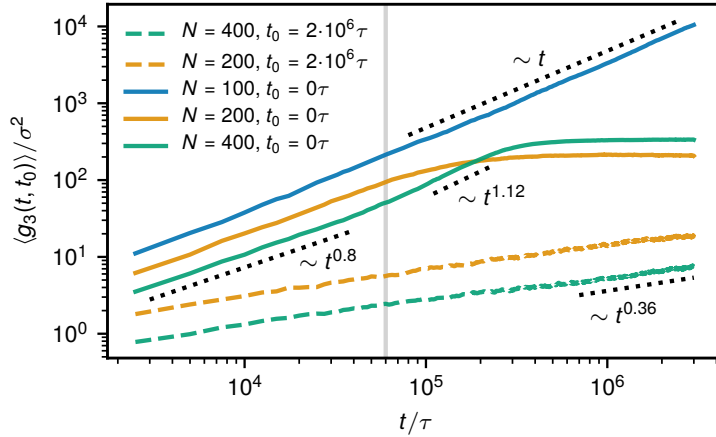


Figure 5.7: Dynamics of the center of mass. Mean-square displacements of the ring’s center of mass in the early ($t_0 = 0\tau$, solid lines) and late ($t_0 = 2 \cdot 10^6\tau$, dashed lines) stages for systems with different N . Partially active rings with $N = 100$ feature equilibrium-like dynamics that does not depend on t_0 . The dotted lines indicate intermediate scaling regimes. The gray line indicates the time $t = 6 \cdot 10^4\tau$. (see also Figure 5.8).

systems considered here, $N_h = N/8$ and $T_h = 3T_c$, therefore $D_{\text{eff}} = 1.25D$ with D being the equilibrium diffusion coefficient ($T_h = T_c$). The Rouse regime is well applicable until the chain starts to explore topological constraints imposed by other chains. For shorter rings, these do not present a significant obstacle, as their (half-)length is only moderately higher than the equilibrium entanglement length, which itself is effectively higher for hotter melt due to enhanced chain flexibility [284].

In Figure 5.5, we show $g_3^{h/c}$ as well as g_3 rescaled by D_{eff}/D and compare them to the equivalent equilibrium cases for all N . While we find a good correspondence between the rescaled displacements for $N = 100$, for $N = 200$ and $N = 400$ certain differences arise already at early times, immediately after the activity onset. In particular, the dynamics of the cold segment and the center of mass are generally consistent with the equilibrium-like system with enhanced D_{eff} at early times, whereas the hot segment still diffuses faster as compared to the latter case. This arises from a more dilute environment around hot segments (see Figure 5.5d) that indicates an early stage of non-equilibrium phase segregation. The active segments not only feature a higher diffusivity because of their coupling to a hotter heat bath, but also because of a lower density around them. In equilibrium, such a moderate decrease in density has a pronounced effect on the effective monomer friction and the resulting diffusion coefficient [282]. As seen in Figure 5.4, the discrepancy between the segment dynamics in the two larger systems only deepens in the steady state, which is consistent with further demixing of hot and cold monomers, as detailed later on in Section 5.5. Similarly to the monomer dynamics, center-of-mass

mean-square displacements $g_3^{\text{h/c}}$, the quantity g_3 in the steady state ($t_0 = 2 \cdot 10^6 \tau$) features a very slow relaxation that scales as $\sim t^{0.2}$ at shorter times and then appears to cross over to $\sim t^{0.3-0.4}$ at longer ones. Note that in the steady state the displacement of the total center of mass is very small ($\simeq 3\sigma$ for time $\simeq 10^7 \tau$), while the hot segment explores distances about 10σ (Figure 5.4b). As the number of active monomers is relatively small compared to the length of the whole ring, the center-of-mass mean-square displacements, g_3 , generally resemble those of the passive segment. This further confirms the picture that the active segments explore the neighboring environment, while the whole ring remains essentially fixed due to pronounced topological constraints.

In equilibrium ring melts, the center of mass of rings of these still relatively short lengths starts to diffuse after traveling about $2\langle R_g^2 \rangle$ ($\langle R_g^2 \rangle$ is the mean-square ring's radius of gyration), which corresponds to the point where g_3 and g_2 cross [51]. In the present non-equilibrium case with $N = 100$, we find that this happens at around $D_{\text{eff}}/D \times 2\langle R_g^2 \rangle = 2.5\langle R_g^2 \rangle$, with $\langle R_g^2 \rangle$ being the equilibrium value. Figure 5.6 shows $\langle g_2(t, t_0) \rangle$ immediately after the activity onset ($t_0 = 0\tau$) and averaged over both active and passive monomers (g_2 computed separately for the two species are practically indistinguishable). While for $N = 100$, g_2 indeed saturates after about $2.5\langle R_g^2 \rangle$, this is not the case for the two longer polymers. In the latter cases, g_2 grows beyond $2.5\langle R_g^2 \rangle$, which is an indication of rings expansion past the equilibrium size. In all cases, at short times g_2 features scaling close to the Rouse-like regime of g_1 , $g_2 \sim t^{1/2}$. For $N = 400$, such regime governs g_2 up to the point where it begins to saturate. For $N = 200$, $g_2 \sim t^{1/2}$ scaling crosses over to $g_2 \sim t^{0.2}$ before saturation. As will be seen in Section 5.4, this corresponds to slower expansion of ring's size for $N = 200$, as compared to $N = 400$.

In Figure 5.7, we further compare the mean-square displacements of the center of mass of the rings for systems with different N . We find that the time of the onset of the slow-down of the dynamics for $N = 200$ and $N = 400$ roughly corresponds to the onset of free diffusion in equivalent equilibrium ring melts [51]. Conversely, $N = 100$ crosses over from the g_3 exponent of about 0.8 to standard diffusion with the corresponding diffusion coefficient being about 25% higher than in equilibrium, in full agreement with considerations in section 5.7.1 and (5.18), giving $D_{\text{eff}} = 1.25D$. While both $N = 200$ and $N = 400$ arrive at an arrested state, the exact mechanism of how they do that differs in these two cases. In particular, the Rouse regime for $g_1^{\text{h/c}}$ in the system with $N = 200$ extends beyond the crossover to diffusion in the equivalent equilibrium system (Figure 5.2b), whereas $g_1^{\text{h/c}}$ in the system with $N = 400$ is crossing over towards diffusion earlier than in equilibrium, however, saturates later on (Figure 5.2c). For $N = 400$, the

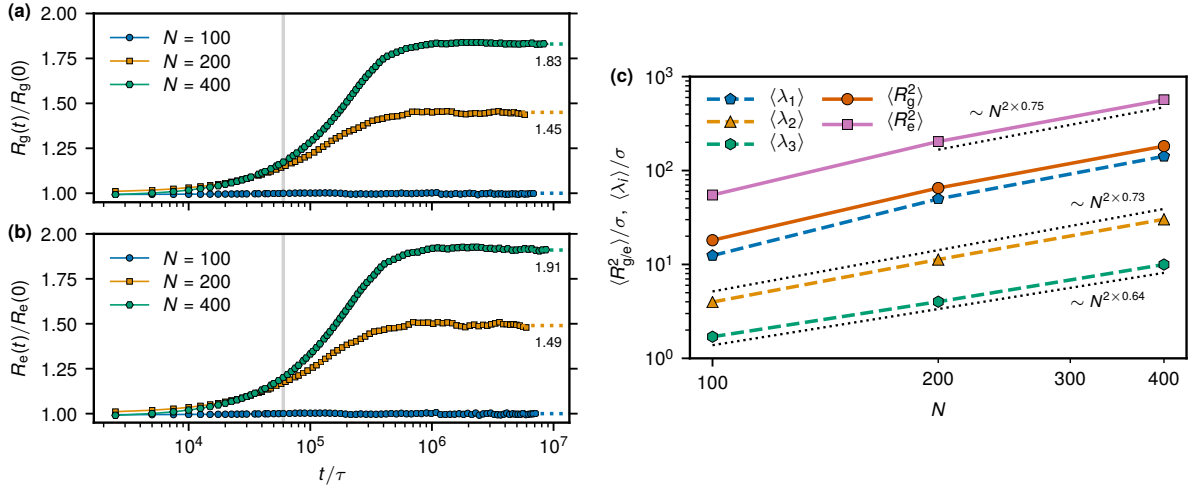


Figure 5.8: Size properties. Time evolution of (a) the mean radius of gyration, R_g , and (b) the mean ‘end-to-end’ distance, R_e , of the rings. The time series of $R_g(t)$ and $R_e(t)$ are scaled with their values at $t = 0\tau$ that correspond to equilibrium conformations. The gray lines in a and b indicate the time $t = 6 \cdot 10^4 \tau$, at which significant slow-down of rings’ dynamics in the two larger systems becomes apparent (see Figure 5.7). Scaling of different size descriptors with N in the steady state ($t > 2 \cdot 10^6 \tau$) is shown in c.

cross-over to diffusion of $g_1^{h/c}$ coalesces with super-diffusive motion of the center of mass (Figure 5.7), during which the rings expand significantly (see also a detailed discussion on the present super-diffusion mechanism in [184]). For $N = 200$, such super-diffusive regime is not observed and it is likely caused by the shorter ring length that limits the amount by which the rings can expand while being driven by the hot segment.

5.4 Conformational properties

In Figure 5.8, we quantify conformational rearrangements of the rings by tracking the time evolution of the mean radius of gyration

$$R_g \equiv \langle R_g^2 \rangle^{1/2} = \left\langle \frac{1}{N} \sum_{i=1}^N (\mathbf{r}_i - \mathbf{R})^2 \right\rangle^{1/2}, \quad (5.10)$$

and the mean ‘end-to-end’ distance

$$R_e \equiv \langle R_e^2 \rangle^{1/2} = \left\langle \frac{1}{N} \sum_{i=1}^N (\mathbf{r}_{i+N/2} - \mathbf{r}_i)^2 \right\rangle^{1/2}, \quad (5.11)$$

where, \mathbf{r}_i denotes the position of the i -th monomer and \mathbf{R} is the position of the center of mass of the ring. Additionally, to quantify shape properties, we computed eigenvalues

λ_i ($i = 1, 2, 3$, $\lambda_1 \geq \lambda_2 \geq \lambda_3$) of the ring's gyration tensor $G_{ij} = N^{-1} \sum_{k=1}^N \Delta r_i^{(k)} \Delta r_j^{(k)}$, where $\Delta r_i^{(k)}$ is the i -th component of the k -th monomer's position vector in its ring's center of mass frame. The angles $\langle \dots \rangle$ stand for the ensemble average over the system of rings. Whereas the system with $N = 100$ that does not vitrify features almost the same R_g and R_e as in equilibrium, the systems with $N = 200$ and 400 are characterized by a considerable growth of these quantities (steady-state size and shape parameters are given in Tab. 5.1). The growth of the rings' size is associated to two effects. Firstly, the change in the dynamics to oriented reptation-like impacts the ring shape that has to adapt to the topological constraints and establish a doubly-folded configuration. Second, the formation of unresolvable threadings, which essentially fix parts of the rings, and the following pulling of the active segment extends the chain. Whether the unresolvable threadings are present from the initial stages, or they appear only after the chain moves significantly is an open question. Currently, we favor the former scenario as the rings move only about their own size. Based on observations of systems with fewer active chains where the vitrification appears later and passive chains are stretched, we think both scenarios are possible.

Such dramatic increase in the rings' size is associated with a similar increase in the number of rings' neighbors, $K_1(a)$, as shown in Figure 5.9 (two rings are considered to be neighbors if their centers of mass lie at a distance smaller than a). Interestingly, a significant slow-down of the dynamics occurs after the rings on average grow by 10% (see Figure 5.8 and 5.7, and note the associated time scale highlighted by the gray lines). This further confirms that the heterogeneous dynamics of rings' segments first promotes the formation of topological constraints, which eventually cause the vitrification of the system. Just before the dynamics significantly slows down, the systems with $N = 200$ and $N = 400$ feature a brief regime of their size growth. This translates into an equivalent simultaneous growth of the average number of neighbors (Figure 5.9). For compact objects, $K_1(a)$ is

Table 5.1: Size and shape properties of the partly active rings in the steady state. $\langle R_g^2 \rangle$ is the mean-square radius of gyration, $\langle R_e^2 \rangle$ is the mean-square distance between two monomers separated by the contour length $N/2$, and λ_i , $i = 1, 2, 3$ are the eigenvalues of the gyration tensor ordered such that $\lambda_1 \geq \lambda_2 \geq \lambda_3$. The value in the parentheses indicates the standard error. For comparison with equilibrium values, please see Table 5.2 in Appendix 5.7.2.

N	N_h	$\langle R_g^2 \rangle / \sigma^2$	$\langle R_e^2 \rangle / \sigma^2$	$\langle \lambda_1 \rangle / \langle \lambda_3 \rangle$	$\langle \lambda_2 \rangle / \langle \lambda_3 \rangle$
100	13	18.1(0.1)	54.9(0.1)	7.3(0.1)	2.34(0.01)
200	25	65.2(0.3)	203.5(3.8)	12.4(0.1)	2.81(0.01)
400	50	182.1(0.7)	566.1(2.1)	14.2(0.2)	3.03(0.02)

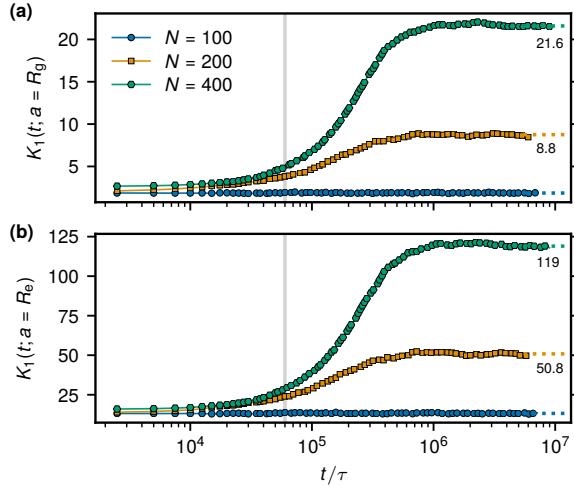


Figure 5.9: The mean number of neighbors. Time evolution of the mean number of neighbors $K_1(t; a)$ for (a) $a = R_g$ and (b) $a = R_e$. The gray line indicates the time scale at which significant slow-down of rings’ dynamics in the two larger systems becomes apparent.

independent of N , while for equilibrium melt of linear chains it is proportional to $N^{1/2}$. Here, in the steady state, $K_1(R_g)$ grows superlinearly, indicating that the stretching of the rings is stronger the longer the ring is. Additionally, as shown in Figure 5.8, we quantified the scaling of different size parameters (R_g , R_e , λ_i) with N , resulting in an apparent scaling $\sim N^\nu$ with ν taking a value 0.64-0.75, distinctly above $1/2$ characterizing linear polymers in melt and $2/5$ and $1/3$ that describe rings of similar length [50]. Although this scaling was extracted from very few points only and can be attributed to a cross-over between two distinct scaling regimes, the effective exponent higher than $1/2$ could be related to results on transversal fluctuations of directed polymers [285]. Similarly to directed polymers, present rings are being driven by the hot segment, although in random directions, and move through a “gel matrix” formed by other rings. However, at these chain lengths N , we are not in the asymptotic limit and, therefore, not only the ring conformations differ slightly for different N , as shown below, but also the gel matrix is different. Therefore, a proper connection between the directed polymers and the present system is yet to be explored. Finally, the rings in the two bigger systems arrive at significantly stretched and elongated conformations with their radius of gyration and eigenvalue ratios being comparable to linear polymer chains of the *same* length [50], but their R_e comparable to the linear chains of *half* the length (compare Tab. 5.1 to Tab. 5.2 in Appendix 5.7.2). This highlights that the rings are mostly doubly-folded and significantly stretched in the vitrified state in comparison to equilibrium.

To gain a better understanding of conformations of such non-equilibrium rings, we

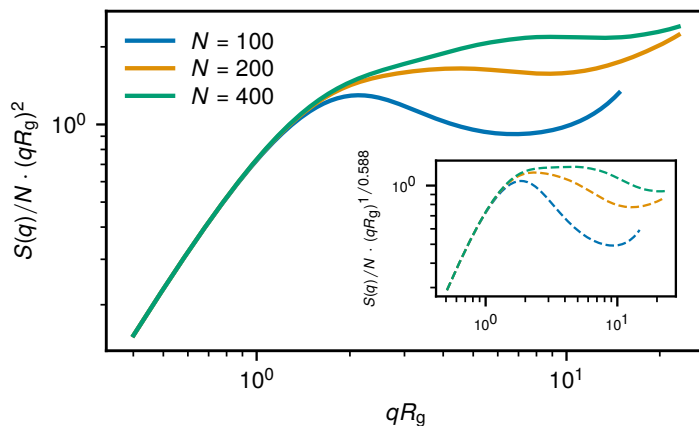


Figure 5.10: Single chain static structure factor. $S(q)$ for different N is multiplied by $q^{1/\nu}$ with $\nu = 1/2$ characterizing linear polymer chains. Inset: $S(q)q^{1/\nu}$ but with $\nu = 0.588$.

evaluated the single chain structure factor $S(q)$, which is shown in Figure 5.10. For a fractal object with dimension $1/\nu$, $S(q)$ shall feature a scaling regime $S(q) \sim q^{-1/\nu}$. The results in Figure 5.10 do not indicate the presence of a regime with $\nu \approx 0.7$ for $N = 200$ and 400. Instead, for $N = 200$, at length scales comparable with R_g we observe ideal linear polymer scaling with $\nu = 1/2$, as shown in Figure 5.10 by plotting $S(q)q^2$. Interestingly, for $N = 400$, we observe scaling $\nu = 0.588$ (see inset of Figure 5.10). The self-avoiding walk regime is observed in a relatively narrow range of q and care should be taken as finite-size effects could play a role. However, the superdiffusive dynamics reported in [184] is consistent with this exponent as well as preliminary results of systems with longer chains (not shown) indicate that this exponent is indeed correct. At lower q that crosses over to $\nu = 1/2$ at higher q . The behavior of $S(q)$ for $N = 100$ is identical to the equilibrium one [50]. Similar results on size scaling with $\nu = 1/2$ can be inferred from the mean-square internal distances shown in Figure 5.12 at intermediate contour segment lengths.

The ideality of rings' conformations at smaller length scales can be further inferred from the contact probability $P(s)$, which gives the probability of finding two monomers separated by contour distance s being at a distance smaller than some cutoff value, shown in Figure 5.11a. While for $N = 100$, we observe the same behavior as in equilibrium, $N = 200$ and $N = 400$, due to very extended conformations, feature an ideal chain regime with $P(s) \sim s^{-\gamma}$ with $\gamma = 3/2$ at small s , which then crosses over to the equilibrium-like crumpled globule regime with γ close to 1 at larger s [50]. The contact probability measured separately for hot and cold segments reveals a finer structure (Figure 5.11b). The exponent $\gamma = 4/3$ found for hot segment is characteristic for smooth fractal globules, such as collapsed unknotted polymer with smooth outer surface [286, 85], which suggests

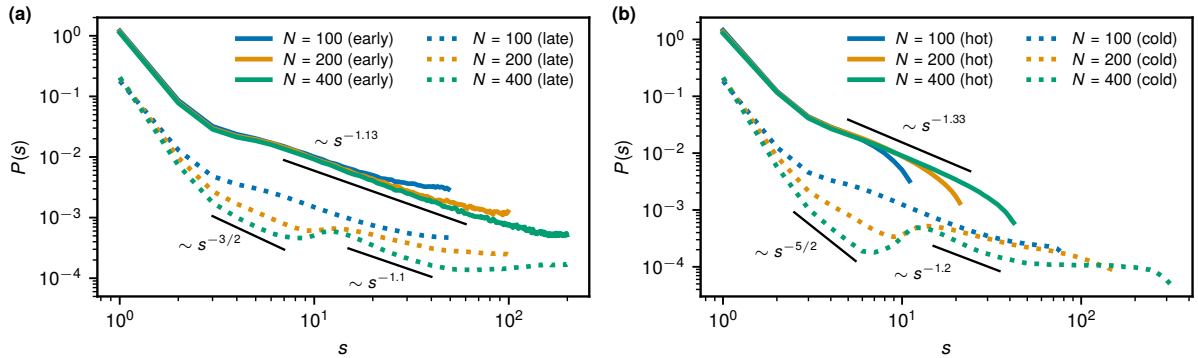


Figure 5.11: Contact probability. **a**, $P(s)$ of rings is shown for all N at early (solid lines) and late (dotted lines) times. **b**, $P(s)$ separately for hot (solid lines) and cold (dotted lines) segments. Here, the $P(s)$ is averaged over the segment's position only within the give segment type. For clarity, dotted curves in **a** and **b** have been shifted vertically. The solid black lines indicated intermediate scaling regimes $P(s) \sim s^{-\gamma}$. Two monomers are considered in contact if they are at a distance smaller than $2^{1/6}\sigma$.

its segregation from the surrounding. This view is confirmed by the finding that $\nu = 1/3$ for the hot segment (see Figure 5.12a), because as shown in [85] $\gamma = 2 - (d-1)\nu$ for space-filling fractals in d dimensions. The cold tail shows non-monotonic behavior with very steep decay at small scales, consistent with very stretched configurations, and shallower decay at longer lengths, that characterize tree-like, doubly folded conformations [62].

Such dramatic changes in the rings' size and, as a consequence, the number of neighbors, result in a significantly enhanced propensity for inter-ring threading, which we describe now. Inter-ring threadings are quantified using the minimal surface approach. Therein, the ring's contour is considered fixed and is spanned by a surface, whose mean-curvature is then minimized, as explained in Refs. [72, 267]. Consequently, a threading between a pair of rings is defined by an intersection between one ring's contour and another ring's minimal surface. This approach provides a straightforward geometric picture of the inter-ring threading, is model-independent above the entanglement length [72], and has been employed to quantify the influence of threadings in bulk and confined equilibrium ring polymer melts [63, 72, 283] or for tadpole-shaped polymers [186]. The depth of threadings is quantified by means of the separation length L_{sep} :

$$L_{\text{sep}} = \min \left(\sum_{i=\text{even}} L_{t_i}, \sum_{i=\text{odd}} L_{t_i} \right), \quad (5.12)$$

where L_{t_i} is the (threading) contour length between the i -th and the $(i+1)$ -th penetrations of the minimal surface. L_{sep} quantifies the portion of the threading ring on one side of the threaded ring. Therefore, the ratio $Q = L_{\text{sep}}/(N - L_{\text{sep}})$ approximates [186] the relative

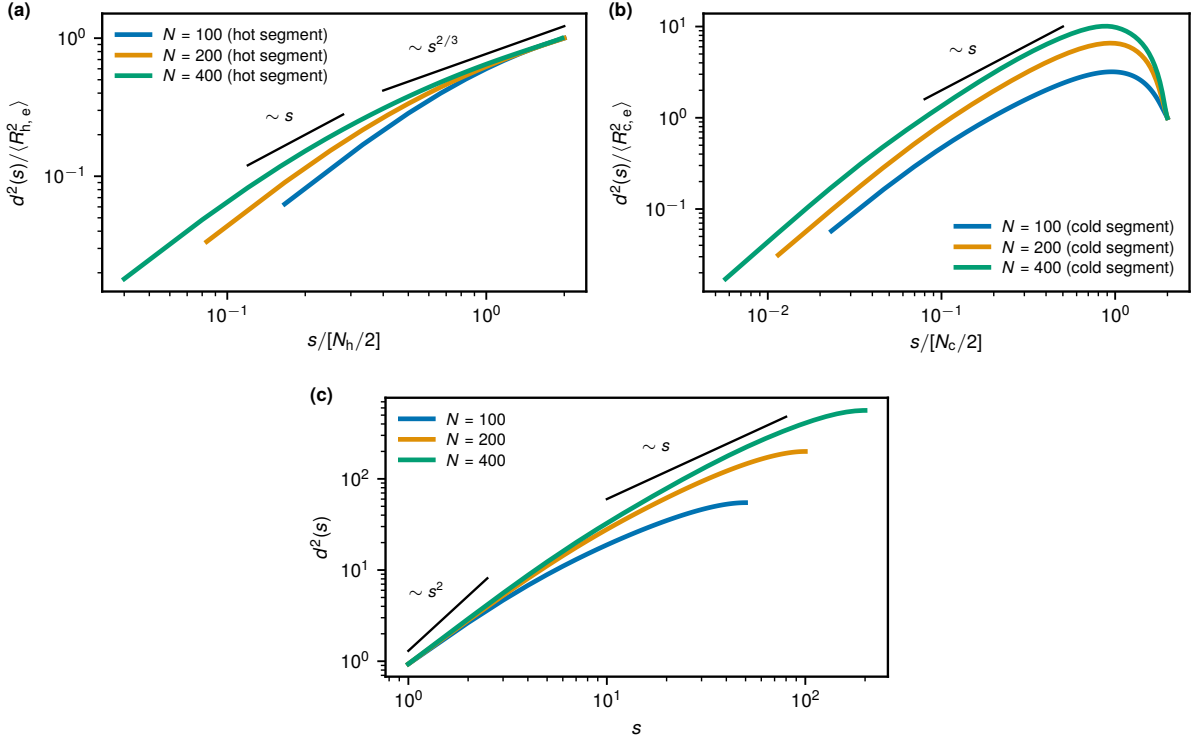


Figure 5.12: Conformational properties of the rings' subchains. Mean-square internal distance $d^2(s)$ between monomers separated by contour length s , computed separately for hot (a) and cold (b) segments as well as the whole rings (c) in the late stage. In a and b, $d^2(s)$ is normalized by the effective segment end-to-end distance $\langle R_{e,c/h}^2 \rangle$, defined as $d^2(N_{c/h})$, where $N_{c/h}$ is the respective length of cold and hot segments. The solid black lines highlight different scaling regimes of $d^2(s)$.

portion of the threading ring's contour on one side compared to the other side of the threaded ring's surface.

The time evolution of mean threading properties after the activity onset is shown in Figure 5.13 for systems with different N . Except for $N = 100$, the mean number of threaded neighbors $\langle n_{\text{tn}} \rangle$ per ring, defined as the total number of threadings in the system n_{tn} divided by M , is increasing with time, saturating at a constant value after about $10^6 \tau$. As expected, $\langle n_{\text{tn}} \rangle$ correlates strongly with the mean number of ring neighbors within its radius of gyration, $K_1(R_g)$ (compare Figure 5.13a and Figure 5.9a). Although the numbers $K_1(R_g)$ and $\langle n_{\text{tn}} \rangle$ in the steady state are almost the same, as we checked, the rings contributing to K_1 are not all threaded and, similarly, some threaded neighbors of a ring are further than R_g from the ring's center of mass. Simultaneously, the threadings are becoming progressively deeper, as evidenced by a rise $\langle Q \rangle$ in Figure 5.13b. Interestingly, even for $N = 100$ we observe a slightly increase in $\langle Q \rangle$, albeit no other influence of activity on rings' conformational properties in this system is apparent. While in equilibrium the

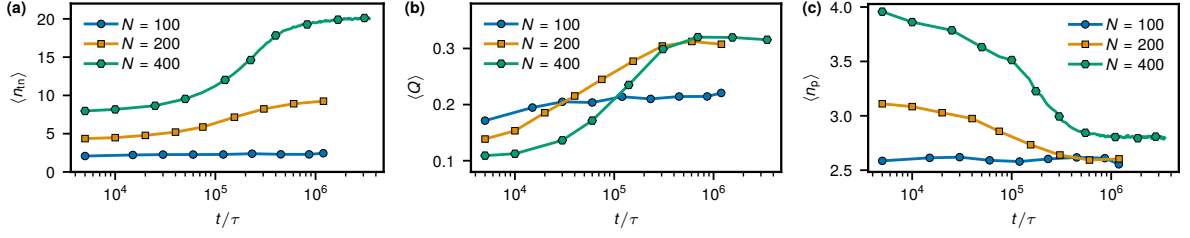


Figure 5.13: Time evolution of threading properties. **a**, Mean number of threaded neighbors $\langle n_{tn} \rangle$ per ring for systems with different N as a function of time after the activity onset. **b**, Mean threading length ratio Q as a function of t for different N . **c**, Mean number of surface penetrations $\langle n_p \rangle$ as a function of t for different N .

amount of shallow threading increases with N , as quantified by the mean number of penetrations of a ring’s minimal surface $\langle n_p \rangle$, in Figure 5.13c we show that $\langle n_p \rangle$ goes down with time for $N = 200$ and $N = 400$. If only surface penetrations longer than N_e were considered, which provides a model-independent view on threading statistics [72], $\langle n_p \rangle$ would actually slightly increase over time [184]. This indicates that many shallow surface piercings disappear, while a few deeper ones appear, which further confirms the increase of threading depth consistent with the evolution of $\langle Q \rangle$. Finally, as we showed in the previous work [184], the mutual ring threadings are responsible for the glassy behavior that emerges from the development of a system-spanning threading cluster.

5.5 Phase separation

The gradual change of conformational properties of the rings as well as the slowed dynamics, ensuing from dramatically enhanced threading, coalesce with demixing of cold and hot segments. The hot segments are bonded with the cold ones and, therefore, *macro*phase separation that would feature a higher resulting temperature contrast [79] is not possible. In fact, we observe the formation of *micro*phase separated regions, with numerous interfaces that mediate the heat flux and decrease the temperature contrast. In the ring systems at hand, block lengths of hot monomers are 13, 25, 50 for $N = 100, 200, 400$, respectively. For the given $\gamma = 2/3\tau^{-1}$ and $T_h = 3\epsilon$, the hot block length in the two longer systems would be sufficient to drive phase segregation in an active-passive mixture of linear polymer chains, which irrespective of their type would have length N_h . In contrast, such a mixture of chains of length only $N_h = 13$ (representing active block in the shortest system) would not phase segregate [78, 79]. Nevertheless, the question whether demixing occurs in systems with polymers of unequal length N_h and N_c at a similar temperature contrast is open. To quantify phase separation in our systems, we compute the order

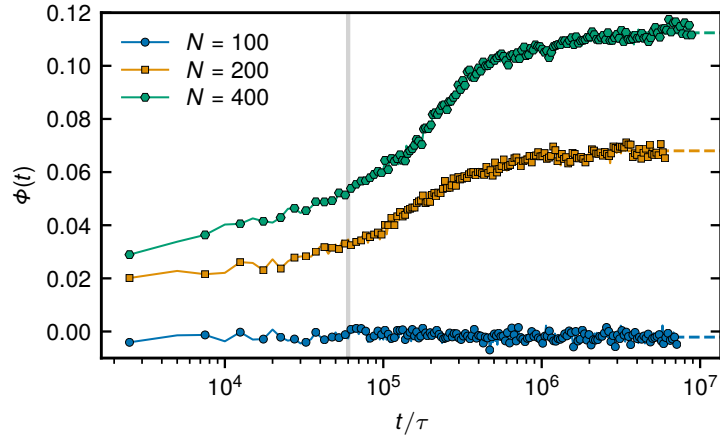


Figure 5.14: The phase segregation order parameter. To render comparison across systems with different N , the initial value of the order parameter $|\bar{\Phi}(0)|$, corresponding to equilibrium, has been subtracted from $|\bar{\Phi}(t)|$. The gray line indicates the time scale at which significant slow-down of rings' dynamics in the two larger systems becomes apparent. The dashed, colored lines represent the steady-state value of Φ of a given system.

parameter $\Phi(t) = x(t)/x(0) - 1$, where $x(t)$ is the particle-averaged number fraction of inter-chain like-particles in a $r_c = 2^{1/6}\sigma$ neighborhood of a given particle at a given time t , and $x(0)$ is the same quantity at $t = 0\tau$ corresponding to equilibrium (at $t = 0\tau$ distinct types were assigned to particles of an equilibrium melt state, but equations of motions were not integrated yet; thus, such state must be reasonably mixed). Such choice of $\Phi(t)$ allows to explicitly compare systems with different fractions of hot monomers along the chain, which are characterized by different values of $x(0)$.

As reported in Figure 5.14, while the system with $N = 100$, which is equilibrium-like and does not vitrify, does not show strong propensity for segregation of cold and hot monomers, the two larger system do. For $N = 200$ and $N = 400$, immediately after the activity onset the cold and hot segments in these systems become somewhat segregated ($t < 10^5\tau$). This agrees well with reduced density around the hot segments and their enhanced diffusion, as reported in Figure 5.4. As the rings are becoming gradually more and more constrained by numerous increased threadings, further separation continues up to around few millions τ . The system with $N = 400$ arrives at a more segregated state than the one with $N = 200$.

The effective temperatures responsible for the phase segregation are obtained as average over particles of the same species. To a good approximation, the velocity distribution of hot/cold particles can be described using the Maxwell-Boltzmann distribution with temperature $T_{h/c}^{\text{eff}}$ [79]. In a phase segregated state, the deviations from the corresponding

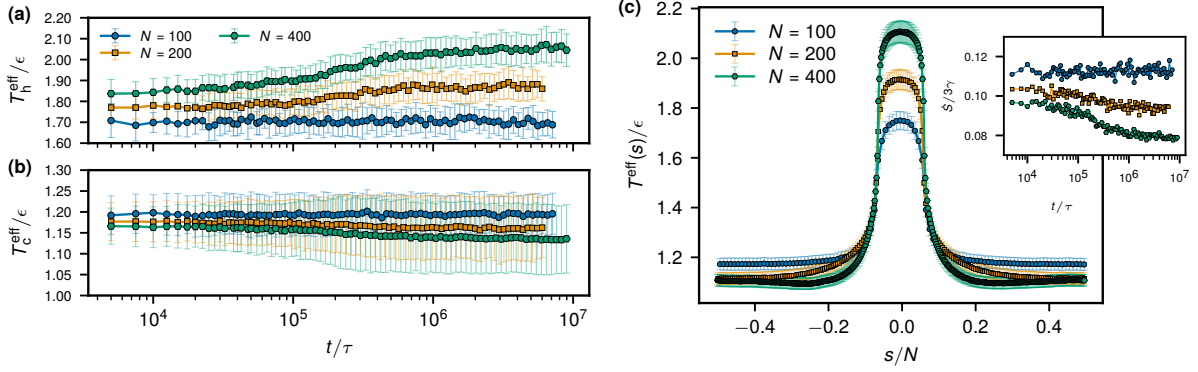


Figure 5.15: Effective temperatures. Time evolution of the system-averaged effective temperature of hot, T_h^{eff} , (a) and cold, T_c^{eff} , (b) monomers. c, Distribution of the effective temperature along the ring's contour in the steady state for different N . (s is centered at the middle of the active segment). Inset: time evolution of the mean entropy production \dot{S} per monomer (5.14) (error bars are not shown for clarity; generally, the standard deviation of $\dot{S}/3\gamma$ is around 0.15 in all cases). In a, b, and c error bars indicate the standard deviation of the corresponding quantity.

Maxwell-Boltzmann distribution arise from particles that sit at the interfaces and, on average, have an intermediate effective temperature, $T_c^{\text{eff}} < T^{\text{eff}} < T_h^{\text{eff}}$. In the steady state, the total average power supplied to the system from the thermostats through random collisions $\dot{E}^{\text{rand}} = -3\gamma(n_h T_h + n_c T_c)$ should balance the total dissipated energy per unit time through friction $\dot{E}^{\text{fric}} = 3\gamma(n_h T_h^{\text{eff}} + n_c T_c^{\text{eff}})$ [78]. Therefore,

$$n_h T_h^{\text{eff}} + n_c T_c^{\text{eff}} = n_h T_h + n_c T_c. \quad (5.13)$$

The relation (5.13) is satisfied for all N at any point in time t , although the two larger systems feature substantial conformational rearrangements at early times. The reason for this is the fact that (5.13) works as long as no *external* work is being produced, which is the case in the systems considered. Note that dividing (5.13) by N provides the equality between the mean effective temperature, governing the center of mass dynamics of the ring, and the mean thermostat temperature. This makes it possible to apply the single chain results like in section 5.7.1 to the melt case where the effect of the other chains, besides the topological constraints, is just in adjusted value of the effective temperatures.

As shown in Figure 5.15a, phase separation in the systems with $N = 200$ and $N = 400$ leads to gradually increased discrepancy between the two effective temperatures in the system. Nevertheless, the ratio $T_h^{\text{eff}}/T_c^{\text{eff}} \approx 1.6$ -1.8 in these systems is still much smaller than the one imposed by the thermostat $T_h/T_c = 3$. The propensity of hot blocks to phase segregate in these systems locally reduces density around them and therefore disproport-

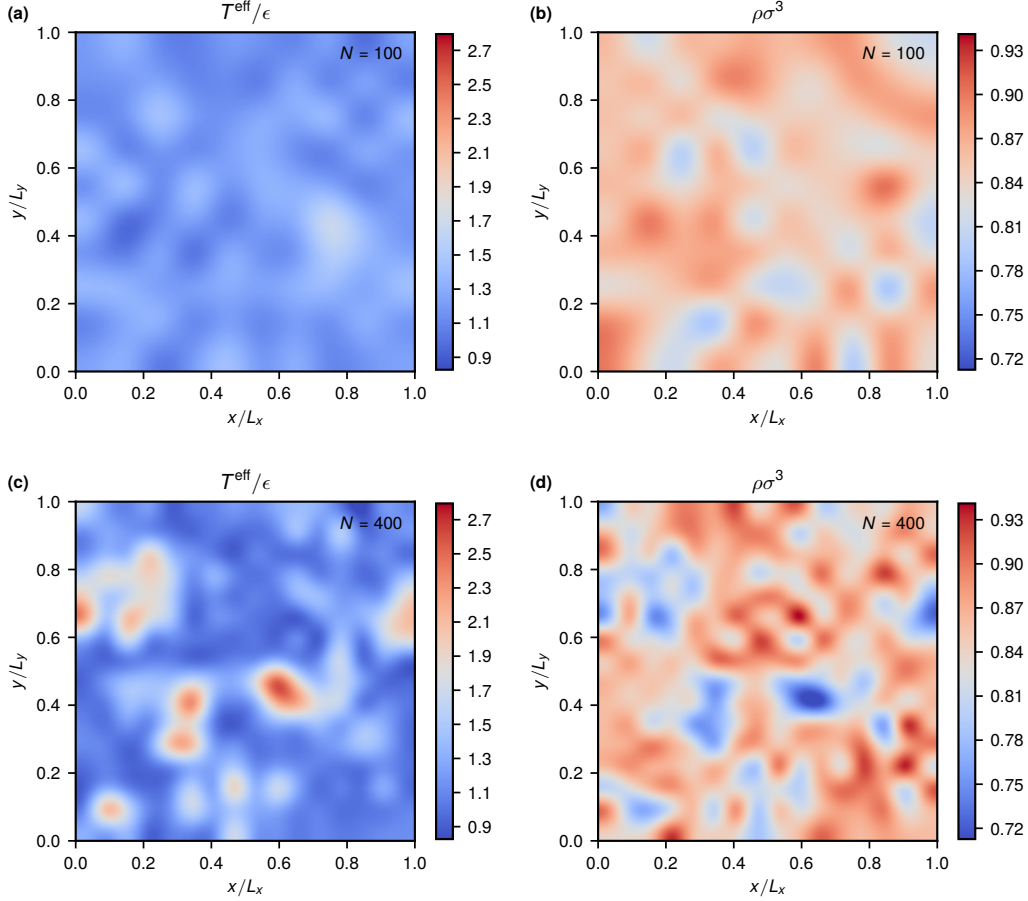


Figure 5.16: Spatial distribution of temperature and density. T^{eff} and ρ are shown for $N = 100$ (a, b) and $N = 400$ (c, d). To compute the distributions, the systems were divided into n_b^3 small sub-boxes of comparable size $\sigma_b \approx 5.7\sigma$. One layer corresponding to a fixed z -elevation is shown. The heat maps for $N = 100$ are normalized with the same scale as for $N = 400$.

tionately increases their diffusivity, as compared to the cold segments. This results in an oriented reptation-like motion, where partially active rings are essentially driven by hot segment displacements, which promotes the formation of inter-ring threading constraints and makes unthreading events less likely. As the rings are getting more constrained by their threading neighbors (Figure 5.13), they continue to locally phase segregate stronger (Figure 5.14), which again increases the difference between segment diffusivities and therefore makes the unthreading processes even more unlikely. Thus, a formed glassy state is maintained by the non-equilibrium microphase separation. In contrast, the smallest system with $N = 100$ that is not segregating stronger, features more contacts between hot and cold monomers and, therefore, heats up the cold subsystem at the expense of the hot one, resulting in $T_h^{\text{eff}}/T_c^{\text{eff}} \approx 1.4$. The rings as a whole in this system follow an equilibrium-like dynamics with diffusivities of hot and cold segments being proportional

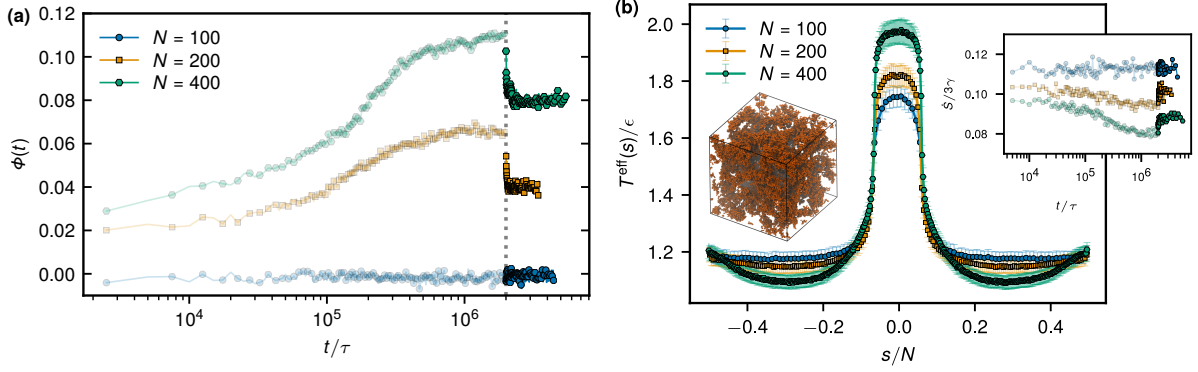


Figure 5.17: Non-equilibrium phase segregation of cut rings (ABA triblocks). **a**, Time evolution of the phase segregation order parameter for rings (transparent curves) before $t < 2 \cdot 10^6 \tau$ and linear polymer chains (opaque curves) obtained after cutting the rings in the middle of the cold segment at $t = 2 \cdot 10^6 \tau$ (dotted gray line). for different N . **b**, Distribution of the effective temperature along the contour of cut rings in the steady state (after equilibrating for $1.5 \cdot 10^6 \tau$) for different N (s is centered at the middle of the active segment). Inset: time evolution of the mean entropy production \dot{S} for rings before (transparent) and after (opaque) cutting. The snapshot on the left illustrates the partially segregated state of hot monomers (cold monomers are not shown for clarity) in the system with $N = 400$ at the end of the simulation. In **b**, error bars indicate the standard deviation of $T^{\text{eff}}(s)$.

to an overall enhanced temperature, as detailed in Section 5.3. Lastly, for all N , the fact that cold and hot segments are bonded, creates intermediate regions with temperature smaller than T_h^{eff} but larger than T_c^{eff} . This effect is quantified in Figure 5.15c, where we show the distribution of effective temperatures along the ring's contour $T^{\text{eff}}(s)$.

The discrepancy between the incoming and outgoing heat fluxes in the cold and hot subsystems, results in a non-vanishing entropy production \dot{S} per particle:

$$\dot{S} = \frac{3\gamma}{N} \sum_{s=0}^N \left\langle \frac{T^{\text{eff}}(s)}{T(s)} - 1 \right\rangle, \quad (5.14)$$

where $\langle \dots \rangle$ is the ensemble average over different polymer chains in the system. In Eq. (5.14), we explicitly take into account deviations from $T_{h/c}^{\text{eff}}$ for boundary monomers. The time evolution of \dot{S} for different N is shown in the inset of Figure 5.15c. For $N = 100$, \dot{S} is the highest, indicating the least degree of phase separation. For $N = 200$ and $N = 400$, \dot{S} decreases with time, highlighting further phase separation of hot and cold monomers in these systems. The fact that \dot{S} is the smallest for $N = 400$ further confirms that it is the most phase separated. Finally, the microphase systems is composed of a less dense active phase and more dense passive phase. This is illustrated in Figure 5.16 showing anti-correlation between temperature and density distributions within the simulation box

for $N = 100$ and $N = 400$.

A similar system of linear chains becomes less phase separated than the one of rings. We show this by taking a steady-state ring configuration ($t = 2 \cdot 10^6 \tau$), cutting all chains in the middle of the cold segment, which results in ABA triblocks, and evolving such system further on, as shown in Figure 5.17. We also observe an increase in the entropy production with a lesser difference between the observed effective cold and hot temperatures, in line with reduced degree of phase separation. Interestingly, the chain ends have more frequent contacts with hot regions that results in their higher effective temperature, as seen in Figure 5.17b. Finally, in the two larger systems of cut rings that have a propensity for demixing, the oriented reptation-like motion driven by the hot segment persists. An interesting question that remains is whether such ABA (cold-hot-cold) triblocks can form ordered structures that correspond to the strongly phase segregated limit in equilibrium block copolymers [287]. For active co-polymer rings, which we have now extensively discussed, such behavior is obviously suppressed due to the topological glass formation, which is disabling the rings to potentially segregate more due to the formed topological constraints. From the evolution of the phase separation order parameter for ABA triblocks (see Figure 5.17a) and from the final system states (see inset of Figure 5.17b), we do not observe the formation of ordered structures. The phase separated regions of active monomers rather reminisce of the weakly segregated regime for equilibrium copolymers. It is instructive to compare the present non-equilibrium ABA systems with the equilibrium ones [288]. In particular, for the three ABA systems considered, we find the non-equilibrium incompatibility parameter $\chi = T_h^{\text{eff}}/T_c^{\text{eff}} - 1$ to be 0.42, 0.51, and 0.68 for $N = 100, 200$, and 400 , respectively. Equilibrium diblocks with a similar fraction of A monomers ($f_A = 7/8$) would form a spherical (micellar) phase at comparable values of (equilibrium) χ -parameters for the two bigger N [288]. In our case, however, we do not observe a tendency for such behavior. Note, however, that this comparison is for the illustration only, as it is not guaranteed that the phase diagrams are similar and it is not clear now if active co-polymers can form ordered structures at all.

A mixture of M cold chains of length N_c and M hot chains of length N_h shows a stronger propensity towards phase segregation, as seen in Figure 5.18a. As recently derived by Ilker and Joanny [75], the critical ratio χ^* needed for segregation ($\chi = T_h^{\text{eff}}/T_c^{\text{eff}} - 1$) scales as

$$\chi^* = \alpha \left(N_h^{-1/2} + N_c^{-1/2} \right) \quad (5.15)$$

with chain lengths (note that the right hand side is not squared, as it would be for equilibrium phase separation). This agrees well with earlier simulation results on phase

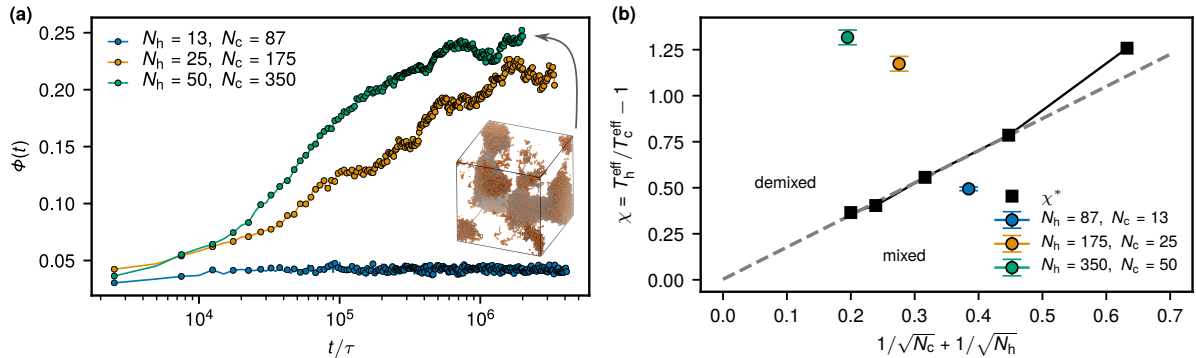


Figure 5.18: Non-equilibrium phase segregation of linear polymer chains of different length. **a**, Time evolution of the phase segregation order parameter for linear polymers mixtures with $M = 1600$ hot chains of length $N_h = N/8$ and $M = 1600$ cold chains of length $N_c = N - N_h$ for $N = 100, 200,$ and 400 . The inset snapshot shows only the hot part of the system with $N = 400$ at late times. **b**, The non-equilibrium incompatibility parameter $\chi = T_h^{\text{eff}}/T_c^{\text{eff}} - 1$ as a function of $N_c^{-1/2} + N_h^{-1/2}$ for the three systems considered (circles). The gray dashed line is the critical line, $\chi^* = \alpha(N_c^{-1/2} + N_h^{-1/2})$ with $\alpha = 1.746 \pm 0.081$, extracted from symmetric linear polymer mixtures in [78]. The five black squares are the measured values of χ^* from [78] for symmetric ($N_h = N_c = 10, 20, 40, 70$ and 100) mixtures of equal number of hot and cold linear chains. The theory [75] supports the numerical results.

separation in symmetric active-passive mixtures [78] (Figure 5.18b). Furthermore, we compared the χ -parameter in the three present cases with the critical line (5.15) with α extracted from [78]. We find that the system with $N_h = 13$ and $N_c = 87$, unlike the other two, lies below the critical line (Figure 5.18b). This further supports that the two systems of active-passive mixtures of linear chains of lengths equivalent to block lengths in our ring systems do phase separate while the shortest one does not, highlighting the role of the non-equilibrium phase separation in the process of formation of the active topological glass.

5.6 Conclusions

In summary, we have considered in detail melts of unknotted and nonconcatenated block co-polymer rings driven out of equilibrium by different thermostats applied to the two different blocks. We focused on systems with different ring length N , while keeping the same length ratio of active blocks $N_h = N/8$ coupled to a heat bath at the temperature $T_h = 3T_c$. We have shown that at early times the segmental and center of mass dynamics is equilibrium-like with an effectively higher temperature. In particular, in the shortest system with $N = 100$ the presence of activity effectively increases the ring's diffusivity, as

given by Eq. (5.18), however, its conformational and threading properties remain essentially unchanged. On the contrary, in the case of $N = 200$ and $N = 400$, already shortly after the activity onset, the hot segments diffuse faster as compared to the relation (5.18). This arises due to a somewhat lower density around them that hallmarks an early stage of non-equilibrium phase separation. The discrepancy in segment dynamics in this case results in an oriented reptation-like regime, where rings are essentially pulled by the hot-segment displacements, which promotes the formation of topological constraints until the motion of rings stops, forming a very slowly relaxing glassy state that is built on topological constraints and activity. The critical diffusivity contrast for the glass formation seems to coincide with the phase separation contrast, but a more detailed study is necessary to determine the relation exactly.

The present non-equilibrium rings, in a sense, represent a hybrid between ring and linear polymers. On the one hand they are strongly influenced by threading constraints, lack ends and, therefore, cannot reptate as linear chains. However, for strong enough temperature discrepancies, the active segments effectively serves as a chain's end, exploring neighboring sites and dragging the rest of the polymer with itself. Such dynamics gives rise to elongated, doubly-folded conformations that locally feature statistics of linear polymers.

Many intriguing questions remain to be answered for the active topological glass. Some of these pertain to other activity models. For instance, in a dilute mixture of self-propelling particles [280] with different propulsion speeds v , densities ρ adjust to equalize the momentum density ρv , not the pressure $p \sim \rho v^2$, across the system. Before the separation, this results in a less dense phase of particles with higher mobility and, therefore, higher pressure, and a more dense phase of lower mobility particles with lower pressure. Similarly, in a segregated two-temperature mixture [78, 79, 73, 75], the phase with particles in contact with a hotter thermostat, locally exerting higher pressure, is more dilute as compared to the phase with colder particles. As the microscopic and phase separation dynamics is different for the thermostat-driven particle systems in comparison to systems with self-propelled particles, it would be interesting to examine the existence of the active topological glass for the latter model. To our knowledge, the non-equilibrium phase separation of polymers composed out of self-propelling particles has not been investigated systematically and certainly it would be interesting to test whether the $N^{-1/2}$ scaling of the incompatibility parameter holds in such systems as well.

Other properties of the active topological glass are yet to be elucidated. In particular, the exact kinetics of the formation of the active topological glass, its response to

external shear stress, as well as the strength of the activity quench on the rings' segments necessary to observe the arrested states are unknown. A proper description of this phenomenon requires understanding of the non-equilibrium *microphase* separation. It is very interesting, for example, whether non-equilibrium active diblock polymers can form ordered structures, such as lamellae, cylinders or micelles, as typical for segregating diblock copolymers in equilibrium [289, 287]. The equilibrium melt of a diblock, or in the case of the cut rings a simple triblock co-polymers of these lengths would form micelles. In our partly-active systems we do not observe these structures, however this might be not only because the glassy state arrests the phase separation, but also the incompatibility parameter and the chain dynamics are different from equilibrium, and, therefore, the phase diagram is yet to be explored. A more complete understanding of these phenomena might further trigger development of active materials with novel properties and shed light on self-organization and dynamics of different biological polymers, in particular chromatin, that are subject to heterogeneous activity along their contours and can feature loopy structure at different length scales. In this context, the main question pertains on the physical mechanism that governs the separation of transcriptionally active (euchromatin) and the passive (heterochromatin) fibers. Since both species exhibit also chemical differences it is difficult to establish if the equilibrium microphase separation or the non-equilibrium analogue plays the pivotal role. Moreover, the potential topoisomerase-induced crossability and the topology of the chromatin fiber affects the accessible morphologies. In this work, we pinpoint the differences in the steady state morphologies (suppressed formation of strongly separated structures) and the segment dynamics (oriented reptation) that can guide the experiments to discern these mechanisms.

5.7 Supplementary Information

5.7.1 Center of mass diffusion of a single chain coupled to two thermostats

Consider a single polymer chain of N monomers out of which N_h are connected to a Langevin thermostat at T_h and N_c monomers are connected to a Langevin thermostat at T_c . The Langevin equation for the i -th monomer is

$$m\dot{\mathbf{v}}_i = -m\gamma\mathbf{v}_i - \nabla_i U + (2m\gamma T_i)^{1/2}\boldsymbol{\eta}_i, \quad (5.16)$$

where γ is the thermostat coupling parameter, m is the monomer's mass, U is the inter-particle interaction potential, each component of $\boldsymbol{\eta}_i$ is a Gaussian random variable satisfying $\langle \eta_{i,\alpha}(t)\eta_{j,\beta}(t') \rangle = \delta_{ij}\delta_{\alpha\beta}\delta(t-t')$. The temperature T_i is T_c or T_h depending on the bead ($k_B = 1$). By summing (5.16) over all monomers, we get the equation for the center of mass velocity, \mathbf{v} :

$$M\dot{\mathbf{v}} = -M\gamma\mathbf{v} + (2M\gamma T_{\text{eff}})^{1/2}\boldsymbol{\eta}, \quad (5.17)$$

where $M = mN$ and $T_{\text{eff}} = (T_c N_c + T_h N_h)/N$. Note that the friction coefficient $M\gamma \equiv m\gamma N$ in (5.17) corresponds to the Rouse model of polymer dynamics [80]. The result (5.17) follows from the facts that $\mathbf{v} = N^{-1}\sum_i^N \mathbf{v}_i$, $\sum_i^N \nabla_i U = 0$, and that the sum of independent Gaussian random variables with unit variance and zero mean is again a Gaussian random variable with zero mean but a larger variance, namely $\sum_i^k \eta_i = k^{1/2}\eta$. This means that the center of mass of the chain moves as a Langevin particle with the effective temperature T_{eff} and effective diffusion coefficient

$$D_{\text{eff}} = \frac{T_{\text{eff}}}{M\gamma} = \frac{T_c N_c + T_h N_h}{m\gamma N^2} = \frac{D_c N_c + D_h N_h}{N^2} \quad (5.18)$$

where D_c and D_h are diffusion coefficients of hot and cold monomers, respectively. Note that the result is independent of the ordering of the monomers.

5.7.2 Shape properties of equilibrium rings and linear chains

In this Appendix we summarize in Table 5.2 the size and shape parameters of equilibrium ring and linear polymer chains in the melt that are mentioned in Section 5.4 of the main paper.

Table 5.2: Size and shape properties of equilibrium ring and linear chains. $\langle R_g^2 \rangle$ is the mean-square radius of gyration, $\langle R_e^2 \rangle$ in the case of rings is the mean-square distance between two monomers separated by the contour length $N/2$, while in the case of linear polymers it is the mean-square end-to-end distance, and λ_i , $i = 1, 2, 3$ are the eigenvalues of the gyration tensor ordered such that $\lambda_1 \geq \lambda_2 \geq \lambda_3$. The value in the parentheses indicates the standard error. The data is adapted from Ref. [50].

Topology	N	$\langle R_g^2 \rangle / \sigma^2$	$\langle R_e^2 \rangle / \sigma^2$	$\langle \lambda_1 \rangle / \langle \lambda_3 \rangle$	$\langle \lambda_2 \rangle / \langle \lambda_3 \rangle$
Ring	100	17.2 (0.4)	50.8 (1.5)	6.4	2.3
	200	30.8 (0.7)	88.8 (2.7)	5.9	2.2
	400	52.9 (1.2)	149.4 (4.8)	5.5	2.1
Linear	100	43.4 (1.2)	263.8 (1.6)	12.9	2.8
	200	88.9 (1.2)	538.9 (1.6)	12.6	2.8
	400	180.8 (1.3)	1095.3 (1.6)	12.3	2.8

Chapter 6

Melts of nonconcatenated rings in spherical confinement

Published: Stanard Mebwe Pachong, Iurii Chubak, Kurt Kremer, and Jan Smrek. Melts of nonconcatenated rings in spherical confinement. *The Journal of Chemical Physics* **153**, 064903 (2020). DOI: 10.1063/5.0013929.¹

Motivated by the chromosomes enclosed in a cell nucleus, we study a spherically confined system of a small number of long unknotted and nonconcatenated polymer rings in a melt and systematically compare it with the bulk results. We find that universal scaling exponents of the bulk system also apply in the confined case, however, certain important differences arise. Firstly, due to confinement effects, the static and threading properties of the rings depend on their radial position within the confining sphere. Secondly, the rings' dynamics is overall subdiffusive but anisotropic along the directions parallel and perpendicular to the sphere's radius. The radial center of mass displacements of the rings are in general much smaller than the angular ones, which is caused by the confinement-induced inhomogeneous radial distribution of the whole rings within the sphere. Finally, we find enhanced contact times between rings as compared to the bulk, which indicates slow and predominantly coordinated pathways of the relaxation of the system.

6.1 Introduction

Nonconcatenated and unknotted ring polymer melts have been fascinating physicists for years and still a complete understanding of their properties is lacking. Static properties

¹Author contributions: S. M. P. and I. C. contributed equally. S. M. P., I. C. and J. S. performed the simulations and data analysis. All authors interpreted the results and wrote the manuscript.

of linear chains in melt are to a good approximation Gaussian [38] and dynamic properties are well-described by tube and reptation theories [290, 291]. However, joining the two ends of each chain, while keeping the created rings unknotted and nonconcatenated, makes it difficult to treat the system with analytical techniques [274]. Therefore, different theoretical models have been developed to tackle the problem under simplifying assumptions, such as treating a ring as in the lattice of fixed obstacles formed by the other rings [41, 42, 43, 89, 40], assuming tree-like conformations [46, 44, 45] or various other [49, 48, 47]. Along these ideas, computer simulations [55, 56, 49, 50, 51, 54, 52, 150] have been an indispensable tool for testing the assumptions and verifying the experimental results [57, 60, 292, 58, 272, 59, 273, 293, 294, 61] under perfectly controlled conditions. This joint effort has proven to be successful and has generated a range of interesting results that highlight how permanent topological constraints of rings impact equilibrium properties, which turned out to be dramatically different from their linear counterparts. In particular, the melt of rings exhibits a power-law stress relaxation modulus with the absence of the rubbery plateau typical for the linear polymer melts [51, 57]. Rings, significantly longer than the entanglement length N_e , adopt compact conformations characterized by the scaling relation $R \sim N^\nu$ between their mean size R and their polymerization degree N with the exponent $\nu = 1/d = 1/3$ where $d = 3$ is the dimension of the space. Furthermore, the probability of two monomers separated by the contour distance s being in mutual proximity in space is also a power-law $P(s) \sim s^{-\gamma}$ with the exponent $\gamma \simeq 1.05 - 1.17$. [50, 52]. The values of the exponents $\nu = 1/3$ and γ close to unity describe the so-called crumpled (fractal) globule ensemble that characterizes melts of long polymers under unknotted and uncrossable topological constraints.

The above-mentioned conformational properties and the corresponding exponent values have sparked further motivation to study these systems in the context of genome folding. The fractal globule model is consistent with the population average ensemble of the chromatin fiber configurations in cell nuclei of higher eukaryotes [295, 90, 87, 85]. In contrast to rings, the chromosomes do have ends, but the rationale behind such connection is the slow chromosomal reptational relaxation mechanism. Due to temporary topological constraints the reptation is much slower than the relevant biological time scales [84]. If the chromatin fiber is mostly uncrossable with very slow or inhibited reptation but otherwise random, the crumpled globule ensemble arises naturally. An account of topological constraints has proven to be useful in finding detailed genome conformations from experimental data [296].

Nevertheless, the above-outlined correspondence is based on the results of bulk simu-

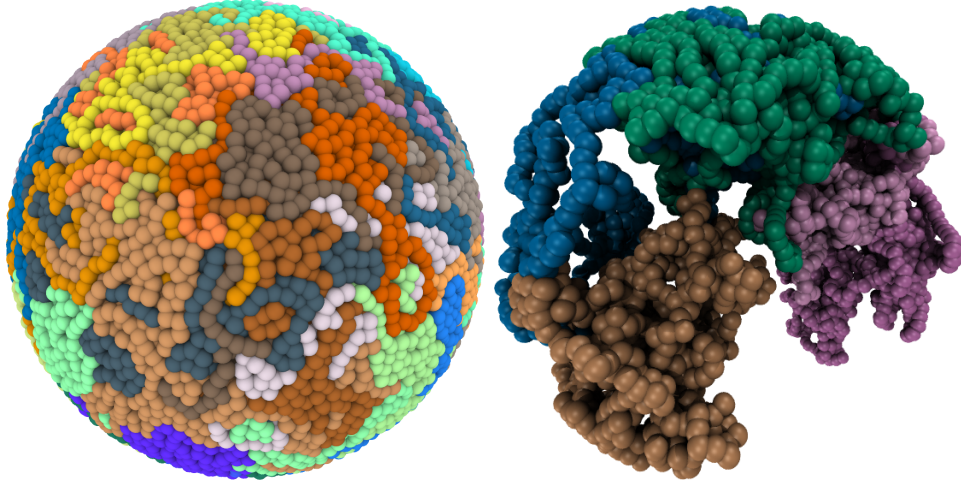


Figure 6.1: System snapshots. Left: The system with $N = 800$ rings. Right: The same system when only five rings are shown. The compact and territorial ring arrangement can be observed.

lations of many rings subject to periodic boundary conditions. Chromatin fiber, on the other hand, is confined in the nucleus and in the case of human diploid cells consists of 46 chromosomes only. Hence, the majority of chromosomes is affected by the confinement geometry and their conformations result from the competition between the confinement and the compression due to topological constraints. In this direction, the work [88] studied a single long ring in cubic confinement and found that the conformations of the ring's subchains are consistent with the crumpled globule picture in terms of $\nu = 1/3$, but found $\gamma \simeq 0.9$. The value of $\gamma < 1$ cannot be a true asymptotic value of the exponent for conformations with $\nu = 1/3$, because $1 \leq \gamma \leq 1 + \nu$ for geometric reasons as detailed in [85, 286]. No dynamics was reported in [88], as the simulations had been carried out using Monte Carlo sampling with non-local moves. Single ring static properties have also been investigated in biaxial confining geometry, which leads to the extension of the ring in the third dimension, markedly different from a linear confined chain [297, 298, 33]. The impact of a cylindrical confinement on the static properties of semiflexible rings has been studied experimentally in [61]. In contrast to the approximate view of the rings as tree-like objects, that work confirms significant inter-ring threadings observed previously in the bulk simulations [63, 65, 71]. The model-independent threading differences between the effective tree-like model [52] and the accurate molecular dynamics simulations have been quantitatively analyzed in [72].

Here, we investigate the impact of confinement, ring topology and a small number of polymer chains on static and dynamic properties of the system. We simulate a spherically confined set of $M = 46$ rings of lengths $N = 200, 400, 800,$ and 1600 with the same model

parameters as in [50] detailed below (see the system snapshot in Figure 6.1). We find and characterize global structural organization of the confined rings as well as differences in their single chain static properties with respect to the bulk results. Additionally, we report mean inter-ring threading properties, which are important for the dynamics of systems with long rings [65, 299, 66, 300, 70, 68, 186, 184]. We find that they are similar to the bulk systems but vary with the rings' radial position within the confining sphere. Finally, we report dynamic properties of the system, which, *inter alia*, exhibit anisotropic mean-squared displacements of the ring's center of mass within the enclosing sphere caused by the confinement-induced density variations.

6.2 Model

We used the well-known polymer model [127], in which the excluded volume interaction between any two monomers is described by a purely repulsive and shifted Lennard-Jones potential

$$U_{\text{LJ}}(r) = \left(4\varepsilon \left[\left(\frac{\sigma}{r} \right)^{12} - \left(\frac{\sigma}{r} \right)^6 \right] + \varepsilon \right) \theta(2^{1/6}\sigma - r) \quad (6.1)$$

with $\theta(x)$ being the Heaviside step function. The polymer bonds were modeled by a finitely extensible nonlinear elastic (FENE) potential

$$U_{\text{FENE}}(r) = -\frac{1}{2}r_{\text{max}}^2 K \log \left[1 - \left(\frac{r}{r_{\text{max}}} \right)^2 \right], \quad (6.2)$$

where $K = 30.0\varepsilon/\sigma^2$ and $r_{\text{max}} = 1.5\sigma$. These parameters make the chains essentially uncrossable. Additionally, we used the angular bending potential

$$U_{\text{angle}} = k_{\theta}(1 - \cos(\theta - \pi)) \quad (6.3)$$

with $k_{\theta} = 1.5\varepsilon$ to induce higher stiffness that corresponds to a lower entanglement length $N_e = 28 \pm 1$ at the studied monomer density $\rho = 0.85\sigma^{-3}$ [301]. The ring lengths therefore correspond to the range from 7 to 57 entanglement lengths. The interaction between monomers and the structureless confining sphere was also purely repulsive and given by $U_{\text{LJ}}(R - r)$, where R is the radius of the sphere, r denotes here the distance between the monomer and the sphere's center, and U_{LJ} is the same as in (6.1). The simulations were performed in the NVT ensemble using the large-scale atomic/molecular massively parallel simulator (LAMMPS) engine [266] using the integration time step $\Delta t = 0.012\tau$, where $\tau = \sigma(m/\varepsilon)^{1/2}$. To maintain the constant temperature $T = 1.0\varepsilon$, all monomers were weakly

coupled to a Langevin thermostat using a coupling constant $\gamma = 1.0\tau^{-1}$. The Langevin thermostat in spherical confinement induces stochastic values of angular momentum that can obscure the real dynamics. To prevent that, we zero the total angular momentum every ten steps by subtracting the appropriate value of the rotational component of the velocity of each monomer. After the subtraction, the velocities are rescaled to maintain the set temperature. Performing this procedure every step is computationally more costly and, as we checked, this has no effect on the dynamics.

6.2.1 System preparation

Initially, a set of M neighboring rings was extracted from the prepared bulk sample of Ref. [50] and placed in the confining sphere that just enclosed all rings. Then, a short (approximately, $10^4\tau$) simulation was run to compress the sphere to reach the target monomer density. The confining sphere radius R is reduced in steps that are much shorter (about 1%) than the equilibrium bond length and thus allow thermalization and equilibration on local scales. The final values of R for each system are listed in Table 6.1. After reaching the final density, the systems have been further equilibrated for over $10^6\tau$ ($N = 200$ and $N = 400$) or $10^7\tau$ ($N = 800$ and $N = 1600$). From Ref. [50] and by computing the radius of gyration autocorrelation function, we know this is long enough to reach equilibrium. Additionally, we checked by computing the linking number between all pairs of rings that during the system preparation the rings had not linked. Only afterwards, production runs were run with a total duration over $2 \cdot 10^7\tau$ for all N considered. Configurations were sampled every 1200τ .

Table 6.1: Size and shape properties of the confined rings. R is the radius of the confining sphere, $\langle R_g^2 \rangle$ is the mean-square radius of gyration, $\langle R_e^2 \rangle$ is the mean-square distance between two monomers separated by the contour length $N/2$, and λ_i , $i = 1, 2, 3$ are the eigenvalues of the gyration tensor ordered such that $\lambda_1 \geq \lambda_2 \geq \lambda_3$. The value in the parentheses indicates the standard error.

N	R/σ	$\langle R_g^2 \rangle / \sigma^2$	$\langle R_e^2 \rangle / \sigma^2$	$\langle \lambda_1 \rangle / \langle \lambda_3 \rangle$	$\langle \lambda_2 \rangle / \langle \lambda_3 \rangle$
200	13.72	26.4(0.2)	73.4(0.6)	5.64(0.04)	2.25(0.01)
400	17.29	44.4(0.7)	120.7(2.5)	5.24(0.08)	2.14(0.02)
800	21.78	73.1(1.1)	195.4(3.8)	4.93(0.10)	2.06(0.01)
1600	27.44	120.5(2.8)	320.2(10.4)	4.89(0.12)	2.03(0.02)

6.3 Results

6.3.1 Conformational properties

We characterize the ring's shape and size by computing the eigenvalues λ_i ($i = 1, 2, 3$, arranged as $\lambda_1 \geq \lambda_2 \geq \lambda_3$) of its gyration tensor:

$$G_{ij} = \frac{1}{N} \sum_{n=1}^N (r_i^{(n)} - R_i)(r_j^{(n)} - R_j), \quad (6.4)$$

where $r_i^{(n)}$ is the i -th component of the position vector $\mathbf{r}^{(n)}$ of the n -th monomer and \mathbf{R} is the center of mass position of the ring. Then, the ring's mean-square radius of gyration $\langle R_g^2 \rangle$ can be computed as $\langle R_g^2 \rangle = \sum_{i=1}^3 \langle \lambda_i \rangle$ with the brackets $\langle \dots \rangle$ standing for the time and ensemble averaging. Certain population average conformational properties are listed in Table 6.1. As shown in Figure 6.2a, both the confined and bulk systems of rings approach the scaling of the radius of gyration with N with exponent $\nu = 1/3$ (see also Supplementary Figure 6.1a for the scaling of eigenvalues and Supplementary Figure 6.2c for $\langle R_g^2 \rangle$ normalized by $N^{2/3}$), however, the confined rings are on average 10-15% smaller than their bulk counterparts (see the inset of Figure 6.2a). This shows that the compression due to topological constraints is "softer" than by the hard walls. Furthermore, as seen in Figure 6.2b, the normalized probability distributions of the rings'

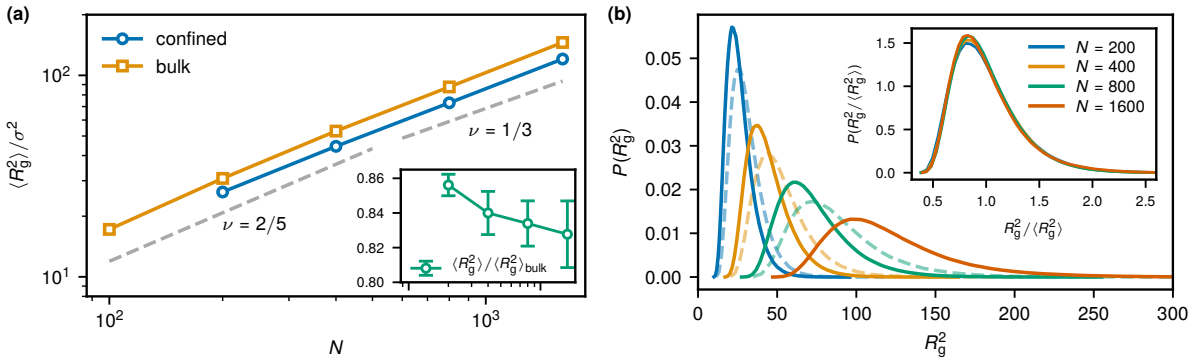


Figure 6.2: Scaling of the confined rings' radius of gyration. **a**, The mean-square radius of gyration $\langle R_g^2 \rangle$ as a function of the ring length N on a log-log scale for the bulk and the confined systems. The bulk data was adapted from Halverson *et al.* [50]. The dashed lines represent power-laws with the marked exponents ν . Inset: Relative decrease of the $\langle R_g^2 \rangle$ in the confined system with respect to the bulk one (x -axis is the same as in the main plot). **b**, Probability distributions of $\langle R_g^2 \rangle$. Dashed curves of the same color correspond to the bulk systems. Inset: The same distributions as in the main plot but scaled by the mean.

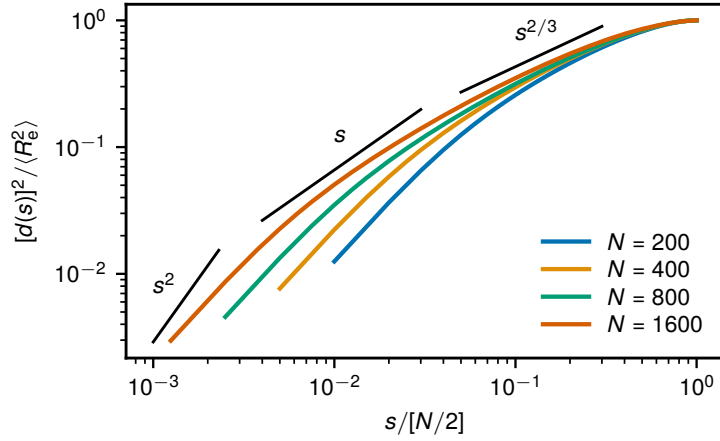


Figure 6.3: Conformational properties of the subchains of the rings. Mean-square internal distance $\langle d^2(s) \rangle$, computed for each segment length s as the squared distance between the endpoints of the segment averaged over the segments position within the ring and averaged over rings. For each N , $\langle d^2(s) \rangle$ is normalized by the ring's mean-square end-to-end distance defined as $\langle R_e^2 \rangle = \langle d^2(N/2) \rangle$.

radius of gyration overlap fairly well for different polymerization degrees.

Additionally, we probed the structure of the subchains of the rings by measuring the mean-squared internal distance $\langle d^2(s) \rangle$ for each segment length s as the squared distance between the endpoints of the segment averaged over the segments position within the ring and averaged over rings. It shows a range of various scaling regimes, from the exponent 2 (straight segments below the persistence length) through 1 for random walk-like configurations to the exponent $2/3$ characterizing the compact fractal structure, as

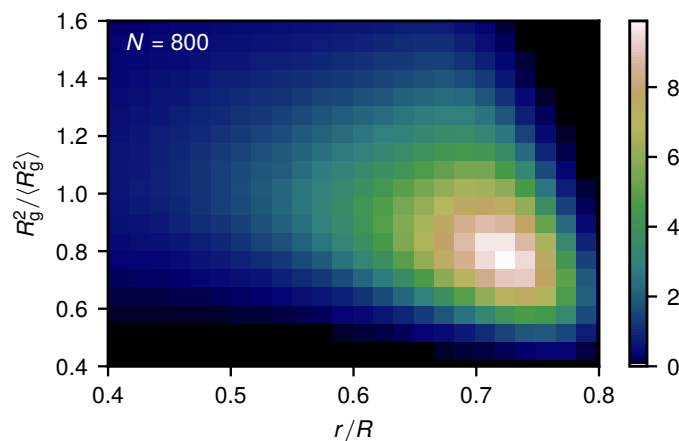


Figure 6.4: Distribution of the rings' radius of gyration within the sphere. Probability density of finding a ring of size R_g with its center of mass located at a distance r from the center of the confining sphere of radius R for the system with $N = 800$. Other systems have very similar distributions (see Supplementary Figure 6.5).

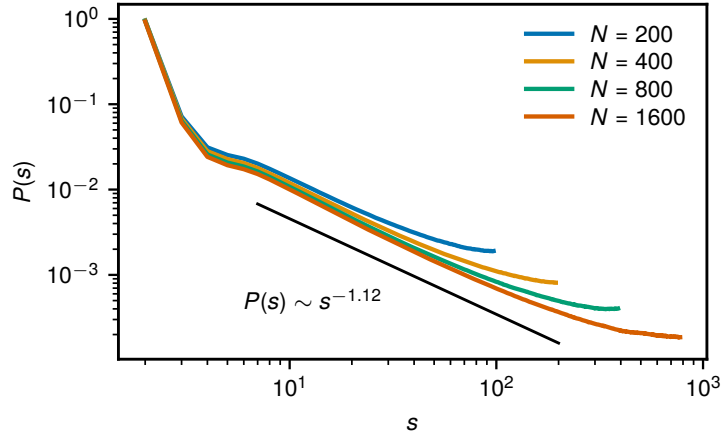


Figure 6.5: Contact probability $P(s)$ as function of the segment length on a log-log scale. The power-law with the marked exponent value is consistent for all ring lengths. For computing $P(s)$, we used $r_c = 2^{1/6}\sigma$ (results for other values of r_c do not differ substantially).

seen in Figure 6.3, in full analogy to the bulk results [50].

As detailed later on in the text, the confinement in this relatively small system of rings causes significant structural rearrangements in comparison to the bulk that, as a consequence, have a pronounced effect on the rings' conformational properties with respect to their radial position within the sphere. In particular, the rings located at the periphery tend to be more compact than the ones positioned more centrally, as shown in Figure 6.4. To quantify this in more detail, we divided the rings into a subset of outer ones, whose center of mass is located at $r > 2R/3$, and inner ones, for which $r < 2R/3$. $2R/3$ is the median of the radial ring's distribution (see Figure 6.8a). We find that the size of outer rings, being closer to the bulk ones, is about 25% larger than the size of the inner ones. Both subsets approach the size scaling with $\nu = 1/3$ for larger N (see Supplementary Figure 6.2). This bias shows that the compression by an external potential and by topological constraints are not equivalent. The external potential is sometimes used to model compact conformations when the topological constraints are neglected [94]. Moreover, from the eigenvalues of the gyration tensor we compute a range of other shape parameters that are reported in the Supplementary Section 6.5. For instance, we observe that the rings located closer to the confining wall are more aspherical and oblate (see Supplementary Figures 6.6 and 6.7).

The contact probability $P(s)$ represents the probability that two monomers of a ring, separated by a contour distance s , are in contact in 3D space. It is computed for each segment length s as the fraction of times the segments endpoints are within a cutoff distance r_c averaged over the segments position within the rings and averaged over rings.

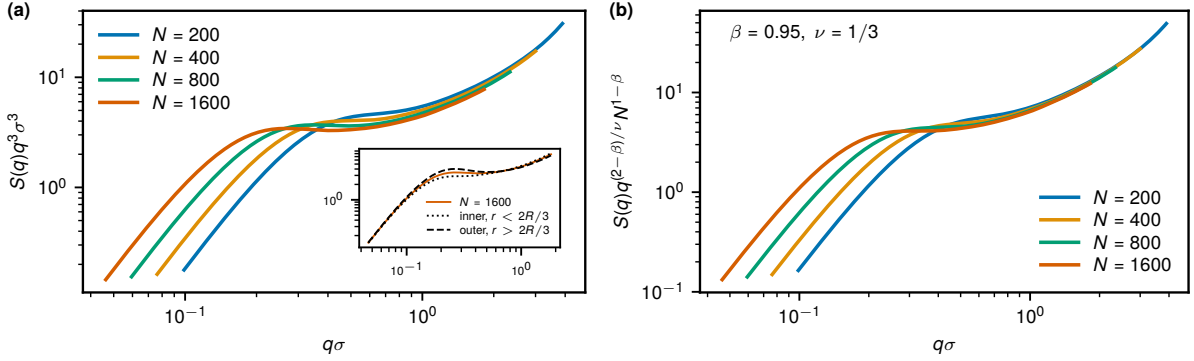


Figure 6.6: The single-chain static structure factor. **a**, $S(q)$ multiplied by q^3 . Inset: $S(q)$ for $N = 1600$ differentiated by the radial position of rings. **b**, $S(q)$ rescaled by $N^{1-\beta}q^{(2-\beta)/\nu}$ motivated by the relation (6.5).

We have found that $P(s)$ remains nearly unaffected by the confinement and, for bigger contour distances, scales as $P(s) \sim s^{-\gamma}$ with the scaling exponent $\gamma = 1.12 \pm 0.02$ (Figure 6.5). The exponent γ is related through the relation $\gamma = 2 - \beta$ to another exponent β characterizing the scaling of the number of surface monomers of a segment $n_{\text{surf}}(s) \sim s^\beta$ [50, 85]. The surface of a segment consists of monomers that neighbor the confining wall or monomers from other segments. For space-filling polymer conformations, that is the ones characterized by $\nu = 1/3$ in three dimensions, the exponent β also gives the fractal dimension d_b of the segment's surface by $d_b = \beta/\nu$. As opposed to the bulk system, the smooth confining wall induces $d_b = 2$ at least for some segments. The fact that we recovered the bulk value of γ suggests that the number of the segments with $d_b = 2$ is inferior to the other segments with higher d_b . Note that this is not a trivial consequence of the fact that the system size scales as $R \sim N^{1/3}$ because the segments aligning the wall smoothly could induce such a smooth surface also in other segments deeper inside the confining volume. We support the analysis by measuring directly the scaling of surface monomers. We find the value of the exponent $\beta = 0.95$ to be the same as in the bulk case [50]. We further looked if the smooth surfaces of the outer rings affect the properties of the single chain structure factor. As shown in Ref. [50], the structure factor of a segment of length s follows

$$S(q) \sim s^{\beta-1}/q^{(2-\beta)/\nu}. \quad (6.5)$$

See also Refs. [302], [303] for a more refined discussion of this result. For $\beta = 1$ and $\nu = 1/3$ the scaling gives $S(q)q^3 \sim \text{const}$, as evinced by the plateau in Figure 6.6a. The inset highlight differences for the inner and outer rings, discriminated by their radial position with respect to $2R/3$ that is the median of the radial distribution (see Figure 6.8a). This difference could be attributed to smaller β of the outer rings due to partly smoother

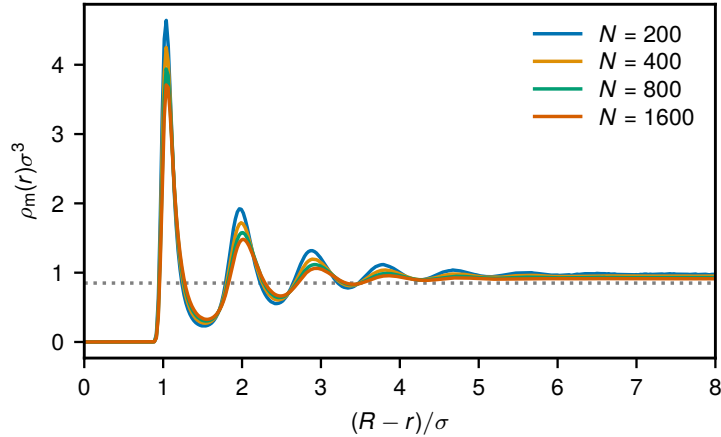


Figure 6.7: Monomer density variations. Radial monomer density profiles as a function of the radial distance from the confining wall for systems with rings of different length N . The dashed gray line indicates the mean monomer density $\rho\sigma^3 = 0.85$.

surface in comparison to the inner rings. It is, however, difficult to confirm this because the inner rings also show a bit more open conformations, and, therefore, smaller effective ν at these scales. Another option is to consider the scaling of the contact probability for the outer and inner rings separately. In contrast, we systematically see the opposite trend with γ being smaller (and, therefore, β higher) for the outer rings. Additionally, only for $N = 200$, γ of the outer rings is below unity and close to 0.9, which is consistent with the findings of [88]. This is the consequence of the conformational change due to the presence of the wall, since it is not found for the inner or bulk rings. More work is necessary to determine the correct scaling of the structure factor and the contact probability for such “hybrid” conformations, where the surface roughness is affected by a smooth interface. Nevertheless, we get a better overall collapse of the structure factor (6.5) when $\beta \simeq 0.95$ is used (Figure 6.6b), similarly to the bulk results [50]. The remaining small inconsistency in the numerical verification of the theoretical relation $\gamma + \beta = 2$ is an open question noticed already for the bulk. A part can be attributed to finite-size scaling corrections [50, 302, 303].

The presence of the confinement induces local monomer density variations in the wall’s proximity (Figure 6.7 and Supplementary Figure 6.4). The small differences between the different systems arise from the different curvature with respect to the local scale. More importantly, the confinement also significantly affects the global ring positioning within the sphere (Figure 6.8a). This shows very little variation for different N . Even at dilute conditions, ring polymers are stronger depletants than linear chains [33] due to enhanced effective repulsion between rings that stems from additional topological uncrossability constraints [32, 275]. At high concentrations, the rings become compact due to topological

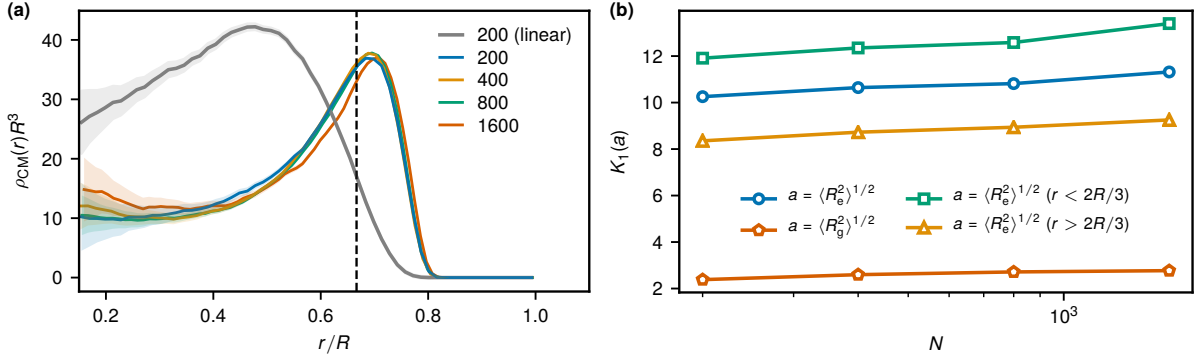


Figure 6.8: Global system order. **a**, Radial density profile (multiplied by R^3) of the ring's center of mass within the confining sphere of radius R . The gray line shows $\rho_{\text{CM}}(r)R^3$ for the melt of linear chains with $N = 200$ at the same mean monomer density $\rho\sigma^3 = 0.85$. In all cases, shaded regions indicate error bars. The dotted black line located at about $r = 2R/3$ indicates the median point of the radial rings' probability distribution within the sphere, $P_{\text{CM}}(r) = 4\pi r^2 \rho_{\text{CM}}(r)$. **b**, The mean number of neighbors $K_1(a)$ of a ring for different threshold a values as a function of N . The green and yellow lines differentiate K_1 by the rings position within the sphere: inner rings are located at $r < 2R/3$, while outer ones at $r > 2R/3$.

interactions and their internal density distribution exhibits a deeper correlation hole in comparison to linear chains [50]. The rings are more compact at the wall and therefore their correlation hole there is even deeper. As a result, the fluid is more structured at the wall, similarly to other effective colloidal particles such as multi-arm stars [304]. In the present system, the positional distribution of the rings' center of mass exhibits a single maximum of the radial distribution at about $2/3$ of the radius from the sphere's center, while the density minimum close to the center of the sphere is much deeper than in the case of the linear chains. This effect arises from the compact conformation of the rings, and their resulting deeper correlation hole. The density profiles collapse well on each other when the length scale is normalized by the confining radius R (see Figure 6.8a), despite the fact that monomer density variations penetrate deeper into the sphere with decreasing N (see Supplementary Figure 6.4). To study relative arrangement of rings within the sphere, we measured their mean number of neighbors $K_1(a)$ (Figure 6.8b). Two rings are considered as neighbors if their centers of mass are located within a certain distance a . The mean values for the longest ring lengths are about 30% lower in comparison to the bulk systems [50]. This is mostly because of the rings located close to the wall ($r > 2R/3$), due to which they are missing about half of the possible neighbors with respect to the bulk. The inner rings ($r < 2R/3$) experience only about a 10% reduction, consistent with the size decrease in this region (Figure 6.2d). Here, we selected the threshold distance

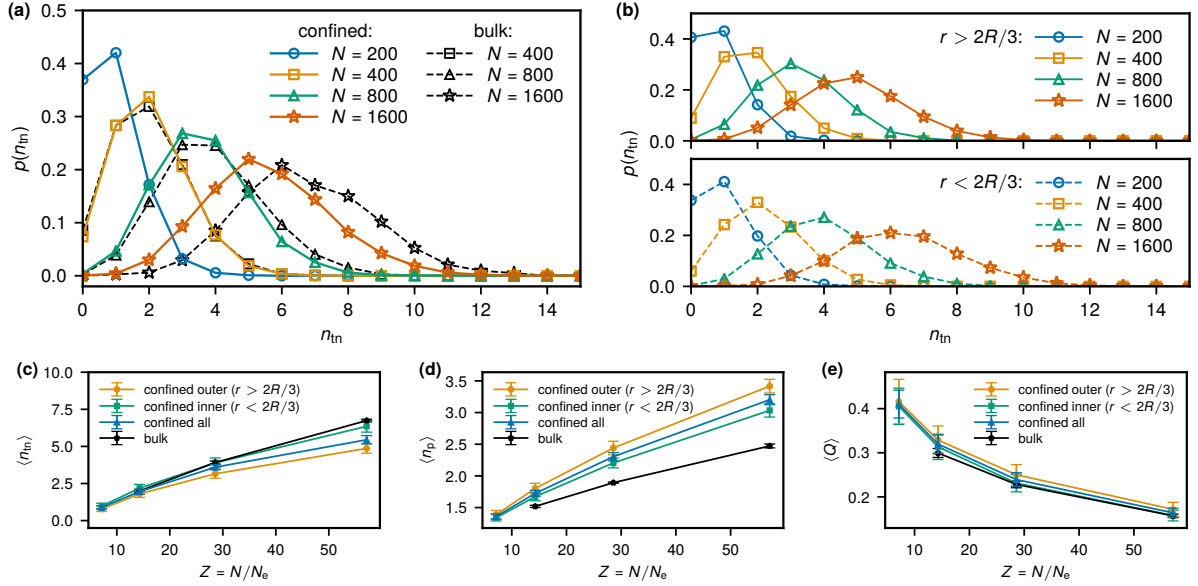


Figure 6.9: Threading statistics. **a**, Probability density of the number of the neighbors threaded by a single ring (see main text for definition); comparison between the confined (colored lines) and bulk (black lines) systems. **b**, Probability density of the number of the neighbors threaded by a single ring that has its center of mass located at $r > 2R/3$ (top panel) and $r < 2R/3$ (bottom panel). **c**, Mean number of threaded neighbors as a function of the ring length, computed from the distributions in the panels **a** and **b**. **d**, Mean number of surface penetrations as a function of N . **e**, Mean values of Q as a function of N (see main text for definition).

$2R/3$ because it represents the median of the ring positional distribution, that is, it is equally likely to find a ring in the regions with $r < 2R/3$ and $r > 2R/3$.

6.3.2 Threading properties

The rings cannot cross and therefore link, but they can thread as one ring pierces through the eye of another ring. The mutual ring threading is an important multi-ring property that due to the topological constraints is believed to strongly affect the dynamics of the system [65, 299, 66, 300, 70, 63, 64, 68, 204, 72, 186, 184]. To analyze threadings, we have used the minimal surface approach. Each ring is considered as a fixed boundary, on which a disc-like surface is spanned and subsequently minimized using a mean-curvature evolution, as detailed in Ref. [72]. Then, the intersection of one ring's contour with another ring's minimal surface represents a threading. This approach has already been used to clarify the extent and the role of threadings in equilibrium bulk systems. Other approaches are also possible [67, 65], however, the minimal surfaces provide an intuitive geometric picture of the inter-ring threading and, moreover, the obtainable threading

statistics is independent of the underlying polymer model [72].

The threadings can be of various depth, that is characterized by the separation length L_{sep} defined as

$$L_{\text{sep}} = \min \left(\sum_{i=\text{even}} L_{t_i}, \sum_{i=\text{odd}} L_{t_i} \right), \quad (6.6)$$

where L_{t_i} is the (threading) length between the i -th and the $(i + 1)$ -th penetrations of the surface (see [63, 72] for details), and its ratio $Q = L_{\text{sep}}/(N - L_{\text{sep}})$ that describes the relative fraction of the threading ring length on the two sides of the threading ring's surface.

In Figure 6.9a, we report the distribution of the number of threaded neighbors for various ring lengths. We consider a ring as threaded if at least one threading length is longer than the entanglement length N_e . We have chosen this definition, because it gives rise to distributions that are independent on the underlying polymer model [72]. The threading properties also vary with the radial position of the ring. In general, the rings closer to the center than $2R/3$ display a higher number of threaded neighbors than the rings at the periphery (Figure 6.9b and 6.9c), being closer to the bulk values. As can be seen in Figure 6.9c, having fewer neighboring rings (Figure 6.8b) in the case of confinement is related to an overall lower number of threaded neighbors in comparison to the bulk case. Interestingly, for ring lengths up to $N = 800$, the distribution of threaded neighbors is consistent with the one found in the bulk (Figure 6.9a), despite the fact that the confined rings have fewer neighbors on average (Figure 6.8b). This is likely because of the fact that smaller rings on average thread much less than the larger ones, having only 1-2 out of 10 neighbors threaded. Furthermore, for $N = 200$ and $N = 400$ even the outer rings have around 8 neighbors, which provides a sufficient number of possibilities to gain 1 or 2 relevant threadings and thus yields marginal differences in the threading statistics. On the other hand, longer rings with $N \geq 800$ that are located close to the wall have a significantly reduced possibilities of potential threadings (it even becomes smaller with higher N as the number of neighbors grows with N rather very slowly) and, therefore, we observe systematically less threaded neighbors for outer rings, while the statistics for inner rings is not affected substantially. In Figure 6.9d, we report the number of surface piercings, that is how many times a threading ring pierces the surface of the threaded ring. We consider only piercings that create threading longer than N_e (see [72]). Interestingly, while n_{tn} is on average lower in confinement in comparison to bulk, the opposite trend holds for n_p , which suggests that the total piercing number $n_{\text{tn}}n_p$ could be a relevant quantity characterizing the free energy penalty for opening the tree-like ring

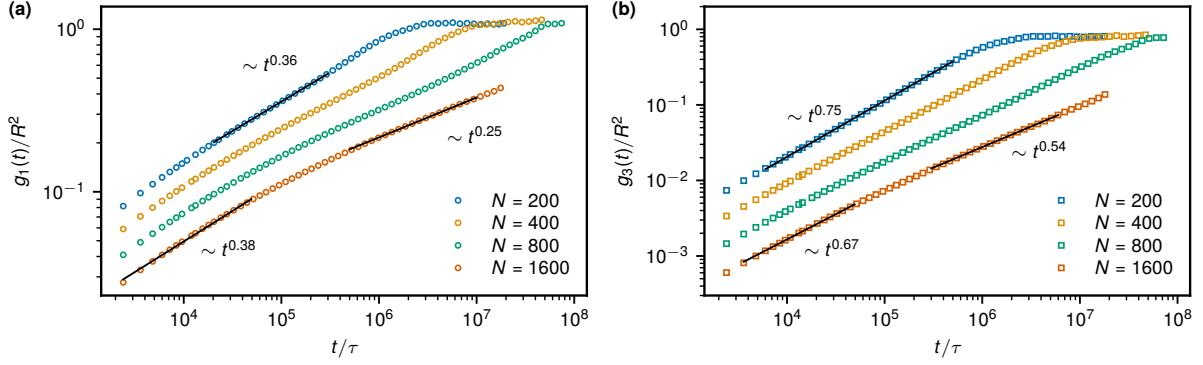


Figure 6.10: Mean-square displacements. The mean-square displacements of monomers, g_1 , (a) and of the rings' center of mass, g_3 , (b) as a function of the lag time t . The solid black lines indicate intermediate scaling regimes.

conformations. Initially, n_{tn} grows linearly with N , consistent with findings in Ref. [64], but saturates for longer rings due to the compact conformations and finite number of neighbors [63]. For longer rings, n_{tn} and n_p grow sub-linearly, but their product scales with N . In summary, the threading statistics of rings in confinement is mainly affected by a decreased threading capability of those rings located closer to the wall, as well as by a generally slightly smaller number of neighboring polymer chains. Finally, we find that the distribution of Q exhibits the same universal behavior as in the bulk with an effective scaling $p(Q) \sim Q^{-1.35}$ [72]. The experimentally measured threading in a system of confined semi-flexible rings [61] also exhibits roughly linear scaling of minimal surface area with ring length and number of piercings of a minimal surface with its area. However, note that rings in that work are only up to two Kuhn segments long and the estimate of the entanglement length of that system is much shorter than the persistence length in contrast to simulations presented here. We, therefore, do not attempt for a detailed quantitative comparison.

6.3.3 Dynamics

We characterize the dynamics of the rings in terms of the mean-square displacements of individual monomers of a chain, g_1 , and the rings' center of mass, g_3 , as a function of the lag time t :

$$g_1(t) = \frac{1}{T-t} \int_0^{T-t} \frac{1}{N} \sum_i^N \langle [\mathbf{r}_i(t'+t) - \mathbf{r}_i(t')]^2 \rangle dt' \quad (6.7)$$

$$g_3(t) = \frac{1}{T-t} \int_0^{T-t} \langle [\mathbf{R}(t'+t) - \mathbf{R}(t')]^2 \rangle dt' \quad (6.8)$$

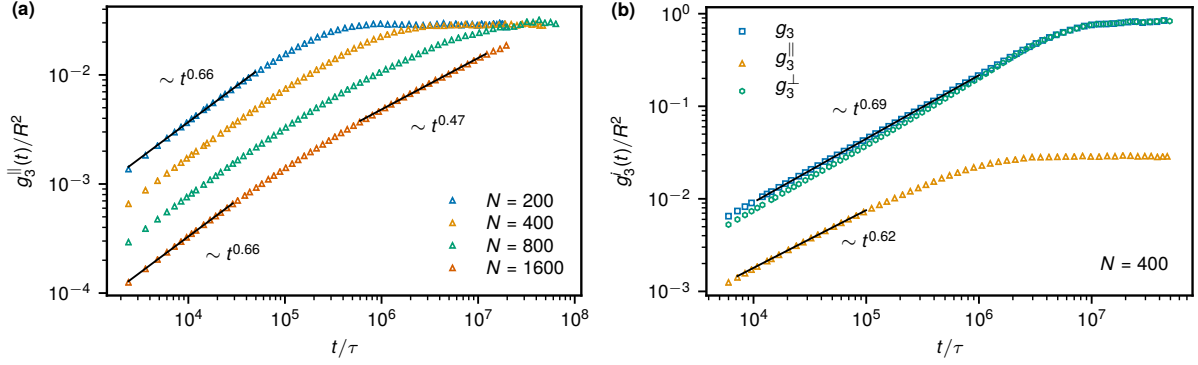


Figure 6.11: Anisotropic dynamics within the confining sphere. **a**, Radial components of the mean-square displacements for different N . **b**, Comparison between different components of g_3 for $N = 400$. Similar results are found for other N (not shown). The solid black lines indicate intermediate scaling regimes.

where $\mathbf{r}_i(t')$ is the position of the i -th monomer belonging to a single ring and $\mathbf{R}(t')$ is the position of the center of mass of a ring at a time t' with respect to the center of mass of the whole system at that time, and T is the total simulation time. The angle brackets in Eqs. (6.7) and (6.8) $\langle \dots \rangle$ stand for averaging over the ensemble of rings. As shown in Figure 6.10, the early and intermediate time dynamics is consistent with the bulk results. g_1 exhibits a subdiffusive regime, $g_1(t) \sim t^\alpha$, with the exponent α below 0.4 at early times that later even slows down to around 0.25 for the longest rings in agreement with the bulk values [51]. $g_3(t)$ shows exponents ranging from 0.75 for smaller rings with $N = 200$ to approximately 0.67 for the bigger ones ($N = 1600$), in full analogy with those observed in the bulk systems (0.75 for $N = 200$ to 0.65 for $N = 1600$) [50]. At the time scale when the bulk system crosses over to diffusion (e.g., $2 \cdot 10^6 \tau$ for $N = 800$), the confined system still subdiffuses. This is because such crossover happens at the scale of $2R_g$ that is comparable to the system size (about $2.5R_g$, as seen in Table 6.1). Here, in contrast, g_3 plateaus due to the confinement and no intermediate diffusive regime could be observed.

To get a better understanding of the dynamics of the rings within the confining sphere, we separately analyzed the mean-square displacements of the rings' center of mass along the radial direction and perpendicular to it, $g_3^{\parallel}(t)$ and $g_3^{\perp}(t)$, respectively, as a function of the lag time t . To do so, for a time interval $[t', t' + t]$ we first evaluated the ring's displacement along the radial direction, $\delta^{\parallel}(t)$ and perpendicular to it, $\delta^{\perp}(t)$:

$$\delta^{\parallel}(t, t') = ((R(t' + t) - R(t')) \hat{\mathbf{R}}(t' + t)), \quad (6.9)$$

$$\delta^{\perp}(t, t') = \mathbf{R}(t' + t) - \mathbf{R}(t') - \delta^{\parallel}(t), \quad (6.10)$$

where $R(t')$ is the magnitude the position vector \mathbf{R} at the time t' assuming that \mathbf{R} is

measured from the sphere's center, and $\hat{\mathbf{R}} = \mathbf{R}/R$. Consequently, for a fixed lag time t , the displacements in Eq. (6.9) are squared and averaged over time and over different rings:

$$g_3^{\parallel/\perp}(t) = \frac{1}{T-t} \int_0^{T-t} \left\langle [\boldsymbol{\delta}^{\parallel/\perp}(t, t')]^2 \right\rangle dt'. \quad (6.11)$$

Note that with such definition $\boldsymbol{\delta}^\perp(t)$ is a sum of two orthogonal displacements along the ϕ - and θ -directions in the spherical coordinate system and, therefore,

$$g_3(t) = g_3^\parallel(t) + g_3^\perp(t). \quad (6.12)$$

Also note that we do not track the cumulative values of the angular components, but consider the values of the angles to $\theta \in [0, \pi]$, $\phi \in [0, 2\pi]$, and, therefore the g_3^\perp is bounded too. As shown in Figure 6.11, the spherical confinement generates an anisotropic behavior of the rings' motion along the different directions. Although both directions exhibit very similar subdiffusive exponents, the angular component dominates $g_3^\perp(t)$ over the radial component $g_3^\parallel(t)$ by almost an order of magnitude. This emerges due to the inhomogeneous radial density distribution (Figure 6.8a). Similar effect, but about factor of two weaker can be observed for linear chains (not shown), where the density anisotropy is weaker due to their shallower correlation hole [50]. Furthermore, we find that the radial (Figure 6.11a) as well as the total (Figure 6.10b) mean-square displacements can be brought on top of each other at longer times, if the time axis is multiplied by $N^{-2.4 \pm 0.1}$, which corresponds to the scaling of the ring's diffusion coefficient in the bulk melts $D \sim N^{-2.3 \pm 0.1}$ [51], as show in Figure 6.12.

We further quantify the dynamics in terms of the relaxation of different quantities. Firstly, we consider the structural relaxation proposed recently in [305] to quantify the effect of threadings in ring-linear blends. The relaxation is in terms of the terminal autocorrelation function (TACF) $\langle \mathbf{u}(t) \cdot \mathbf{u}(0) \rangle$, where $\mathbf{u}(t)$ is the unit vector connecting two monomers contourwise $N/2$ apart and the average is performed over all such possible monomers within rings, over different chains and time. The resulting function is shown in Figure 6.13a with the inset showing the scaling of the corresponding relaxation time with N . The exponent 2.4 is comparable to the one obtained in the bulk (2.2) [51] for a similar structural relaxation quantity computed as the autocorrelation of a vector $\mathbf{c} = \mathbf{u}_1 \times \mathbf{u}_2$, where the two vectors are connecting monomers 0 to $N/2$ and $N/4$ to $3N/4$ respectively. In Figure 6.13b, we compare the TACF of rings that are located close to the confining wall to those in the sphere's interior. Such TACF was averaged over time periods when a ring is continuously residing in the respective region. We find that the structural relaxation

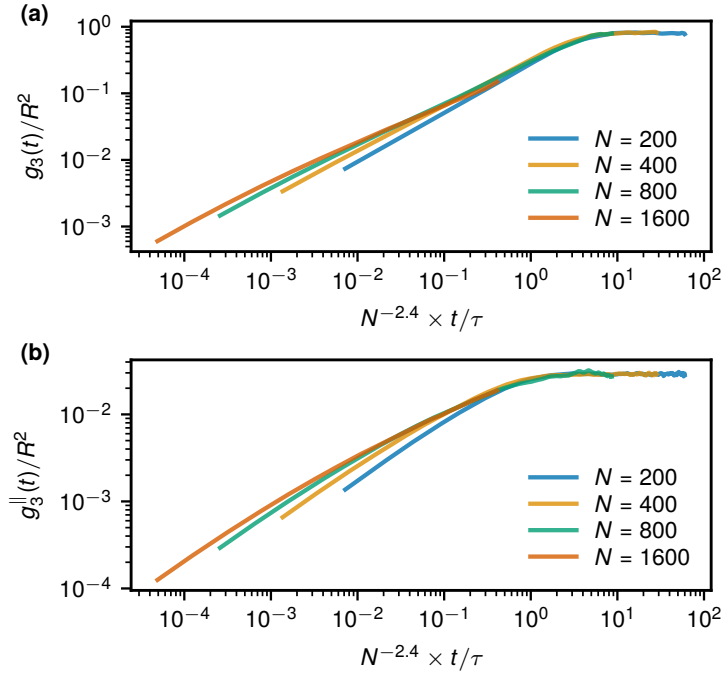


Figure 6.12: Rescaled mean-square displacements. Total $g_3(t)$ (a) and radial $g_3^{\parallel}(t)$ (b) mean-square displacements of the rings with the vertical axis divided by the squared enclosing sphere’s radius R^2 and the horizontal axis multiplied by $N^{-2.4}$, which describes the scaling of ring’s diffusion coefficient with N , $D \sim N^{2.3 \pm 0.1}$, in equivalent bulk systems [51].

of inner rings is inhibited in comparison to the outer ones, which can be attributed to more pronounced threading in the former region. Unfortunately, due to the lack of long time statistics for the region-resolved TACF, we were not able to accurately estimate the relaxation times in the two regions separately and verify their scaling with N .

Additionally, we quantify the dynamics of the neighbor exchange. We compute the two-point contact correlation function $\hat{\chi}_c(t) = \langle n_{ij}(t_0)n_{ij}(t_0+t) \rangle_{t_0,ij}$, where $n_{ij}(t)$ is unity if ring i is a neighbor of ring j in the sense of $K_1(a)$ with $a = R_e$, and zero otherwise (see Figure 6.8b). The correlation $\hat{\chi}_c$ is non-vanishing at long times because in a finite system there is a probability p_n that any two rings are neighbors at any time is given by the average number of neighbors of a ring divided by all the possible number of neighbors. Therefore, $p_n = \langle \sum_j n_{ij}(t) \rangle_{t,i} / (M - 1)$, where the mean number of neighbors of a ring i is averaged over i and time. In Figure 6.14a, we plot $\chi_c(t) = \hat{\chi}_c(t) - p_n$ as a function of time. Furthermore, from $\chi_c(t)$ we extract the mean exchange time τ_{ex} given by $\tau_{\text{ex}} = \int \chi_c(t) dt$. The exchange time τ_{ex} scales with N with the exponent $\simeq 2.7 \pm 0.1$, which is consistent with the exponent found for the relaxation time in the bulk systems [51, 45]. The tails of $\chi_c(t)$ can be accurately fit with a stretched exponential $\exp\left(- (t/t_0)^\beta\right)$ with $\beta = 0.6 - 0.8$

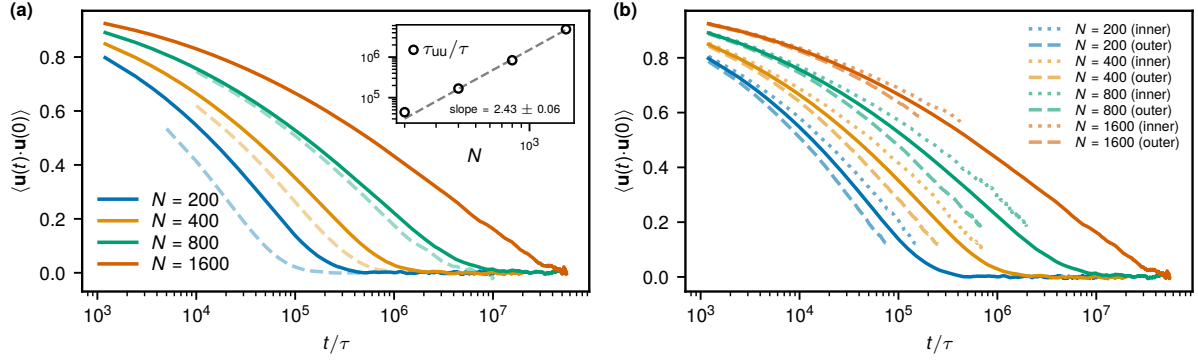


Figure 6.13: Terminal autocorrelation functions. **a**, TACF of confined rings (solid lines) compared to equivalent bulk systems (dashed lines). Inset: the relaxation time τ_{uu} computed as $\tau_{uu} = \int \langle \mathbf{u}(t) \cdot \mathbf{u}(0) \rangle dt$ as a function of N on a log-log scale. **b**, TACF of confined rings averaged over all chains in the system (solid lines) and over those that are located in the inner shell with their center of mass position $r < 2R/3$ (dotted lines) and in the outer shell with $r > 2R/3$ (dashed lines).

(smaller values correspond to larger N). The significant prefactor in this scaling relation makes the exchange time about one order of magnitude larger than the diffusion time in bulk [51]. This behavior arises not only from a slow neighbor exchange dynamics but also from the finite volume of the enclosing sphere, in which the rings frequently meet repeatedly. Such behavior is expected as χ_c is more related to the diffusional properties rather than the structural relaxation. Interestingly, χ_c of the bulk system (dashed line in 6.14a) decays to zero slightly faster for the confined case, and its shape is different at early times suggesting a different process of χ_c relaxation in the two cases. This is illustrated in Figure 6.14b, in which the distribution of contact times $P_c(t)$ is plotted for the bulk case with $N = 200$ and for different N in the confined case. Note that $P_c(t) \sim t^{\alpha/2-2}$ is connected to the distribution of the return times of a random walker with the subdiffusive exponent α [186, 306, 307] characterizing the dynamics of rings. This agrees well with the subdiffusion of the rings with $\alpha \in [0.5, 0.75]$. The presence of the wall enhances the contact time in the confined case in comparison to bulk, as is clear from the later decay of the P_c (blue solid and dashed lines in 6.14b). This explains also the different χ relaxation process. The mean contact time $\langle \tau_c \rangle$ scaling as $\langle \tau_c \rangle \sim N^{0.55}$ grows more slowly with N in comparison to τ_{uu} and τ_{ex} . The scaling exponent of τ_c with N is a consequence of the rings' subdiffusion. The average contact time based on the distribution above is $\langle \tau_c \rangle \sim \lambda^{\alpha/2}$, where λ is a typical time scale characterizing the power-law regime. Then, λ must be proportional to typical relaxation times for rings. The relaxation time scales as $\lambda \sim N^x$ with x being $\simeq 2.4$ in case of the structural and 2.7 for the diffusional relaxation mechanism, both of which can contribute to the contact

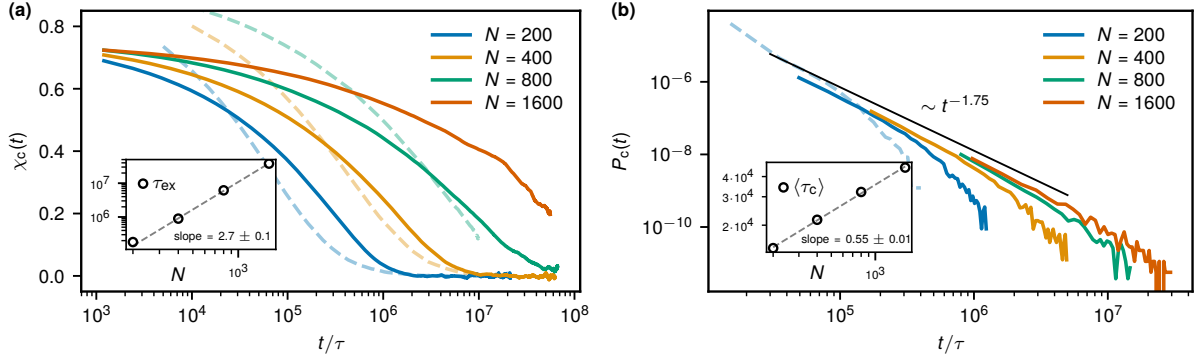


Figure 6.14: Neighbor exchange dynamics. **a**, The neighbor exchange correlation function $\chi_c(t)$ as a function of time for different ring lengths N . Inset: the mean neighbor exchange time τ_{ex} defined as $\tau_{\text{ex}} = \int \chi_c(t) dt$ as function of N in log-log scale. To estimate τ_{ex} for $N = 1600$, the tail of $\chi_c(t)$ was extended with a stretched exponential fit. **b**, Contact duration distribution P_c for different ring lengths N . The solid black line highlights the scaling regime $P_c(t) \sim t^{-1.75 \pm 0.01}$. Inset: the mean contact time $\langle \tau_c \rangle$ as function of N on a log-log scale. The dashed lines in **a** and **b** of the respective color corresponds to the bulk systems of rings.

breaking events. This gives $\langle \tau_c \rangle \sim N^{x\alpha/2}$ i.e. exponent somewhat above α in either case in agreement with our findings.

Similarly to the neighbor exchange, we analyzed the threading dynamics, only for the two shorter systems. We compute the two-point threading correlation as $\hat{\chi}_{\text{th}}(t) = \langle n_{ij}(t_0)n_{ij}(t_0 + t) \rangle_{t_0, ij}$, where now the indicator function $n_{ij}(t)$ is unity if ring i threads ring j with $L_{\text{sep}} > N_e$ and zero otherwise. In full analogy to the neighbor correlation, the $\hat{\chi}_{\text{th}}$ is non-vanishing at long times. The probability p_{th} that any two rings are threading at any time is given by the average number of threaded neighbors of a ring n_{tn} divided by all the possible number of neighbors $p_{\text{th}} = n_{\text{tn}}/(M - 1)$. We plot the threading correlation in Figure 6.15 and, as the inset, we show the distribution of the threading duration $P_{\text{th}}(t)$. We find that the longest threading durations are almost an order of magnitude shorter than the relaxation of the threading correlations and this discrepancy is larger for the longer rings. This could mean that although the duration of each threading is relatively short, it requires a number of correlated threading events to be relaxed in order for a ring to move. Consistent with that is the fact that the threading duration agrees with the structural relaxation (when terminal autocorrelation functions vanish in Figure 6.13), and additionally, the neighbor exchange dynamics (χ_c) agrees with the threading de-correlation. The former fact contrasts with the bulk findings in Ref. [64], where the structural relaxation is faster than the threading. However, here we only take into account threadings that are deeper than the entanglement length. When threadings

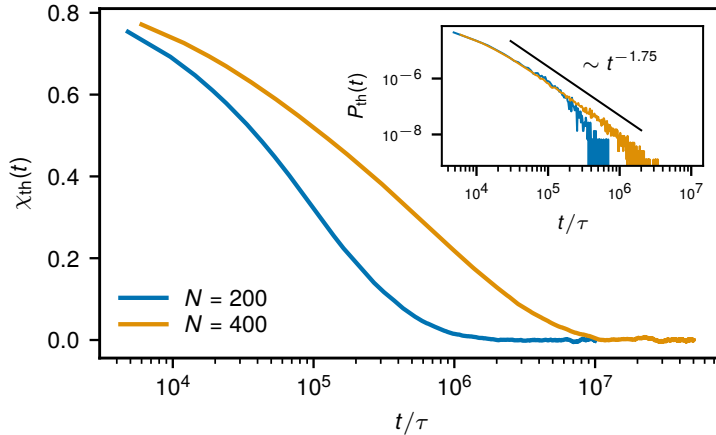


Figure 6.15: Threading exchange dynamics. The two time-points threading correlator $\chi_{\text{th}}(t)$ for the two systems with $N = 200$ and $N = 400$. Inset: the distribution of threading times $P_{\text{th}}(t)$ for these systems. The solid black line highlights the scaling regime $P_{\text{th}}(t) \sim t^{-1.75 \pm 0.01}$.

of any depth are considered, we find that the threading state can be maintained by the short threadings for longer time. However, the short threadings do not have impact on the final de-correlation time, which is governed by the deep threadings (see Supplementary Section 6.5 and Supplementary Figure 6.3).

Although the view of the ring relaxation being governed by the correlated sequence of unthreading events is plausible, we cannot rule out that the threading is only a consequence of spatial proximity that is maintained by another mechanism. Specifically, the rings form compact structures with a pronounced correlation hole. As such, rings could be viewed on the scale of R_g as soft colloids that, especially in confined space, might require collective mode of relaxation, similarly to systems approaching a glass transition. In other words, for a ring to move, other have to rearrange to make space for it which prolongs the exchange times. The confinement induces an effectively higher density in the center of the volume interior (Supplementary Figure 6.4) and also restricts the possible motion directions at the periphery. Both these effects would enhance the relaxation times in comparison to the bulk in agreement with our observation (Figure 6.14a).

6.4 Discussion and conclusions

We have shown that a small number of spherically confined, unknotted and non-concatenated rings in melt maintain the universal features of the main static and dynamic characteristics known from the bulk systems [50, 51]. Therefore, the connection between the conformational properties of the topologically constrained polymers and the chromatin of higher

eukaryotes “survives” the enclosure of the former in the confinement.

The ring conformations at the boundary display γ close to unity despite the fact that a part of the ring has smooth surface ($d_b = 2$) and as such would be represented by the exponent $\gamma = 2 - (2/3) = 1.33$. This means that the conformations of the confined rings are from the geometrical perspective well represented by space-filling curves that have smooth outer, but fractal inner boundary. Examples of such space-filling curves have been constructed in [286, 85]. Further work is necessary to unambiguously determine the structure factor and contact probability scaling properties for these “hybrid” space-filling conformations. We hypothesize that this could be relevant when interpreting the scaling of the contact probabilities within different chromatin (epigenomic) domains. If the domain formation is due to different interaction energies (proposed, e.g., in Ref. [308]), the domain boundaries would be governed by minimizing the interfacial area which would lead to a smooth interface affecting the contact probability of the segment similarly to a smooth confining wall. In this context, very interesting would be the comparison of our structural data with the scattering experiments performed on chromatin at the periphery of the nucleus. Indeed, such a system is much more complex than the present simple coarse-grained model and, therefore, the results would also depend on the nature of the interaction of the chromatin with the nuclear lamina. In contrast to our simulations here, recent results conjecture this interaction to be attractive in most cells, however, the rod photoreceptors of nocturnal mammals do not exhibit this attraction and therefore might be good candidates for the tests of our results [249].

Other differences between the bulk and confined case include radially-dependent conformational and threading properties of the rings as well as the anisotropic dynamics along the directions parallel and perpendicular to the sphere’s radius. These effects arise from the confinement-induced radial density variations of the rings as well as their compact structure at melt densities. Despite the threading differences with respect to the bulk, the confinement does not reduce the threading to the extent comparable to the effective tree-like model [52, 72]. Therefore, the question of the construction of an effective model of equilibrated ring melt remains open not only in the bulk [72], but also in the confinement.

The confinement in the present work represents one of many recently proposed mechanisms affecting the phase-space of the uncrossable polymers, such as more complex topology [186], controlled concatenation [181, 180, 179, 183, 309], supercoiling [310] or activity [184]. Considering the effects of these perturbations brings the system closer to a practical material or biological situation, but also improves our understanding of the unperturbed topologically constrained matter. Considering the activity, recently it has been shown

that a bulk system of nonconcatenated rings with active segments can lead to a very slowly relaxing state, the so-called active topological glass [184]. The relaxation is slowed down by the increased number of threadings and their spatial and temporal extent that dramatically differs from the one found in equilibrium ring melts. Such a system possess many similarities with the chromatin of living cells, such as the slow relaxation, dynamic heterogeneity and polymer size dependence on the level of the activity. The questions whether such state is possible to create in a confined geometry and whether it is relevant for biological conditions, remain open. The results of the present work, however, provide the reference equilibrium values of the observables that the system would originate from.

6.5 Supplementary Information

6.5.1 Additional shape parameters

First, for each ring we obtain the eigenvalues λ_1, λ_2 and λ_3 ($\lambda_1 \geq \lambda_2 \geq \lambda_3$) of the gyration tensor

$$G_{ij} = \frac{1}{N} \sum_{k=1}^N r_i^{(k)} r_j^{(k)}, \quad (6.13)$$

where $r_i^{(k)}$ is the i -th component of the position vector $\mathbf{r}^{(k)}$ of the k -th monomer in the ring in its center of mass frame. Using the latter, we compute the invariants

$$I_1 = \lambda_1 + \lambda_2 + \lambda_3, \quad (6.14)$$

$$I_2 = \lambda_1 \lambda_2 + \lambda_1 \lambda_3 + \lambda_2 \lambda_3, \quad (6.15)$$

where $I_1 = R_g^2$. Using the eigenvalues and the two above-defined invariants, we can define dimensionless asphericity, δ^* , and prolateness, S^* , parameters:

$$\delta^* = 1 - 3\langle I_2/I_1^2 \rangle, \quad (6.16)$$

$$S^* = \langle (3\lambda_1 - I_1)(3\lambda_2 - I_1)(3\lambda_3 - I_1)/I_1^3 \rangle, \quad (6.17)$$

where $\langle \dots \rangle$ denotes an average over rings and over time. Note that $\delta^* \in [0, 1]$ with 0 corresponding to completely spherical conformations and $S^* \in [-0.25, 2]$ acquiring negative values for oblate conformations and positive for prolate ones [35].

Squared magnetic ring radius of each ring is defined as in [53] by

$$R_m^2 = |\mathbf{A}|/\pi, \quad (6.18)$$

where

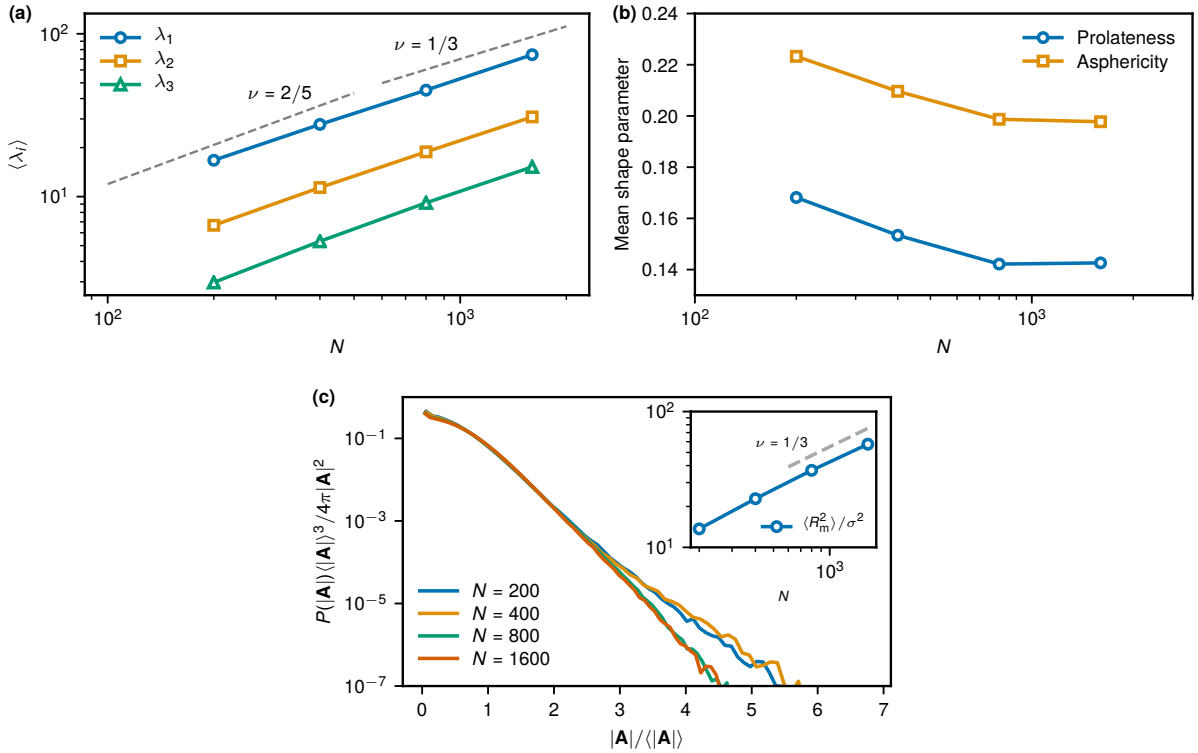
$$\mathbf{A} = \frac{1}{2} \sum_{k=1}^N \mathbf{r}^{(k)} \times \mathbf{r}^{(k+1)}. \quad (6.19)$$

is the rings' enclosed area.

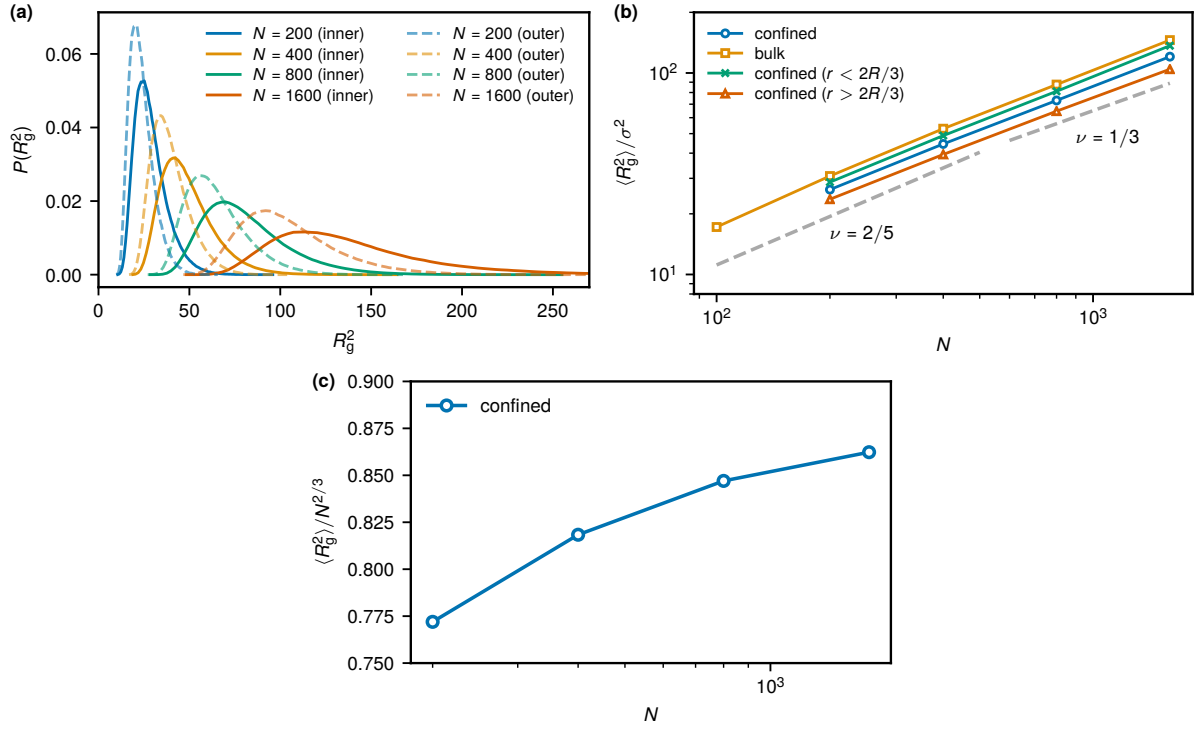
6.5.2 Threading dynamics details

In Figure 6.3 we show the threading time correlation function and the threading duration distributions when threadings of any depths ($L_{\text{sep}} > 0$) are considered. The threading duration distribution spans a slightly greater range, but the de-correlation time is exactly

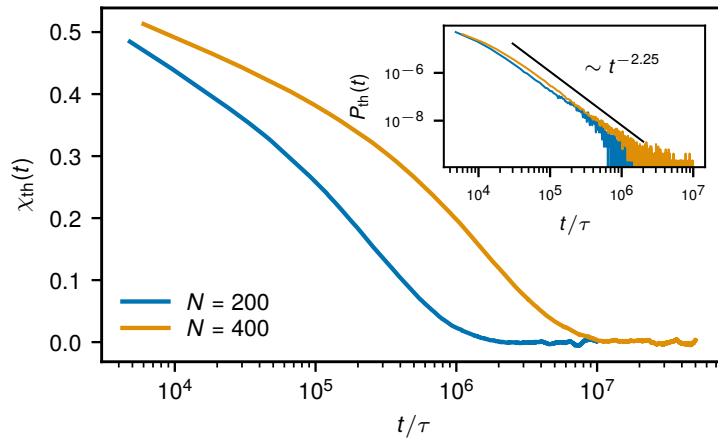
the same as if only sufficiently deep threadings are taken into account (Figure 6.15). This means, when the rings are closely associated, the threading state can be maintained by short threadings longer, however, the short threadings do not have impact on the final de-correlation time, which is governed by the deep threadings.



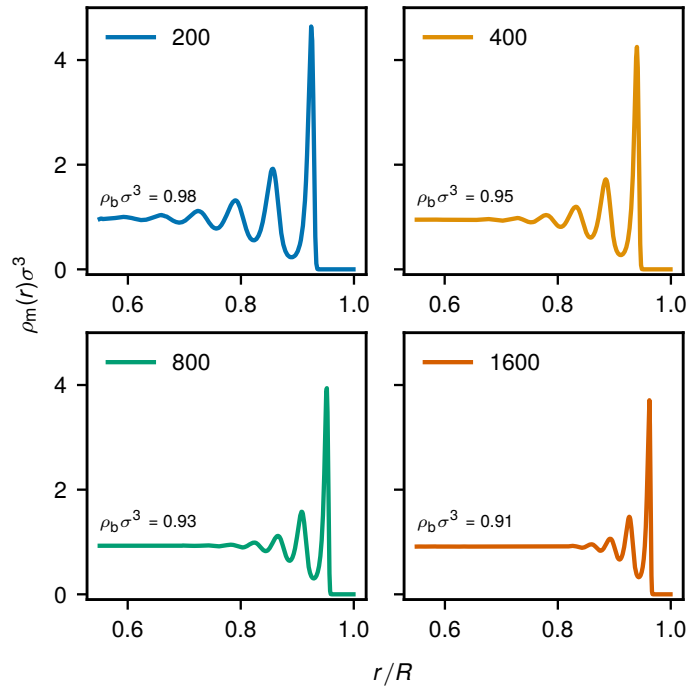
Supplementary Figure 6.1: Additional conformational properties of the confined rings. **a**, Scaling of the three mean eigenvalues of the gyration tensor. The dashed lines represent power-laws with the marked exponents ν . **b**, Scaling of the mean prolateness, $\langle S^* \rangle$, and asphericity, $\langle \delta^* \rangle$, with N . **c**, Distribution of the enclosed area as computed from Eq. 6.19. Inset: squared magnetic radius (Eq. 6.18) averaged over rings and time as a function of the ring length N .



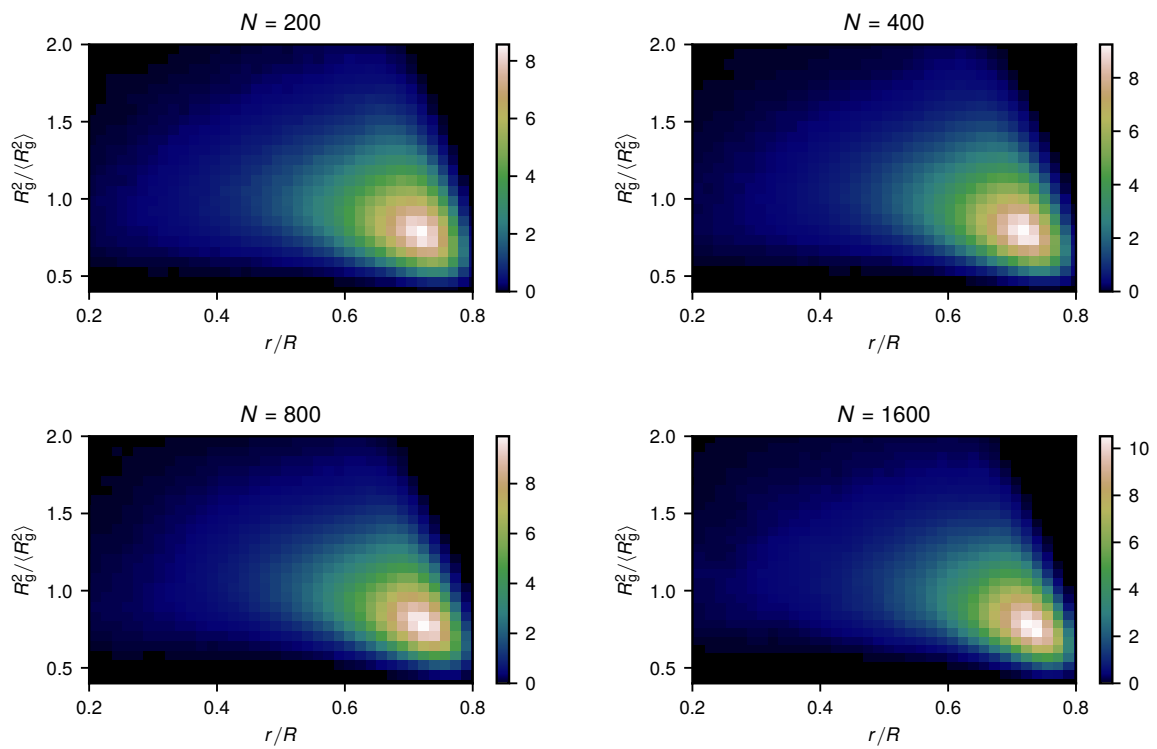
Supplementary Figure 6.2: Additional scaling properties. **a**, Distribution of R_g^2 for rings in the inner shell with their center of mass located at $r < 2R/3$ (solid lines) and in the outer shell with $r > 2R/3$ (dashed lines). **b**, Scaling of $\langle R_g^2 \rangle$ in the two shells in comparison to the average over all rings in the confined systems as well as in the bulk. **c**, $\langle R_g^2 \rangle$ divided by $N^{2/3}$ for confined rings to indicate their cross-over to asymptotic scaling with $\nu = 1/3$.



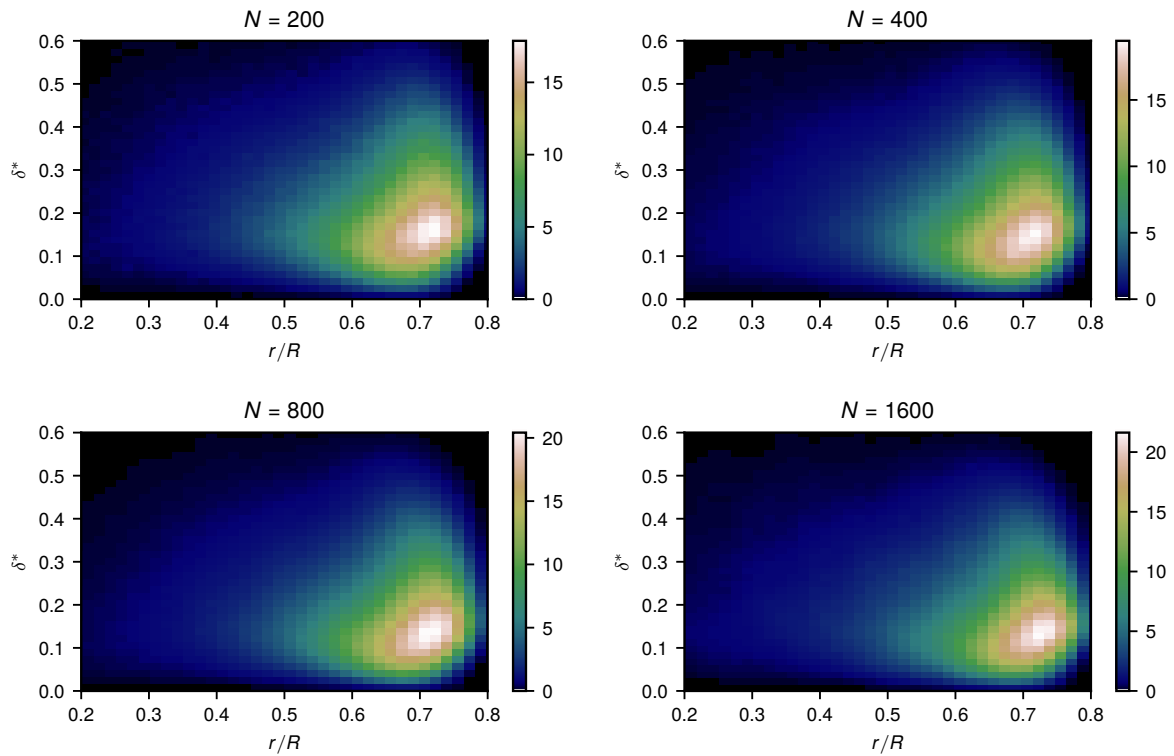
Supplementary Figure 6.3: Threading exchange dynamics. The two time-points threading correlator $\chi_{\text{th}}(t)$ for the two systems with $N = 200$ and $N = 400$ when threadings of any length are accounted for. Inset: the distribution of threading times $P_{\text{th}}(t)$ for these systems. The solid black line highlights the scaling regime $P_{\text{th}}(t) \sim t^{-2.25 \pm 0.01}$.



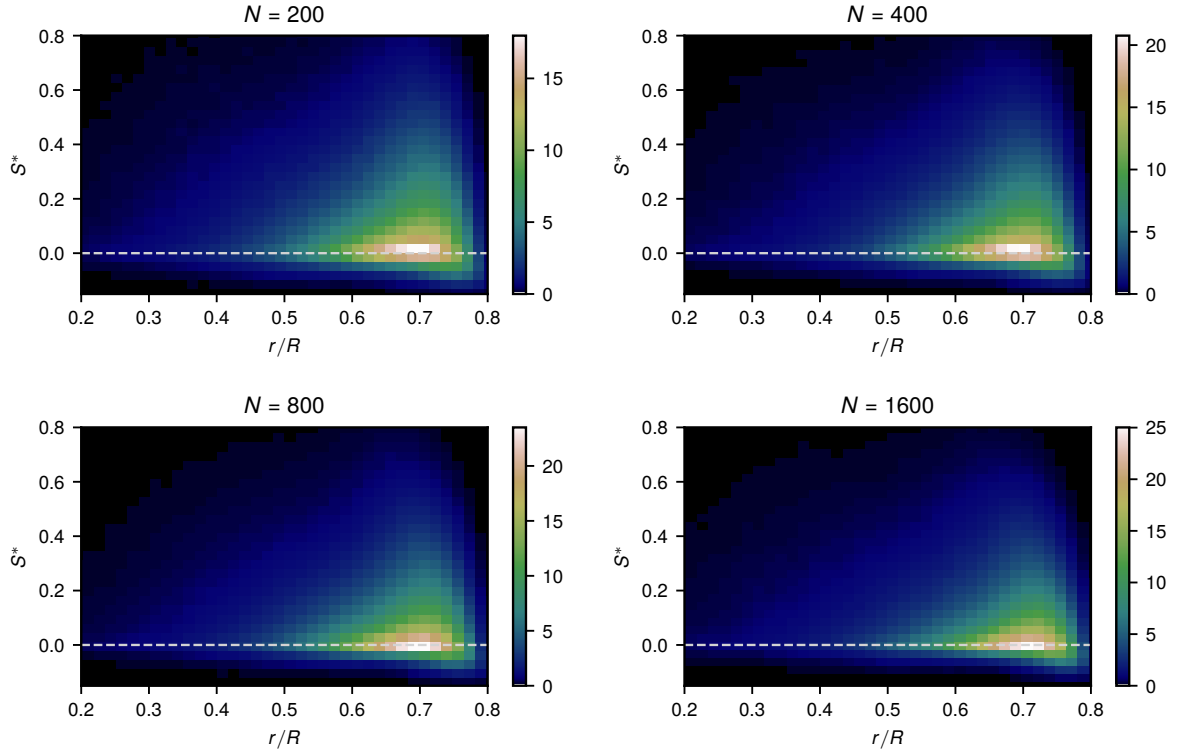
Supplementary Figure 6.4: Monomer density variations. Radial monomers density profiles within the confining sphere for systems with rings of different length N . In all cases, the mean monomer density is $\rho\sigma^3 = 0.85$. All subplots share the same x - and y -axis. On each plot the value ρ_b represents the plateau value of the monomer density in the interior of the confining sphere. Note that this is higher than the average density $\rho\sigma^3 = 0.85$.



Supplementary Figure 6.5: Distribution of the ring's radius of gyration within the confining sphere. Probability density of finding a ring of size R_g with its center of mass at a distance r from the center of the confining sphere of radius R for different N . In all cases, more compact rings are located at the surface, whereas bigger ones are found closer to the center.



Supplementary Figure 6.6: Distribution of the ring’s asphericity within the confining sphere. Probability density of finding a ring with asphericity $\delta^* \in [0, 1]$ with its center of mass at a distance r from the center of the confining sphere of radius R for systems with different N . In all cases, more aspherical rings are found close to $r \approx 0.7R$, and their deformation is highly likely caused by the interaction with the wall.



Supplementary Figure 6.7: Distribution of the ring's prolateness within the confining sphere. Probability density of finding a ring with prolateness $S^* \in [-0.25, 2]$ with its center of mass at a distance r from the center of the confining sphere of radius R for systems with different N . The dashed line separates oblate ($S^* < 0$) and prolate ($S^* > 0$) conformations. We see that more prolate rings are located close to $r \approx 0.7R$, whereas oblate shapes are found even closer to the wall, around $r \approx 0.75R$.

Chapter 7

Active topological glass as a model for coherent motion of chromatin

Manuscript in preparation: Stanard Mebwe Pachong, Iurii Chubak, Kurt Kremer, Christos N. Likos, and Jan Smrek. Active topological glass as a model for coherent motion of chromatin.¹

Motivated by the chromosomes enclosure in the cell nucleus, we study a spherically confined system of a small number of long unknotted and nonconcatenated partly active polymer rings in a melt. The same bulk system arrives at a glassy steady state due to activity-enhanced topological constraints mediated by highly expanded ring conformations. These expanded states limit the ring lengths that can be simulated because of prohibitively large system sizes, which are needed to avoid unphysical self-interactions due to periodic boundary conditions. Here we show that the enclosure of the system into an impenetrable cavity, which naturally limits the degree of ring expansion, does not disrupt the topological vitrification. This allows us to reach the active topological glass with ring lengths that at equilibrium exhibit the same conformational properties as the chromatin at large scales. In analogy to chromatin observations, we find large scale coherent motion due to the induced topological constraints, but also large scale structure inconsistent with the chromatin. We discuss the evidence for, and, against the activity-driven topology-induced coherence in chromatin on smaller scales.

¹Author contributions: S. M. P. and I. C. contributed equally. S. M. P., I. C. and J. S. performed the simulations and data analysis. All authors interpreted the results and wrote the manuscript.

7.1 Introduction

The active topological glass is a state of matter composed of polymers with fixed circular topology that vitrifies upon turning the polymers active and fluidizes if the activity is turned back off [184]. Unlike classical glasses, where the transition is driven by the change in temperature or density, the active topological glass results from physical, tight, threading entanglements, generated and maintained by the activity of polymer segments. The activity operating on the ring segments, modeled here as stronger-than-thermal fluctuations, triggers a directed snake-like motion that overcomes entropically unfavourable states and results in significantly enhanced inter-ring threading [311]. A topological glass is conjectured to exist in equilibrium solutions of sufficiently long ring polymers, where rings naturally thread (pierce through each other), however, the conjectured critical ring length is currently beyond the experimental or computational reach [66, 70, 204]. Although the active topological glass exhibits accessible critical ring lengths, a formidable challenge in simulating these systems stems from large system sizes that are necessary to avoid self-threading of significantly elongated partly active rings due to periodic boundary conditions [184]. To overcome the difficulty, a much smaller system confined to an impenetrable cavity can be simulated. However, in analogy to classical glasses, where the confinement affects the vitrification mechanism and shifts the glass transition temperature in comparison to the bulk value [312, 313], it is necessary to ask the question if the active topological glass, the existence of which relies on highly extended configurations that promote inter-molecular entanglement, can exist in confinement at all. To answer this question and potentially ease the exploration of the active topological glass transition, here we study a confined melt of unknotted and nonconcatenated rings with active segments.

Besides the active topological glass, the confined melt of uncrossable polymer rings with active segments has an interesting biological connection. The *equilibrium* melt of rings exhibits conformational properties consistent with the large scale, population-averaged properties of chromatin fiber in the interphase nuclei of higher eukaryotes [84, 85, 283]. In detail, the spatial segregation of distinct chains, the critical exponents $\nu = 1/3$ and $\gamma \simeq 1.1$ governing the scaling of the gyration radius $R(s) \sim s^\nu$ and the probability of end-contacts $P(s) \sim s^{-\gamma}$ of a segment of length s , respectively, coincide for the two systems and characterize the so-called fractal (crumpled) globule conformation ensemble [89]. The rationale behind the connection is the separation of time scales: the long chromatin chains do not equilibrate on biological time scales if they were mostly

uncrossable [84]. The ensemble of their conformations can be then related to that of permanently uncrossable, topologically constrained polymers in equilibrium – the melt of rings. However, similarly to the partly active rings, chromatin is out of equilibrium on smaller scales as well. Various processes, such as transcription, repair, remodeling or loop extrusion inject energy to the system by the action of their respective molecular machines on the chromatin fiber. Fluorescence experiments [100] and the related analytical theory [278] suggest that some active events at small scales render fluctuations with thermal spectrum at the effective temperature about twice higher than the ambient one.

In the context of chromatin, several groups studied partly active confined polymers [94, 95, 97, 96, 98, 314], however did not focus explicitly on the connection of the activity with the topology. The works [94, 95] study the activity-driven phase separation [77, 73, 78] as a model for the segregation and positioning of the active and the passive chromatin. In contrast to our work, where the compact, territorial conformations arise from the topological constraints, in [94, 95, 314] the compact state is created and maintained by explicit cross-linkers. Nuebler et al. [98] observed that the activity of loop extruders, as given by their speed, weakens the interaction-based phase-separated structure, but strengthens the contacts within the extruded loops. The latter work, however, uses a model with partly crossable polymers and therefore it is difficult to judge on the role of topology. The works [97, 96, 314] focus on the spatio-temporal correlations in the dynamics. While the first one, uses the thermal-like model of activity, the latter two investigate the effects of active force dipoles. These are coupled with hydrodynamic interaction in Ref. [96], while in Ref. [314] the active force dipoles act on highly cross-linked chromatin connected to deformable lamina. All three works find large scale correlated motion, but of different origins. In Ref. [97], the correlated domains coincide with the micro-phase separated domains due to preferential intra-domain interaction potential, because while the short-time correlation of active and inactive systems are found to be the same, at longer time lags, the activity opposes the coherence (similarly to Ref. [98]) and decreases the correlation length. Although such non-monotonic dependence of the correlation length on the time lag has been observed [100, 101], it does not seem to be a general phenomenon (see Figure 2 in Ref. [101]) and in contrast to Ref. [97], the coherence even at short time lags is larger for the active systems [100, 101]. The correlated motion in Ref. [96] comes from the coupling of the hydrodynamic flow due to contractile motors and the nematic ordering of the chromatin fiber (not yet observed), with no discernible effect of local topology (unknottedness) of the conformation. The contractile motor activity in Ref. [314] generates the correlated motion as a result of a high number of

cross-links between chromatin fiber, and is even enhanced when more cross-links are used with a deformable nuclear envelope. Last but not least, apart from the role of activity in correlated motions, other passive mechanisms are possible [315, 221]. The latter work also highlights glassy features of the chromatin dynamics, such as dynamic heterogeneity.

Our work does *not* aim at a faithful representation of the chromatin, as each of our polymer rings has only one, long, continuous active segment, but we rather explore how the active topological glass is consistent with the fractal globule model, both of which represent some aspects of the chromatin conformations in space and time. In this work, we show that essentially the same phenomenon of the active topological glass formation is present in the confined systems with a small number of polymer chains. While the territorial structure of the fractal globule is distorted, we observe active-passive microphase-separated domains and large scale correlated motion arising from the glassy phase due to the activity-driven topological constraints. In contrast to works [97, 314], where the coherence arises from explicit interaction potentials or cross-links, here we show that the activity-induced entanglement can mediate the coherence.

7.2 Model

We use the well-established polymer model [127], in which the excluded volume interaction between any two monomers is described by a repulsive and shifted Lennard-Jones potential

$$U_{\text{LJ}}(r) = \left(4\epsilon \left[\left(\frac{\sigma}{r} \right)^{12} - \left(\frac{\sigma}{r} \right)^6 \right] + \epsilon \right) \theta(2^{1/6}\sigma - r) \quad (7.1)$$

where $\theta(x)$ is the Heaviside step function, σ is the bead's diameter, and ϵ sets the energy scale. As in Ref. [283], the same potential was used for the interaction between monomers and the confining sphere of radius R . We simulated a fixed number of polymer chains M and adjusted R to match the target monomer density $\rho = 0.85\sigma^{-3}$ (the used values of R are listed in Table 7.1). The polymer bonds were modeled by a finitely extensible nonlinear elastic (FENE) potential

$$U_{\text{FENE}}(r) = -\frac{1}{2}r_{\text{max}}^2 K \log \left[1 - \left(\frac{r}{r_{\text{max}}} \right)^2 \right], \quad (7.2)$$

where $K = 30.0\epsilon/\sigma^2$ and $r_{\text{max}} = 1.5\sigma$. These parameters make the chains essentially noncrossable. We also used the angular bending potential

$$U_{\text{angle}} = k_{\theta}(1 - \cos(\theta - \pi)) \quad (7.3)$$

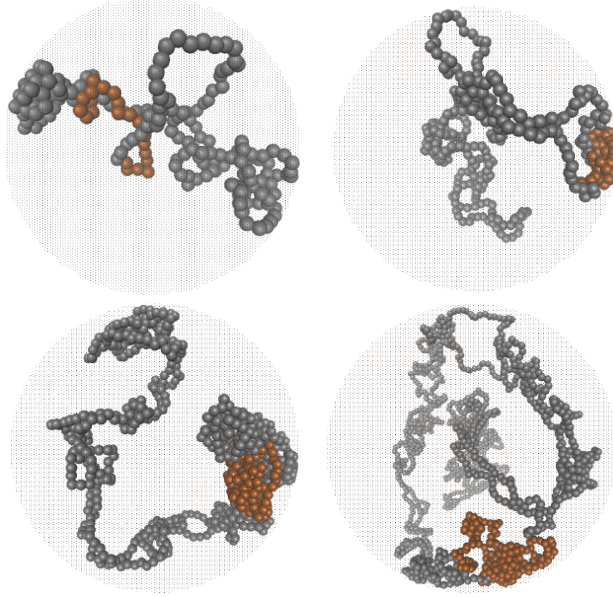


Figure 7.1: Typical conformations of partly active rings in spherical confinement. The snapshots correspond to $N = 200$ (top left), 400 (top right), 800 (bottom left), and 1600 (bottom right).

with the parameter $k_\theta = 1.5\varepsilon$ to induce higher stiffness that corresponds to a lower entanglement length $N_e = 28 \pm 1$ at the studied monomer density $\rho = 0.85\sigma^{-3}$ [50].

Our simulations start from well-equilibrated configurations of completely passive ring polymer melts in spherical confinement produced in Ref. [283]. Each system contains $M = 46$ ring polymer chains, each of length N ($N = 200, 400, 800$ and 1600 , corresponding to chain entanglement number $Z = N/N_e = 7, 14, 28$ and 57). The choice of $M = 46$ chains was inspired by the 23 pairs of chromosomes in the human diploid cell nucleus, but the main reason is to demonstrate the existence of a topological glass in small systems to ease future exploration of the phenomenon. At time $t = 0$, the activity was introduced by coupling a consecutive segment of length $N/8$ to a Langevin thermostat at temperature $T_h = 3.0\varepsilon$, whereas the rest of the chain is still maintained at $T_c = 1.0\varepsilon$ by another Langevin heat bath. We choose this value of $T_h = 3T_c$, despite the experimental indications of active fluctuations being only about twice the thermal fluctuations [278]. The reason is the heat flux between active and passive constituents establishes effective temperatures that are in between the temperatures set by the thermostat. The effective temperatures (measured by the mean kinetic energy) would be the ones measured in the experiments and have the correct ratio about 2 [311]. The equation of motion of the systems were integrated using the LAMMPS simulation package [266] with the time step $\Delta t = 0.005\tau$ and the damping constant $\gamma = 2/3\tau^{-1}$, where $\tau = \sigma(m/\varepsilon)^{1/2}$.

The Langevin thermostat in spherical confinement can induce stochastic values of

N	N_h	R/σ	$\langle R_g^2 \rangle / \sigma^2$	$\langle R_e^2 \rangle / \sigma^2$	$\langle \lambda_1 \rangle / \langle \lambda_3 \rangle$	$\langle \lambda_2 \rangle / \langle \lambda_3 \rangle$	$\langle R_g^2 \rangle / R^2$	$\langle R_e^2 \rangle / R^2$
200	25	13.72	62.4(0.7)	164.8(6.2)	12.0(0.7)	4.3(0.2)	0.33	0.87
400	50	17.29	129.3(0.6)	304.4(6.2)	6.5(0.4)	3.1(0.7)	0.41	1.01
800	100	21.78	227.7(0.5)	468.6(3.1)	4.6(0.2)	2.7(0.8)	0.47	0.98
1600	200	27.44	376.1(0.7)	810.8(4.7)	3.5(0.5)	2.2(0.1)	0.49	1.07

Table 7.1: Size and shape properties of partly active rings in a confining sphere. The mean values as well as their standard errors (indicated in the parentheses) were estimated in the steady states. R is the radius of the sphere. $\langle R_g^2 \rangle$ and $\langle R_e^2 \rangle$ are the mean-square radius of gyration and the mean-square spanning distance between monomers $N/2$ apart, respectively. λ_i ($i = 1, 2, 3$, $\lambda_1 \geq \lambda_2 \geq \lambda_3$) are the eigenvalues of the gyration tensor.

angular momentum that affects the real dynamics of the system. This effect can be neutralized by zeroing the total angular momentum of the system periodically during the simulation runs. In the present case, unlike to our equilibrium simulations in Ref. [283], we do not perform this operation due to non-equilibrium character of the studied system as well as potential global flows that can arise in active matter states. When compared to dynamic equilibrium quantities across this work, we also used trajectories produced in a similar fashion without zeroing the angular momentum. We note, however, that the difference in dynamic relaxation times in equilibrium simulations with and without zeroing the angular momentum is rather small.

7.3 Results

When the activity is switched on, after about $10^5\tau$ the chains start to expand from their equilibrium sizes until they reach a steady state after about $3 \cdot 10^6\tau$ with significantly enhanced mean-square radii of gyration R_g^2 (see snapshot of a chain conformation in Figure 7.2d and more in Figure 7.1), time evolution of R_g^2 in Figure 7.2a and Table 7.1 for shape parameter comparison. In comparison to the bulk [184], the confined rings are significantly less expanded in terms of R_g and R_e and the ratio of the two biggest eigenvalues of the gyration tensor (see Figure 7.3a and compare Table 7.1 to Table 5.1 for $N = 400$). Nevertheless, the conformations are mostly doubly-folded and the change in the shape parameters is due to “reflections” of the doubly-folded structure from the walls. This can be seen in the mean-square internal distance of the longest rings being a non-monotonic function of the contour length (see Figure 7.3b). In comparison to equilibrium (see Table 6.1), the rings are highly stretched and exhibit self-avoiding walk-like scaling at intermediate distances (see Figure 7.3c) with a consistent scaling of the contact probability with the exponent γ close to 1.75 (Figure 7.3d) [85] and a plateau at largest distances

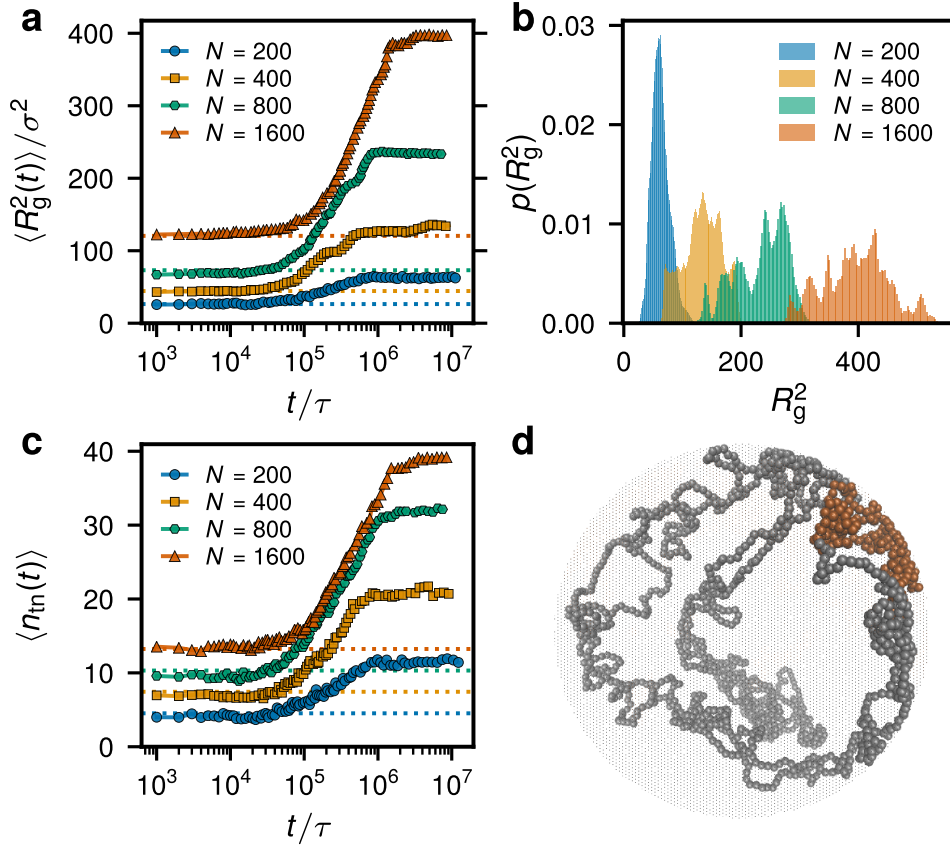


Figure 7.2: Static properties of confined partly active rings. **a**, Evolution of the ring’s radius of gyration after the activity onset at $t = 0$ for systems with different N . **b**, Multi-peak distributions of R_g^2 in the steady state highlighting non-ergodic behavior in these systems. **c**, Evolution of the mean number of threaded neighbors after the activity onset. **d**, Conformation of a partly active ring with $N = 1600$ at the end of the simulation run. In **a** and **c**, the dashed lines of the respective color indicate the values in equivalent equilibrium ring melts [283].

signifying the loss of correlation due to reflections of rings from the walls. The stretching due to snake-like motion is caused by strong dynamic asymmetry between the active and the passive segments, apparently triggered by non-equilibrium phase separation, as described in [184, 311]. The dynamics of the mutual ring threading coincides with the stretching dynamics and exhibits significantly enhanced number of threaded neighbors n_{tn} by a single ring in the steady state in comparison to equilibrium (Figure 7.2c), as we showed by analyzing piercings of rings through other rings’ minimal surfaces – the method used successfully for ring threading detection before [63, 72, 283, 184, 311]. Interestingly, the number of threaded neighbors is the same as for the active topological glass in the bulk, despite the different ring shape [184, 311]. In the longest system, each ring practically threads all the other rings in the system. Although this does not hold for the shorter rings, their dynamic behavior is comparable as detailed later below. The steady states

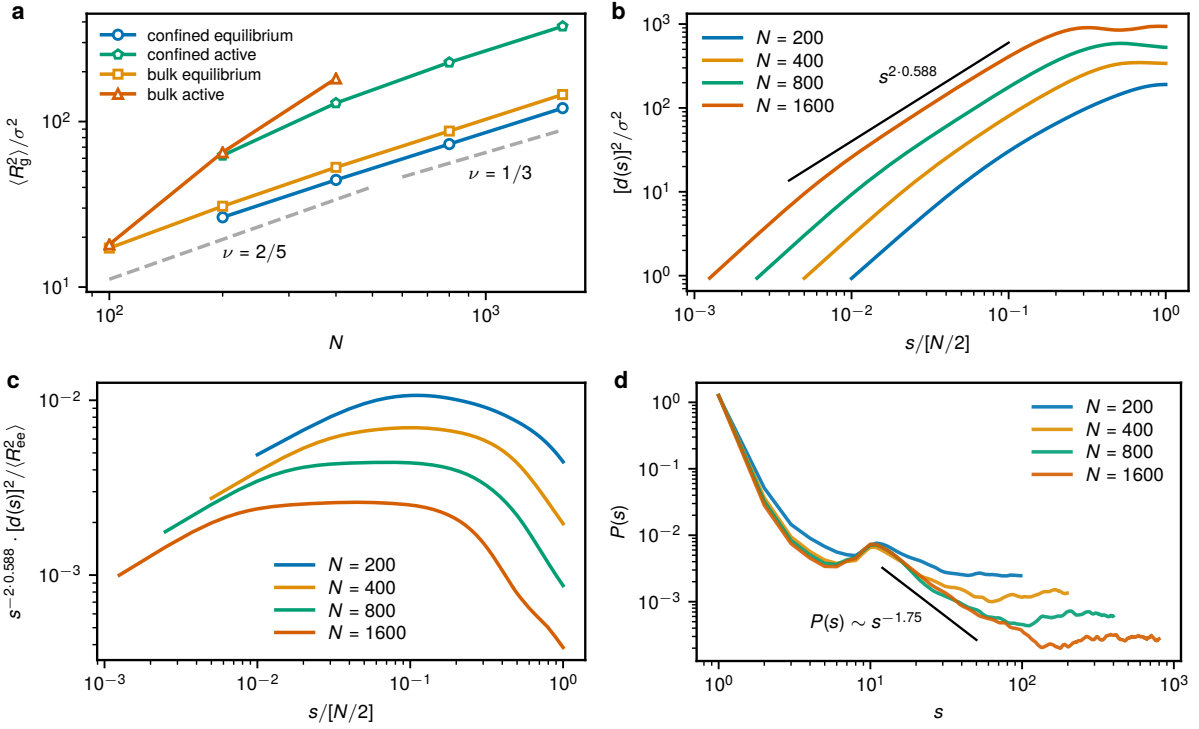


Figure 7.3: Additional conformational properties. **a**, Comparison of the scaling of the radius of gyration with the ring length for different systems. The confined active rings are from the present work, the confined equilibrium rings are from Ref. [283], the bulk equilibrium are from Ref. [50], and the bulk active rings from Ref. [184]. The equilibrium scaling exponent $\nu = 1/3$ is shown as well as the crossover with “effective exponent” $2/5$. The seeming compact scaling of the active confined rings is not due to their internal structure (see **b**), but just because systems of different N were simulated with the same number of chains and the same density. **b**, The mean-square internal-distance $d(s)$ is computed as the mean-square end-to-end vector of a segment of length s averaged over its position within a ring and over different rings in the steady state. At intermediate distances ($s/(N/2) \in [10^{-2}; 10^{-1}]$), we recover self-avoiding walk scaling exponent 0.588 for the longer ($N \geq 400$) rings. These exhibit also monotonic profile for large contour distances. **c**, The mean-square internal-distance $d(s)$ rescaled by $s^{0.588}$. The broadening plateau for the rings of $N \geq 400$ shows the asymptotic self-avoiding regime. **d**, The contact probability $P(s)$ is the probability of finding the endpoints of a segment s at distance below $2^{1/6}\sigma$. It is an average over the segment’s position within a ring and over different rings in the steady state. At intermediate distances and for long rings we recover exponent γ close to 1.75 consistent with the self-avoiding random walk configuration. At longer lengths, $P(s)$ goes to a constant, signifying the positional decorrelation due to reflections from the wall – this is typical profile of an equilibrium globule, i.e. confined melt of linear chains. The exponent γ is smaller for shorter rings. The non-monotonic character is due to the phase separation of the hot and cold segments and the doubly-folded structure.

are non-ergodic as shown by the rugged distribution of R_g^2 (Figure 7.2b), despite averaging over about $10^7\tau$, time that is more than one order of magnitude above the equilibrium diffusion times for $N \leq 800$.

The chosen model parameters trigger active-passive (micro)phase separation in all the systems [311, 78, 79]. We track the degree of phase separation by the order parameter $\Phi(t) = x(t)/x(0) - 1$, where $x(t)$ is the average number fraction of inter-chain like-particles in a $r_c = 2^{1/6}\sigma$ neighborhood around a particle at a given time t (Figure 7.4a). The initial increase of the segregation somewhat precedes the ring stretching and threading dynamics. The phase separation is dynamic in nature, showing periods of a single mostly-hot region, but also subsequent dissociation into several hot blobs, reminiscent of the dynamics of activity-driven colloidal crystals [316]. When the shape properties arrive at a steady state and the phase separation is incomplete (that is, there are multiple hot regions, as seen in Figure 7.4b), we still observe some changes in the hot blobs. As described below, these are the consequence of a rare tank treading motion of some of the rings, by which the hot segment joins the hot phase without changing the overall shape of the ring and the system as a whole. The radial density distribution of the hot monomers averaged over 10 different runs for $N = 200$ displays confinement induced layering at the wall as in equilibrium [283], and displays another broad maximum around $R/2$ (Figure 7.4c). However, the analysis of single runs for $N = 200$ and for other N shows that the positioning of hot monomers is history-dependent, arrested by the topological constraints, and allows for both, internal or peripheral locations (Figure 7.4d).

In Figure 7.5, we report dynamical and relaxation properties of rings in the system with $N = 200$ (averaged over 10 independent runs). We focus on the late stage dynamics by discarding the initial period of length $3 \cdot 10^6\tau$, where major configurational rearrangements occur. To do so, we compute the mean-square displacement of the ring's center of mass, $g_3(t)$, as

$$g_3(t; t_0, T) = \left\langle \frac{1}{T-t} \int_{t_0}^{t_0+T-t} [\mathbf{R}(t'+t) - \mathbf{R}(t')]^2 dt' \right\rangle \quad (7.4)$$

where t_0 is the initial time point chosen as the onset of the steady state ($3 \cdot 10^6\tau$ in the case of active rings and 0 for equilibrium), T is the total simulation time, \mathbf{R} is the position of the ring's center of mass with respect to the global center of mass, and the angles denote averaging over different rings. In addition, we compute the relative mean-square distance $g_{3,\text{rel}}(t; t_0, T)$:

$$g_{3,\text{rel}}(t; t_0, T) = \left\langle \frac{1}{T-t} \int_{t_0}^{t_0+T-t} [d_{ij}(t'+t) - d_{ij}(t')]^2 dt' \right\rangle_{ij} \quad (7.5)$$

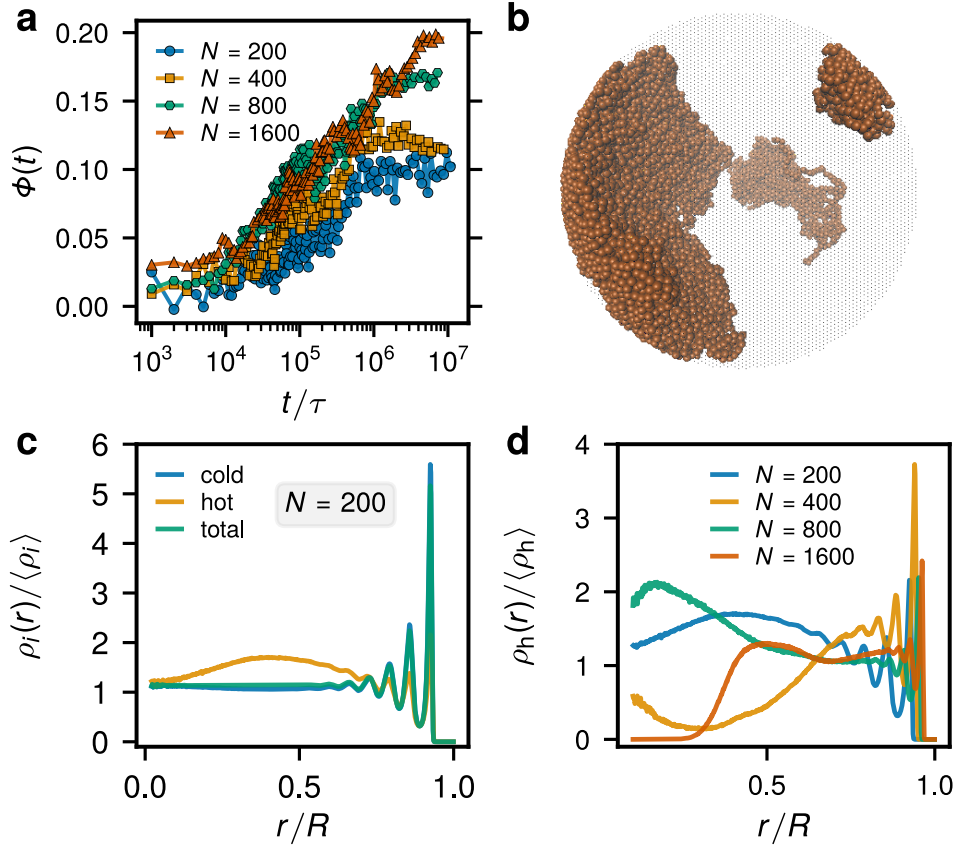


Figure 7.4: Phase segregation of partly active rings in spherical confinement. **a**, Time evolution of the phase segregation order parameter $\Phi(t)$ for systems with different N . **b**, Phase segregated regions of hot monomers for the system with $N = 1600$ (cold monomers are not shown for clarity). **c**, Radial distribution of cold (blue), hot (yellow), and all (green) monomers within the enclosing sphere for the system with $N = 200$ (averaged over 10 independent runs). **d**, Radial distribution of hot monomers for systems with different N .

where t_0 and T are as above, d_{ij} is the relative *distance* between rings i and j and $\langle \dots \rangle_{ij}$ is the average over all distinct ring pairs in the system. The late-stage (steady-state) dynamics of the ring's center of mass, $g_3(t)$ is much slower than in the equilibrium case [283], with negligible relative displacements between the rings $g_{3,\text{rel}}(t)$, as shown in Figure 7.5a. Importantly, the latter quantity is invariant under global rotations and shows that the relative motion of the rings essentially stalls. The systems with longer rings display the same behavior. In confined systems, $g_3(t)$ saturates at a constant value, as a consequence of a finite volume of phase space available for diffusion. For the rings with $N = 200$, we find that $g_3(t \rightarrow \infty) \approx 0.4R^2$, which is about two times smaller than in the equivalent equilibrium case (Figure 7.5a). This arises mostly from extremely elongated and practically frozen rings conformations, due to which the exploration of the available volume is significantly suppressed.

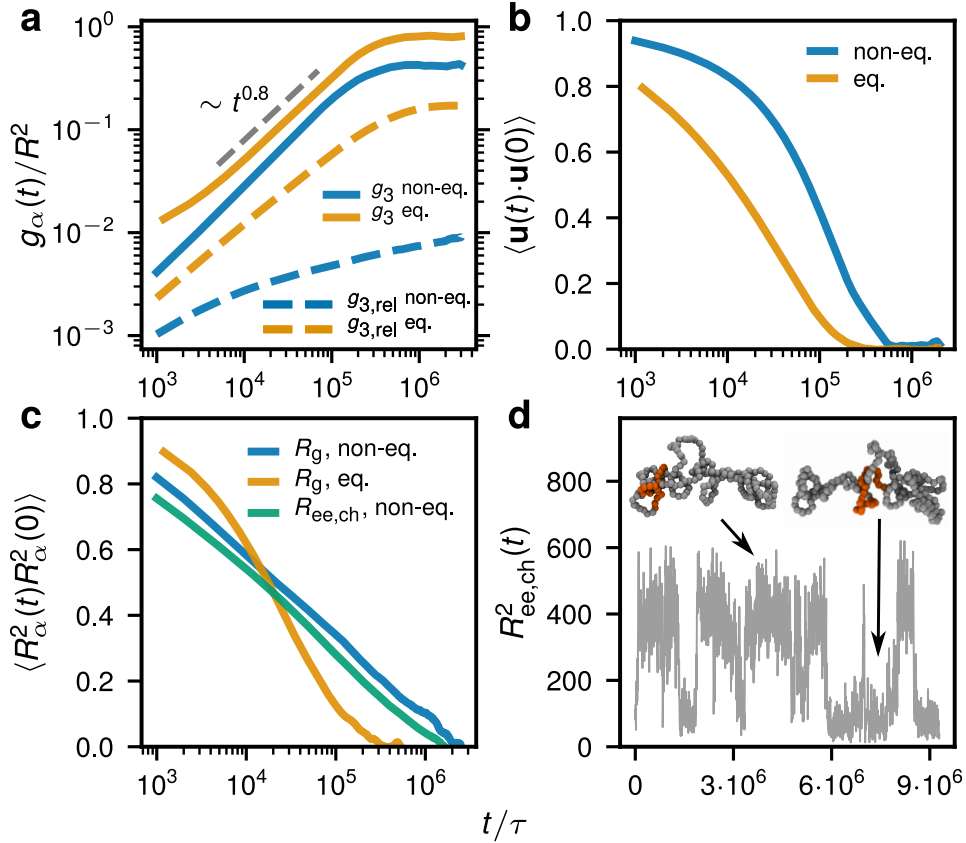


Figure 7.5: Dynamics and relaxation of partly active rings in spherical confinement. **a**, Mean-square displacements of the ring's center of mass g_3 normalized by the squared sphere's radius, R^2 as function of time, for non-equilibrium partly active rings with $N = 200$ (solid blue) in comparison to a fully passive equilibrium system (solid yellow) computed according to Eq. (7.4). The relative mean-square displacement $g_{3,rel}(t)$ for non-equilibrium partly active rings (dashed blue) and equilibrium (dashed yellow) is computed according to Eq. (7.5). **b**, Terminal autocorrelation function in the equilibrium (yellow) and non-equilibrium case (blue). **c**, Autocorrelation function for the squared ring's radius of gyration for the equilibrium (yellow) and non-equilibrium system (blue). In the latter case, we additionally show the autocorrelation function for the squared end-to-end distance $R_{ee,ch}$, which is the distance between an active and a passive monomer separated by segment length $N/2$. **d**, Time dependence of $R_{ee,ch}^2(t)$ for one of the rings in the system that illustrates tank treading motion along the chain's contour.

We characterize the ring structural relaxation by considering the terminal autocorrelation function (TACF) $\langle \mathbf{u}(t) \cdot \mathbf{u}(0) \rangle$, where $\mathbf{u}(t)$ is the unit vector connecting two monomers separated by contour distance $N/2$, and the average is taken over all such monomer configurations within a ring and time. The full decorrelation time of the TACF ($\approx 6 \cdot 10^5 \tau$) is about three times longer than in the counterpart equilibrium case without zeroing of the angular momentum (Figure 7.5b). In the steady state, the rings are found in a heavily threaded arrangement with their configurations being essentially frozen, as evidenced by

the static properties.

In what follows, we show that the main pathway that contributes to the decorrelation of the TACF are correlated, stochastic rotations of the whole system. The other possible decorrelation mechanism is the internal ring rearrangements, caused by the local explorations of the hot segments or tank treading motion. To show that these do not dominate, in Figure 7.5c we plot the autocorrelation function for the ring's squared radius of gyration, $\langle R_g^2(t)R_g^2(0) \rangle$, which decorrelates at a much later time ($\approx 2 \cdot 10^6 \tau$) and features a three decades long logarithmic decay. This contrasts with the equilibrium behavior, where both structural quantities $\langle R_g^2(t)R_g^2(0) \rangle$ and $\langle \mathbf{u}(t) \cdot \mathbf{u}(0) \rangle$ decorrelate at about the same time (yellow curves in Figure 7.5b and Figure 7.5c). Although the size of the rings remains essentially the same during the TACF relaxation, there remains a possibility of tank treading motion that can significantly impact the TACF decorrelation but keep the overall size given by R_g fixed. As highlighted in Figure 7.5d, the tank treading, a tangential motion of the hot segment along the ring's contour, is indeed observed. However, we observe this happening, only if the hot segment on a ring is not phase separated with the like blocks; then the only possibility for such hot block to segregate is the tank treading. We show that the tank treading does not significantly impact the terminal relaxation by computing the autocorrelation function for the squared end-to-end distance $R_{\text{ee, ch}}^2$ between a hot and a cold monomer contour-wise $N/2$ apart (Figure 7.5c). Although it decorrelates slightly faster than $\langle R_g^2(t)R_g^2(0) \rangle$, its relaxation time is still much larger than that of the TACF. Therefore, correlated, collective rotations provide the dominant contribution to the TACF decorrelation, whereas its relaxation time scale can be used as an estimate for the rotational diffusion time.

Global rotations lead to correlated particle displacements, as detailed by computing the spatio-temporal correlation function. The latter is computed similarly to Refs. [100, 97] as

$$C_s(r; \Delta t) = \left\langle \frac{\sum_{i>j} [\Delta \mathbf{R}_i(t, \Delta t) \cdot \Delta \mathbf{R}_j(t, \Delta t)] \delta(\mathbf{R}_{ij} - r)}{\sum_{i>j} \delta(\mathbf{R}_{ij} - r)} \right\rangle \quad (7.6)$$

where $\Delta \mathbf{R}_i(t, \Delta t)$ is the displacement of the i -th monomer in lag time Δt as measured in time t . The angles represent averaging over time, in the active case only over the steady state. In the active system, the correlation decays significantly slower in comparison to equilibrium and there is a strong anticorrelation at longer lag times at the opposing positions in the spherical confinement ($r \simeq 1.5R$) (Figure 7.6a). In part, this is a consequence of the Langevin dynamics that induces stochastic angular momentum also in equilibrium (Figure 7.6b). However, the anticorrelation is much more pronounced in the active topological glass state, and almost nonexistent in equilibrium with zeroed angular momentum

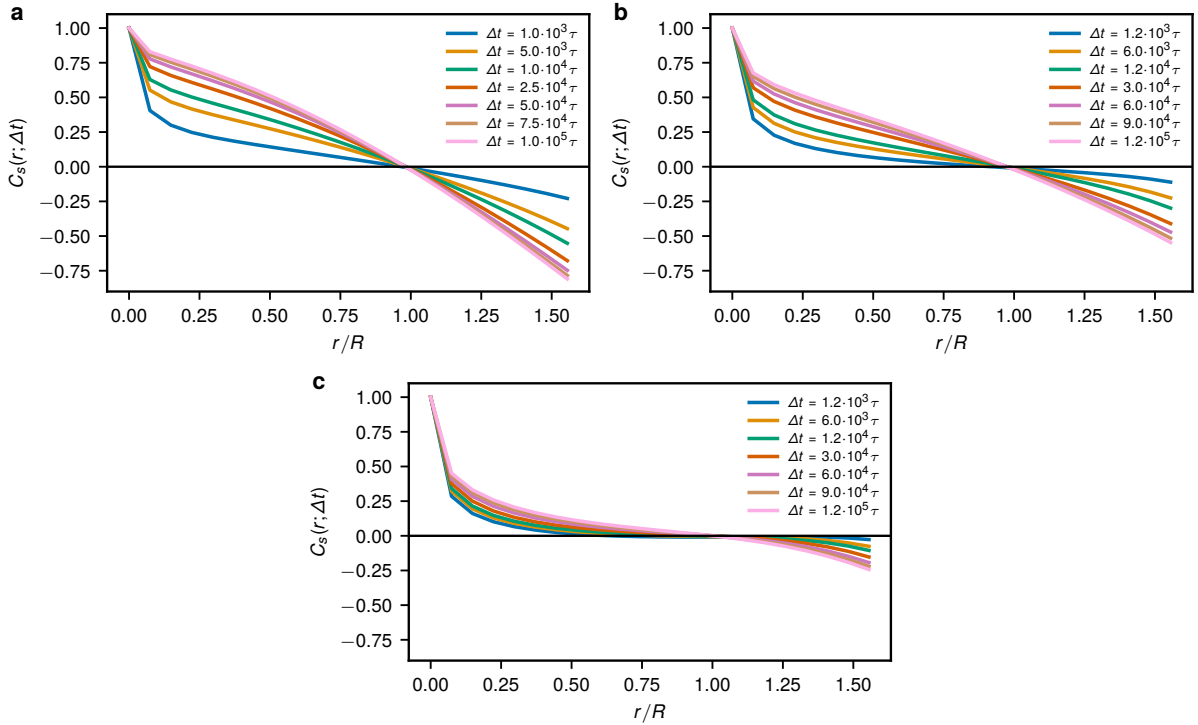


Figure 7.6: Spatio-temporal displacement correlation. The correlation for $N = 200$ system computed using Eq. (7.6) for (a) the active confined rings, (b) equilibrium rings without zeroing the angular momentum, (c) equilibrium rings with zeroing the angular momentum from Ref. [283].

(Figure 7.6c). We observe larger correlation length for the active case consistent with Refs. [100, 101, 314], but in contrast to Ref. [97]. However, the correlation length seems to be monotonically increasing and saturating with time that is consistent with some cases in Ref. [101], but non-monotonic correlation length has been observed in other cases at longer time lags [101, 100, 314, 97]. Finally, note that such stochastic rotations can also arise spontaneously in confined equilibrium systems coupled to a Langevin thermostat (see discussion in Section 7.2).

7.4 Conclusions

We have shown that the confinement and the use of a small number of the partly active rings does not break the active topological vitrification. This is an important step for a detailed investigation of this new type of glass transition, as it allows to work with much smaller systems. We took the advantage and simulated longer ring lengths to investigate how the universal properties of the fractal globule change under the influence of segmental activity. We have shown that the rings in the steady state exhibit doubly-

folded, extended structures reflecting from the confining walls with self-avoiding statistics at large ring lengths. The same numbers of threaded neighbors as in the bulk suggest the same mechanism of the formation of the glassy state in confinement. We have found a new tank treading relaxation mechanism that allows for optimizing the phase separation without changes in the chain conformation and its location.

As a result of the glassy state, the whole interior of the confining volume exhibits large correlated motions (rotational diffusion). Similarly, the interior of the whole nucleus has been observed to move coherently on micron scale [100, 101], interpreted also as rotations [317]. As noted in the introduction, many different mechanisms can cause large correlated motions such as the role of cohesive interactions or hydrodynamics coupled to orientation and activity [269]. Here we show a yet another mechanism that can give rise to such correlated motion, namely, the activity-induced topological interactions that entangle neighboring domains that subsequently have to move in a correlated fashion.

Although it is tempting to suggest these play a role in the nuclear dynamics, based on the conformational data, we conclude that the active topological glass in the present form is inconsistent with the chromatin conformational data and the fractal globule model. The conflict of the dynamics and the large-scale conformational properties is, however, a persistent issue also in other models that aim at elucidating the physical mechanisms rather than the capturing the conformational details [96]. More work is necessary to conclude if other types of topological glass can be consistent with fractal globule. For example, the glassy steady states would certainly depend on the contour distribution of the active segments [311]. In this context, the simulations in Ref. [97] use partly active uncrossable chains with fractal-globule large scale conformational properties and distribution of the active sites based on the epigenetic information, but conformational changes of the active loci are not reported. Despite some active segments being long (20-80 beads), a relatively lower density and differential interactions between the two chromatin types could suppress or obscure the activity-driven changes we report here. This could be also the reason why that work did not observe the correlation length to depend on the activity level at short times as reported in experiments [100, 101]. Nevertheless, these results together with the conformational changes (ring stretching) we report here suggest that it is unlikely that nucleus-wide activity-driven conformational changes appear *in vivo*. However, at scales below 1 Mbp the chromatin fiber is more consistent with the active topological glass features as the chromatin fiber has nontrivial topology (due to cohesin mediated loops) [99] and features less compact statistics [318, 86]. Some dynamics observations at these scales are also similar to the active topological glass behavior, namely, (*i*) activated

loci exhibit directed dynamics [256], (ii) constraint release after polymerase inhibition [319] and (iii) long transcribed genes exhibit large scale expansion [320]. We speculate that the large correlated motions could be the consequence of the activity-enhanced topological interaction at these smaller scales. This hypothesis is further supported by the decrease of the local coherence upon application of ATPase inhibiting drugs [100, 101] (Inhibiting topoisomerase 2 should support the coherence if the topological picture was valid, however, the drug itself is creating DNA damage, which in principle could alleviate the topological constraints [100]). As evidenced in the experiments, the coherence depends on the ATP-consuming processes in a nontrivial way and therefore might not be only interactions-based. An experiment that would trace the chromatin type in 3D simultaneously with the coherence in dynamics might elucidate the mechanism.

Chapter 8

Conclusions and outlook

In summary, in this thesis we have focused on how different types of functional blocks can affect self-assembly properties of polymers with nontrivial (non-linear) architecture. In the first part of the thesis, we have considered star-shaped co-polymers with end-functionalized blocks. Computational models have been compared to a specific experimental realization of a three-arm TSP. We have found the emergence of two sub-classes in very dilute conditions upon increasing the association strength between the functionalized blocks (in this case, *via* decreasing temperature that worsens the solvent quality for the end-blocks): single stars and interconnected micellar aggregates comprising many TSPs. We have observed the reduction in size of both components in the solution with decreasing temperature. At the single-star level, as seen from simulations, such reduction corresponds to the formation of a single patch, where all star arms come together through associations between functionalized blocks. Furthermore, the transition temperature for the single patch formation has been found to shift to lower temperatures with decreasing the length of the associating block. On the other hand, for a fixed number ratio of the associating monomers, the transition shifts to higher temperatures with increasing the arm length. Using an effective blob model, we have found the formation of interconnected micellar clusters whose aggregation size decreases with increasing the attraction strength between the functionalized blocks, being in line with experimental findings. The particular star architecture together with associating blocks located at the tips of star arms facilitates the formation of a network-like structure with pronounced inter-star connections even at relatively dilute conditions. As has been shown on the model TSP system, stronger associations between the functionalized blocks result in a higher solution viscosity. The solutions also exhibit interesting shear thinning behavior that stems from the reorganization of the TSP network under shear flow. While in the carried out studies we focused on three-arm TSP systems that have a rather limited propensity for network formation,

it is possible that gel states with a solid-like response can form if the connectivity of the TSP network is further enhanced. The latter can be achieved by investigating TSPs with a higher number of arms. The response of such systems, therefore, could be tuned by adjusting the external stimulus, and would lead to controllable (i.e., liquid- or solid-like) rheological response. Work in this direction is currently in progress.

In the second part of this thesis, we have shown that the presence of functionalized blocks, which have a locally enhanced mobility, on polymer rings in the melt can lead to a topologically jammed state, the so-called active topological glass. The latter state arises from significantly deformed ring conformations that sharply contrast with the compact ring structure in equilibrium melts. More specifically, the enhanced mobility on certain ring segments was modeled as an effectively higher temperature as compared to non-functionalized blocks. This inherently non-equilibrium mechanism, stemming from local temperature differences, has been recently shown to trigger phase separation in active-passive colloid and polymer mixtures, provided that the temperature contrast is high enough. In this work, we find that the phenomenon of active topological glass formation and non-equilibrium active-passive phase segregation are closely related. In particular, a peculiar single ring dynamics is observed in those systems of rings with functionalized active blocks that feature a tendency towards active-passive segregation. In such cases, the rings are directed by active segments, which serve as an effective polymer end that explores the nearest environment and drives the whole chain through the mesh of constraints imposed by other rings in the system. Such directed dynamics results in a build-up of special topological constraints, threadings, that are unique for circular polymer chains. Some of them form the so-called reef knots (see Figure 5.1) and are particularly hard to be resolved. Furthermore, the formation of especially tight threadings together with constantly driven dynamics, results in a notable expansion of the rings, significantly beyond their equilibrium size. This reinforces the accumulation of threadings and consequently leads to suppression of relative motion of the rings, yielding a glassy state developed on topological constraints and active driving.

Many properties on active topological glasses are still unclear and, therefore, offer a promising research direction in the future. Those are broadly related to its emergence, macroscopic response, as well as potential experimental realization. In my view, it would be especially interesting to unravel the precise mechanism that relates non-equilibrium phase separation and the ensuing topological glass formation. Such mechanism might stem from a distinctive non-equilibrium phase separation kinetics that gives rise to the observed microscopic dynamics of partly active rings. As the used activity model is quite

generic, multiple mechanism can be potentially employed to create this state of matter experimentally. These can be either based on a local action of certain molecular motors or on a coupling between specific ring segments to external fields. In any case, a full phase diagram for the active topological glass, e.g. in terms of the temperature ratio between active and passive blocks, T_h/T_c , versus the relative fraction of active blocks, N_h/N , would be of prime importance to stimulate experimental explorations. A study in this direction is on the way.

In the third part of this thesis, we have considered fully passive as well as partly active ring melts composed of a relatively small number of polymer chains confined in a sphere in relation to phenomena that arise in the cell nucleus at different length scales. Most importantly, we have found that the scaling properties of fully passive ring melts remain practically unaffected despite the presence of strong confinement. This finding, therefore, confirms the analogy between equilibrium configurations of rings in the melt and non-equilibrium configurations of chromosomes in the cell nucleus, both of which are consistent with the fractal globule model. However, the presence of the confining sphere affects to a certain degree static and dynamic properties of rings that are located in close contact with it. More specifically, the peripheral rings are generally more compact, less threaded, and structurally relax faster. The previously-described equilibrium ring melts have been then used to study the formation of active topological glass in spherical confinement. Such setting enabled us to study the active topological glass for ring lengths up to $N = 1600$, which are otherwise inaccessible in the bulk regime for the reasons explained in Chapter 7. We have found that the active topological glass formation in a cavity generally resembles that in the bulk. A notable difference, however, arises from the fact that, for the longer rings considered, the sphere is not able to completely accommodate significantly stretched conformations of partly active rings from the bulk. This results in multiple “reflections” of the rings from the confining wall, as seen in Figure 1.2b. Furthermore, we have found that such ring conformations locally feature self-avoiding statistics. A high degree of inter-ring threading makes the relaxation of the system significantly correlated. Albeit ring conformations in the active topological glass are inconsistent with the large-scale chromatin organization, we speculate that the interplay between topological constraints and activity, which can result in a highly correlated dynamics, might play a role in explaining experimentally observed coherent motion of chromatin at smaller scales.

Bibliography

- [1] Glotzer, S. C. & Solomon, M. J. Anisotropy of building blocks and their assembly into complex structures. *Nat. Mater.* **6**, 557–562 (2007).
- [2] Liu, F. & Urban, M. W. Recent advances and challenges in designing stimuli-responsive polymers. *Prog. Polym. Sci.* **35**, 3–23 (2010).
- [3] de las Heras Alarcón, C., Pennadam, S. & Alexander, C. Stimuli responsive polymers for biomedical applications. *Chem. Soc. Rev.* **34**, 276–285 (2005).
- [4] Wei, M., Gao, Y., Li, X. & Serpe, M. J. Stimuli-responsive polymers and their applications. *Polym. Chem.* **8**, 127–143 (2017).
- [5] Schattling, P., Jochum, F. D. & Theato, P. Multi-stimuli responsive polymers – the all-in-one talents. *Polym. Chem.* **5**, 25–36 (2014).
- [6] Balkenende, D. W. R., Monnier, C. A., Fiore, G. L. & Weder, C. Optically responsive supramolecular polymer glasses. *Nat. Commun.* **7**, 10995 (2016).
- [7] Heskins, M. & Guillet, J. E. Solution properties of poly(N-isopropylacrylamide). *J. Macromol. Sci. A* **2**, 1441–1455 (1968).
- [8] Thévenot, J., Oliveira, H., Sandre, O. & Lecommandoux, S. Magnetic responsive polymer composite materials. *Chem. Soc. Rev.* **42**, 7099–7116 (2013).
- [9] Dai, S., Ravi, P. & Tam, K. C. pH-responsive polymers: synthesis, properties and applications. *Soft Matter* **4**, 435–449 (2008).
- [10] Davis, D. A. *et al.* Force-induced activation of covalent bonds in mechanoresponsive polymeric materials. *Nature* **459**, 68–72 (2009).
- [11] Tan, S., Saito, K. & Hearn, M. T. Stimuli-responsive polymeric materials for separation of biomolecules. *Curr. Opin. Biotechnol.* **53**, 209–223 (2018).

- [12] Randolph, L. M., Chien, M.-P. & Gianneschi, N. C. Biological stimuli and biomolecules in the assembly and manipulation of nanoscale polymeric particles. *Chem. Sci.* **3**, 1363–1380 (2012).
- [13] Webber, M. J., Appel, E. A., Meijer, E. W. & Langer, R. Supramolecular biomaterials. *Nat. Mater.* **15**, 13–26 (2016).
- [14] Stuart, M. A. C. *et al.* Emerging applications of stimuli-responsive polymer materials. *Nat. Mater.* **9**, 101–113 (2010).
- [15] Vlassopoulos, D., Pakula, T., Fytas, G., Pitsikalis, M. & Hadjichristidis, N. Controlling the self-assembly and dynamic response of star polymers by selective telechelic functionalization. *J. Chem. Phys.* **111**, 1760–1764 (1999).
- [16] C. Gârlea, I., Bianchi, E., Capone, B., Rovigatti, L. & N. Likos, C. Hierarchical self-organization of soft patchy nanoparticles into morphologically diverse aggregates. *Curr. Opin. Colloid Interface Sci.* **30**, 1–7 (2017).
- [17] Capone, B., Coluzza, I., Lo Verso, F., Likos, C. N. & Blaak, R. Telechelic star polymers as self-assembling units from the molecular to the macroscopic scale. *Phys. Rev. Lett.* **109**, 238301 (2012).
- [18] Rovigatti, L., Capone, B. & Likos, C. N. Soft self-assembled nanoparticles with temperature-dependent properties. *Nanoscale* **8**, 3288–3295 (2016).
- [19] Bianchi, E., Largo, J., Tartaglia, P., Zaccarelli, E. & Sciortino, F. Phase diagram of patchy colloids: Towards empty liquids. *Phys. Rev. Lett.* **97**, 168301 (2006).
- [20] Bianchi, E., Blaak, R. & Likos, C. N. Patchy colloids: state of the art and perspectives. *Phys. Chem. Chem. Phys.* **13**, 6397–6410 (2011).
- [21] Koch, C., Panagiotopoulos, A. Z., Lo Verso, F. & Likos, C. N. Customizing wormlike mesoscale structures via self-assembly of amphiphilic star polymers. *Soft Matter* **11**, 3530–3535 (2015).
- [22] Koch, C., Likos, C. N., Panagiotopoulos, A. Z. & Lo Verso, F. Self-assembly scenarios of block copolymer stars. *Mol. Phys.* **109**, 3049–3060 (2011).
- [23] Lo Verso, F., Panagiotopoulos, A. Z. & Likos, C. N. Phase behavior of low-functionality, telechelic star block copolymers. *Faraday Discuss.* **144**, 143–157 (2010).

- [24] Lo Verso, F., Panagiotopoulos, A. Z. & Likos, C. N. Aggregation phenomena in telechelic star polymer solutions. *Phys. Rev. E* **79**, 010401 (2009).
- [25] Gârlea, I. C., Jaramillo-Cano, D. & Likos, C. N. Self-organization of gel networks formed by block copolymer stars. *Soft Matter* **15**, 3527–3540 (2019).
- [26] Capone, B., Coluzza, I., Blaak, R., Verso, F. L. & Likos, C. N. Hierarchical self-assembly of telechelic star polymers: from soft patchy particles to gels and diamond crystals. *New J. Phys.* **15**, 095002 (2013).
- [27] Hamley, I. W. *Block copolymers in solution: fundamentals and applications* (John Wiley & Sons, 2005).
- [28] Frank-Kamenetskii, M. D., Lukashin, A. V. & Vologodskii, A. V. Statistical mechanics and topology of polymer chains. *Nature* **258**, 398–402 (1975).
- [29] Moore, N. T., Lua, R. C. & Grosberg, A. Y. Topologically driven swelling of a polymer loop. *Proc. Natl. Acad. Sci. U.S.A.* **101**, 13431–13435 (2004).
- [30] des Cloizeaux, J. Ring polymers in solution: topological effects. *J. Physique Lett.* **42**, 433–436 (1981).
- [31] Bohn, M. & Heermann, D. W. Topological interactions between ring polymers: Implications for chromatin loops. *J. Chem. Phys.* **132**, 044904 (2010).
- [32] Narros, A., Moreno, A. J. & Likos, C. N. Influence of topology on effective potentials: coarse-graining ring polymers. *Soft Matter* **6**, 2435–2441 (2010).
- [33] Chubak, I., Locatelli, E. & Likos, C. N. Ring polymers are much stronger depleting agents than linear ones. *Mol. Phys.* **116**, 2911–2926 (2018).
- [34] Weiss, L. B., Likos, C. N. & Nikoubashman, A. Spatial demixing of ring and chain polymers in pressure-driven flow. *Macromolecules* **52**, 7858–7869 (2019).
- [35] Narros, A., Moreno, A. J. & Likos, C. N. Effects of knots on ring polymers in solvents of varying quality. *Macromolecules* **46**, 3654–3668 (2013).
- [36] Liebetreu, M. & Likos, C. N. Hydrodynamic inflation of ring polymers under shear. *Comms. Mater.* **1**, 4 (2020).
- [37] Doi, M. & Edwards, S. F. *The theory of polymer dynamics* (Oxford University Press, 1988).

- [38] de Gennes, P. *Scaling concepts in polymer physics* (Cornell University Press, Ithaca, 1979).
- [39] McLeish, T. Polymers without beginning or end. *Science* **297**, 2005–2006 (2002).
- [40] Obukhov, S. P., Rubinstein, M. & Duke, T. Dynamics of a ring polymer in a gel. *Phys. Rev. Lett.* **73**, 1263–1266 (1994).
- [41] Khokhlov, A. R. & Nechaev, S. K. Polymer chain in an array of obstacles. *Phys. Lett. A* **112**, 156–160 (1985).
- [42] Cates, M. E. & Deutsch, J. M. Conjectures on the statistics of ring polymers. *J. Phys. France* **47**, 2121–2128 (1986).
- [43] Rubinstein, M. Dynamics of ring polymers in the presence of fixed obstacles. *Phys. Rev. Lett.* **57**, 3023–3026 (1986).
- [44] Grosberg, A. Y. Annealed lattice animal model and Flory theory for the melt of non-concatenated rings: towards the physics of crumpling. *Soft Matter* **10**, 560–565 (2014).
- [45] Smrek, J. & Grosberg, A. Y. Understanding the dynamics of rings in the melt in terms of the annealed tree model. *J. Phys. Condens. Matter* **27**, 064117 (2015).
- [46] Obukhov, S., Johner, A., Baschnagel, J., Meyer, H. & Wittmer, J. P. Melt of polymer rings: The decorated loop model. *EPL* **105**, 48005 (2014).
- [47] Ge, T., Panyukov, S. & Rubinstein, M. Self-similar conformations and dynamics in entangled melts and solutions of nonconcatenated ring polymers. *Macromolecules* **49**, 708–722 (2016).
- [48] Sakaue, T. Ring polymers in melts and solutions: scaling and crossover. *Phys. Rev. Lett.* **106**, 167802 (2012).
- [49] Suzuki, J., Takano, A., Deguchi, T. & Matsushita, Y. Dimension of ring polymers in bulk studied by Monte-Carlo simulation and self-consistent theory. *J. Chem. Phys.* **131**, 144902 (2009).
- [50] Halverson, J. D., Lee, W. B., Grest, G. S., Grosberg, A. Y. & Kremer, K. Molecular dynamics simulation study of nonconcatenated ring polymers in a melt. I. Statics. *J. Chem. Phys.* **134**, 204904 (2011).

- [51] Halverson, J. D., Lee, W. B., Grest, G. S., Grosberg, A. Y. & Kremer, K. Molecular dynamics simulation study of nonconcatenated ring polymers in a melt. II. Dynamics. *J. Chem. Phys.* **134**, 204905 (2011).
- [52] Rosa, A. & Everaers, R. Ring polymers in the melt state: The physics of crumpling. *Phys. Rev. Lett.* **112**, 118302 (2014).
- [53] Schram, R. D., Rosa, A. & Everaers, R. Local loop opening in untangled ring polymer melts: a detailed “Feynman test” of models for the large scale structure. *Soft Matter* **15**, 2418–2429 (2019).
- [54] Lang, M. Ring conformations in bidisperse blends of ring polymers. *Macromolecules* **46**, 1158–1166 (2013).
- [55] Müller, M., Wittmer, J. P. & Cates, M. E. Topological effects in ring polymers: A computer simulation study. *Phys. Rev. E* **53**, 5063–5074 (1996).
- [56] Müller, M., Wittmer, J. P. & Cates, M. E. Topological effects in ring polymers. II. Influence of persistence length. *Phys. Rev. E* **61**, 4078–4089 (2000).
- [57] Kapnistos, M. *et al.* Unexpected power-law stress relaxation of entangled ring polymers. *Nat. Mater.* **7**, 997 (2008).
- [58] Brás, A. R. *et al.* Compact structure and non-gaussian dynamics of ring polymer melts. *Soft Matter* **10**, 3649–3655 (2014).
- [59] Vlassopoulos, D. Macromolecular topology and rheology: beyond the tube model. *Rheol. Acta* **55**, 613–632 (2016).
- [60] Goöben, S. *et al.* Influence of the solvent quality on ring polymer dimensions. *Macromolecules* **48**, 1598–1605 (2015).
- [61] Gómez, L. R., García, N. A. & Pöschel, T. Packing structure of semiflexible rings. *Proc. Natl. Acad. Sci. U.S.A* **117**, 3382–3387 (2020).
- [62] Rosa, A. & Everaers, R. Conformational statistics of randomly branching double-folded ring polymers. *Eur. Phys. J. E* **42**, 7 (2019).
- [63] Smrek, J. & Grosberg, A. Y. Minimal surfaces on unconcatenated polymer rings in melt. *ACS Macro Lett.* **5**, 750–754 (2016).

- [64] Tsalikis, D. G., Mavrantzas, V. G. & Vlassopoulos, D. Analysis of slow modes in ring polymers: Threading of rings controls long-time relaxation. *ACS Macro Lett.* **5**, 755–760 (2016).
- [65] Michieletto, D., Marenduzzo, D., Orlandini, E., Alexander, G. P. & Turner, M. S. Threading dynamics of ring polymers in a gel. *ACS Macro Lett.* **3**, 255–259 (2014).
- [66] Michieletto, D. & Turner, M. S. A topologically driven glass in ring polymers. *Proc. Natl. Acad. Sci. U.S.A* **113**, 5195–5200 (2016).
- [67] Lee, E., Kim, S. & Jung, Y. Slowing down of ring polymer diffusion caused by inter-ring threading. *Macromol. Rapid Commun.* **36**, 1115–1121 (2015).
- [68] Lee, E. & Jung, Y. Slow dynamics of ring polymer melts by asymmetric interaction of threading configuration: Monte Carlo study of a dynamically constrained lattice model. *Polymers* **11** (2019).
- [69] Obukhov, S. P. Talk at KITP Santa Barbara. Accessed Apr. 2019 (1997).
- [70] Michieletto, D., Nahali, N. & Rosa, A. Glassiness and heterogeneous dynamics in dense solutions of ring polymers. *Phys. Rev. Lett.* **119**, 197801 (2017).
- [71] Michieletto, D., Marenduzzo, D., Orlandini, E., Alexander, G. P. & Turner, M. S. Dynamics of self-threading ring polymers in a gel. *Soft Matter* **10**, 5936–5944 (2014).
- [72] Smrek, J., Kremer, K. & Rosa, A. Threading of unconcatenated ring polymers at high concentrations: double-folded vs time-equilibrated structures. *ACS Macro Lett.* **8**, 155–160 (2019).
- [73] Grosberg, A. Y. & Joanny, J.-F. Nonequilibrium statistical mechanics of mixtures of particles in contact with different thermostats. *Phys. Rev. E* **92**, 032118 (2015).
- [74] Grosberg, A. Y. & Joanny, J.-F. Dissipation in a system driven by two different thermostats. *Polym. Sci. Ser. C* **60**, 118–121 (2018).
- [75] Ilker, E. & Joanny, J.-F. Phase separation and nucleation in mixtures of particles with different temperatures. *Phys. Rev. Research* **2**, 023200 (2020).
- [76] Tanaka, H., Lee, A. A. & Brenner, M. P. Hot particles attract in a cold bath. *Phys. Rev. Fluids* **2**, 043103 (2017).

- [77] Weber, S. N., Weber, C. A. & Frey, E. Binary mixtures of particles with different diffusivities demix. *Phys. Rev. Lett.* **116**, 058301 (2016).
- [78] Smrek, J. & Kremer, K. Small activity differences drive phase separation in active-passive polymer mixtures. *Phys. Rev. Lett.* **118**, 098002 (2017).
- [79] Smrek, J. & Kremer, K. Interfacial properties of active-passive polymer mixtures. *Entropy* **20** (2018).
- [80] Rubinstein, M. & Colby, R. H. *Polymer physics* (Oxford University Press, New York, 2003).
- [81] Alberts, B. *Molecular biology of the cell* (Garland Science, Taylor and Francis Group, 2018).
- [82] Jeppsson, K., Kanno, T., Shirahige, K. & Sjögren, C. The maintenance of chromosome structure: positioning and functioning of SMC complexes. *Nat. Rev. Mol. Cell Biol.* **15**, 601–614 (2014).
- [83] Cremer, T. & Cremer, C. Chromosome territories, nuclear architecture and gene regulation in mammalian cells. *Nat. Rev. Genet.* **2**, 292–301 (2001).
- [84] Rosa, A. & Everaers, R. Structure and dynamics of interphase chromosomes. *PLOS Comput. Biol.* **4**, 1–10 (2008).
- [85] Halverson, J. D., Smrek, J., Kremer, K. & Grosberg, A. Y. From a melt of rings to chromosome territories: the role of topological constraints in genome folding. *Rep. Prog. Phys.* **77**, 022601 (2014).
- [86] Sazer, S. & Schiessel, H. The biology and polymer physics underlying large-scale chromosome organization. *Traffic* **19**, 87–104 (2018).
- [87] Lieberman-Aiden, E. *et al.* Comprehensive mapping of long-range interactions reveals folding principles of the human genome. *Science* **326**, 289–293 (2009).
- [88] Imakaev, M. V., Tchourine, K. M., Nechaev, S. K. & Mirny, L. A. Effects of topological constraints on globular polymers. *Soft Matter* **11**, 665–671 (2015).
- [89] Grosberg, A. Y., Nechaev, S. K. & Shakhnovich, E. I. The role of topological constraints in the kinetics of collapse of macromolecules. *J. Phys. France* **49**, 2095–2100 (1988).

- [90] Grosberg, A., Rabin, Y., Havlin, S. & Neer, A. Crumpled globule model of the three-dimensional structure of DNA. *EPL* **23**, 373–378 (1993).
- [91] Cremer, T. *et al.* The 4D nucleome: Evidence for a dynamic nuclear landscape based on co-aligned active and inactive nuclear compartments. *FEBS Lett.* **589**, 2931–2943 (2015).
- [92] Solovei, I., Thanisch, K. & Feodorova, Y. How to rule the nucleus: divide et impera. *Curr. Opin. Cell Biol.* **40**, 47–59 (2016).
- [93] Jost, D., Carrivain, P., Cavalli, G. & Vaillant, C. Modeling epigenome folding: formation and dynamics of topologically associated chromatin domains. *Nucleic Acids Res.* **42**, 9553–9561 (2014).
- [94] Ganai, N., Sengupta, S. & Menon, G. I. Chromosome positioning from activity-based segregation. *Nucleic Acids Res.* **42**, 4145–4159 (2014).
- [95] Agrawal, A., Ganai, N., Sengupta, S. & Menon, G. I. Chromatin as active matter. *J. Stat. Mech.: Theory Exp.* **2017**, 014001 (2017).
- [96] Saintillan, D., Shelley, M. J. & Zidovska, A. Extensile motor activity drives coherent motions in a model of interphase chromatin. *Proc. Natl. Acad. Sci. U.S.A* **115**, 11442–11447 (2018).
- [97] Liu, L., Shi, G., Thirumalai, D. & Hyeon, C. Chain organization of human interphase chromosome determines the spatiotemporal dynamics of chromatin loci. *PLOS Comput. Biol.* **14**, 1–20 (2018).
- [98] Nuebler, J., Fudenberg, G., Imakaev, M., Abdennur, N. & Mirny, L. A. Chromatin organization by an interplay of loop extrusion and compartmental segregation. *Proc. Natl. Acad. Sci. U.S.A.* **115**, E6697–E6706 (2018).
- [99] Fudenberg, G. *et al.* Formation of chromosomal domains by loop extrusion. *Cell Rep.* **15**, 2038–2049 (2016).
- [100] Zidovska, A., Weitz, D. A. & Mitchison, T. J. Micron-scale coherence in interphase chromatin dynamics. *Proc. Natl. Acad. Sci. U.S.A.* **110**, 15555–15560 (2013).
- [101] Shaban, H. A., Barth, R. & Bystricky, K. Formation of correlated chromatin domains at nanoscale dynamic resolution during transcription. *Nucleic Acids Res.* **46**, e77–e77 (2018).

- [102] Cloitre, M. (ed.) *High solid dispersions* (Springer, Berlin, Germany, 2010).
- [103] Cordier, P., Tournilhac, F., Soulié-Ziakovic, C. & Leibler, L. Self-healing and thermoreversible rubber from supramolecular assembly. *Nature* **451**, 977–980 (2008).
- [104] Bianchi, E., Capone, B., Kahl, G. & Likos, C. N. Soft-patchy nanoparticles: Modeling and self-organization. *Faraday Discuss.* **181**, 123–138 (2015).
- [105] Chakrabarty, R., Mukherjee, P. S. & Stang, P. J. Supramolecular coordination: Self-assembly of finite two- and three-dimensional ensembles. *Chem. Rev.* **111**, 6810–6918 (2011).
- [106] Mather, P. T., Luo, X. & Rousseau, I. A. Shape memory polymer research. *Annu. Rev. Mater. Res.* **39**, 445–471 (2009).
- [107] Wu, Y. *et al.* Self-healing supramolecular bioelastomers with shape memory property as a multifunctional platform for biomedical applications via modular assembly. *Biomaterials* **104**, 18–31 (2016).
- [108] Fameau, A.-L. & Saint-Jalmes, A. Yielding and flow of solutions of thermoresponsive surfactant tubes: Tuning macroscopic rheology by supramolecular assemblies. *Soft Matter* **10**, 3622–3632 (2014).
- [109] Zhuge, F., Hawke, L. G. D., Fustin, C.-A., Gohy, J.-F. & van Ruymbeke, E. Decoding the linear viscoelastic properties of model telechelic metallo-supramolecular polymers. *J. Rheol.* **61**, 1245–1262 (2017).
- [110] Xing, Z., Ness, C., Frenkel, D. & Eiser, E. Structural and linear elastic properties of DNA hydrogels by coarse-grained simulation. *Macromolecules* **52**, 504–512 (2019).
- [111] Fernandez-Castanon, J., Bianchi, S., Saglimbeni, F., Di Leonardo, R. & Sciortino, F. Microrheology of DNA hydrogel gelling and melting on cooling. *Soft Matter* **14**, 6431–6438 (2018).
- [112] Bomboi, F. *et al.* Re-entrant DNA gels. *Nat. Commun.* **7**, 13191 (2016).
- [113] Zhang, Z., Chen, Q. & Colby, R. H. Dynamics of associative polymers. *Soft Matter* **14**, 2961–2977 (2018).
- [114] Winnik, M. A. & Yekta, A. Associative polymers in aqueous solution. *Curr. Opin. Colloid Interface Sci.* **2**, 424–436 (1997).

- [115] Lo Verso, F. & Likos, C. N. End-functionalized polymers: Versatile building blocks for soft materials. *Polymer* **49**, 1425–1434 (2008).
- [116] Pitsikalis, M., Hadjichristidis, N. & Mays, J. W. Model mono-, di-, and tri- ω -functionalized three-arm star polybutadienes. Association behavior in dilute solution by dynamic light scattering and viscometry. *Macromolecules* **29**, 179–184 (1996).
- [117] Charalabidis, D., Pitsikalis, M. & Hadjichristidis, N. Model linear and star-shaped polyisoprenes with phosphatidylcholine analogous end-groups. Synthesis and association behavior in cyclohexane. *Macromol. Chem. Phys.* **203**, 2132–2141 (2002).
- [118] Vlassopoulos, D., Pitsikalis, M. & Hadjichristidis, N. Linear dynamics of end-functionalized polymer melts: Linear chains, stars, and blends. *Macromolecules* **33**, 9740–9746 (2000).
- [119] Zilman, A. G. & Safran, S. A. Entropically driven attraction between telechelic brushes. *Eur. Phys. J. E* **4**, 467–473 (2001).
- [120] Van Ruymbeke, E. *et al.* Rheology and structure of entangled telechelic linear and star polyisoprene melts. *Macromolecules* **43**, 4401–4411 (2010).
- [121] Lo Verso, F., Likos, C. N., Mayer, C. & Löwen, H. Collapse of telechelic star polymers to watermelon structures. *Phys. Rev. Lett.* **96**, 187802 (2006).
- [122] Lo Verso, F., Likos, C. N. & Löwen, H. Computer simulation of thermally sensitive telechelic star polymers. *J. Phys. Chem. C* **111**, 15803–15810 (2007).
- [123] Koch, C., Panagiotopoulos, A. Z., Lo Verso, F. & Likos, C. N. Phase behavior of rigid, amphiphilic star polymers. *Soft Matter* **9**, 7424–7436 (2013).
- [124] Giacomelli, F. C., Riegel, I. C., Petzhold, C. L., da Silveira, N. P. & Štěpánek, P. Internal structural characterization of triblock copolymer micelles with looped corona chains. *Langmuir* **25**, 3487–3493 (2009).
- [125] Giacomelli, F. C., Riegel, I. C., Petzhold, C. L., da Silveira, N. P. & Štěpánek, P. Aggregation behavior of a new series of ABA triblock copolymers bearing short outer A blocks in B-selective solvent: From free chains to bridged micelles. *Langmuir* **25**, 731–738 (2009).

- [126] Geerissen, H. & Wolf, B. A. Phenylalkanes as theta-solvents for polystyrene. *Makromol. Chem., Rapid Commun.* **3**, 17–21 (1982).
- [127] Kremer, K. & Grest, G. S. Dynamics of entangled linear polymer melts: A molecular-dynamics simulation. *J. Chem. Phys.* **92**, 5057–5086 (1990).
- [128] Huissmann, S., Blaak, R. & Likos, C. N. Star polymers in solvents of varying quality. *Macromolecules* **42**, 2806–2816 (2009).
- [129] Ladanyi, B. M. & Chandler, D. New type of cluster theory for molecular fluids: Interaction site cluster expansion. *J. Chem. Phys.* **62**, 4308–4324 (1975).
- [130] Provencher, S. W. CONTIN: A general purpose constrained regularization program for inverting noisy linear algebraic and integral equations. *Comput. Phys. Commun* **27**, 229–242 (1982).
- [131] Müller-Plathe, F. Reversing the perturbation in nonequilibrium molecular dynamics: An easy way to calculate the shear viscosity of fluids. *Phys. Rev. E* **59**, 4894–4898 (1999).
- [132] Malevanets, A. & Kapral, R. Mesoscopic model for solvent dynamics. *J. Chem. Phys.* **110**, 8605–8613 (1999).
- [133] Howard, M. P., Panagiotopoulos, A. Z. & Nikoubashman, A. Efficient mesoscale hydrodynamics: Multiparticle collision dynamics with massively parallel GPU acceleration. *Comput. Phys. Commun.* **230**, 10–20 (2018).
- [134] Glaser, J. *et al.* Strong scaling of general-purpose molecular dynamics simulations on GPUs. *Comput. Phys. Commun.* **192**, 97–107 (2015).
- [135] Anderson, J. A., Lorenz, C. D. & Travesset, A. General purpose molecular dynamics simulations fully implemented on graphics processing units. *J. Comput. Phys.* **227**, 5342–5359 (2008).
- [136] <https://github.com/mphoward/azplugins>.
- [137] Pan, S. *et al.* Shear thinning in dilute and semidilute solutions of polystyrene and DNA. *J. Rheol.* **62**, 845–867 (2018).
- [138] Graessley, W. W. *The entanglement concept in polymer rheology*, 1–179 (Springer Berlin Heidelberg, Berlin, Heidelberg, 1974).

- [139] Larson, R. G. The rheology of dilute solutions of flexible polymers: Progress and problems. *J. Rheol.* **49**, 1–70 (2005).
- [140] Pamies, R., Lopez Martinez, M. C., Hernandez Cifre, J. G. & Garcia de la Torre, J. Non-newtonian viscosity of dilute polymer solutions. *Macromolecules* **38**, 1371–1377 (2005).
- [141] Singh, S. P., Chatterji, A., Gompper, G. & Winkler, R. G. Dynamical and rheological properties of ultrasoft colloids under shear flow. *Macromolecules* **46**, 8026–8036 (2013).
- [142] Berne, B. J. & Pecora, R. *Dynamic light scattering: with applications to chemistry, biology, and physics* (Courier Corporation, 2000).
- [143] Kroeger, A., Belack, J., Larsen, A., Fytas, G. & Wegner, G. Supramolecular structures in aqueous solutions of rigid polyelectrolytes with monovalent and divalent counterions. *Macromolecules* **39**, 7098–7106 (2006).
- [144] Bockstaller, M., Köhler, W., Wegner, G., Vlassopoulos, D. & Fytas, G. Levels of structure formation in aqueous solutions of anisotropic association colloids consisting of rodlike polyelectrolytes. *Macromolecules* **34**, 6359–6366 (2001).
- [145] Ashbaugh, H. S. & Hatch, H. W. Natively unfolded protein stability as a coil-to-globule transition in charge/hydrophathy space. *J. Am. Chem. Soc.* **130**, 9536–9542 (2008).
- [146] Fetters, L. J., Lohse, D. J. & Colby, R. H. *Chain dimensions and entanglement spacings*, 447–454 (Springer New York, New York, NY, 2007).
- [147] Weeks, J. D., Chandler, D. & Andersen, H. C. Role of repulsive forces in determining the equilibrium structure of simple liquids. *J. Chem. Phys.* **54**, 5237–5247 (1971).
- [148] Pierleoni, C., Addison, C., Hansen, J.-P. & Krakoviack, V. Multiscale coarse graining of diblock copolymer self-assembly: From monomers to ordered micelles. *Phys. Rev. Lett.* **96**, 128302 (2006).
- [149] Pierleoni, C., Capone, B. & Hansen, J.-P. A soft effective segment representation of semidilute polymer solutions. *J. Chem. Phys.* **127**, 171102 (2007).
- [150] Narros, A., Likos, C. N., Moreno, A. J. & Capone, B. Multi-blob coarse graining for ring polymer solutions. *Soft Matter* **10**, 9601–9614 (2014).

- [151] Capone, B., Pierleoni, C., Hansen, J.-P. & Krakoviack, V. Entropic self-assembly of diblock copolymers into disordered and ordered micellar phases. *J. Phys. Chem. B* **113**, 3629–3638 (2009).
- [152] Capone, B. *Coarse-graining polymer solutions in the semi-dilute regime*. Ph.D. thesis, University of Cambridge (2010).
- [153] Capone, B., Coluzza, I. & Hansen, J.-P. A systematic coarse-graining strategy for semi-dilute copolymer solutions: from monomers to micelles. *J. Phys. Condens. Matter* **23**, 194102 (2011).
- [154] Attard, P. Spherically inhomogeneous fluids. I. Percus-Yevick hard spheres: Osmotic coefficients and triplet correlations. *J. Chem. Phys.* **91**, 3072–3082 (1989).
- [155] Attard, P. Lennard-Jones bridge functions and triplet correlation functions. *J. Chem. Phys.* **95**, 4471–4480 (1991).
- [156] Louis, A. A., Bolhuis, P. G., Hansen, J. P. & Meijer, E. J. Can polymer coils be modeled as “soft colloids”? *Phys. Rev. Lett.* **85**, 2522–2525 (2000).
- [157] Moe, N. E. & Ediger, M. D. Calculation of the coherent dynamic structure factor of polyisoprene from molecular dynamics simulations. *Phys. Rev. E* **59**, 623–630 (1999).
- [158] Salacuse, J. J., Denton, A. R. & Egelstaff, P. A. Finite-size effects in molecular dynamics simulations: Static structure factor and compressibility. I. Theoretical method. *Phys. Rev. E* **53**, 2382–2389 (1996).
- [159] Salacuse, J. J., Denton, A. R., Egelstaff, P. A., Tau, M. & Reatto, L. Finite-size effects in molecular dynamics simulations: Static structure factor and compressibility. II. Application to a model krypton fluid. *Phys. Rev. E* **53**, 2390–2401 (1996).
- [160] Noguchi, H., Kikuchi, N. & Gompper, G. Particle-based mesoscale hydrodynamic techniques. *EPL* **78**, 10005 (2007).
- [161] Gompper, G., Ihle, T., Kroll, D. M. & Winkler, R. G. *Multi-particle collision dynamics: A particle-based mesoscale simulation approach to the hydrodynamics of complex fluids*, 1–87 (Springer Berlin Heidelberg, Berlin, Heidelberg, 2009).
- [162] Kapral, R. *Multiparticle collision dynamics: simulation of complex systems on mesoscales*, 89–146 (Wiley-Blackwell, 2008).

- [163] Huang, C.-C., Varghese, A., Gompper, G. & Winkler, R. Thermostat for nonequilibrium multiparticle-collision-dynamics simulations. *Phys. Rev. E* **91**, 013310 (2015).
- [164] Huang, C., Chatterji, A., Sutmann, G., Gompper, G. & Winkler, R. Cell-level canonical sampling by velocity scaling for multiparticle collision dynamics simulations. *J. Comput. Phys.* **229**, 168–177 (2010).
- [165] Ripoll, M., Mussawisade, K., Winkler, R. & Gompper, G. Dynamic regimes of fluids simulated by multiparticle-collision dynamics. *Phys. Rev. E* **72**, 016701 (2005).
- [166] Müller-Plathe, F. Reversing the perturbation in nonequilibrium molecular dynamics: An easy way to calculate the shear viscosity of fluids. *Phys. Rev. E* **59**, 4894 (1999).
- [167] Statt, A., Howard, M. P. & Panagiotopoulos, A. Z. Unexpected secondary flows in reverse nonequilibrium shear flow simulations. *Phys. Rev. Fluids* **4**, 043905 (2019).
- [168] Tenney, C. & Maginn, E. Limitations and recommendations for the calculation of shear viscosity using reverse nonequilibrium molecular dynamics. *J. Chem. Phys.* **132**, 014103 (2010).
- [169] Petersen, M. K. *et al.* Mesoscale hydrodynamics via stochastic rotation dynamics: Comparison with Lennard-Jones fluid. *J. Chem. Phys.* **132**, 174106 (2010).
- [170] Pavlovic, M., Antonietti, M., Schmidt, B. V. & Zeininger, L. Responsive Janus and Cerberus emulsions via temperature-induced phase separation in aqueous polymer mixtures. *J. Colloid Interface Sci.* **575**, 88–95 (2020).
- [171] Salonen, A., Langevin, D. & Perrin, P. Light and temperature bi-responsive emulsion foams. *Soft Matter* **6**, 5308–5311 (2010).
- [172] Vandenhaute, M., Schelfhout, J., Van Vlierberghe, S., Mendes, E. & Dubruel, P. Cross-linkable, thermo-responsive pluronic® building blocks for biomedical applications: Synthesis and physico-chemical evaluation. *Eur. Polym. J.* **53**, 126–138 (2014).
- [173] Dong, J. *et al.* Multiple stimuli-responsive polymeric micelles for controlled release. *Soft Matter* **9**, 370–373 (2013).
- [174] Deng, X., Livingston, J. L., Spear, N. J. & Jennings, G. K. pH-responsive copolymer films prepared by surface-initiated polymerization and simple modification. *Langmuir* **36**, 715–722 (2020).

- [175] Fan, T.-F. *et al.* Transformation of hard pollen into soft matter. *Nat. Commun.* **11**, 1–10 (2020).
- [176] Han, P. *et al.* UV-responsive polymeric superamphiphile based on a complex of malachite green derivative and a double hydrophilic block copolymer. *Langmuir* **27**, 14108–14111 (2011).
- [177] Balkenende, D. W., Monnier, C. A., Fiore, G. L. & Weder, C. Optically responsive supramolecular polymer glasses. *Nat. Commun.* **7**, 1–9 (2016).
- [178] Weiss, L. B., Nikoubashman, A. & Likos, C. N. Topology-sensitive microfluidic filter for polymers of varying stiffness. *ACS Macro Lett.* **6**, 1426–1431 (2017).
- [179] Ahmadian Dehaghani, Z., Chubak, I., Likos, C. N. & Ejtehadi, M. R. Effects of topological constraints on linked ring polymers in solvents of varying quality. *Soft Matter* **16**, 3029–3038 (2020).
- [180] Rauscher, P. M., Rowan, S. J. & de Pablo, J. J. Topological effects in isolated poly[n]catenanes: Molecular dynamics simulations and rouse mode analysis. *ACS Macro Lett.* **7**, 938–943 (2018).
- [181] Wu, Q. *et al.* Poly[n]catenanes: Synthesis of molecular interlocked chains. *Science* **358**, 1434–1439 (2017).
- [182] Slimani, M. Z. *et al.* Cluster glasses of semiflexible ring polymers. *ACS Macro Lett.* **3**, 611–616 (2014).
- [183] Rauscher, P. M., Schweizer, K. S., Rowan, S. J. & de Pablo, J. J. Thermodynamics and structure of poly[n]catenane melts. *Macromolecules* **53**, 3390–3408 (2020).
- [184] Smrek, J., Chubak, I., Likos, C. N. & Kremer, K. Active topological glass. *Nat. Commun.* **11**, 26 (2020).
- [185] Klotz, A. R., Soh, B. W. & Doyle, P. S. Equilibrium structure and deformation response of 2D kinetoplast sheets. *Proc. Natl. Acad. Sci. U.S.A.* **117**, 121–127 (2020).
- [186] Rosa, A., Smrek, J., Turner, M. S. & Michieletto, D. Threading-induced dynamical transition in tadpole-shaped polymers. *ACS Macro Lett.* **9**, 743–748 (2020).
- [187] Biffi, S. *et al.* Equilibrium gels of low-valence DNA nanostars: a colloidal model for strong glass formers. *Soft Matter* **11**, 3132–3138 (2015).

- [188] Mirkin, C. A., Letsinger, R. L., Mucic, R. C. & Storhoff, J. J. A DNA-based method for rationally assembling nanoparticles into macroscopic materials. *Nature* **382**, 607–609 (1996).
- [189] Dreyfus, R. *et al.* Simple quantitative model for the reversible association of DNA coated colloids. *Phys. Rev. Lett.* **102**, 048301 (2009).
- [190] Angioletti-Uberti, S., Mognetti, B. M. & Frenkel, D. Re-entrant melting as a design principle for DNA-coated colloids. *Nat. Mater.* **11**, 518–522 (2012).
- [191] Broze, G., Jérôme, R. & Teyssié, P. Halato-telechelic polymers. 4. Synthesis and dilute-solution behavior. *Macromolecules* **15**, 920–927 (1982).
- [192] Moghimi, E. *et al.* Self-organization and flow of low-functionality telechelic star polymers with varying attraction. *ACS Macro Lett.* **8**, 766–772 (2019).
- [193] Groot, R. D. & Warren, P. B. Dissipative particle dynamics: Bridging the gap between atomistic and mesoscopic simulation. *J. Chem. Phys.* **107**, 4423–4435 (1997).
- [194] Phillips, C. L., Anderson, J. A. & Glotzer, S. C. Pseudo-random number generation for Brownian dynamics and dissipative particle dynamics simulations on GPU devices. *J. Comput. Phys.* **230**, 7191–7201 (2011).
- [195] Verlet, L. Computer “experiments” on classical fluids. I. Thermodynamical properties of Lennard-Jones molecules. *Phys. Rev.* **159**, 98–103 (1967).
- [196] Wolff, T., Burger, C. & Ruland, W. Synchrotron SAXS study of the microphase separation transition in diblock copolymers. *Macromolecules* **26**, 1707–1711 (1993).
- [197] Groot, R. D. & Madden, T. J. Dynamic simulation of diblock copolymer microphase separation. *J. Chem. Phys.* **108**, 8713–8724 (1998).
- [198] Likos, C. N. Effective interactions in soft condensed matter physics. *Phys. Rep.* **348**, 267–439 (2001).
- [199] Daoud, M. & Cotton, J. Star shaped polymers : A model for the conformation and its concentration dependence. *J. Phys. France* **43**, 531–538 (1982).
- [200] Hsu, H.-P., Nadler, W. & Grassberger, P. Scaling of star polymers with 1–80 arms. *Macromolecules* **37**, 4658–4663 (2004).

- [201] Ye, X. & Khomami, B. Self-assembly of linear diblock copolymers in selective solvents: from single micelles to particles with tri-continuous inner structures. *Soft Matter* **16**, 6056–6062 (2020).
- [202] Berthier, L. & Biroli, G. Theoretical perspective on the glass transition and amorphous materials. *Rev. Mod. Phys.* **83**, 587–645 (2011).
- [203] Gnan, N. & Zaccarelli, E. The microscopic role of deformation in the dynamics of soft colloids. *Nat. Phys.* (2019).
- [204] Lo, Wei-Chang & Turner, Matthew S. The topological glass in ring polymers. *EPL* **102**, 58005 (2013).
- [205] Biroli, G., Bouchaud, J.-P., Cavagna, A., Grigera, T. S. & Verrocchio, P. Thermodynamic signature of growing amorphous order in glass-forming liquids. *Nat. Phys.* **4**, 771 (2008).
- [206] Cammarota, C. & Biroli, G. Ideal glass transitions by random pinning. *Proc. Natl. Acad. Sci. U.S.A* **109**, 8850–8855 (2012).
- [207] Karmakar, S. & Parisi, G. Random pinning glass model. *Proc. Natl. Acad. Sci. U.S.A* **110**, 2752–2757 (2013).
- [208] Berthier, L. & Kurchan, J. Non-equilibrium glass transitions in driven and active matter. *Nat. Phys.* **9**, 310 (2013).
- [209] Nandi, S. K. *et al.* A random first-order transition theory for an active glass. *Proc. Natl. Acad. Sci. U.S.A* **115**, 7688–7693 (2018).
- [210] Berthier, L., Flenner, E. & Szamel, G. How active forces influence nonequilibrium glass transitions. *New J. Phys.* **19**, 125006 (2017).
- [211] Berthier, L., Flenner, E. & Szamel, G. Glassy dynamics in dense systems of active particles. *J. Chem. Phys.* **150**, 200901 (2019).
- [212] Nandi, S. K. & Gov, N. S. Nonequilibrium mode-coupling theory for dense active systems of self-propelled particles. *Soft Matter* **13**, 7609–7616 (2017).
- [213] Zhang, R., Zhou, Y., Rahimi, M. & de Pablo, J. J. Dynamic structure of active nematic shells. *Nat. Commun.* **7**, 13483 (2016).

- [214] Sknepnek, R. & Henkes, S. Active swarms on a sphere. *Phys. Rev. E* **91**, 022306 (2015).
- [215] Khoromskaia, D. & Alexander, G. P. Vortex formation and dynamics of defects in active nematic shells. *New J. Phys.* **19**, 103043 (2017).
- [216] Alaimo, F., Köhler, C. & Voigt, A. Curvature controlled defect dynamics in topological active nematics. *Sci. Rep.* **7**, 5211–5211 (2017).
- [217] Janssen, L. M. C., Kaiser, A. & Löwen, H. Aging and rejuvenation of active matter under topological constraints. *Sci. Rep.* **7**, 5667 (2017).
- [218] Fecko, M. *Differential geometry and Lie groups for physicists* (Cambridge University Press, 2011).
- [219] Parry, B. R. *et al.* The bacterial cytoplasm has glass-like properties and is fluidized by metabolic activity. *Cell* **156**, 183–194 (2014).
- [220] Angelini, T. E. *et al.* Glass-like dynamics of collective cell migration. *Proc. Natl. Acad. Sci. U.S.A.* **108**, 4714–4719 (2011).
- [221] Shi, G., Liu, L., Hyeon, C. & Thirumalai, D. Interphase human chromosome exhibits out of equilibrium glassy dynamics. *Nat. Commun.* **9**, 3161 (2018).
- [222] Bi, D., Lopez, J. H., Schwarz, J. M. & Manning, M. L. A density-independent rigidity transition in biological tissues. *Nat. Phys.* **11**, 1074 (2015).
- [223] Bi, D., Yang, X., Marchetti, M. C. & Manning, M. L. Motility-driven glass and jamming transitions in biological tissues. *Phys. Rev. X* **6**, 021011 (2016).
- [224] Binder, K. & Kob, W. *Glassy materials and disordered solids* (World Scientific, 2011), revised edn.
- [225] Cavagna, A. Supercooled liquids for pedestrians. *Phys. Rep.* **476**, 51–124 (2009).
- [226] Götze, W. & Sjörgen, L. Relaxation processes in supercooled liquids. *Rep. Prog. Phys.* **55**, 241–376 (1992).
- [227] Frick, B. & Richter, D. The microscopic basis of the glass transition in polymers from neutron scattering studies. *Science* **267**, 1939–1945 (1995).
- [228] van Megen, W. & Pusey, P. N. Dynamic light-scattering study of the glass transition in a colloidal suspension. *Phys. Rev. A* **43**, 5429–5441 (1991).

- [229] Krakoviack, V. Liquid-glass transition of a fluid confined in a disordered porous matrix: a mode-coupling theory. *Phys. Rev. Lett.* **94**, 065703 (2005).
- [230] Krakoviack, V. Mode-coupling theory for the slow collective dynamics of fluids adsorbed in disordered porous media. *Phys. Rev. E* **75**, 031503 (2007).
- [231] Krakoviack, V. Tagged-particle dynamics in a fluid adsorbed in a disordered porous solid: Interplay between the diffusion-localization and the liquid-glass transitions. *Phys. Rev. E* **79**, 061501 (2009).
- [232] Franosch, T., Fuchs, M., Götze, W., Mayr, M. R. & Singh, A. P. Asymptotic laws and preasymptotic correction formulas for the relaxation near glass-transition singularities. *Phys. Rev. E* **55**, 7153–7176 (1997).
- [233] Fuchs, M., Götze, W. & Mayr, M. R. Asymptotic laws for tagged-particle motion in glassy systems. *Phys. Rev. E* **58**, 3384–3399 (1998).
- [234] Götze, W. & Sperl, M. Logarithmic relaxation in glass-forming systems. *Phys. Rev. E* **66**, 011405 (2002).
- [235] Sperl, M. Logarithmic relaxation in a colloidal system. *Phys. Rev. E* **68**, 031405 (2003).
- [236] Zaccarelli, E. Colloidal gels: equilibrium and non-equilibrium routes. *J. Phys. Condens. Matter* **19**, 323101 (2007).
- [237] Battle, C. *et al.* Broken detailed balance at mesoscopic scales in active biological systems. *Science* **352**, 604–607 (2016).
- [238] Chaudhuri, P., Berthier, L. & Kob, W. Universal nature of particle displacements close to glass and jamming transitions. *Phys. Rev. Lett.* **99**, 060604 (2007).
- [239] Huang, Q. *et al.* Unexpected stretching of entangled ring macromolecules. *Phys. Rev. Lett.* **122**, 208001 (2019).
- [240] O’Connor, T. C., Ge, T., Rubinstein, M. & Grest, G. S. Topological linking drives anomalous thickening of ring polymers in weak extensional flows. *Phys. Rev. Lett.* **124**, 027801 (2020).
- [241] Bechinger, C. *et al.* Active particles in complex and crowded environments. *Rev. Mod. Phys.* **88**, 045006 (2016).

- [242] Nandi, S. K., Biroli, G., Bouchaud, J.-P., Miyazaki, K. & Reichman, D. R. Critical dynamical heterogeneities close to continuous second-order glass transitions. *Phys. Rev. Lett.* **113**, 245701 (2014).
- [243] Dawson, K. *et al.* Higher-order glass-transition singularities in colloidal systems with attractive interactions. *Phys. Rev. E* **63**, 011401 (2000).
- [244] Sciortino, F., Tartaglia, P. & Zaccarelli, E. Evidence of a higher-order singularity in dense short-ranged attractive colloids. *Phys. Rev. Lett.* **91**, 268301 (2003).
- [245] Nandi, S. K., Bhattacharyya, S. M. & Ramaswamy, S. Mode-coupling glass transition in a fluid confined by a periodic potential. *Phys. Rev. E* **84**, 061501 (2011).
- [246] Chaudhuri, P., Berthier, L., Hurtado, P. I. & Kob, W. When gel and glass meet: A mechanism for multistep relaxation. *Phys. Rev. E* **81**, 040502(R) (2010).
- [247] Hurtado, P. I., Berthier, L. & Kob, W. Heterogeneous diffusion in a reversible gel. *Phys. Rev. Lett.* **98**, 135503 (2007).
- [248] Milner, S. T. & McLeish, T. C. B. Parameter-free theory for stress relaxation in star polymer melts. *Macromolecules* **30**, 2159–2166 (1997).
- [249] Falk, M. *et al.* Heterochromatin drives compartmentalization of inverted and conventional nuclei. *Nature* **570**, 395–399 (2019).
- [250] Meyer, K. N. *et al.* Cell cycle-coupled relocation of types I and II topoisomerases and modulation of catalytic enzyme activities. *J. Cell Biol.* **136**, 775–788 (1997).
- [251] Uhlmann, F. SMC complexes: from DNA to chromosomes. *Nat. Rev. Mol. Cell Biol.* **17**, 399 (2016).
- [252] Szabo, Q., Bantignies, F. & Cavalli, G. Principles of genome folding into topologically associating domains. *Sci. Adv.* **5** (2019).
- [253] Siebert, J. T. *et al.* Are there knots in chromosomes? *Polymers* **9** (2017).
- [254] Goundaroulis, D., Aiden], E. L. & Stasiak, A. Chromatin is frequently unknotted at the megabase scale. *Biophys. J.* **118**, 2268–2279 (2020).
- [255] Szabo, Q. *et al.* TADs are 3D structural units of higher-order chromosome organization in *Drosophila*. *Sci. Adv.* **4** (2018).

- [256] Chuang, C.-H. *et al.* Long-range directional movement of an interphase chromosome site. *Curr. Biol.* **16**, 825–831 (2006).
- [257] Michieletto, D., Orlandini, E. & Marenduzzo, D. Polymer model with epigenetic recoloring reveals a pathway for the de novo establishment and 3D organization of chromatin domains. *Phys. Rev. X* **6**, 041047 (2016).
- [258] Naughton, C. *et al.* Transcription forms and remodels supercoiling domains unfolding large-scale chromatin structures. *Nat. Struct. Mol. Biol.* **20**, 387 (2013).
- [259] Buckle, A., Brackley, C. A., Boyle, S., Marenduzzo, D. & Gilbert, N. Polymer simulations of heteromorphic chromatin predict the 3D folding of complex genomic loci. *Mol. Cell* **72**, 786–797.e11 (2018).
- [260] Barbieri, M. *et al.* Complexity of chromatin folding is captured by the strings and binders switch model. *Proc. Natl. Acad. Sci. U.S.A.* **109**, 16173–16178 (2012).
- [261] Stasiak, A., Racko, D., Benedetti, F. & Dorier, J. Are TADs supercoiled? *Nucleic Acids Res.* **47**, 521–532 (2018).
- [262] Dixon, J. R. *et al.* Topological domains in mammalian genomes identified by analysis of chromatin interactions. *Nature* **485**, 376 (2012).
- [263] Misteli, T. Beyond the sequence: cellular organization of genome function. *Cell* **128**, 787–800 (2007).
- [264] Japaridze, A. *et al.* Spatial confinement induces hairpins in nicked circular DNA. *Nucleic Acids Res.* **45**, 4905–4914 (2017).
- [265] <http://book.bionumbers.org/how-much-energy-is-released-in-atp-hydrolysis/>. Accessed 02 Oct 2019.
- [266] Plimpton, S. Fast parallel algorithms for short-range molecular dynamics. *J. Comput. Phys.* **117**, 1–19 (1995). <http://lammps.sandia.gov>.
- [267] Brakke, K. A. The surface evolver. *Exp. Math.* **1**, 141–165 (1992).
- [268] Marchetti, M. C. *et al.* Hydrodynamics of soft active matter. *Rev. Mod. Phys.* **85**, 1143–1189 (2013).
- [269] Woodhouse, F. G. & Goldstein, R. E. Spontaneous circulation of confined active suspensions. *Phys. Rev. Lett.* **109**, 168105 (2012).

- [270] Sanchez, T., Chen, D. T. N., DeCamp, S. J., Heymann, M. & Dogic, Z. Spontaneous motion in hierarchically assembled active matter. *Nature* **491**, 431 (2012).
- [271] Baule, A., Kumar, K. V. & Ramaswamy, S. Exact solution of a Brownian inchworm model for self-propulsion. *J. Stat. Mech.: Theory Exp.* **2008**, P11008 (2008).
- [272] Gooßen, S. *et al.* Molecular scale dynamics of large ring polymers. *Phys. Rev. Lett.* **113**, 169302 (2014).
- [273] Iwamoto, T. *et al.* Conformations of ring polystyrenes in bulk studied by SANS. *Macromolecules* **51**, 1539–1548 (2018).
- [274] Ferrari, F. & Lazzizzera, I. Polymer topology and Chern-Simons field theory. *Nucl. Phys. B* **559**, 673–688 (1999).
- [275] Narros, A., Moreno, A. J. & Likos, C. N. Effective interactions of knotted ring polymers. *Biochem. Soc. Trans.* **41**, 630–634 (2013).
- [276] Chichak, K. S. *et al.* Molecular Borromean rings. *Science* **304**, 1308–1312 (2004).
- [277] Tsalikis, D. G., Mavrantzas, V. G. & Vlassopoulos, D. Analysis of slow modes in ring polymers: Threading of rings controls long-time relaxation. *ACS Macro Lett.* **5**, 755–760 (2016).
- [278] Bruinsma, R., Grosberg, A., Rabin, Y. & Zidovska, A. Chromatin hydrodynamics. *Biophys. J.* **106**, 1871–1881 (2014).
- [279] Solon, A. P. *et al.* Pressure and phase equilibria in interacting active Brownian spheres. *Phys. Rev. Lett.* **114**, 198301 (2015).
- [280] Solon, A. P. *et al.* Pressure is not a state function for generic active fluids. *Nat. Phys.* **11**, 673–678 (2015).
- [281] Stenhammar, J., Wittkowski, R., Marenduzzo, D. & Cates, M. E. Activity-induced phase separation and self-assembly in mixtures of active and passive particles. *Phys. Rev. Lett.* **114**, 018301 (2015).
- [282] Abrams, C. F. & Kremer, K. Effects of excluded volume and bond length on the dynamics of dense bead-spring polymer melts. *J. Chem. Phys.* **116**, 3162–3165 (2002).

- [283] Pachong, S. M., Chubak, I., Kremer, K. & Smrek, J. Melts of nonconcatenated rings in spherical confinement. *J. Chem. Phys.* **153**, 064903 (2020).
- [284] Svaneborg, C. & Everaers, R. Characteristic time and length scales in melts of Kremer–Grest bead–spring polymers with wormlike bending stiffness. *Macromolecules* **53**, 1917–1941 (2020).
- [285] Kardar, M. & Zhang, Y.-C. Scaling of directed polymers in random media. *Phys. Rev. Lett.* **58**, 2087–2090 (1987).
- [286] Smrek, J. & Grosberg, A. Y. A novel family of space-filling curves in their relation to chromosome conformation in eukaryotes. *Physica A* **392**, 6375–6388 (2013).
- [287] Hamley, I. W. & Hamley, I. W. *The physics of block copolymers* (Oxford University Press, 1998).
- [288] Matsen, M. W. & Thompson, R. B. Equilibrium behavior of symmetric ABA triblock copolymer melts. *J. Chem. Phys.* **111**, 7139–7146 (1999).
- [289] Leibler, L. Theory of microphase separation in block copolymers. *Macromolecules* **13**, 1602–1617 (1980).
- [290] Edwards, S. F. The theory of rubber elasticity. *Br. Polym. J.* **9**, 140–143 (1977).
- [291] de Gennes, P. G. Reptation of a polymer chain in the presence of fixed obstacles. *J. Chem. Phys.* **55**, 572–579 (1971).
- [292] Brás, A. R. *et al.* Structure and dynamics of polymer rings by neutron scattering: breakdown of the Rouse model. *Soft Matter* **7**, 11169–11176 (2011).
- [293] Iwamoto, T. *et al.* Conformations of ring polystyrenes in semidilute solutions and in linear polymer matrices studied by SANS. *Macromolecules* **51**, 6836–6847 (2018).
- [294] Kruteva, M., Allgaier, J., Monkenbusch, M., Porcar, L. & Richter, D. Self-similar polymer ring conformations based on elementary loops: A direct observation by SANS. *ACS Macro Lett.* **9**, 507–511 (2020).
- [295] Grosberg, A. Y., Nechaev, S. K. & Shakhnovich, E. I. The role of topological constraints in the kinetics of collapse of macromolecules. *J. Phys.* **49**, 2095–2100 (1988).

- [296] Rosa, A., Di Stefano, M. & Micheletti, C. Topological constraints in eukaryotic genomes and how they can be exploited to improve spatial models of chromosomes. *Front. Mol. Biosci.* **6**, 127 (2019).
- [297] Benková, Z. & Cifra, P. Simulation of semiflexible cyclic and linear chains moderately and strongly confined in nanochannels. *Macromolecules* **45**, 2597–2608 (2012).
- [298] Benková, Z., Námer, P. & Cifra, P. Comparison of a stripe and slab confinement for ring and linear macromolecules in nanochannel. *Soft Matter* **12**, 8425–8439 (2016).
- [299] Lee, E., Kim, S. & Jung, Y. Slowing down of ring polymer diffusion caused by inter-ring threading. *Macromol. Rapid Comm.* **36**, 1115–1121 (2015).
- [300] Michieletto, D. On the tree-like structure of rings in dense solutions. *Soft Matter* **12**, 9485–9500 (2016).
- [301] Everaers, R. *et al.* Rheology and microscopic topology of entangled polymeric liquids. *Science* **303**, 823–826 (2004).
- [302] Wittmer, J. P., Meyer, H., Johner, A., Obukhov, S. & Baschnagel, J. Comment on “Molecular dynamics simulation study of nonconcatenated ring polymers in a melt. I. Statics” [J. Chem. Phys. 134, 204904 (2011)]. *J. Chem. Phys.* **139**, 217101 (2013).
- [303] Halverson, J. D., Lee, W. B., Grest, G. S., Grosberg, A. Y. & Kremer, K. Response to “Comment on ‘Molecular dynamics simulation study of nonconcatenated ring polymers in a melt. I. Statics’” [J. Chem. Phys. 139, 217101 (2013)]. *J. Chem. Phys.* **139**, 217102 (2013).
- [304] Dzubiella, J., Harreis, H. M., Likos, C. N. & Löwen, H. Sedimentation profiles of systems with reentrant melting behavior. *Phys. Rev. E* **64**, 011405 (2001).
- [305] Katsarou, A. F., Tsamopoulos, A. J., Tsalikis, D. G. & Mavrantzas, V. G. Dynamic heterogeneity in ring-linear polymer blends. *Polymers* **12** (2020).
- [306] Molchan, G. M. Maximum of a fractional Brownian motion: Probabilities of small values. *Commun. Math. Phys.* **205**, 97–111 (1999).
- [307] Metzler, R. *et al.* First passage behavior of multi-dimensional fractional Brownian motion and application to reaction phenomena. *First-Passage Phenomena and Their Applications* **3**, 175–202 (2014).

- [308] Jost, D. & Vaillant, C. Epigenomics in 3D: importance of long-range spreading and specific interactions in epigenomic maintenance. *Nucleic Acids Res.* **46**, 2252–2264 (2018).
- [309] Rauscher, P. M., Schweizer, K. S., Rowan, S. J. & de Pablo, J. J. Dynamics of poly[n]catenane melts. *J. Chem. Phys.* **152**, 214901 (2020).
- [310] Peddireddy, K. R. *et al.* Unexpected entanglement dynamics in semidilute blends of supercoiled and ring DNA. *Soft Matter* **16**, 152–161 (2020).
- [311] Chubak, I., Kremer, K., Likos, C. N. & Smrek, J. Emergence of active topological glass through directed chain dynamics and non-equilibrium phase segregation (2020).
- [312] Jackson, C. L. & McKenna, G. B. The glass transition of organic liquids confined to small pores. *J. Non-Cryst. Solids* **131-133**, 221–224 (1991).
- [313] Pissis, P., Daoukaki-Diamanti, D., Apekis, L. & Christodoulides, C. The glass transition in confined liquids. *J. Phys. Condens. Matter* **6**, L325–L328 (1994).
- [314] Liu, K., Patteson, A. E., Banigan, E. J. & Schwarz, J. M. Dynamic nuclear structure emerges from chromatin crosslinks and motors (2020).
- [315] Di Pierro, M., Potoyan, D. A., Wolynes, P. G. & Onuchic, J. N. Anomalous diffusion, spatial coherence, and viscoelasticity from the energy landscape of human chromosomes. *Proc. Natl. Acad. Sci. U.S.A.* **115**, 7753–7758 (2018).
- [316] Palacci, J., Sacanna, S., Steinberg, A. P., Pine, D. J. & Chaikin, P. M. Living crystals of light-activated colloidal surfers. *Science* **339**, 936–940 (2013).
- [317] Strickfaden, H., Zunhammer, A., van Koningsbruggen, S., Köhler, D. & Cremer, T. 4D chromatin dynamics in cycling cells: Theodor Boveri’s hypotheses revisited. *Nucleus* **1**, 284–297 (2010).
- [318] van den Engh, G., Sachs, R. & Trask, B. Estimating genomic distance from DNA sequence location in cell nuclei by a random walk model. *Science* **257**, 1410–1412 (1992).
- [319] Nagashima, R. *et al.* Single nucleosome imaging reveals loose genome chromatin networks via active RNA polymerase II. *J. Cell Biol.* **218**, 1511–1530 (2019).

[320] Leidescher, S. *et al.* Spatial organization of transcribed eukaryotic genes (2020).
Preprint on bioRxiv at <https://www.biorxiv.org/content/early/2020/05/21/2020.05.20.106591>.

Iurii Chubak | Curriculum Vitae

Computational and Soft Matter Physics Group
Faculty of Physics, University of Vienna
Sensengasse 8/15, 1090 Vienna, Austria

📞 +4366 (565) 106 182 • ✉ iurii.chubak@univie.ac.at
🔍 [Google Scholar](#) • [R^G Researchgate](#) • [ORCID](#)

Education

University of Vienna <i>PhD, Physics</i> <i>Thesis title:</i> Novel states of matter for topological polymers <i>Advisor:</i> Christos N. Likos	Vienna, Austria 2017–present
University of Vienna <i>MSc with distinction, Physics</i> <i>Thesis title:</i> Interfacial behavior of ring polymer solutions on planar, hard walls <i>Advisor:</i> Christos N. Likos	Vienna, Austria 2015–2017
Lviv National University <i>BSc with distinction, Physics</i>	Lviv, Ukraine 2010–2014

Research Experience

University of Vienna <i>University Assistant</i>	Vienna, Austria 2017–present
<ul style="list-style-type: none">○ Investigated properties of equilibrium and non-equilibrium polymeric materials.○ Performed and analyzed coarse-grained molecular simulations.○ Developed simulation and data analysis codes.	

Fellowships & Honours

Vienna Doctoral School in Physics Fellowship	2017–present
Dean's List honour for outstanding academic performance in the Master's programme at the Faculty of Physics, University of Vienna	2017

Skills & Techniques

- Programming languages: C/C++, CUDA, Python (NumPy, SciPy, Numba, Matplotlib).
- Experience with molecular dynamics and Monte Carlo simulations (worked with LAMMPS and HOOMD-blue simulation engines), principal path analysis, coarse-graining via free energy differences, umbrella sampling, density functional theory for classical fluids.
- Experience with mesoscopic particle-based hydrodynamics approaches (multi-particle collision dynamics, dissipative particle dynamics).

Teaching Experience

University of Vienna	Vienna, Austria
Co-supervised two bachelor students	2019–2020
Teaching Assistant, <i>Advanced Statistical Physics and Soft Matter Physics</i>	Fall 2020
Teaching Assistant, <i>Quantum Mechanics I</i>	Spring 2020
Teaching Assistant, <i>Introduction to Calculus</i>	Fall 2018
Student Tutor, <i>Thermodynamics and Statistical Physics I</i>	Spring 2017, Spring 2018
Student Tutor, <i>Introduction to Calculus</i>	Fall 2016

Conferences & Workshops

CMD2020GEFES Conference, <i>online</i> , virtual contributed talk	Sep 2020
MPI for Dynamics and Self-Organization, <i>Göttingen (Germany)</i> , virtual seminar talk	May 2020
Machine Learning in Physics VDSP-ESI Winter School, <i>Vienna (Austria)</i>	Jan 2020
Polymers and Soft Materials: Glasses, Gels and Networks School, <i>Erice (Italy)</i> , poster	Jul 2019
2nd Vienna Polymer-Group Symposium, <i>Tulln (Austria)</i> , contributed talk	Jun 2019
Winter School on Motile Active Matter, <i>Jülich (Germany)</i> , poster	Mar 2019
Molsim 2019, <i>Amsterdam (Netherlands)</i> , poster	Jan 2019
ViCoM Conference: From Electrons to Phase Transitions, <i>Vienna (Austria)</i> , poster	Apr 2018
1st Vienna Polymer-Group Symposium, <i>Vienna (Austria)</i>	Feb 2018
Fundamental Problems In Statistical Physics XIV School, <i>Bruneck (Italy)</i> , poster	Jul 2017

Publications

- [1] Iurii Chubak, Emanuele Locatelli, and Christos N. Likos. Ring polymers are much stronger depleting agents than linear ones. *Molecular Physics*, **116**, 2911–2926 (2018). DOI: [10.1080/00268976.2018.1503744](https://doi.org/10.1080/00268976.2018.1503744)
- [2] Esmaeel Moghimi, Iurii Chubak, Antonia Statt, Michael P. Howard, Dimitra Founta, George Polymeropoulos, Konstantinos Ntetsikas, Nikos Hadjichristidis, Athanassios Z. Panagiotopoulos, Christos N. Likos, and Dimitris Vlassopoulos. Self-organisation and flow of low-functionality telechelic star polymers with varying attraction. *ACS Macro Letters*, **8**, 766–772 (2019). DOI: [10.1021/acsmacrolett.9b00211](https://doi.org/10.1021/acsmacrolett.9b00211)[§]
- [3] Jan Smrek*, Iurii Chubak*, Christos N. Likos, and Kurt Kremer. Active topological glass. *Nature Communications*, **11**, 26 (2020). DOI: [10.1038/s41467-019-13696-z](https://doi.org/10.1038/s41467-019-13696-z)[§]
- [4] Zahra Ahmadian Dehaghani, Iurii Chubak, Christos N. Likos, and Mohammad Reza Ejtehadi. Effects of topological constraints on linked ring polymers in solvents of varying quality. *Soft Matter*, **16**, 3029–3038 (2020). DOI: [10.1039/C9SM02374G](https://doi.org/10.1039/C9SM02374G)
- [5] Stanard Mebwe Pachong*, Iurii Chubak*, Kurt Kremer, and Jan Smrek. Melts of nonconcatenated rings in spherical confinement. *The Journal of Chemical Physics*, **153**, 064903 (2020). DOI: [10.1063/5.0013929](https://doi.org/10.1063/5.0013929)[§]
- [6] Esmaeel Moghimi*, Iurii Chubak*, Dimitra Founta, Konstantinos Ntetsikas, George Polymeropoulos, Nikos Hadjichristidis, Christos N. Likos, and Dimitris Vlassopoulos. The influence of arm composition on the self-assembly of low-functionality telechelic star polymers in dilute solutions. *Colloid and Polymer Science*, in press (2020).[§]

Works in progress

- [7] Iurii Chubak, Christos N. Likos, Kurt Kremer, and Jan Smrek. Emergence of active topological glass through directed chain dynamics and non-equilibrium phase segregation, submitted.[§]
- [8] Stanard Mebwe Pachong*, Iurii Chubak*, Kurt Kremer, Christos N. Likos, and Jan Smrek. Active topological glass as a model for coherent motion of chromatin, in preparation.[§]
- [9] Iurii Chubak*, Esmaeel Moghimi*, Antonia Statt, George Polymeropoulos, Nikos Hadjichristidis, Kell Mortensen, Athanassios Z. Panagiotopoulos, Christos N. Likos and Dimitris Vlassopoulos. Re-entrant gels from telechelic star polymers, in preparation.
- [10] Iurii Chubak, Christos N. Likos, and Jan Smrek. Topological effects in polydisperse ring polymer solutions, in preparation.
- [11] Iurii Chubak, Christos N. Likos, and Sergei Egorov. Microscopic and mesoscopic modeling of confined ring polymers, in preparation.

*Joint first authorship

[§]Is a part of this thesis